UNIVERSIDAD COMPLUTENSE DE MADRID
FACULTAD DE CIENCIAS QUÍMICAS

TESIS DOCTORAL

Diseño y desarrollo de biomateriales para la reparación de la médula espinal lesionada

Design and development of biomaterials for spinal cord injury repair

MEMORIA PARA OPTAR AL GRADO DE DOCTORA

PRESENTADA POR

Ana Domínguez Bajo

DIRECTORES

María Concepción Serrano López-Terradas
Elisa López Dolado

Madrid

UNIVERSIDAD COMPLUTENSE DE MADRID

Facultad de Química

TESIS DOCTORAL

Diseño y desarrollo de biomateriales para la reparación de la médula espinal lesionada

-

Design and development of biomaterials for spinal cord injury repair

MEMORIA PARA OPTAR AL GRADO DE DOCTOR

PRESENTADA POR

Ana Domínguez Bajo

DIRECTORAS

María Concepción Serrano López-Terradas

Elisa López Dolado

Instituto de Ciencia de Materiales de Madrid (ICMM-CSIC)

2020

This thesis project has been made partially possible thanks to the financial support received from the European Union's Horizon 2020 research and innovation programme under grant agreement No. 737116 corresponding to the ByAxon project (H2020-FET-OPEN-RIA, EC; 2017-2020).

Concretely, the ByAxon project is focused on the development of novel platforms composed of sensors and electrodes able of acting as an active bypass when implanted in the injured spinal cord. This project has been supported by an interdisciplinary consortium, in which researchers from different fields such as Materials science, Neuroscience, Nanotechnology, Medicine, and Electronics, worked together in the fabrication of some of the biomaterials studied in this thesis, eventually serving as an alternative approach for spinal cord injury treatment. The PhD student and her supervisors want also to thank all the consortium members belonging to the Fundación IMDEA Nanociencia (Spain), *Scuola Internazionale Superiore di Studi Avanzati di Trieste* (Italy), Servicio de Salud de Castilla-La Mancha (Spain), *Centre National de la Recherche Scientifique* (France), and Mfd-Diagnostics GmbH (Germany) for their support in the development of this experimental work.

This thesis project has been also funded by the *Agencia Estatal de Investigación* of Spain and the *Fondo Europeo de Desarrollo Regional* (MAT2016-78857-R, AEI/FEDER, UE).

Acknowledgements / Agradecimientos

En primer lugar, me gustaría agradecer a mis padres el esfuerzo que han hecho para que pudiera estudiar lo que yo quería, y a mi hermana por haberme apoyado desde el primer momento que dije que quería intentar dedicarme a la investigación. A mis amigos/as de toda la vida, especialmente a Isa, Marin, Torre, Carlos, Cogo, y Ángela… por llevar tanto tiempo al lado en las buenas y en las malas, por apoyarme en todas las idas de pinza y cada vez que he empezado a buscar un reto o un destino nuevo, y por todo lo vivido y lo que queda, mil gracias! A Claudia por estar ahí desde enanas, y demostrar que las barreras geográficas y de idiomas no existen si una no quiere. Muchas gracias también a Sandra, por haberme ayudado tanto desde que empezamos a correr juntas a la salida del máster para no perder el metro.

Extendiéndome más con las personas que he conocido gracias a la tesis: Muchas gracias a toda la gente del HNP, por tratarme como si llevara años trabajando allí desde el primer segundo, por las mil horas en microscopía, por ayudarme cada vez que queríamos intentar algo nuevo y en todos los cursos que he ido haciendo, y por animarme a participar en cualquier actividad o ciclo de seminarios que se ha organizado. A Hugo, por todos los consejos que me has ido dando desde que fuiste tan majo de pararte a hablar conmigo en el Alcázar hace unos años ya! Y a todas las personas del grupo de Juan de los Reyes, por todas las discusiones dentro y fuera del labo, por toda la ayuda y los proyectos en común, y por todas las cerves, los vinos, y lo que haga falta!! Especial mención a Marta: mil gracias por hacer de confidente, por todos los debates, las cerves, el tenis, los congresos, y todas las personas que he conocido gracias a ti! No se puede ser más buena gente! Muchas gracias también a Silvia por el apoyo desde que me adoptó como hermana pequeña en Berlín.

Mil gracias también a la gente del ICMM! Especialmente a Raquel, Óscar, María, Alfonso, María Jesús, Álvaro, Vicente, Fer, César y Dani, por estar peor

de la neura que yo, pero sobre todo por hacer que me lo haya pasado tan bien por allí y evitar que el orde saliera por la ventana!, desde las rutas y los cafés con fruta… hasta el surf, los chistes y los tomates! Gracias también a Puerto por dejarme ser parte de uno de sus proyectos, y a todas las personas del campus de la UAM que han colaborado con nuestro labo.

Grazie mille anche ai miei amici di Trieste!! Ai miei coinquilini in Viale, l'ufficio 421, via Giulia, e le altre persone della SISSA, per le lezioni d'italiano, e per fare il mio viaggio meraviglioso dentro e fuori il laboratorio! Many thanks to André as well, hope to see you in Aveiro!

Muchas gracias también a Teresa Portolés, por estar tan disponible y por toda la ayuda dentro de la Complu. Por último pero no menos importante, mil gracias a LINER! A Elisa, por todo lo aprendido, por ayudarnos tanto a entender el enfoque clínico, y por tomarte todo siempre con una sonrisa, aunque a veces la vida sea dura. Mil gracias Mari. A Conchi, por haber confiado en mi para formar parte del laboratorio, por estar siempre al pie del cañón, siendo la que más trabaja, incluso cuando parece que la vida no puede ponerse más difícil. Por todos los consejos y el apoyo durante estos años, y por ser un claro ejemplo a seguir en la carrera investigadora. Ojalá los/as jefes/as de laboratorio que me encuentre a partir de ahora sean tan buenos/as como tú. Muchas gracias de verdad. Para el final, a Don Francisco Ankor, o Ankor para los amigos. Mil gracias por el esfuerzo y todas las horas de más, especialmente al principio, cuando viste que el desorden ordenado en persona había llegado a tu vida laboral, a dejarlo todo lleno de papeles con la radio de fondo. Por haberme ayudado y apoyado tanto dentro y fuera del labo (y con las recetas de cocina, y las rutinas de ejercicio…), y lo más importante, por haberme reído tanto contigo y haberte convertido en mi hermano mayor en 3 años y pico. Esta tesis hubiera sido imposible sin ti, un placer haber sido también tu estudiante.

Gracias por hacer de la tesis una de las mejores etapas de mi vida.

Entre tanta relatividad,
el que mejor vive
es aquél que sabe moldear
su espacio y su tiempo.
Sin importar
el tiempo o el espacio
del que disponga.

- **Ignacio Fornés.**

Index of Contents

Index of Figures and Tables

INTRODUCTION

MATERIAL AND METHODS

RESULTS

GDMs (II): rGO-Microfibres

List of abbreviations

5-HT: Serotonine

AC: Acetoxymethyl group

AFM: Atomic force microscopy

Ag: Silver

ANOVA: Analysis of variance

ArgI: Arginase I

ASIA: American Spinal Injury Association

ATR: Attenuated total reflection mode (see also in ATR-FTIR)

Au: Gold

Au-NWs: arrays made of gold NWs

BBB: Blood brain barrier

BDNF: Brain-derived neurotrophic factor

bFGF: Basic fibroblast growth factor

BSEs: Backscattered electrons

ChABC: Chondroitinase ABC

CIF: Caudal interface of the lesion

CLSM: Confocal laser scanning microscopy

CNS: Central nervous system

CNTs: Carbon nanotubes

CPG: central pattern generator

CSPGs: Chondroitin sulphate proteoglycans

CST: Corticospinal tract

DAPI: 4′,6-diamidino-2-phenylindole

DIV: Days *in vitro*

DPI: Days post-injury

ECM: Extracellular matrix

EGF: Epidermal growth factor

ENPCs: Embryonic neural progenitor cells

ESCs: Embryonic stem cells

EthD-1: Ethidium homodimer-1

FESEM: Field emission scanning electron microscopy

FGF2: Fibroblast growth factor 2

FID: Free-induction decay signal

FTIR: Fourier-transform infrared spectroscopy

FWHM: Full width at half maximum (of XPS spectra peaks)

GaP: Gallium phosphide

GDMs: Graphene-derived materials

GDNF: Glial-derived growth factor

GFAP: Glial fibrillary acidic protein

GM: Grey matter

GO: Graphene oxide

H&E: Hematoxylin and eosin staining

HA: Hyaluronic acid

hESCs: Human embryonic stem cells

HOPG: Highly oriented pyrolytic graphite

I: Injury

IGF-1: Insulin-like growth factor 1

IINs: Intraspinal/propiospinal interneurons

I-MF: Animals carrying rGO microfibers scaffold

IP: Intraperitoneal

ISNCSCI: International Standard for the Neurological Classification of Spinal Cord Injury

L: Lesion area without implant

LFP: Left forepaw

LH: Left hemicord

MAG: Myelin-associated glycoprotein

MAP2: Microtubule-associated protein 2

MEAs: Microelectrode arrays

MF: Close proximities of the rGO microfibers area

MFs: Microfibers

MRI: Magnetic resonance imaging

MSCs: Mesenchymal stem cells

NGF: Nerve growth factor

NGS: Normal goat serum

Ni: Nickel

Ni-NWs: Arrays made of nickel NWs

NIR: Near-infrared

NMR: Nuclear magnetic resonance

NPCs: Neural progenitor cells

NSCs: Neural stem cells

NT-3: Neurotrophin 3

NWs: Nanowires

OB: Olfactory bulb

OECs: Olfactory ensheathing cells

OMgp: Oligodendrocyte myelin glycoprotein

OPCs: Oligodendrocyte precursor cells

PB: Phosphate buffer

PBS: Phosphate-buffered saline

PC12: Pheochromocytoma cell line

PCL: Polycaprolactone

PDMS: Polydimethylsiloxane

PEDOT: Poly(3,4-ethylenedioxythiophene)

PEG: Polyethylene glycol

PFA: Paraformaldehyde

PGA: Poly(glycolic acid)

pHEMA: Poly(2-hydroxyethyl methacrylate)

PL12: Perilesional areas at 1-2 mm from the lesion site

PLA: Poly(lactic acid)

PLGA: Poly(lactic-co-glycolic acid)

PLL: Poly-L-lysine

PLLA: Poly(L-lactic acid)

PLL-FITC: Poly-L-lysine - fluorescein isothiocyanate

PNS: Peripheral nervous system

Pt: Platinum

RECA-1: Rat endothelial cell antigen 1

RF: Radiofrequency

RFP: Right forepaw

RGD: Arginine-glycine-aspartic acid

rGO: Reduced graphene oxide

rGO-SC: Animals carrying the rGO foam scaffold

RIF: Rostral interface of the lesion

rNCCs: Rat neural cortical cells

ROS: Reactive oxygen species

RT: Room temperature

SC: rGO-foam inner part area

SCI: Spinal cord injury

SEM: Scanning electron microscopy

Sema3A: Semaphorin 3A

SPPC: cervical proprio-spinal premotoneuronal system

StaUp: Stand-ups on both hindpaws

TB: *Triceps brachii*

TEM: Transmission electron microscopy

TGA: Thermogravimetric analysis

TH: Tyrosine hydroxylase

TS: *Triceps surae*

VGluT2: Vesicular glutamate transporter 2

WM: White matter

XPS: X-ray photoelectron spectroscopy

1. ABSTRACT

Spinal cord injury (SCI) continues to be a therapeutic challenge as there is no cure to date. This complex syndrome is characterized by a plethora of events at the molecular and cellular levels, including the disruption of neuronal axons and the creation of an inhibitory environment for spinal tissue regeneration at the lesion site. Thus, the implementation of novel implantable devices that could be placed at the injured tissue, in order to bridge the lesion as well as to induce its repair and the recovery of its functionality, has been widely explored by researchers working in different areas of Tissue Engineering and Materials Science and clinicians. For instance, nanotechnology advances in the last decades have enabled the creation and improvement of cell non-invasive extracellular arrays. These platforms are composed of nanoelectrodes, which can be manipulated to achieve desired biological responses by means of electrical stimulation that modulates neural networks development and activity. Another strategy that is receiving increasing attention consists of the design of 3D biomaterials to fill and stabilize the lesion cavity, acting as a support and guide of the different neural tissue components, such as blood vessels, glial components and neurites, for neural reconnection.

In this thesis, we have investigated two different substrates as potentially efficient neural interfaces based on different strategies. On the one hand, we tested the *in vitro* biocompatibility of 2D metal-based nanowires (NWs) that could work as nanoelectrodes. These NWs will be eventually included in a device able of acting as a bypass once placed at the lesion site after SCI. Concretely, these nanoelectrodes consisted of vertically arranged metal NWs made of either nickel (Ni) or gold (Au) grown over a flexible Au base by template-assisted electrodeposition. *In vitro* tests were focused on how chemical composition and nanotopography features could modulate the biological behaviour of primary neural cells in culture. On the other hand, two kinds of

biocompatible 3D scaffolds made of reduced graphene oxide (rGO) were chronically implanted in the right hemisected cervical spinal cord (C6 level) of a rat experimental model of SCI. *In vivo* biocompatibility, in terms of behaviour affectation along with systemic and local tissue responses, was thoroughly studied four months after implantation following an interdisciplinary approach. Specifically, the two scaffolds under investigation were a rGO highly porous cylindrical foam (rGO foam) and rGO microfibers integrated in a gelatin hydrogel (rGO-MFs), both without any additional biological functionalization.

Regarding metallic electrodes, results demonstrated that chemical composition and nanotopography, either separately or in combination, modulate neural cells behaviour. Particularly, Ni-NWs increased cell survival, boosted neuronal differentiation and reduced the amount of glial cells with respect to their flat counterparts. Conversely, nanotopography seemed to have negligible effects on these parameters when cells were cultured on Au substrates. With respect to rGO-based biomaterials, both rGO foams and rGO-MFs fostered the stabilization of the injured spinal tissue, as well as the presence of neuronal structures along with blood vessels at the lesion epicentre. Moreover, rGO foams reduced perilesional damage as well as caused no compressive or tensile harm in the contralateral hemicord and rostral/caudal regions. Indeed, their presence modulated the inflammatory response. Finally, none of the implants provoked impairments in rat spontaneous behaviour or induced systemic toxicity as evidenced in major organs. Taken together, these results demonstrate the promising potential of both NWs and rGO scaffolds as neural interfaces capable of fostering the repair of the injured spinal cord. Further studies including biological functionalization and the application of rehabilitation protocols, such as aerobic motor training, might improve their therapeutic potential by a synergistic effect of topographical, chemical, mechanical and sensory stimuli, thus boosting neural repair after SCI.

1. RESUMEN

La lesión medular espinal continúa siendo un gran desafío terapéutico, ya que sigue sin existir ningún tratamiento que permita su curación completa. Este síndrome clínico se caracteriza por un conjunto complejo de cambios a nivel molecular y celular entre los que destacan el daño de los axones neuronales y la creación de un entorno inhibitorio para la regeneración del tejido lesionado. Por ello, clínicos y científicos especialistas en los campos de Ingeniería de Tejidos y Ciencia de Materiales llevan años explorando la implementación de nuevos dispositivos implantables que puedan colocarse en el lugar de la lesión con el fin de inducir tanto la regeneración tisular como su recuperación funcional. Por ejemplo, los avances en nanotecnología de las últimas décadas han permitido la creación y optimización de plataformas de *arrays* extracelulares no invasivos. Dichas plataformas están compuestas por nanoelectrodos, cuyas características pueden manipularse para lograr las respuestas biológicas deseadas una vez en contacto con redes neuronales *in vitro*, o implantados en el tejido neural lesionado *in vivo*. Estos dispositivos se basan en el uso de procedimientos de estimulación eléctrica para modular el desarrollo y la actividad de las redes neuronales, lo que podría resultar beneficioso para la recuperación del tejido medular dañado. Otra estrategia que está recibiendo una atención creciente consiste en el diseño de biomateriales 3D que puedan ser implantados en la lesión con el fin de estabilizar la médula espinal, y actuar como soporte y guía de los diferentes componentes del tejido espinal, entre los que cabe citar las estructuras vasculares, los componentes gliales y las neuritas, para alcanzar reconexión.

En esta tesis, hemos investigado dos plataformas diferentes capaces de actuar como interfaces neurales basadas en las dos estrategias citadas anteriormente. Por un lado, hemos estudiado la biocompatibilidad *in vitro* de nanohilos metálicos (NWs) que funcionarán como nanoelectrodos dentro de un

dispositivo capaz de actuar como "bypass" en el sitio de la lesión. Concretamente, estos nanohilos metálicos se han fabricado mediante electrodeposición de níquel (Ni) u oro (Au) sobre una base plana y flexible de Au, de manera que queden anclados y dispuestos verticalmente sobre ella. Las pruebas *in vitro* se centraron en el efecto que ejercen la composición química y la nanotopografía en el comportamiento biológico de cultivos primarios de células neurales. Por otro lado, dos tipos de plataformas 3D fabricadas a partir de óxido de grafeno reducido (rGO) se implantaron crónicamente en un modelo de hemisección lateral derecha de la médula espinal cervical (C6) en rata. La biocompatibilidad de estos implantes se estudió en detalle siguiendo un enfoque interdisciplinar. En concreto, los estudios de biocompatibilidad *in vivo* se centraron en examinar posibles cambios en el comportamiento de los animales, así como en el estudio de las respuestas tisulares locales y sistémicas causadas por su implantación. Específicamente, los implantes consistieron, por un lado, en una espuma cilíndrica y altamente porosa ("rGO foam"), y, por otro lado, en microfibras de rGO integradas en un hidrogel de gelatina ("rGO-MFs"), ambos sin ninguna funcionalización biológica adicional.

Con respecto a los electrodos metálicos, los resultados demostraron que la composición química y la nanotopografía, ya sea por separado o combinadas, modulan el comportamiento de las células neurales *in vitro*. Particularmente, los nanohilos de Ni aumentaron tanto la supervivencia celular como la diferenciación hacia fenotipo neuronal, y además redujeron la presencia de células de glía, con respecto a sus equivalentes planos. Por el contrario, la nanotopografía pareció no ejercer efectos relevantes sobre el comportamiento de las células neurales crecidas sobre sustratos de Au. Con respecto a los biomateriales basados en rGO, tanto las espumas como las microfibras promovieron la estabilización del tejido espinal lesionado, así como la presencia de estructuras neuronales acompañadas de vasos sanguíneos en el epicentro de

la lesión. Además, las espumas de rGO redujeron el daño perilesional y no causaron efectos adversos por compresión ni tracción, ni en la hemimédula izquierda, ni en las regiones rostral y caudal con respecto al centro de la lesión. De hecho, su presencia moduló las respuestas inflamatorias. Finalmente, ninguno de los implantes provocó alteraciones en el comportamiento espontáneo de las ratas, ni toxicidad sistémica, tal y como se evidenció tras el análisis de varios órganos internos. En conclusión, estos resultados demuestran el potencial de ambas plataformas como interfaces neurales capaces de promover la reparación de la médula espinal lesionada. La funcionalización biológica de estos materiales, además de su aplicación combinada con terapias de rehabilitación, como el entrenamiento físico aeróbico, podrían mejorar su potencial terapéutico mediante un efecto sinérgico, impulsando así la reparación neural después de la lesión medular.

2. INTRODUCTION

2.1. Neurophysiology of the spinal cord

The spinal cord is a cylindrical organ (~8-12 mm in diameter in humans and ~3-4 mm in rats), part of the central nervous system (CNS), which is protected by the backbone. Between the spinal tissue and the vertebrae, the spinal cord is surrounded by 3 membranes mostly composed of connective tissue, called meninges: dura matter, arachnoid and pia matter. Moreover, between arachnoid and pia matter membranes, there is a space, called subarachnoid space, which is filled with cerebrospinal liquid and contains arteries and other vessels that supply blood to the spinal tissue [**Figure I1A**; **Papa *et al.* 2020**].

The spinal cord and the backbone are divided into five regions from the base of the skull: cervical, thoracic, lumbar, sacral and coccyx. From birth, the spinal cord does not occupy the entire length of the vertebral canal but ends in the first lumbar vertebras. Thus, the relative shortening of the spinal cord with respect to the vertebral column explains why there is not an exact match between the spinal segments and the vertebrae [**Figure I1B; García-Porrero *et al.* 2015a**]:

- The 8 cervical spinal segments correspond to the first 7 cervical vertebrae.
- The following 12 thoracic spinal segments continue until the middle of the T11 vertebra.
- The 5 lumbar spinal segments project from T11 to the upper limit of the L1 vertebra.
- The final 5 sacral spinal segments and the coccygeal segment are located at the level of L1.

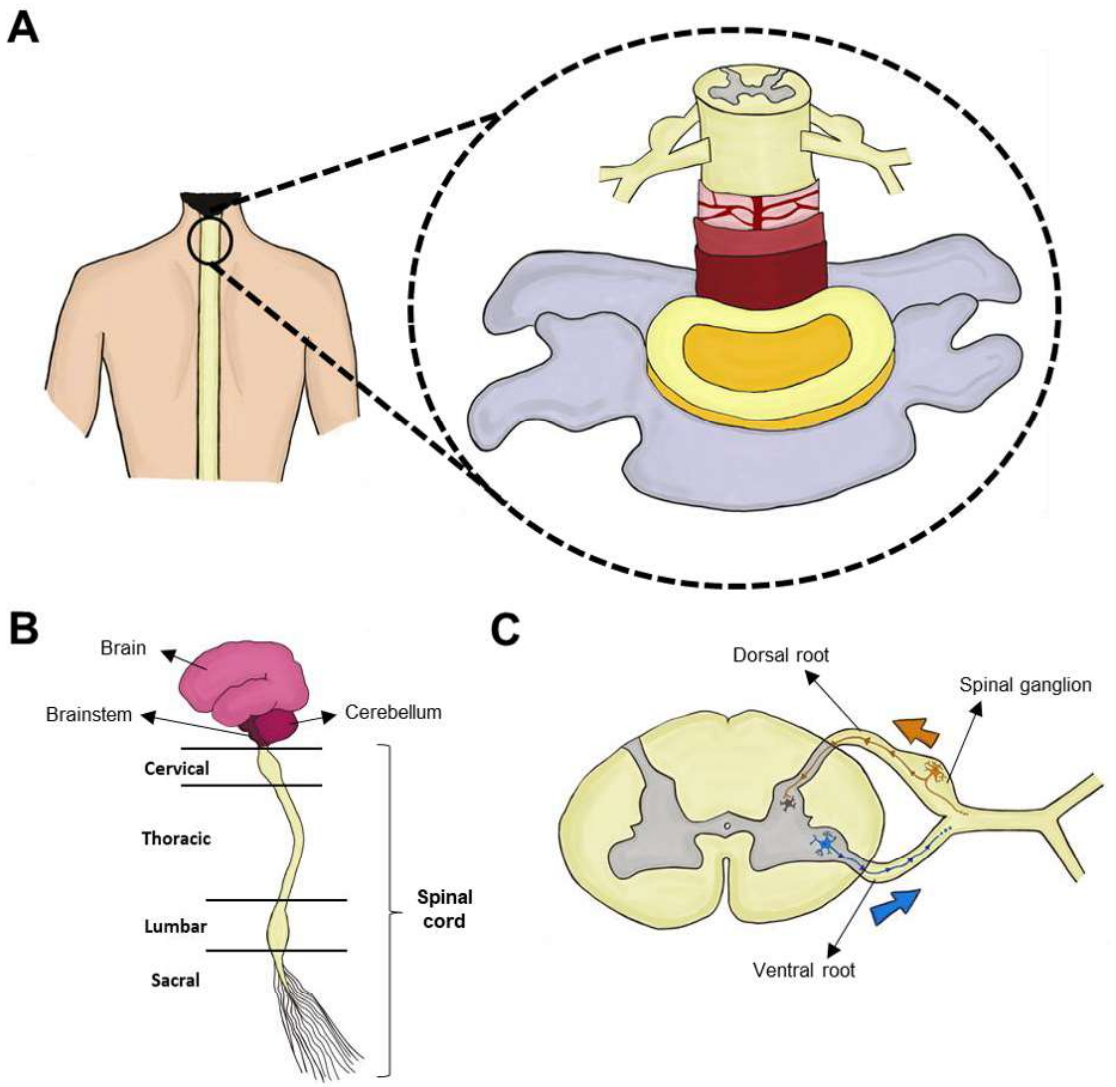

Figure I1. Basic insights in spinal cord neuroanatomy. A) Scheme of the spinal cord surrounded by the meninges and protected by a backbone vertebra. B) Spinal cord regions. C) Spinal nerve scheme.

The CNS communicates with the rest of the body through 31 pairs of spinal nerves that emerge from the spinal cord. Spinal nerves are groups of nervous terminals that convey either sensory information to the spinal cord or motor information to the peripheral effectors (*i.e.* organs, groups of muscles). Each pair ends at/starts from a different spinal segment. Concretely, each spinal nerve pair is attached to the spinal cord by a dorsal (posterior) root and a ventral (anterior) root (**Figure I1C**). At each dorsal root there is a spinal

ganglion, where the bodies of the sensory neurons of the different neural pathways are located. Laterally to the ganglion, the dorsal root and the ventral root converge forming the trunk of the spinal nerve that leaves the vertebral column through the intervertebral foramina [**García-Porrero *et al.* 2015b**]. Then, each spinal nerve divides into a dorsal and a ventral ramus. Each ramus contains both sensory and motor nervous terminals. Indeed, these motor and sensory terminals coming from different nerve roots intermix to form nerves of another division of the nervous system known as peripheral nervous system (PNS). Thus, spinal cord (which belongs to the CNS) supplies neural innervation to all muscle and cutaneous areas through PNS. [**Ferrero and Di Liberto, 2020**]. Concretely, PNS contains the autonomic nervous system, which in turn, it is divided in sympathetic and parasympathetic systems. Both systems, contain afferent sensitive (from the organs to the spinal cord) and efferent motor spinal (from the spinal cord to the organs) nerves that control and coordinate internal organs activity all over the organism. Importantly, each spinal segmental region innervates a specific region of the skin (called dermatome), muscle (being the specific group of muscles innervated by a spinal nerve called myotome) or organ group [**Ahuja *et al.* 2017; Puelles López *et al.* 2008a; Ferrero and Di Liberto, 2020**].

The spinal cord itself is organized into grey matter areas (which mainly contain neuronal cell body clusters of different kinds of neurons, such as interneurons and motoneurons, also called neuronal nuclei, along with terminals of axons that synapse with these neurons) and white matter areas (which mainly contain myelinated axons ordered in tracts of diverse size) [**Figure I2A**; **Ahuja *et al.* 2017; Garcia-Porrero *et al.* 2015c; Puelles Lopez *et al.* 2008b**].

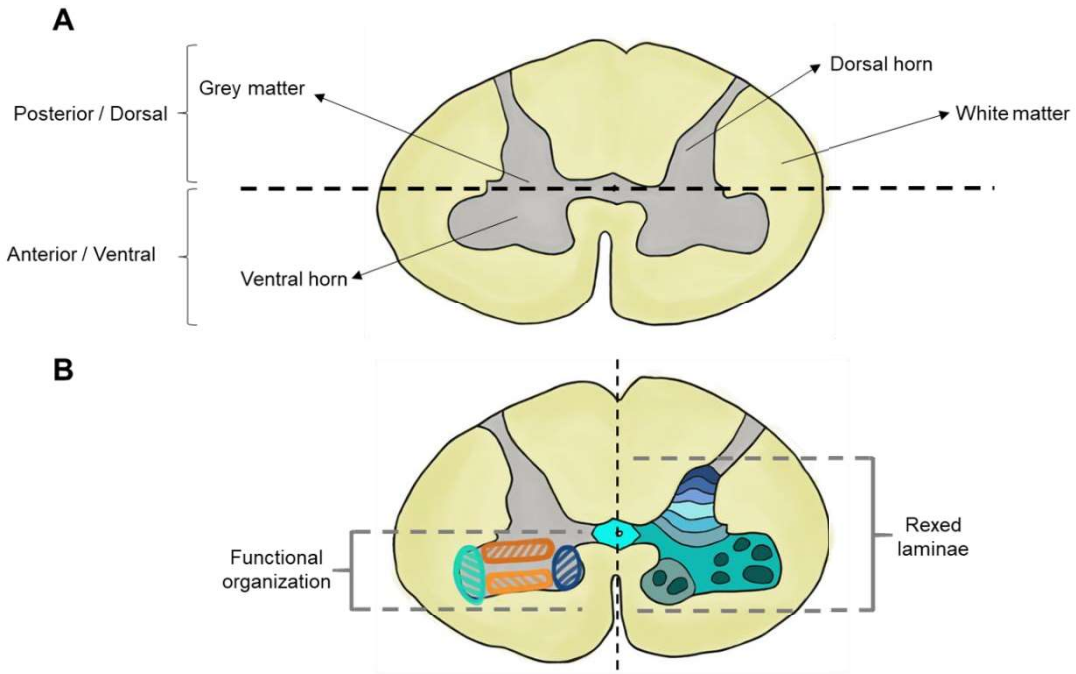

Figure I2. Spinal cord internal organization. A) General division of the spinal cord in white and grey areas. B) Organization of the grey matter by functionality (left hemicord) or Rexed laminae (right hemicord). Redrawn from [**Ojeda *et al.* 2004**].

More specifically, grey matter is divided into the dorsal/posterior horns, the intermediate region and the ventral/anterior horns. Neuronal nuclei can be classified attending to different criteria (**Figure I2B**). The most known classification is the ten layers of Rexed laminae, where neurons are organized according to their size, shape and packing density of their cell bodies. Although originally this division was not made due to functional differences, neurons contained in the grey matter are also grouped according to their function [**Ojeda *et al.* 2004a**]. For example, motoneurons are concentrated at the ventral/anterior horn of the spinal cord. Their axons send motor information through the ventral/anterior root to the striated musculature of the locomotor system of the trunk and extremities. Indeed, motoneurons occupy a specific region within the ventral horn according to the major function of the muscles innervated (dorsally located, flexor; ventrally located, extensor of a determined joint) and based on the location of the limb muscles innervated (located

medially within the dorsal horn: muscles more proximal to the spinal cord such as the pelvis and the shoulders; located laterally: muscles that control the joints situated farther from the centre of the body, such as the hands and feet). Ventral roots of the grey matter are also known as motor roots due to the fact that motor terminals leave the spinal cord through them, whereas the dorsal/posterior roots are also called sensory roots, because nervous terminals which transmit sensory information enter the spinal cord to make synapses with the neurons located within the grey matter through them [**Garcia-Porrero *et al.* 2015d; Ojeda *et al.* 2004b**].

The white matter [**Figure I3; Garcia-Porrero *et al.* 2015e; Puelles Lopez *et al.* 2008b; Champney, 2017a**], in its turn, can be subdivided into several ascending and descending tracts, which are composed of the bundles of axons that originate from and project to specific regions in the brain and periphery effectors, located in the same (ipsilateral) or the opposite (contralateral) sides of the body. Commissural tracts are those that cross the spinal cord centreline. Each of these tracts transmits specific information and responds to the following organization:

- Ascending pathways (from the rest of the body to the brain). General somatic sensitivity coming from the trunk and limbs is driven by two different systems: The posterior cord-medial lemniscus system and the anterolateral - spinothalamic system [**Garcia-Porrero *et al.* 2015f**]:
    - Dorsal lemniscal columns tracts (ipsilateral) are responsible for epicritic sensibility (light touch, pression, vibration sensitivity) and body posture (proprioceptive sensitivity) [**Garcia-Porrero *et al.* 2015f; Champney, 2017b**], and contain:

- Fasciculus gracilis (or Goll fasciculus): Light touch and conscious proprioception of lower limbs.
- Fasciculus cuneatus (or Burdach fasciculus): Light touch and conscious proprioception of upper limbs.

  These tracts start from sensory receptors at the skin and the last neurons of this pathway have their cell bodies in the thalamus, with connections to the cerebral cortex.

- Lateral columns pathways transmit unconscious proprioception and are necessary for motor coordination. They include:
  - Anterior spinocerebellar tract (ipsilateral and contralateral).
  - Posterior spinocerebellar tract (ipsilateral).

    The cell bodies of the neurons that start this pathway are located at the dorsal root of the spinal ganglia and the prolongations of the last neurons finish at the cerebellum.

- Anterolateral spinothalamic pathways (contralateral) transport gross sensitivity (non-discriminatory pressure and touch sensations), pain sensitivity, itching, tickling sensation and sexual sensitivity [**Garcia-Porrero *et al.* 2015f**]. They can be divided into [**Ojeda *et al.* 2014c**]:
  - Neospinothalamic tract: Thermal, non-discriminatory pressure and touch sensations, acute and localized pain sensation.

- Paleospinothalamic tract: Diffuse pain, itching, tickling sensation, and sexual sensitivity.
- Spinoreticular tract: Same information as the paleospinothalamic tract.

  These pathways start in the grey matter of the spinal cord and end at the thalamus.

- Descending pathways (from the brain to the spinal cord):
  - Lateral motor pathway is responsible for fine mobility of the upper limb (including arm and hand) and contain:
    - Pyramidal pathways coming from the primary motor cortex and reaching the ventral horn of the spinal cord. They include:
      - Lateral corticospinal tract (contralateral).
      - Ventral corticospinal tract (ipsilateral).
    - Rubrospinal tract coming from the red nucleus of the midbrain to the ventral horn of the spinal cord.
  - Extrapyramidal system is important in automatic and learnt activities and includes:
    - Reticulospinal tract, from the reticular formation located in the pons and the medulla oblongata to the ventral horn of the spinal cord.
    - Tectospinal tract, from the tectum of the midbrain to the ventral horn of the spinal cord.
    - Vestibulospinal tract, from the vestibular nuclei of the pons to the ventral horn of the spinal cord.

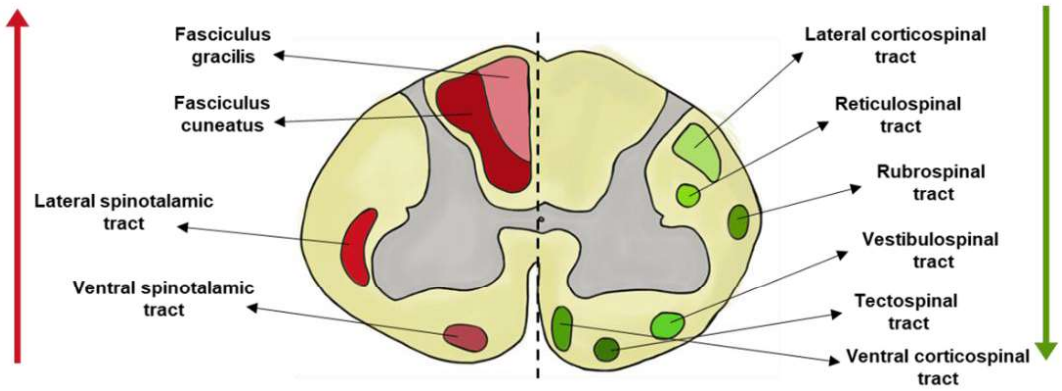

Figure I3. Organization of the white matter tracts. Ascending pathways represented in red and descending pathways represented in green. Redrawn from [**Ahuja *et al.* 2017**].

Moreover, the spinal cord has an internal neural network formed by the propriospinal tracts, which connect the different spinal segments among them [**Chung and Coggeshall, 1983; Chung *et al.* 1987**]. The neural fibres that form these tracts follow a very rigorous organization. Thus, axons which travel through a specific area of the white matter, project to a specific area contained in the grey matter. For example, fibres located at the dorsolateral part of the white matter project to the dorsolateral portion of the intermediate grey matter and to the motoneurons which innervate the distal limb muscles. On the other hand, fibres located at the ventromedial area of the white matter project to the medial portion of lamina VII and the motoneurons which innervate the proximal muscles at the grey matter. In addition, there are long propiospinal neurons able to communicate cervical with lumbar enlargements through descending and ascending pathways. However, while descending cervico-lumbar projections are usually bilateral (ipsilateral and contralateral), ascending lumbo-cervical views are usually only contralateral. Moreover, there are two neuronal circuits involved in the control of locomotion and forelimb motility: the cervical proprio-spinal premotoneuronal system (SPPC) and the central pattern generator generator. The somas of the neurons that form the SPCC are located mainly in C3 and C4, and their axons project to the motoneurons of C7

and C8, as well as to the lateral reticular nucleus of the brain stem. Experiments with different animal models and humans [**Alstermark and Sadaki, 1986; Lundberg, 1999; Pauvert *et al.* 1998**] demonstrated that SPPC receives excitatory inputs from the CST, rubrospinal, tectospinal, and reticulospinal tracts, along with sensory inputs from muscles, joints, and skin [**Baldissera *et al.* 1987**], and inhibitory connections from intraspinal interneurons. Thanks to this fact, the SPPC could act as a relay between the tracts coming from supraspinal centres (e.g., cortical and subcortical tracts), and the motor nuclei of the spinal cord, thus, modulating and updating the information from supraspinal centres before transmitting it to the motoneurons. Additionally, the SPPC sends a copy of the signals produced by the spinal motoneurons to the cerebellum through collaterals to the lateral reticular nucleus [**Alstermark *et al.* 1981**]. On the other hand, the central pattern generator (CPG) [**Brown, 1911; Grillner and Zangger, 1984**] control the flexion and extension patterns of the different joints during locomotion. The spinal CPG is in the lumbar enlargement, and it receives instructions from the subthalamic, midbrain and cerebellar locomotion regions [**Eidelberg *et al.* 1981**], and receives information from the cerebral cortex, the basal ganglia, the brainstem and from the sensory systems.

Apart from these neuronal structures, within the spinal cord there are many kinds of neural cells forming inter- and intraspinal segment circuits (such as interneurons) and glial cells (such as astrocytes and those responsible for the myelination of neuronal axons within the CNS known as oligodendrocytes), among others. As in other organs, all these cells along with other tissue components are integrated by the extracellular matrix (ECM). The ECM is responsible for maintaining tissue integrity by anchoring all the components contained within the spinal tissue. This is possible thanks to its topography features at the macro, micro and nanoscales. Moreover, there is a liquid

medium that bathes the cells and facilitates waste removal, nutrient supply, and the transit of organic molecules such as proteins, called interstitial fluid. Cells at the spinal cord are also supported by a highly dense vasculature that contributes to nutrients and waste transport [**Ahuja *et al.* 2017; Mahumane *et al.* 2018**].

2.2. General aspects of spinal cord injury (SCI) and demographics: Focus on traumatic SCI

Spinal cord injury (SCI) is caused by the impairment of the spinal cord due to either non-traumatic or traumatic causes. The most frequent aetiologies of non-traumatic SCI include cervical spondylotic myelopathy (spinal stenosis), followed by neoplastic and developmental tumours, multiple sclerosis, vascular ischemia, motor neuron disease, and other congenital diseases [**McKinley *et al.* 1999; Grassner *et al.* 2016**]. On its turn, traumatic SCI is caused when a physical impact damages the spinal cord [**Ahuja *et al.* 2017**]. It induces an immediate breakage, dislocation or compression of one or more vertebras, and this is followed by a serious impairment of the vascular and nervous tissue of the spinal cord [**Papa *et al.* 2020**]. This thesis will be focused on traumatic SCI. Traumatic SCI affects about two and a half millions of people worldwide [**Papa *et al.* 2020**], leaving these patients with a life-long disability characterized by loss of sensation and/or voluntary motor function (paralysis) below the level of the injury, as well as impairment of autonomic and sexual functions [**Papa *et al.* 2020; Ahuja *et al.* 2017**]. Thus, SCI provokes a significant decrease both in the quality of life and life expectancy of these patients.

Traumatic SCI can be mainly classified depending on the level where the damage has been produced (*i.e.* cervical, thoracic, lumbar or sacral), but also if the spinal cord fragment has been fully severed or not (complete or incomplete, respectively) [**Ahuja *et al.* 2017**]. SCI occurs most frequently at the cervical spine (~60%), followed by thoracic and lumbosacral (~40% in total), being incomplete tetraplegia (affectation of cervical levels of the spinal cord) the most frequent neurological category nowadays (almost half of the total cases of SCI: ~47.6%). The frequency of incomplete and complete paraplegia (affectation of the thoracic spinal cord towards lower spinal levels) is virtually the same [**National Spinal Cord Injury Statistical Center 2020**].

To date, no clinical trial has demonstrated the efficacy of a repair strategy for improving functional recovery from SCI. In fact, less than 1% of SCI patients experienced complete neurological recovery by the time of hospital discharge. As expected, the risk of mortality increases with more severe injuries (the upper, the worst) and age. Although the survival of patients with traumatic SCI has improved in the last decades thanks to the application of more efficient pharmacological, surgical, and rehabilitation procedures, patients continue to have mortality rates that exceed those of age-matched controls. The average age at injury has increased from 29 years during the 1970s to 43 years at presents, in clear parallelism with the ageing population of the world. Regarding gender, about 78% of new SCI cases are men versus 22% of women [**National Spinal Cord Injury Statistical Center 2020**].

Traumatic aetiologies vary in the world differently from country to country and are mostly related to vehicular accidents (*e.g.* crashes), closely followed by falls, violence (*e.g.* gunshot wounds) or sport recreation activities. Sanitary burdens associated to medical care and rehabilitation of SCI patients cost millions of dollars, with an estimated lifetime costs that range from 1 to 5 million dollars per patient, depending on the age and the severity of the lesion [**Courtine and Sofroniew, 2019; National Spinal Cord Injury Statistical Center 2020**].

Data from Spain are mainly handled by the National Hospital for Paraplejics, a national and international reference centre for SCI treatment. Specifically, along 2015, 275 patients from all over the country were admitted to the hospital, being mostly men (67%) with an average age of 49 years old. Falls were the first cause of traumatic SCI, followed by traffic accidents, dives into the pool, and risky sports and leisure activities, such as quads, karts, gliding and scuba diving [**Torres Alaminos *et al.* 2018**].

2.3. Physiopathology of SCI: Systemic and local changes

The varied clinical manifestations of SCI largely depend on the level of the neurological injury (the upper the lesion is, the worse the symptoms are) and the amount of preserved spinal cord tissue (complete or incomplete), as explained before. A complete lesion implies the physical separation of the spinal tissue in two unconnected stumps, causing the disruption of neural communication and therefore the loss of sensitive and motor skills below the lesion level. On the contrary, in an incomplete lesion, the remaining tissue is able to support and maintain some of these motor and sensitive functionalities [**Laliberte *et al.* 2019; Bradbury and McMahon, 2006; Papa *et al.* 2020**].

In traumatic SCI, the first vertebral damage triggers the impairment of the spinal tissue, either by comprising or sectioning this organ. Following, a cascade of events that can be temporally divided in phases will take place. Depending on the severity of the damage, SCI can be classified into acute (<48 h), subacute (48 h to 14 days), intermediate (14 days to 6 months) and chronic (> 6 months) [**Ahuja *et al.* 2017**]. The duration of these periods can vary among patients. For example, functional recovery usually starts within the first months after the injury, although in some particular cases the onset of signs of recovery could happen after 1-2 years post-injury. Indeed, the improvement seen in these subjects is mainly thanks to hematoma reabsorption, reduction of the inflammatory state, injured tissue stabilization and spontaneous neuroplasticity mechanisms, not to neural or axonal regeneration [**Papa *et al.* 2020; Bradbury and McMahon, 2006**].

2.3.1. Systemic changes after SCI (I): Sensory-motor impairments

One of the main events that take place during the acute phase of SCI is known as the spinal shock, characterized by the decrease or even absence of reflexes functions at or/and below the level of injury, causing impairments in motor and sensitive skills, as well as internal organ functionality. Spinal shock

should not be confused with neurogenic shock, which in turn refers to the appearance of hypotension mainly due to blood loss produced also in the first stages after SCI, and subsequent bradycardia and vasodilatation [**Bradbury and McMahon, 2006; Ahuja *et al.* 2017**]. All these symptoms are reduced as patients recover.

Regarding sensory-motor systemic impairments, the most significant advancement so far to diagnose and classify SCI is the use of the American Spinal Injury Association (ASIA) scale, included in the International Standard for the Neurological Classification of Spinal Cord Injury (ISNCSCI) [**Figure I4**; **Kirshblum *et al.* 2011a and 2011b**]. The ASIA scale includes one motor, one sensory and one impartment scales. Specifically, the ASIA motor score evaluates muscle power from each myotome, while ASIA sensory score assesses light touch and pinprick sensation in dermatomes from C2 to S5. The ASIA impairment scale is used to make a global assessment of the extent of sensory-motor function. In each patient, these tests are applied both to left and right sides of the body [**Kirshblum *et al.* 2011a; Ahuja *et al.* 2017; Papa *et al.* 2020**]. ASIA score comprises 5 different grades from the worst to the best prognosis (A - E):

- **Grade A**: Complete absence of sensory and motor functions below the injury level, including the anal area.
- **Grade B**: Some sensation remains below the injury level, including the anal area, but not motor function is preserved.
- **Grade C**: Some motor function is preserved below the injury level, but 50% of the muscles below the injury level cannot move against gravity.
- **Grade D**: More than 50% of the muscles that are spared below the injury level are strong enough to move against gravity, including distal sacral segments.

- **Grade E**: Patient has recovered all neurological functions.

Beside sensory-motor impairments, other important systemic complications that can appear include [**Ahuja *et al.* 2017**]:

- **Neuropathic arthropathy**: It consists of the slow but progressive destruction of joints due to bone resorption. It appears due to the occurrence of repeated microtraumas unnoticed because of the loss of sensation, along with an exacerbated blood supply to the affected joints.

- **Spasticity**: It refers to the increase in muscle tone with exaggerated tendon reflexes caused by the affectation of neurons from supraspinal centres that are connected to the spinal cord. It affects a considerable percentage (~70%) of patients with chronic SCI (> 1 year) and can disturb mobilization, activities of the day living and sleep.

- **Neuropathic pain**: It appears after the first year of SCI in almost half of the chronic patients (40%). It is thought to occur because of an aberrant or exaggerated sprouting of affected nervous terminals, which would lead to a non-desired new-formed connections between neurons of intraspinal circuits (but this sprouting mechanisms could also facilitate neural recovery, as later explained in section 2.4). On the other hand, it is also related to an impairment in the inhibitory connections due to intraspinal circuits damage and reorganization.

2.3.2. Systemic changes after SCI (II): Internal organs affectation

Depending on the injury level, SCI can lead to compromised respiratory and cardiovascular functions. For example, apart from the neurogenic shock explained before, SCI could provoke the loss of innervation to lymphatic organs (such as the spleen), which could prompt many grades of immunodeficiency. Therefore, SCI patients are more likely to suffer from infections affecting lungs,

among others. SCI can also lead to genitourinary and gastrointestinal dysfunction, as well as to sexual dysfunction (*e.g.* erection and vaginal lubrication problems). All these organic alterations might change with the evolution/recovery of the patient [**Schwab *et al.* 2014; Ahuja *et al.* 2017; Guha *et al.* 1989; Guha and Tator, 1988**].

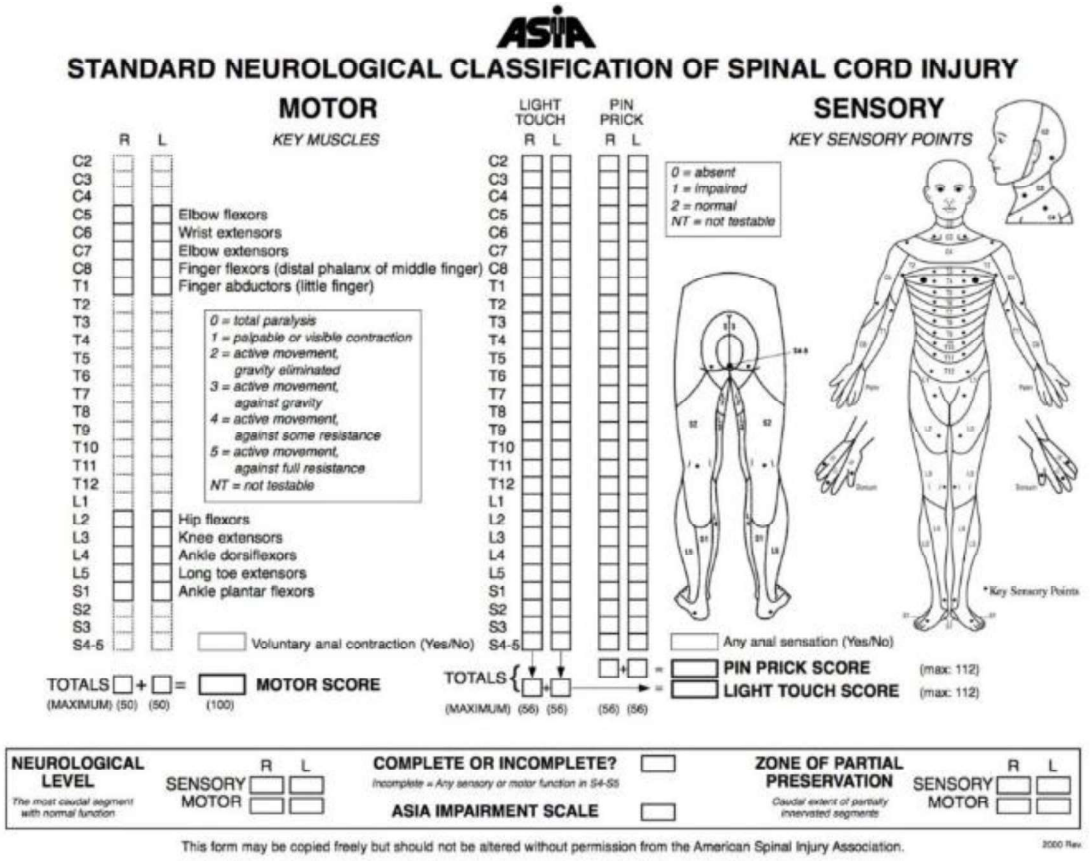

Figure I4. ASIA scale parameters. Reproduced from [**Kirshblum *et al.* 2011b**].

2.3.3. Local changes after SCI: Damage at cellular and tissue levels

Once the initial traumatic event occurs, a focal region of injury appears at the spinal cord (**Figure I5**). This localized damage starts with the affectation of the blood-spinal cord barrier, the disruption of the vasculature, and the injury of neurons, astrocytes and oligodendrocytes. All these events (primary damage) initiate an injury cascade that leads to further damage (secondary damage) to the spinal cord tissue and neurological dysfunction [**Ahuja *et al.* 2017**].

Cellular changes happening in the first acute phase involve cell damage and death, which causes the liberation of chemical signals (due to the disruption of cell membranes) that augment cell death. In addition, the destruction of microvasculature and larger blood vessels causes ischaemic injury, which characterizes by severe haemorrhages. This bleeding exposes the cord to the influx of different molecules and induces the activation of the immune system response. So, these molecules attract inflammatory cells, such as monocytes/macrophages (among others) to the injury site. All these reactions progressively drive to spinal cord swelling, leading to mechanical compression of the cord and worsening of the injury. So, the focal damage originated at one concrete spinal level could provoke the damage of several spinal segments by the extension of the damage.

In the subacute state, excitotoxicity and bleeding contribute to the loss of intracellular and extracellular ionic homeostasis. Ongoing necrosis of neural cells maintains the continuous release of molecules, which also activate microglia (the local inflammatory cells of the CNS), as well as increase the infiltration of the injury site with inflammatory cells. These cells are primarily attracted to clear cellular debris, but they can also induce further damage through the augmented release of cytotoxic products and neurotransmitters, which in excess behave as neurotoxic agents (*e.g.* glutamate).

As the inflammatory response subsides, the lesion evolves to phases that are marked by attempts of remyelination, vascular reorganization, alterations in the composition of the extracellular environment, and remodelling of neural circuits. However, this stage is primarily characterized by events that support the formation of a hostile environment for neural tissue regeneration, where one could find:

- Cysts formation, which contain extracellular fluid, bands of connective tissue and macrophages. Importantly, their presence aggravates the loss

of tissue volume. The persistence and enlargement of these cysts with time induces syringomyelia, which is defined as a longitudinal fluid filled cavity that can span through many segments of the spinal cord. This would lead to a myelopathy that can occur months after SCI.

- The formation of the fibro-glial scar, where astrocytes proliferate and, together with infiltrated collagen, other kind of cells, creates a barrier surrounding the site of damage. Moreover, signalling from activated astrocytes, microglia and macrophages causes the secretion of ECM proteins that hamper axonal regrowth (*e.g.* chondroitin sulphate proteoglycans, CSPGs). Additionally, pericytes that are wrapping around endothelial cells of the vessels contained in the spinal cord tissue proliferate and release additional ECM molecules. Finally, due to meninges disruption, fibroblasts can also infiltrate the lesion and perilesional regions and replace the neural tissue with fibrous connective tissue including dense collagen deposit, even across the glial scar, to fill the injury cavity.

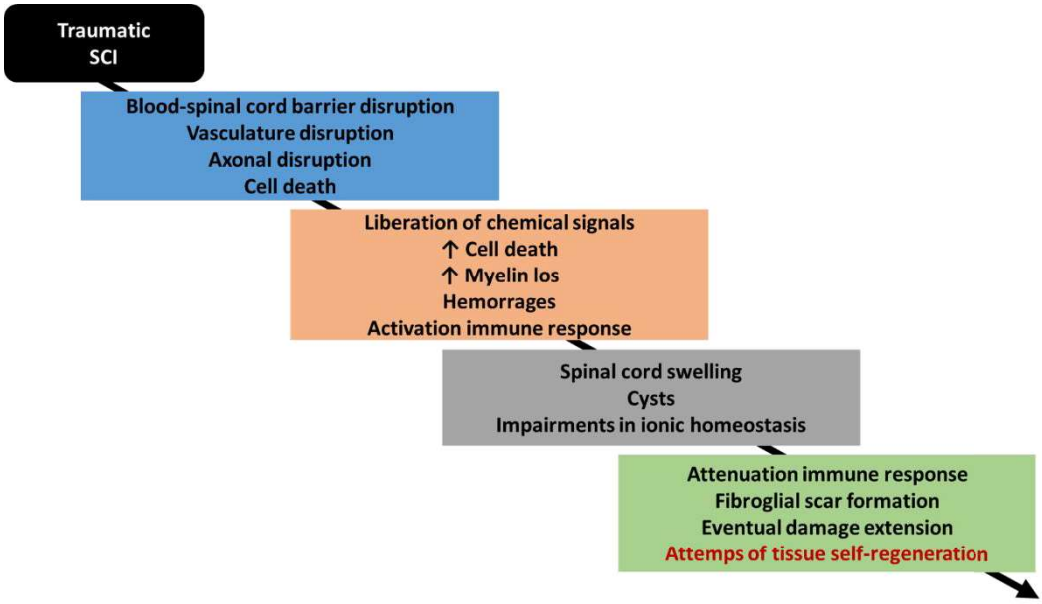

Figure I5. Scheme of the local changes after SCI.

All these physiopathological features of SCI make neural tissue regeneration particularly challenging. However, although at first sight these changes seem to impede neural tissue regeneration, some of them are necessary to recover tissue integrity and functionality [**Ahuja *et al.* 2017; Courtine and Sofroniew, 2019**]. For example, it has been shown that the formation of the fibro-glial scar mainly composed by the progeny of pericytes type A is necessary for neural tissue regeneration after SCI [**Göritz *et al.* 2011**]. Indeed, a moderate inhibition of its appearance generates a smaller (but still present) scar able of preventing damage extension, decreasing inflammation and astrogliosis, and enabling axonal regrowth at the lesion site [**Dias *et al.* 2018**]. Moreover, spinal nervous tissue has developed its own strategies for self-repair after damage, as will be described below.

2.4. Spinal cord tissue self-repair: Focus on neuronal damage and axonal connectivity

Although axonal regeneration is extremely limited in the mammalian adult CNS, partial (*i.e.* incomplete) lesions of the spinal cord can be followed by spontaneous, and often substantial, functional improvements. The mechanisms underlying this recovery are not yet fully understood, but include recuperation from the spinal shock, remyelination and axonal sprouting. This last refers to the capacity of spared axonal segments (which belong to neurons that have suffered an axotomy because of the injury) to create new collateral axonal terminals of different lengths [**Figure I6; Laliberte *et al.* 2019; Bradbury and McMahon, 2006**]. Thus, it can be classified as a plasticity process because an adaptive reorganization of intraspinal circuits occurs after SCI in order to minimize damage consequences and regain some of the lost functions [**Bradbury and McMahon, 2006**].

The occurrence of spontaneous sprouting of axons has been shown after the axotomy of axonal tracts (*e.g.* corticospinal, rubrospinal) and in intraspinal interneurons. Intraspinal interneurons (IINs) are propiospinal neurons that have both their cell body and their prolongations within the spinal cord. IINs receive input from descending pathways involved in locomotor activity (*i.e.* supraspinal centres located at the cortex and the brainstem) and propagate the information to locomotor circuits from rostral to caudal levels of the spinal cord. IINs axons can either travel through one or two segments (*i.e.* short), or project to segments located further from their cell body, thus being able to connect cervical with lumbar levels (*i.e.*, long). Short and long IINs axons can stay within the same side of their cell bodies (*i.e.*, ipsilateral), while others cross to the other side (*i.e.*, commissural), as previously explained [**Laliberte *et al.* 2019**]. These last ones could be possibly involved in forming detour circuits able of bypassing the tissue gap created following SCI [**Figure I6; Laliberte *et al.* 2019; Bradbury and McMahon, 2006**].

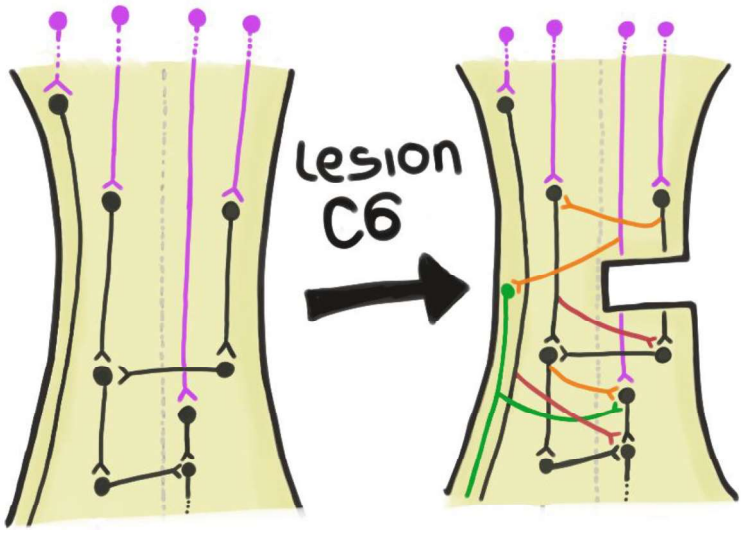

Figure I6. Scheme of possible mechanisms of axonal sprouting of IINs after a hemisection at C6 cervical level. Violet represents neurons descending from supraspinal centres. Black corresponds to IINs. Orange refers to the new collaterals that injured neurons can create in order to reorganize intraspinal circuits to bypass the lesion. Green refers to neurons recruited to assist

intraspinal circuits reorganization. Red refers to sprouting produced in neurons located in the contralateral side.

IINs present a key role controlling locomotor patterns, such as gait generation, among others. Taking this fact into consideration, as well as their location along the spinal cord (i.e., the shorter distance in comparison to neurons coming from supraspinal centres that they need to regrow to reconnect both sides of spinal tissue after a lesion), IINs have been investigated as candidates for the rostro-caudal propagation of the motor instructions to neural circuits below the level of injury. In fact, several changes to neural circuits involving IINs have been observed to facilitate the recovery of locomotor functions. For example, spared axons of injured tracts could form new terminals by axonal sprouting, which would contact IINs capable of creating new collaterals (also by sprouting mechanisms) to reorganize intraspinal circuits to bridge the lesion (e.g., after spinal cord transection) [**Laliberte *et al.* 2019**].

Early evidences of possible intraspinal new circuits formation due to plasticity processes was shown when Alstermark *et al*. [**1987**] demonstrated the capacity of rubrospinal and bulbospinal tracts to facilitate the recovery of forepaw function after corticospinal tract lesion in cats. Following, spared axons belonging to supraspinal tracts were found to increase their connections with intraspinal circuits already formed within the spinal cord to restore their function. Since then, the formation of new connections between spared descending terminals and IINs after SCI have been reported in many works with different animal models of this pathology, such as in work by Bareyre *et al*. [**2004**]. In their work, lesioned CST axons at mid-thoracic level were able to form new contacts with both short and long IINs by sprouting mechanisms. However, only projections with long IINs which were able to bridge the lesion were maintained 12 weeks after SCI. In addition, the number of direct contacts between long propiospinal axonal terminals and lumbosacral motoneurons was

doubled 8 weeks after the dorsal hemisection. More recently, axons of the reticulospinal tract lesioned by a unilateral hemisection caused an increase in the number of contacts between nervous terminals of the reticulospinal tract and IINs [**Filli *et al.* 2014**].

Some other works involving two hemisections at the spinal cord (first one at certain spinal level and a second hemisection in the contralateral hemicord at a more rostral level, either immediately after or some weeks after) demonstrated the capacity of IINs to form new intraspinal circuits to restore spinal cord function. In work by Courtine *et al*. [**2008**], when an initial hemisection at T12 was followed by a second contralateral hemisection at T7 ten weeks later, greater recovery of locomotor activity was observed compared to animals that received the contralateral hemisection simultaneously. These results suggested that the initial hemisection promoted remodelling of propiospinal circuits to form detours around the initial injury that were not disrupted by the second. Thus, locomotor recovery seen in animals following the delayed staggered hemisection was associated with connectivity between the spared lumbar circuits and IINs in the region between lesions (T8-T10). However, no direct connectivity of supraspinal locomotor nuclei with lumbar circuits was found. In line with this, May *et al*. [**2017**] evidenced an increased connectivity between reticulospinal tracts and IINs due to the formation of new intraspinal circuits between T10 (first hemisection) and T7 (second hemisection).

IINs are also being studied for their hypothetical role in the integration and propagation of sensory feedback during movement. If true, proprioceptive and sensory inputs from the outside could influence the remodelling of the intraspinal circuits where IINs are included, facilitating the formation of new synapses with the spared axons to bridge a spinal hemisection [**Laliberte *et al.* 2019; Bradbury and McMahon, 2006**]. First insights into this matter were

published by Mckenna and Whishaw [**1999**], where the spontaneous recovery of reaching ability was related to other sensory-motor pathways following a dorsal column lesion in rats. The influence of the activation of sensory feedback for the recovery of locomotor function has been showed in animal models of complete SCI, being hypothesized that this sensory feedback could act as a possible stimulus for the remodelling of intraspinal circuits [**Laliberte *et al.* 2019; Bouyer and Rossignol, 2003; Lavrov *et al.* 2008; Slawinska *et al.* 2012; Takeoka *et al.* 2014**]. However, more research should be done in order to confirm this hypothesis.

Regarding remyelination, although oligodendrocyte precursor cells (OPCs) are recruited to the injury site [**Keirstead *et al.* 1998**], the subsequent spontaneous remyelination will usually remain abnormal or incomplete [**Frankin *et al.* 2008**]. Even when successful, the mechanisms underlying these processes are still under study. It has been also proposed that Schwann cells (myelinating cells of the PNS) migrating into the lesion site or arising from resident OPCs also participate in the remyelination process, but their survival is rapidly compromised in the CNS [**Oudega and Xu, 2006; Bunge and Wood, 2012**], so further research is also needed in this arena [**Soares *et al.* 2020**].

For all the reasons exposed above, experts working in different fields related to tissue engineering continue collaborating in order to find and develop novel and more efficient approaches for traumatic SCI treatment.

2.5. Tissue engineering

The gold standard for patients suffering from diseased and injured organs continues to be organ transplantation. However, donor shortages worsen every year as the population ages due to an increase of organ failure with age and an increasing demand [**Langer and Vacanti, 1993**]. This situation leads to an increasing number of patients that die on waiting lists. For this

reason, scientists in the field of regenerative medicine and tissue engineering have applied for a few decades the principles of cell transplantation, biology, chemistry, material science, nanotechnology, and bioengineering to construct biological substitutes that will recover normal function in diseased and injured tissues [**Atala, 2009; Langer and Vacanti, 1993; Salgado *et al.* 2013**]. As defined by Langer and Vacanti, tissue engineering is "an interdisciplinary field that applies the principles of engineering and life sciences toward the development of biological substitutes that restore, maintain, or improve tissue function or a whole organ" [**Langer and Vacanti, 1993**]. Thus, tissue engineering is mainly based on the combination of cells, biomaterials and exogenous factors [**Seif-Naraghi and Christman, 2013**]. Both tissue engineering and regenerative medicine have as a common purpose to reinstate normal body function, so its definition can be virtually the same [**Baptista and Atala, 2016**]. Nonetheless, it is also correct to say that regenerative medicine uses tissue engineering, among many other tools, to design new strategies for the repair of damaged organs and tissues, so being the last a part of the former [**Lazurko *et al.* 2019**]. The replacement of organ function and living tissues with synthetic lab-made substitutes represents one of the most noteworthy contributions of the 20th century translational science to clinical medicine, eventually improving the lives of millions of patients worldwide [**Lysaght and Reyes, 2001**].

It is difficult to determine the origins of this field, because there are many references of body regeneration attempts throughout history. Early allusions could be attributed to ancient Greek myths where organs were regenerated from one day to another, to the use of "healthy" legs from recently deceased men to replace an ulcerated or cancerous legs in Egypt, or to the iron hand prosthesis documented at the beginning of the sixteen century [**Baptista and Atala, 2016**]. It was in 1910 when Harrison and colleagues were the first scientists capable of maintaining cells in culture, providing the bases of cell

biology for classical tissue engineering applications [**Harrison *et al.* 1910; Baptista and Atala, 2016**]. Forty years later, the kidney was the first entire organ to be replaced in humans in 1955 [**Guild *et al.* 1955; Atala, 2009**]. However, this implant was performed between identical twins. Few years later (early 1960s), the Nobel Laureate Murray performed a kidney transplantation from a non-genetically identical patient into another. This transplant marked a new era in medical therapy, offering new possibilities for other organ systems transplantation. However, difficulties with the clinical resources available in this period, as well as with monitoring patient's reaction to the implanted organs, among others, forced both clinicians and researchers to improve and refine transplant operations. At this point, synthetic materials were introduced to replace or rebuild diseased tissues or parts of the human body [**Atala, 2009**]. Next, the concept of cell transplantation emerged and was definitely set with the first human bone marrow cell transplant in the 1970s. In this period, materials and cell biology approaches started to be combined in medical therapies, creating a new field [**Atala, 2009**]. The concept of tissue engineering matured into preclinical developments during 1990s, and it was in 1993 when Langer and Vacanti defined this new field [**Langer and Vacanti, 1993**].

2.6. Tissue engineering focused on SCI treatment

To date, no randomized clinical trial has demonstrated the efficacy of a repair strategy for improving functional recovery after SCI. The only treatment for human SCI approved is methylprednisolone administration [**Ahuja *et al.* 2017**], that only marginally improves clinical outcomes despite promising clinical trials results. Last and on-going clinical trials related to SCI (**https://clinicaltrials.gov/**) include the following:

- Drugs treatment (4-aminopyridine, MT-3921 - **NCT03899584, phase III not yet recruiting**).

- Robotics (locomotor training using adaptive robotics - **NCT03504826, recruiting -not applicable in phase**).
- Physical exercise for rehabilitation (**NCT03925077, not yet recruiting – not applicable in phase**).
- Studies which use tissue engineering approaches such as:
    - Cells therapy (intrathecal transplantation of allogeneic umbilical cord derived mesenchymal stem cells - **NCT03505034, phase II recruiting**-, human umbilical cord blood-derived mesenchymal stem cells - **NCT04213131, recruiting phase not applicable**-, autologous mesenchymal stem cells - **NCT02574572, recruiting** and **NCT01676441, phase II/III recruiting**).
    - Scaffolds (poly(lactic-co-glycolic acid)-b-poly(L-lysine) scaffold)- **NCT02138110, active not recruiting, phase not applicable** and **NCT03762655, recruiting, phase not applicable**).
    - Scaffolds loaded with cells (collagen scaffolds loaded with mesenchymal stem cells - **NCT02510365, phase I recruiting** and **NCT02688049, phase I/II enrolling by invitation**-, neural stem cells - **NCT02688049**-, or bone marrow mononuclear cells - **NCT02688062, phase I/II enrolling by invitation**-, and autologous olfactory glial cells as well as implants from peripheral nerves - **NCT03933072, phase I/II recruiting**).
    - Implanted materials for electrical stimulation combined with other strategies (scaffolds for epidural electrical stimulation - **NCT03966794, phase I/II recruiting** and **NCT04196114, not yet recruiting**).

However, most of them are at the very beginning of the clinical evaluation, so no clear benefits have been reported in SCI patients yet. For a

more detailed explanation of the goal of each phase included in clinical trials, please refer to: https://www.clinicaltrials.gov/ct2/help/glossary/phase.

In the specific scenario of SCI, researchers and clinicians are making great efforts to develop novel therapeutic approaches to stabilize the lesion area and reconnect neural axons in order to regain functionality [**Führmann *et al.* 2017; Zustiak *et al.* 2020**]. As evidenced by clinical trials, most procedures which are currently under investigation in basic research are based on drug delivery, neurotrophic factors and cell therapy. However, there are many limitations related to drug/molecules delivery. For instance, it is difficult to ensure the time that these molecules can be active within the organism, especially in chronic diseases, based on biodistribution and biodegradation profiles. Other drawback is the difficulty in controlling the concentration of the molecule that is certainly reaching the lesion epicentre. In stem cell-based therapies, a prominent hurdle is the low cell survival rate following transplantation. So, alternative promising candidates are implantable devices made from a wide range of biomaterials. In fact, biomaterials can be applied either alone or in combination with drugs and/or cells, where they can act both as a carrier of the different molecules and/or as a support to protect cells when implanted.

2.7. Biomaterial definition

The most accepted definition of the term "biomaterial" is the one by the American National Institutes of Health, that describes a biomaterial as "any substance or combination of substances, other than drugs, of synthetic or natural origin, which can be used for any period of time, which augments or replaces partially or totally any tissue, organ or function in the body, in order to maintain or improve the quality of life of the individual" [**Bergmann and Stumpf, 2013**]. Thus, biomaterials not only provide some functions, but also, evoke or induce biological responses. Importantly, the interface of a biomaterial

is not static, but it is changing over the biomaterial lifetime. As understood from the definition, a biomaterial must be biocompatible. The William dictionary of biomaterials defines biocompatibility as "the ability of a biomaterial to perform its desired function with respect to a medical therapy, without eliciting any undesirable local or systemic effects in the recipient or beneficiary of that therapy (thus, including toxicity and minimal foreign body response), but generating the most appropriate beneficial cellular or tissue response to that specific situation, and optimizing the clinically relevant performance of that therapy" [**Williams, 2009; Bergmann and Stumpf, 2013**].

The first biomaterials created did not interact with the organism, were just located to physically replace the damaged organ implanted within the human body. So, they intended to have similar physical properties to the damaged organs either partially or completely replaced (some examples are ceramics, metals or rubber). In other words, they were commonly used as prosthetics. However, they had poor compatibility with the body, so they were often rejected [**Lazurko *et al.* 2019**]. Once tissue engineering emerged as a field, what it is widely considered as first generation of biomaterials evolved during 1960-1970s for their application as medical implants. Their main goal was to mimic tissue that was lost, maintaining a balance between physical properties together with minimal corrosion and toxicity to the host tissue [**Hench, 1980; Bath *et al.* 2013; Ning *et al.* 2016**]. Later, second generation of biomaterials were developed to be bioactive. Examples include bioactive glasses, ceramics and other components mainly envisioned for orthopaedic and dental usage. These materials had a better integration with the host tissue and created an active interface with the organ where they were placed. Here appeared also resorbable materials, such as fracture fixation plates and screws used in orthopaedic surgeries [**Hench and Thompson, 2010; Bath *et al.* 2013**]. Further advances led to the third generation, which combined the advantages of the second type of

biomaterials, and were able to stimulate specific cellular/tissue responses of interest after implantation for the regeneration of living tissues, even acting at the molecular level [**Bath *et al.* 2013; Ning *et al.* 2016**]. A good example of this last group are those materials which present certain physico-chemical properties, such as determined topography, surface chemical composition, porosity and elastic modulus, that act altogether promoting structural, cellular and genetic changes that ultimately drive to functional changes to prompt organ recovery. Finally, the current and future vision of the fourth generation of biomaterials refers to those materials which can specifically induce desired cell responses, for instance through electrical stimulation by modulating cellular ion channels and pumps, as well as monitor and record the cell responses generated [**Ning *et al.* 2016**]. This last group includes electronic devices developed by nanotechnology tools to be interfaced with the human body, modern cardiac pacemakers, cochlear implants for patients with profound hearing loss, and electrodes for deep-brain stimulation to alleviate symptoms of diseases such as Parkinson's disease [**Feiner and Dvir, 2018**], for instance. Thus, electrodes are used to stimulate electrogenic tissues, such as skeletal, cardiac and smooth muscle and neural tissues. Research into this type of devices and their biomedical application is an intensively active area nowadays.

2.8. Biomaterials for SCI treatment

Taking all the above into consideration, biomaterials face design challenges derived from the inherent properties of the spinal cord and their aimed regeneration of the injured spinal tissue. So, biomaterials should first have a 3D architecture embracing the heterogeneity of the spinal neural tissue, which is comprised of varied anatomical regions due to diverse density and alignment of neural tissue components. Implants should also tolerate and integrate within the complex microenvironment formed by the neural ECM, the

interstitial fluid and the intricate blood vessels network [**Mahumane *et al.* 2018; Liu *et al.* 2019**].

Based on these specific neural tissue features, biomaterials for SCI should ideally fulfil the following set of requirements (**Figure I7**):

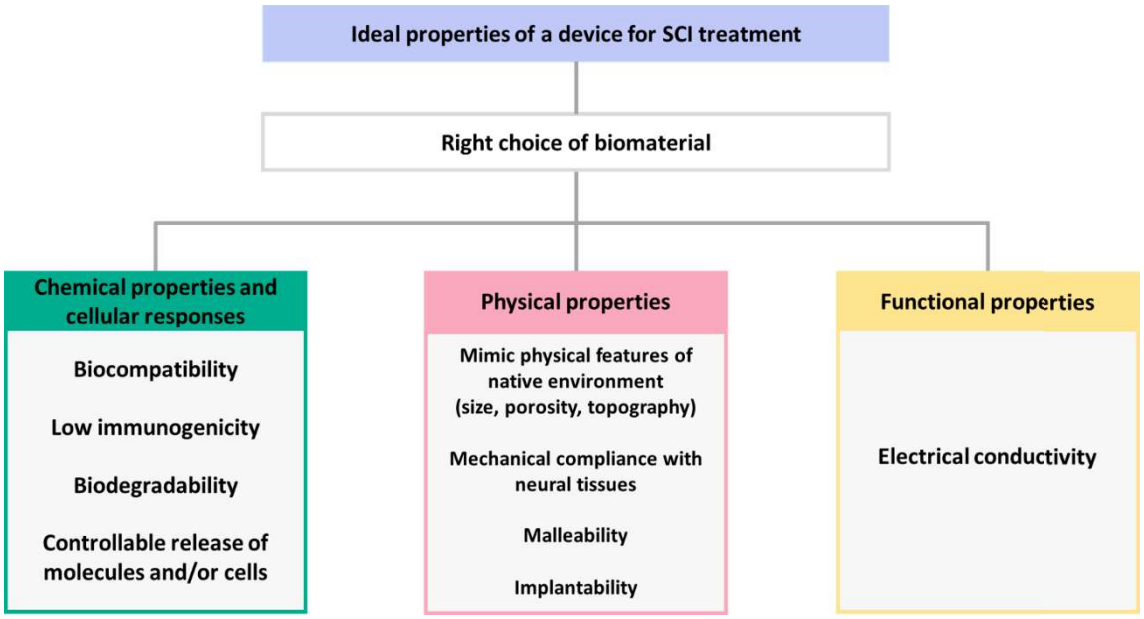

Figure I7. Biomaterial requirements for implantation at the injured spinal cord. Adapted from [**Mahumane *et al.* 2018**].

Biocompatibility: The implantation of the biomaterial should not cause any damage to cellular and tissue components at the spinal cord. Besides this local toxicity, the material should be also non-toxic systemically, neither producing toxic degradation products. If this property is not present in the material itself, surface modification with biocompatible molecules such as ECM proteins (*e.g.*, laminin, fibronectin and short peptide sequences) and synthetic polymers could be implemented. Finally, factors such as dose, physico-chemical properties and way of administration play an important role to this regard, and should be considered for all materials tested [**Mahumane *et al.* 2018; Sensharma *et al.* 2017**].

Low immunogenicity: The biomaterial implanted should not elicit a host inflammatory response or cellular reaction severe enough to result in chronic inflammation at the biomaterial interface and encapsulation within the organism [**Orive *et al.* 2009; Sensharma *et al.* 2017**].

Desirable interaction with host cells: The physico-chemical properties of the biomaterial should be controllable to a large extent. It should provide good adhesion and structural support to the surrounding cells and tissues. Moreover, it should facilitate local neurite regrowth, as well as vascular remodelling, by recreating the 3D inherent neural structure. This can be achieved, for instance, by modifying material porosity and pore dimensions to let cellular components grow and integrate into the 3D native architecture, functionalizing the material surface (to control cell functions such as adhesion, migration and proliferation), and mimicking the ECM to facilitate neurites and blood vessels guidance. Alternatively, changes in material topography, such as adapting a microfiber configuration imitating a neural fibre tract, can serve to boost neural growth in the desired direction [**Mahumane *et al.* 2018; Acarón Ledesma *et al.* 2019; Orive *et al.* 2009; Marcus *et al.* 2017**].

Mechanical compliance: It is important to note that mechanical features of tissues are modified after pathological conditions, including traumatic injury. Thus, biomaterials used should present mechanical properties in accordance with those of neural tissues (*i.e.,* soft tissues) not to cause damage by friction forces. Moreover, body movement (or, in this case, movements of the trunk of the body and the backbone) should not affect to material proper stabilization neither in the short nor in the long term. Furthermore, it is noteworthy to mention that biological features such as the final fate and conformation of stem cells and cellular structures respond to the mechanical properties of the substrate [**Moeendarbary *et al.* 2017; Feiner and Dvir, 2018; Pathak *et al.* 2014; Koch *et al.* 2012; Moshayedi *et al.* 2010**], so the mechanical impact of the

biomaterial on those features should be in line with the tissue response ambitioned.

Biodegradability: Biomaterials should be chemical and structurally stable for long enough to allow the repair and/or reorganization of the spinal cord tissue. Ideally, this scenario should overlap with a step-by-step degradation according to tissue remodelling, without releasing any foreign residues that could either permanently remain in the body or cause local and/or systemic toxicity [**Orive *et al.* 2009; Sensharma *et al.* 2017**].

Controllable release of bioactive compounds and cells: In those cases in which local delivery of potentially therapeutic molecules and/or cells is desired, biomaterials should provide a spatial and temporal controlled delivery of such elements. This can be accomplished by anchoring bioactive molecules through diverse chemical strategies (*e.g.,* covalent bonding, electrostatic interactions and incorporation of degradable nanocarriers, among many others) [**Orive *et al.* 2009**]. Some of the molecules that have been proposed to make the lesion environment more permissive to spinal cord tissue regrowth include:

- Molecules able to neutralize myelin-associated inhibitors such as Nogo receptor [**Wen *et al.* 2016**], myelin-associated glycoprotein (MAG) and oligodendrocyte myelin glycoprotein (OMgp). However, results regarding this strategy are controversial [**Zheng *et al.* 2005; Lee *et al.* 2010**]. Other inhibitors of axonal regeneration such as semaphorin3A (Sema3A) have been also tested [**Kaneko *et al.* 2006**].

- Molecules or enzymes able to break down inhibitors associated with the ECM such as chondroitinase ABC (ChABC) against CSPGs [**Pakulska et al. 2017; DePaul *et al.* 2017**].

- Neurotrophic factors and neurotrophins, such as brain-derived neurotrophic factor [BDNF; **Pan *et al.* 2019]**, and neurotrophin-3 [NT-3;

Alto *et al.* 2009; Rao *et al.* 2018] to boost neuronal survival, growth and differentiation.

- Other factors such as fibroblast growth factor 2 (FGF2), epidermal growth factor (EGF) and glial-derived growth factor (GDNF) [**Chen *et al.* 2015; Anderson *et al.* 2018; Grulova *et al.* 2015**] to improve neural cells support and development, or micro-RNA molecules [**Nguyen *et al.* 2017**].
- Experimental drugs under research, apart from methylprednisolone, such as paclitaxel, a microtubule-stabilizing agent [**Roman *et al.* 2016; Li *et al.* 2018**].

Regarding cells transplantation for SCI treatment [**Assinck *et al.* 2017**], due to their potential of manipulation towards neuronal phenotypes and myelinating functions, the most studied ones so far are few types of stem cells (such as neural stem cells [NSCs; **Li *et al.* 2018; Marchini *et al.* 2019**] and mesenchymal stem cells [MSCs; **Yang *et al.* 2017; Boido *et al.* 2019**]), neural progenitor cells [NPCs; **Dulin *et al.* 2018; Koffler *et al.* 2019**], pluripotent stem cell-derived neuroepithelial cells [**Führmann *et al.* 2018**], olfactory ensheating cells [**Assinck *et al.* 2017**] and Schwann cells [**Yang *et al.* 2017**]. Although it has been reported the existence of a stem cells-like niche within the spinal cord, the ependymal cells located around the ependymal canal, work by García-Ovejero and colleagues [**García-Ovejero *et al.* 2015; Paniagua-Torija *et al.* 2018**] demonstrated that ependymal canal degenerates in adulthood in humans. Moreover, its composition is not the same as the one described for animal models and remaining ependymal cells are not able to proliferate after SCI. Thus, based on these results, ependymal cells would not favour neural tissue regeneration after spinal cord damage.

For more details about the combination of molecules and cells for SCI treatment, please refer to elsewhere [**Pires and Pêgo, 2015; Führmann and Soichet, 2018; Hodgetts and Harvey, 2017; Kubinová, 2020; Zustiak *et al.* 2020; Bradbury and McMahon, 2006**].

Malleability and implantability: An ideal biomaterial should be malleable into a variety of sizes and shapes and/or adaptable to the lesion size and shape to perfectly fill the cavity left [**Orive *et al.* 2009; Mahumane *et al.* 2018**].

Electrical conductivity: It has been demonstrated that electrical stimulation can influence neural cell development and circuits maturation [**Chen *et al.* 2019b; Park *et al.* 2011**]. This is also relevant because neural communication is highly dependent on electrical signals, such as the action potentials. So, electrically conductive materials are being under exploration.

Based on this, the implementation of novel implantable devices that could be placed at the injured tissue must take into consideration most of these features. For instance, nanotechnology advances in the last decades have enabled the creation and improvement of non-invasive flexible platforms (i.e., as non-penetrating platforms, they are not expected to damage the cell membrane of neural cells once they are implanted) which might contain a high density of electrodes (made from biocompatible metals such as gold), with different topographical features (either flat or presenting various shapes such as nanowires) at different scales (i.e., micro- or nanoscales), embedded in polymeric substrates (such as PDMS) for the extracellular recording and stimulation of the neural networks activity. These platforms are defined as non-invasive extracellular arrays, and their features can be manipulated to achieve desired biological responses, such as, in the SCI context, neuronal electrical stimulation to modulate neural networks development and activity. Another strategy that is becoming more and more popular consists on the design of 3D biomaterials to fill and stabilize the lesion cavity, acting as a support and guide

of the different tissue components including blood vessels, glial components and neurites. Both strategies have been explored in this thesis and are explained more in detail below.

2.9. Approaching SCI treatment using electrically conductive neural interfaces

Most of the understanding that we have from the organization and functioning of neural cells of the CNS has been acquired by using electrodes to perform intracellular recordings [**Feiner and Dvir, 2018**]. Furthermore, electrodes have been widely used for neuronal stimulation in patients with Parkinson disease, tremor, dystonia and chronic pain, and even to restore hearing integrated in cochlear implants [**Grill, 2008**]. Thanks to advances in nanotechnology, the integration of a considerable number of electrodes with micro and even nano-architectures in the same flexible platform, in order to increase the number of contacts interfacing the neural cells, has been possible. This fact enabled the implementation and improvement of microelectrode array (MEA) devices for neuronal recording and stimulation in biomedical research [**Ajetunmobi *et al.* 2014**].

Concretely, one approach to restore spinal cord functionality after injury is the fabrication of devices able to act as a bidirectional local bypass at the injury site to re-establish the connection between both sides of the lesion. These devices could be constituted, as in the ByAxon project, by two main different parts: one acting as a sensor (*i.e.* receiving signals from the neural cells at the spinal cord) and the other working as an electrical actuator (*i.e.* triggering new electrical potentials). This thesis is focused on the electrodes contained in these devices. In order to obtain this type of neural interfaces, scientists specialized in nanotechnology, physics, neuroscience, medicine and tissue engineering, are currently working together in the fabrication of improved electrodes with nanometre size features for neural stimulation and recording. Four of the main characteristics that these devices should ideally have are: (A) Biocompatibility, (B) Mechanical compliance with neural tissues, (C) Capacity to maintain a long-term stable contact with neural cells and tissues, and (D) Ability to

simultaneously record and stimulate hundreds of individual neurons with a good sensibility [**Spira and Hai, 2013**].

2.9.1. Enhanced *in vitro* biocompatibility thanks to improvements in topographical features of electrodes

Biocompatibility, mechanical compliance, and the capacity to stablish good interactions with the host tissue in the long term are highly related to the incorporation of nanoscale features to the electrodes. By doing so, electrodes achieve a better mimicking of the native neural architecture and, thus, an eventual reduction of the foreign body response (including both the fibro-glial scar and the device encapsulation) upon implantation in the CNS [**Das *et al.* 2016; Salatino *et al.* 2017; Seidlits *et al.* 2008**]. Contrary to this principle, most of the MEAs currently under study have no specific topography (*i.e.* they are flat structures) [**Marcus *et al.* 2017**]. So, in order to improve the interface tissue-electrode, as well as to better control cell migration and differentiation through the device, the use of topography as a customizable parameter is being investigated [**Figures I8 and I9**; **Marcus *et al.* 2017; Yang *et al.* 2014**]. For instance, a nanopillar-based topography is typically isotropic (*i.e.* no preferential directions exist), contrary to those anisotropic like grooves, channels and microfibers [**Marcus *et al.* 2017**]. Anisotropic topography has shown to influence more cell guidance and alignment, whereas an isotropic one has more effect on developmental acceleration and neurite branching [**Tan *et al.* 2018**]. In comparison to flat substrates, nanowires (NWs) and nanopillars can limit cell adhesion sites to highly concentrated contact points [**Marcus *et al.* 2017**]. In these cases, even single cells will interact with single NWs, leading to a reduction of the gap distance between the cell membrane and the electrode and, consequently, enhancing the tissue area that can be in close contact with the device. Besides supporting cell adhesion and axonal outgrowth, studies with NWs have proved enhanced cell survival over planar control substrates [**Timko**

***et al.* 2010**]. Moreover, the configuration of NWs-axon junctions in arrays makes possible to control signal propagation by both electrical stimuli and the eventual production of chemical reactions, as vertical NWs afford parallel electrical interfacing of multiple neurons [**Patolsky *et al.* 2006**]. A NWs-based topography was chosen for the fabrication of the nanoelectrodes in this thesis.

There are many examples in the literature which evidence the beneficial effects of the presence of topography and, in particular, NWs-like topography. For instance, gold (Au) films varying in surface nano-roughness have been proved to induce differential responses in embryonic stem cells [ESCs; **Bakeine *et al.* 2009**], with higher adhesion and differentiation profiles over plane substrates. Xie *et al*. [**2010**] used vertical nanopillars of 1 μm in height and 150 nm in diameter on top of a MEA to prevent cell migration during activity measurements. In line with this, Au microelectrodes (1.5 μm in height) were developed for in-cell recording without mechanically damaging cell plasma membranes as these structures were engulfed by the cells [**Hai *et al.* 2010**]. In these cases, the tight wrap with the vertical geometry led to a reduction of the membrane-electrode gap distance and higher seal resistance, which is crucial for enhanced signal detection, increasing neuron-substrate adherence. In a different study, dissociated sensory neurons were cultured on epitaxial gallium phosphide (GaP) NWs (2.5 μm in length and 50 nm in width) grown vertically from a GaP surface [**Hällström *et al.* 2007**]. Cells interacted closely with the nanostructures and were penetrated by hundreds of wires. In summary, all these works demonstrate the potential of incorporating NWs within electrically active neural interfaces to form strongly coupled interfaces with cell membranes able to measure signals from neurons and stimulate them.

Regarding the last point of the above-mentioned ideal features for neural interfaces, which refers to the ability of neural interfaces to simultaneously record and stimulate hundreds of individual neurons with a good sensibility,

current strategies for recording and stimulating neuronal activity include: (A) Intracellular recording and stimulation by sharp and patch electrodes, (B) Extracellular recording and stimulation by substrate-integrated MEAs, (C) Optical imaging and stimulation technologies of extrinsic fluorescent indicators and genetically encoded molecular probes, and (D) Other methods such as functional magnetic resonance imaging (MRI), electroencephalography, electrocorticography and magnetoencephalography, designed to record activity from very large scale neural populations (therefore not suitable for single neuron resolution) [**Spira and Hai, 2013**]. Although research on intracellular neural activity have been more widely explored by using intracellular sharp/patch electrodes (*i.e.* classical electrodes for intracellular recording and stimulation, in which the electrical tips are forced through the plasma membrane to directly contact the cytosol or the cytosol and the patch electrode interior solution) [**Hai *et al.* 2010**], efforts are currently focused on the use of substrate-integrated MEAs. These interfaces are able to record and stimulate large populations of excitable cells for days and months in a non-invasive way [**Hai *et al.* 2010**], without inflicting mechanical damages to cell membranes.

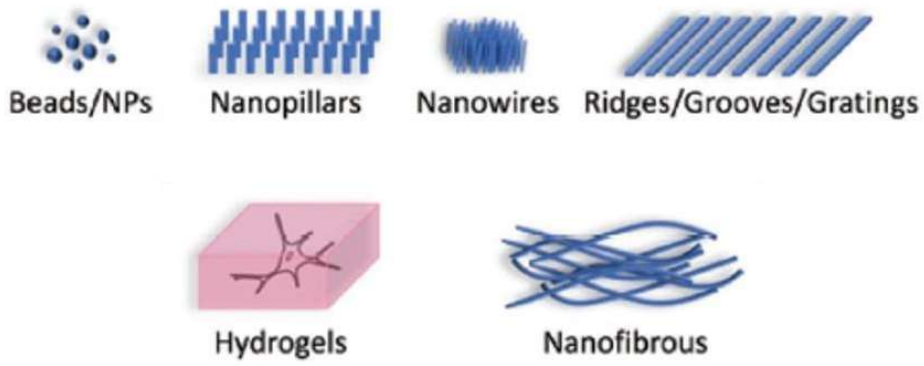

Figure I8. Examples of different biomaterial topographies. Adapted from [**Marcus *et al.* 2017**].

One of the main advantages of using MEAs with nanometric dimensions is that they could provide enhanced biocompatibility by minimizing tissue

damage while improving electrode sensitivity [**Das *et al.* 2016**]. Moreover, although extracellular devices typically show a worse signal quality recording than intracellular ones, nanoscale features favour best coupling with the cell membrane as a larger surface of it will be in direct contact with the nanoelectrode, improving the signal to noise ratio. So, another important feature regarding efficient electrical stimulation (which is also related to biocompatibility) is the cell-electrode interface [**Isik *et al.* 2005; Brüggemann *et al.* 2011; Lacour *et al.* 2016**]. Specifically, when cells are cultured *in vitro* on such structures, their interactions highly depend on the geometry, dimension and spacing between adjacent electrodes [**McGuire *et al.* 2018**]; whereas, *in vivo*, mechanical compliance with the native neural tissue becomes of large importance to adapt its shape and movements and avoid friction forces and fibrotic scarring. For further details on the interface between cells and vertical structures, please refer to elsewhere [**Chiappini, 2017; Chang *et al.* 2016**].

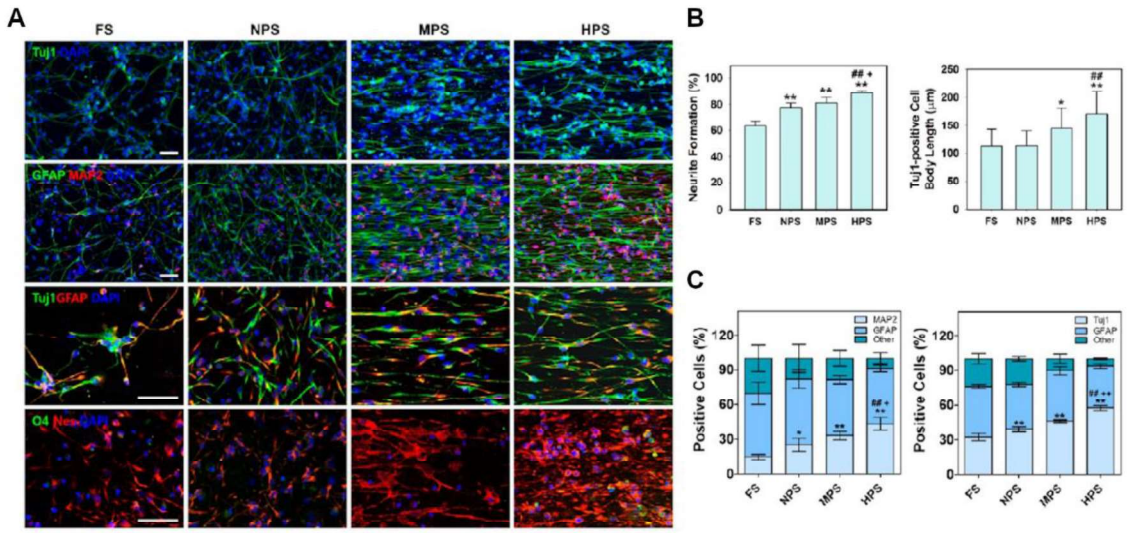

Figure I9. Differentiation of hNSCs on substrates presenting different topographies (FS: Flat substrate; NPS: Nanopore patterned substrate; MPS: Microgroove patterned substrate; HPS: Hierarchically patterned substrate consisting of both microgroove and nanopore patterns) after 5 days in culture. A) Immunofluorescent staining of hNSCs differentiated on each substrate for

neuronal (Tuj1 and MAP2), astrocyte (GFAP), oligodendrocyte (O4), and undifferentiated NSC (nestin)markers; scale bars = 50 μm. B) Quantification of neurite formation and the length of neurite outgrowth in the Tuj1-stained images (*$p < 0.05$, **$p < 0.01$, compared to the FS group; ##$p < 0.01$, compared to the NPS group; $^{+}p < 0.05$, compared to the MPS group). C) Relative proportion of MAP2- or GFAP-positive cells and Tuj1- or GFAP-positive cells on each substrate; *$p<0.05$, **$p < 0.01$, compared to the FS group; ##$p < 0.01$, compared to the NPS group; $^{+}p<0.05$, $^{++}p < 0.01$, compared to the MPS group). Adapted from [**Yang *et al.* 2014**].

2.9.2. Exploration of electrodes with different chemical composition to obtain improved neural biocompatibility and recording/stimulation.

Other than topography, chemical composition is also a particularly important feature to assure biocompatibility of these electrodes, including adequate interaction with neural, vascular and immune components [**Lacour *et al.* 2016**]. Most common nanoelectrodes in this scenario are made of Au [**Dipalo *et al.* 2017; Brüggemann *et al.* 2011**], platinum (Pt) [**Xie *et al.* 2012**], iridium oxide (IrO_2) [**Lin *et al.* 2014**], GaP [**Suyatin *et al.* 2013**] and doped silicon [**Robinson *et al.* 2012**]. The criteria by which they are selected are their biocompatibility, low electrical impedance for electrophysiological recording, stability in aqueous solutions of neutral pH and physiological temperature, tunable geometry and topography at the micro and nanoscales, and easy-fabrication processing [**McGuire *et al.* 2018**]. Moreover, these materials can be modified with a diversity of polymers and/or biological molecules to improve their biocompatibility and stability once implanted.

Recent advances in the field include Au mushroom-shaped microelectrodes functionalized with RGD peptides (arginine-glycine-aspartic acid), which induce the phagocytosis of the microelectrodes [**Hai *et al.* 2010**],

vertical NWs electrode arrays [**Robinson *et al.* 2012**], and Pt-back electrodes with nanoscale roughness [**Abbott *et al.* 2020**], to name a few. Furthermore, work by Patolsky *et al*. [**2006**] reported the ability of high-density silicon NWs transistor arrays to record signals from up to 50 different spatial points in a single axon.

In a different set of applications, nanostructured electrodes are being also considered as promising materials for the development of wearable and implantable bioelectronic devices. For instance, silver (Ag)-Au coresheat nanocomposites composed of ultra-long (100 μm) Au-coated Ag NWs embedded in an elastomeric polymer matrix of poly(styrene-butadiene-styrene) have shown promise for the development of implantable soft devices that could be conformally integrated in skin and cardiac tissue for continuous electrophysiological recording and electrical thermal stimulation [**Choi *et al.* 2018**]. These composites allow electrophysiological signals recording including surface electromyograms, surface electrocardiograms and intracardiac electrograms, as well as thermal and electrical stimulations.

2.10. Approaching SCI treatment using implantable 3D scaffolds

This strategy is the most studied regarding biomaterials use for the treatment of SCI to date. **Table I1** summarizes the major achievements to this respect. Briefly, biomaterials under investigation are largely diverse, and generally they can be classified according to their origin. On the one hand, biomaterials of natural origin, such as collagen and chitosan, present relative abundance, easy processing and more importantly, outstanding biocompatibility with low immunological rejection response after transplantation. Moreover, they are biodegradable, and their degradation products are typically nontoxic. As drawbacks, these materials can exhibit batch

to batch variations in composition, limited mechanical properties, eventual pathogen transmission, and, in some cases, their degradation rate is faster than desired [**Kim *et al.* 2011; Liu *et al.* 2019**]. On the other hand, biomaterials of synthetic origin, such as Poly(ε-caprolactone) and Poly(lactic acid), allow researchers to find customized physicochemical properties (such as controlled porosity), better reproducibility, more controlled biodegradability and low inflammatory response, but sometimes they need to be modified to improve their biocompatibility and to avoid the possible toxic response of their degradation products [**Subramanian *et al.* 2009**]. Additional examples of natural biomaterials under research for SCI are fibrin [**Yao *et al.* 2018**], agarose [**Han *et al.* 2018**], alginate [**Grijalvo *et al.* 2019**], self- assembly peptides [**Liu *et al.* 2013**] and acellular scaffolds made from porcine brain decellularized ECM [**Hong *et al.* 2020**], among others. Contrarily, another example of synthetic materials is the poly-β-hydroxybutyrate [**Novikova *et al.* 2008**], among others. All these materials have been used either alone or as scaffolding materials for different kinds of cells and/or carriers for a large diversity of drugs and factors for the treatment of various types of SCI, as shown in the references provided.

Table I1: Examples of biomaterials of both natural and synthetic origin for the design and fabrication of implantable 3D scaffolds for their use in SCI models.

Biomaterials for the design of 3D scaffolds					
Natural origin			**Synthetic origin**		
Collagen	Most abundant protein of the ECM in human and animal organisms [**Liu *et al.* 2019**]		**Poly(ε-caprolactone) (PCL)**	Derived from a biocompatible and slow-bioresorbable polyester [**Kim *et al.* 2011**]	
	Collagen scaffolds functionalized with collagen-binding EGFR antibody Fab fragment	**Fan *et al.* 2017** **Li *et al.* 2016**		Porous PCL microtubes	**Shahriari *et al.* 2017**
	Collagen scaffolds tethered with antibodies which bind receptors of growth factors (concretely, with the EGF receptor)	**Xu *et al.* 2017**		PCL used in combination with collagen for hydrogels fabrication	**Nguyen *et al.* 2017**
	Collagen scaffolds built in combination with porcine brain decellularized ECM	**Hong 2020**		Electrospun PCL scaffolds loaded with stem cells	**Terraf *et al.* 2016**
	Collagen scaffolds seeded with MSCs derived from human umbilical cord	**Li *et al.* 2017**		Composites of PCL with spider dragline silk proteins loaded with NPCs	**Baklaushev *et al.* 2019**
Gelatin	Natural protein polymer produced by partial hydrolysis of collagen [**Kim *et al.* 2011**]		**Poly(lactic acid) and poly(lactic-co-glycolic acid) (PLA and PLGA)**	PLA and PLGA are commercially available, FDA-approved biomaterials which can be modified to increase their biocompatibility and biodegradability [**Kim *et al.* 2011; Liu *et al.* 2019**]	
	Gelatin sponge scaffolds	**Du *et al.* 2014**		Multiwall conduits	**Hurtado *et al.* 2011**
	Porous microspheres based on gelatin loaded with FGF	**Lan *et al.* 2017** **Kim *et al.* 2011**		Highly porous scaffolds	**Slotkin *et al.* 2017**
Hyaluronic acid (HA)	Non-sulfated glycosaminoglycan polymer found in many tissues of the body, with a high concentration in the ECM of the CNS [**Pettikiriarachchi *et al.* 2010**]			Microfibers scaffolds	**Roman *et al.* 2016**
	HA scaffolds combined with stem cells	**Li *et al.* 2017**		Composite materials in the shape of modified liposomes loaded with drugs	**Gao *et al.* 2017**
	HA-based hydrogels containing an IKVAV (Ile- Lys-Val-Ala-Val) peptide derived from laminin, and BDNF	**Park *et al.* 2010**	**Poly(2-hydroxyethyl methacrylate) (pHEMA)**	It consists of a network of copolymers [**Liu *et al.* 2019**]	
	HA hydrogels without functionalization	**Kushchayev *et al.* 2016**		Biofunctionalized by anchoring the peptide SIKVAV into pHEMA hydrogels	**Kubinová *et al.* 2015**
Chitosan	Linear polysaccharide polymer obtained from chitin, which is widely found in cell walls of crustaceans, bacilli and fungi [**Patel *et al.* 2011; Ikeda *et al.* 2014**]		**polyethylene glycol (PEG)**	Polyether composed of repeated ethylene glycol units FDA-approved biomaterial [**D'souza and Shegokar 2016**]	
	Chitosan scaffolds biofunctionalized with NT-3 and loaded with cells	**Sun et al. 2017** **Oudega *et al.* 2019**		Cross-linked poly(N-isopropylacrylamide)-PEGcopolymer hyfrogel	**Bonnet *et al.* 2020**

Within customized materials, we must also include conducting biomaterials, such as conducting polymers and nanoparticles, which, apart from being present in the production of electrode platforms, are also considered for the fabrication of 3D scaffolds. Concrete materials include polypyrrole [**Shu *et al.* 2019**], poly(3,4-ethylenedioxythiophene) (PEDOT), which has been investigated for its use in combination with other materials for the fabrication of electrodes [**Vara and Collazos-Castro, 2019; Moral-Vico *et al.* 2014; Lichtenstein *et al.* 2018**], and carbon nanotubes (CNTs) in the shape of 3D frames [**Usmani *et al.* 2016**] and as part of composites with elastomers such as polydimethylsiloxane (PDMS) [**Aurand *et al.* 2018**].

In this line, the outstanding physico-chemical properties of carbon-based materials including CNTs, carbon nanofibers and graphene are encouraging their exploration as attractive materials to interface damaged neural tissues as part of novel platforms with potential utility in neural repair [**Tavangarian and Li, 2012**]. Concretely, the use of graphene-derived materials (GDMs), which might provide novel therapeutic approaches in the field of regenerative medicine and tissue engineering, is receiving increasing attention these days.

2.10.1. Graphene as a biomaterial of selection for CNS restoration: Focus on SCI

In the past decade, it has been demonstrated that GDMs not only increase neural cells adhesion, but also support the growth of hippocampal neurons, MSCs and NSCs [**Xia *et al.* 2019**], as well as their respective differentiation towards neuronal phenotypes. Moreover, graphene inherent electrical conductivity has been used to direct stem cells migration and to regulate their differentiation. GDMs can be malleable to add biophysical signals that can improve graphene effects on cell morphology, adhesion, migration, proliferation and differentiation, among many others. Thus, GDMs are becoming popular for potential applications in clinical neurology. However, the

underlying mechanisms behind most of these phenomena have been poorly investigated. For instance, to further understand the mechanisms responsible for graphene-regulated NSCs differentiation, Tang *et al*. [**2019**] used RNA-seq profiling (*i.e.,* next-generation RNA sequencing) on the genome-wide transcriptome to analyse the influence of graphene on the differentiation of NSCs in comparison to other substrates. They identified both upregulation and downregulation in the expression of many genes. Although the functions of many of them have not been comprehensively studied, several ones were related to development control (*e.g.,* wnt7a and Bmp2). Changes at the metabolic level on stem cells cultured onto 3D graphene substrates in comparison to 2D graphene and glass substrates, eventually relevant for cell proliferation, have been also reported [**Fang *et al.* 2020**].

Within the wide family of GDMs, graphene oxide (GO) and reduced graphene oxide (rGO) are the most used in biomedical applications because of their enhanced biocompatibility in comparison to "pure" graphene (**Figure I10**). GO is characterized by a variable amount of oxygen containing functional groups (*i.e.,* mainly hydroxyls, -OH; carboxyls, -COOH; and epoxies, >O) in the closely packed honeycomb lattice of a sp^2-bonded monolayer of carbon atoms [**Kumar *et al.* 2020; Dreyer *et al.* 2010**]. These groups (that can be present on both sides of GO nanosheets) significantly increase the hydrophilicity (which is very important for implantation into living organisms, mainly composed by water) as well as the adsorptive properties of graphene, making it more biocompatible and thus boosting its utility in biomedicine, where these functional groups would be available for anchoring therapeutic molecules [**Reina *et al.* 2017; Singh *et al.* 2018; Yang *et al.* 2013**]. Nonetheless, the incorporation of functional oxygenated groups within the chemical structure of pure graphene deteriorates some of its outstanding advantages [**Singh *et al.* 2018**]. For example, GO is not as good conductor of electricity as graphene [**Bai**

et al. **2011**] and it is mechanically poorer [**Cheng *et al.* 2017**]. To overcome some of these limitations of GO while still taking advantage of a superior hydrophilicity and ability for functionalization, chemical and/or thermal reduction of GO [**Fadeel *et al.* 2018**] (in order to remove some of the oxygenated groups and regenerate, at least in part, the sp^2 network) has been widely explored, thus attaining rGO. rGO can be considered as an intermediate chemical structure between the ideal graphene sheet and the highly oxidized GO, thus maintaining some properties of both materials and reducing others [**Reina *et al.* 2017**]. In this context, tuneable surface chemistry opens many possibilities to obtain useful and functional derivatives of graphene. In neural applications, as for many other applications in tissue engineering, GDMs have been explored as either biomaterials entirely composed of GDMs or as doping agents of other material frameworks.

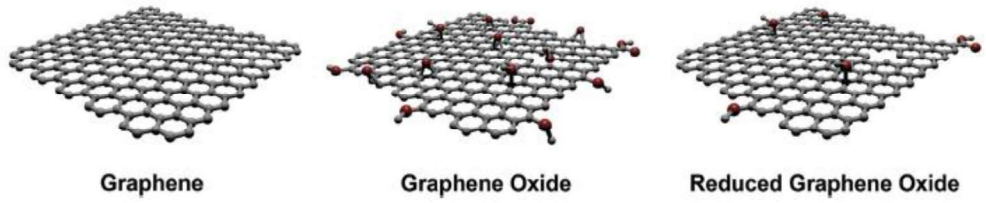

Figure I10. Graphene, GO and rGO chemical structures [**Reina *et al.* 2017**; Reproduced by permission of The Royal Society of Chemistry].

2.10.1.1. *In vitro* neural studies with GDMs

Most of these works focused on the ability of GDMs (alone or in combination with electrical stimulation) to induce the preferred differentiation of stem cells toward neuronal phenotypes rather than glial cells. The main conformations used for *in vitro* tests include nanosheets, films, microfibers and foams (3D). For example, Park *et al*. [**2011**] demonstrated that graphene 2D substrates placed onto glass coverslips and coated with laminin augmented the viability, as well as the differentiation toward neuronal phenotypes, of human NSCs in comparison to the control glass region of the same coverslips. In other

work, Wang *et al*. [**2012**] showed that functionalized graphene promoted the differentiation of MSCs toward neuronal phenotypes by causing cytoskeletal changes in these cells. Guo *et al*. [**2017**] found that nanostructured rGO MFs not only offered a more powerful substrate for NSCs adhesion and proliferation compared with 2D graphene films and tissue culture plates, but also facilitated NSCs differentiation into neurons (rather than glial cells) as well as the formation of dense neural networks surrounding the MFs. In previous studies in our group, interconnected neural networks composed of highly viable neurons and glial cells developed onto 3D porous and flexible PLL-functionalized GO-based scaffolds [**Serrano *et al.* 2014**] and on rGO MFs functionalized with either PLL or N-cadherin [**González-Mayorga *et al.* 2017**]. In a different study, electrical stimulation of MSCs cultured onto highly conductive rGO–PEDOT MFs increased their viability, proliferation and neuronal differentiation [**Guo *et al.* 2016**]. Feng *et al*. [**2015**] also took advantage of the synergistic effect of GO coating combined with electrical stimulation to enhance and accelerate the growth and development of primary motor neurons *in vitro* when cultured on GO-coated poly(vinyl chloride) nanofibers. Moreover, electrical stimulation promoted neuronal differentiation over glial phenotypes when cells were interfaced to 3D graphene [**Li *et al.* 2013**] and GO foams [**Akhavan *et al.* 2016**]. Interestingly, GO nanoparticles of different sizes could modulate self-renewal and differentiation of mouse NSCs, even triggering neuronal differentiation, through the modulation of intracellular molecular pathways [**Lin *et al.* 2020**].

Some of these GDMs also facilitate the differentiation of oligodendrocyte fates (also important in neural tissue regeneration based on their role in axons myelination at the CNS) and the proliferation of Schwann cells (myelin-forming cells at the PNS that have been also found to assist axonal regeneration in the injured CNS). Concretely, an enhanced differentiation towards mature

oligodendrocytes of NSCs was observed after increasing the GO amount on PCL nanofibers [**Shah *et al.* 2014**]. Furthermore, scaffolds composed of aligned and aminolyzed poly(L-lactic acid) (PLLA) nanofibers coated with GO nanosheets promoted Schwann cells proliferation [**Zhang *et al.* 2016**]. Other important parameters measured in *in vitro* studies include neurite sprouting and outgrowth, as well as neural maturation. For example, graphene substrates enhanced neurite number and average length of primary hippocampal neuronal cells, as well as general cytocompatibility parameters, in comparison to tissue culture polystyrene substrates [**Li *et al.* 2011**]. Zhang *et al*. [**2016**] demonstrated that PLLA nanofibers coated with GO improved the proliferation and neurite growth along the nanofibers of pheochromocytoma 12 (PC-12) cells in the presence of NGF. Graphene films also boosted neuronal maturation of hippocampal cells by increasing neurite sprouting and outgrowth [**He *et al.* 2016**].

When looking at intracellular mechanisms, consequences of long-term exposure of primary rat astrocytes to pristine graphene and GO flakes were studied. Chiacchiaretta *et al*. [**2018**] observed that these flakes interfered with a variety of intracellular processes as a result of their internalization through the endolysosomal pathway. It has been also studied that GDMs can modulate neural excitability, as demonstrated by Tang *et al*. [**2013**] when studying neural cells communication and activity on graphene films. More specifically, studies with graphene nanosheets revealed their capacity to modulate neural network activity. For example, Rauti *et al*. [**2016**] described how small lateral dimensions GO nanosheets downregulated neuronal signalling without affecting cell viability when hippocampal neurons were exposed to culture medium containing this material. Small GO flakes also modified the excitatory activity of dissociated amygdala neurons *in vitro* [**Secomandi *et al.* 2020**]. Moreover, it has been demonstrated that this modulation on neuronal activity could be due to

changes in the distribution of extracellular ions caused by the interaction of single-layer graphene with cell membranes [**Pampaloni *et al.* 2018**]. For cell internalization, it has been reported that graphene flakes preferentially interact with cholesterol present in the neural cell membrane, thus altering cell processes related to neural communication such as release and recycling rate of synaptic vesicles [**Kitko *et al.* 2018**].

2.10.1.2. *In vivo* neural studies with GDMs

As previously mentioned, López-Dolado *et al*. [**2015**] were first to study the *in vivo* tissue response of the injured rat spinal cord to the implantation of flexible and porous 3D scaffolds composed of rGO. These scaffolds were fabricated by using the ice segregation-induced self-assembly technique. The lesion model of choice was a right lateral hemisection of approximately 8 mm^3 at the C6 level, rostral to the bulk of *triceps brachii* (TB) motoneurons. rGO scaffolds were placed at the lesion site and covered with a thin gelatin hydrogel film. Animals without injury and those hemisected but not receiving scaffolds served as control groups. In order to study the subacute tissue response to these implants, both locally (at the spinal cord) and systemically (in liver, kidney, lung and spleen), rats were sacrificed at 10 days after injury. The results revealed that these hierarchically-oriented scaffolds allowed the formation of a soft interface at the injury site, with no significant differences in fibro-glial scar features with respect to lesions without scaffolds. Due to their porous structure, ECM molecules (*e.g.*, collagen) and different kinds of cells were able to infiltrate and migrate to the inner parts of the scaffolds contributing to the stabilization of both the scaffold and the lesion site. Colonizing cells were mainly positive for vimentin (indicative of connective tissue cells, glial cells and pericytes, among others) and the β receptor of the platelet-derived growth factor (a regulator of blood vessels formation and early hematopoiesis). In addition, pro-regenerative M2-like macrophages were present both at the interface tissue-material and

within the scaffold, which could be potentially involved in the initiation of neural repair responses. Finally, neural cell populations were preserved at the perilesional areas and no toxic systemic responses were found, thus indicating the positive biocompatibility of these GDMs with both neural and non-neural tissue components once implanted *in vivo* for short periods of time. Fuelled by these encouraging findings, the authors focused on the tissue responses at 30 days after injury (early chronic state; **López-Dolado *et al.*, 2016**). In this study, rGO scaffolds were fabricated in the shape of randomly porous 3D foams by a conventional freeze-casting methodology. It was first confirmed that the scaffolds were properly stabilized, as already achieved at 10 days. As expected from the progression of the lesion, enhanced cell and collagen infiltration within the scaffold was found despite a significant reduction in cells positive for vimentin in comparison to the subacute state. Furthermore, blood vessels increased their size and number over time, both at the interface and, more importantly, inside the rGO foams. Even though the total amount of macrophages was reduced in comparison with the subacute state, M2 macrophages increased with respect to those with M1-like phenotype (pro-inflammatory). All these changes prompted the formation of a new pro-regenerative ambient that allowed the growth of some neuronal axons within the scaffold (not observed at the subacute state), which were close to blood vessels. As found in earlier time points, no evidences of atrophy, inflammation or fibrosis were detected in peripheral organs. Our group also performed preliminary *in vivo* studies to test flexible rGO MFs as guidance platforms in the same cervical model [**González-Mayorga *et al.* 2017**]. Ten days after injury, some axons were able to reach the proximities of the MFs at the lesion site, even in some cases spreading on their rGO surface. Moreover, no signs of subacute local toxicity due to this material implantation were detected. All these beneficial results encouraged further exploration of the potential of both rGO 3D foams and MFs as suitable platforms for SCI treatment. So, in this thesis, we

focused on the evaluation of the implantation of both materials at a more chronic state (120 days post-injury, DPI), whose results will be later presented.

Apart from Serrano and López-Dolado groups, very few researchers have investigated GDMs as implants within the injured spinal cord *in vivo*. Kim *et al*. [**2018**] showed that PEGlylated graphene nanoribbons implantation in the transected lumbar (L1) spinal cord augmented the presence of neural components as well as showed signs of glial scar attenuation after 5 weeks of implantation. These results were indicated as responsibles for the locomotor improvements observed in rats at the end of this period. Alternatively, Pan *et al*. [**2019**] demonstrated that hybrid nanofibers made of an admixture of GO and PLGA could work as carriers for the local delivery of insulin-like growth factor 1 (IGF-1) and BDNF in the injured hemisected thoracic (T9) spinal cord. Results demonstrated that local delivery of both growth factors immobilized into PLGA/GO nanofibers significantly improved functional locomotor recovery, reduced cavity formation and increased the number of neurons at the injury site. It is important to note that all these studies have been performed in the last 5 years, so indicating that this is a recent topic with increasing interest.

Despite this progress, there are still many concerns about GDMs toxicity and biodegradability for their use in biomedical applications. This is partly because there are few studies which systematically address this issue, along with the fact that there is not a clear differentiation between the biocompatibility of the different GDMs (*e.g.*, pristine graphene, GO, rGO), which present different chemical (*e.g.*, oxidation level, amount of oxygenated functional groups, number of graphene layers) and physical (*e.g.*, size, shape, mechanical properties) characteristics. Moreover, the lack of standardized procedures for toxicity assessments makes results difficultly comparable and often contradictory. An additional issue identified is that an inefficient purification of the material could lead to non-desired effects, instead of the

material itself. Taking all this into consideration, efforts are being made to characterize in more detail how these different factors contribute to the capacity of agglomeration, long-term stability, and elimination of these compounds from the organism, but further research is needed to clarify this issue [**Reina *et al.* 2017; Fadeel *et al.* 2018**]. For instance, studies focused on the biocompatibility of GDMs within the brain, rather than their regenerative capacity, explored the biocompatibility of rGO and its influence on neurogenesis in the adult mice olfactory bulb (OB) *in vivo* [**Defterali *et al.* 2016**]. Results revealed that rGO had no deleterious effects either on the survival of the resident populations of neurons and astrocytes (measured as number of cells and detection of apoptosis) or on the newly generated neurons (measured as number of cells). By looking at the number and morphology of microglia cells (Iba1C), authors evidenced that alterations on the microglial response at the OB were related to the injection itself rather than the presence of rGO. Studies by Mendonça *et al*. [**2016**] focused on the effect of rGO on the blood-brain barrier (BBB) components both *in vitro* and *in vivo*. Under *in vitro* conditions, the exposure to high concentrations of rGO (100 mg/mL) produced a lower toxicity in both rat astrocytes and endothelial cells than rGO functionalized with PEG, which induced a dose- and time-dependent toxicity. For *in vivo* studies, rGO and rGO-PEG were injected intravenously and their toxic effects on the BBB integrity analyzed for different times. Both materials caused a notable downregulation of astrocyte markers (GFAP and connexin-43), endothelial tight (occludin) and adherens (b-catenin) junctions and basal lamina (laminin) at 3 h after administration. Interestingly, this effect disappeared after 7 days of exposure to rGO, while it was permanent and increased over time in the rGO-PEG group. The increase in proteins related to the antioxidant system, such as catalase, in the animals treated with rGO-PEG, accompanied by high levels of intracellular reactive oxygen species, pointed out towards oxidative stress as one of the main causes of rGO-PEG-mediated damage.

All the major findings of the state-of-the-art exposed above support the need for further studies in the promising potential of both NWs and graphene-derived scaffolds as neural interfaces capable of stimulating the repair of the injured spinal cord.

3. OBJECTIVES

The experimental work of this thesis arose in the context of two funded research projects at the time of its realization: ByAxon (H2020-FET-OPEN-RIA, EC) and MAT2016-78857-R (Spanish AEI/FEDER, UE). Both projects share a common main goal, coincident with the general aim of this thesis, which is the design and development of biocompatible platforms able to promote repair and/or enable reconnection of the injured spinal cord. Based on this, we proposed six different highly interconnected objectives for this thesis, three for each of the projects, as described below.

On the one hand, in the context of the ByAxon project, we received from IMDEA-Nanociencia vertically arranged metallic NWs made of either nickel (Ni) or gold (Au) and grown by template-assisted electrodeposition over a flexible Au base. Comparable flat substrates of both metals were also provided as nanotopography controls. PDMS substrates, developed during a short-stage (3 months) in the International School for Advanced Studies (SISSA), were additionally fabricated and tested as an eventual biocompatible coating of the bypass components. The nanoelectrodes and PDMS substrates were evaluated for their further implementation in more complex devices able of acting as a biocompatible local bypass within the injured spinal cord. To this aim, the following specific objectives were defined:

1. Evaluation of basic *in vitro* biocompatibility parameters (including morphology, viability and differentiation) of the metallic nanoelectrodes with primary neural cell cultures.

2. Understanding of the role that topography and chemical composition of the electrodes plays in the interaction of these materials with primary neural cell cultures *in vitro*.

3. Examination of the capacity of PDMS samples to enable the formation of active neuronal networks *in vitro* by analysing spontaneous calcium transient elevations.

On the other side, our laboratory has pioneered the exploration of rGO-based biomaterials as suitable 3D platforms to support neural repair in an experimental animal model of SCI. Motivated by positive previous findings of the group in this regard, the experimental work of this thesis focused on the examination of the regenerative potential of these rGO-based biomaterials when chronically implanted (four months) in the injured cervical spinal cord. To this aim, the following specific objectives were defined:

1. Synthesis and detailed physico-chemical characterization of 3D rGO foams and rGO MFs for their examination at the injured spinal cord.

2. Exploration, by means of a multidisciplinary approach, of the long-term ability of these rGO materials to promote a local regenerative scenario in terms of vascular and neural remodelling, as well as attenuation of the immune response, when chronically implanted at the injured spinal cord.

3. Examination of the systemic effects derived from the spinal implantation of these rGO materials regarding organ toxicity and impairments in rat spontaneous behaviour.

4. MATERIAL AND METHODS

All materials and biological samples in this thesis were manipulated according to standard regulations so no safety concerns arose. Chemical reagents, biological molecules and antibodies were purchased from Sigma-Aldrich, Life Technologies, and Panreac, unless otherwise indicated. Neurobasal™ media, B-27, and other culture supplements were purchased from Life Technologies, Fisher Scientific and Lonza. GO slurry was purchased from Graphenea, S.A. (Batch #C1250/GOB125/D, 4.6 wt% concentration, >95% monolayer content). All reagents were used as received unless otherwise indicated.

4.1. Biomaterials fabrication

4.1.1. Metallic NWs arrays

These samples were fabricated and provided by our collaborators at IMDEA-Nanociencia in the context of the ByAxon project. Briefly, nanostructured electrodes were prepared by template-assisted electrochemical deposition using as templates polycarbonate nanoporous membranes, with 100 nm pore diameter (Whatman). The pores density of the template was 10^8 cm^{-2}. Electrodeposition was carried out in a three-electrode electrochemical cell with a Metrohm Autolab PGSTAT204 potentiostat, using a Pt mesh as a counter electrode and an Ag/AgCl (3 M NaCl) electrode as a reference electrode. Before electrodeposition, a 100 nm-thick Au film was sputtered on one side of the membrane using a Leica EM ACE600 sputtering, which was thicken to 1 μm using pulse-plating Au electrodeposition, with an on pulse at -1.5 V and an off/rest pulse of 0 V. This Au film constituted the base of the final electrode over which NWs were deposited.

Electrodes with NWs of Au (Au-NWs) and Ni (Ni-NWs) were prepared, in order to explore two different materials with significantly different physico-chemical properties. For Au electrodeposition, an Orosene commercial electrolyte (ORE+4, Italogalvano) was used at room temperature (RT), whereas for Ni growth a Watts-type electrolyte composed by $NiSO_4$ (0.8 M), $NiCl_2$ (0.2 M) and H_3BO_3 (0.4 M) was utilized, working at 45 °C. Finally, samples were removed with dichloromethane, followed by extensive washing in acetone, ethanol, and deionized water, while leaving the network of vertical NWs attached to the Au base.

Plane flat Au (Au-Flat) and Ni (Ni-Flat) electrodes were also prepared and investigated to explore the effect of nanotopography. For Au, the bases described above prior NW growth served as Au-Flat, while, for Ni, a thin Ni layer was deposited on top of the Au bases under the same electrochemical conditions as those used for Ni NWs growth.

Prior to cell culture, all electrodes were first sterilized by UV radiation in a biosafety cabinet and then functionalized by adsorbing low molecular weight poly-L-lysine molecules (PLL; 30,000 – 70,000 Da; 45 $\mu g\ ml^{-1}$, 1h incubation at RT). The homogeneity of the coating was confirmed by immunofluorescence after PLL-FITC adsorption. Control glass substrates were functionalized following the same protocol as for metallic electrodes.

4.1.2. PDMS 2D substrates

For the preparation of the PDMS (polydimethylsiloxane) substrates, commercial PDMS silicon elastomer (Sylgard® 184-Down Corning Co.) was prepared by mixing 10 parts of elastomer and one part of curing agent following manufacturer instructions. Then, one drop of this mixture was placed over each glass rectangular coverslip (12 x 24 mm, 0.17 mm thickness; Hindler) and layered to cover the entire surface with the aid of forceps and a glass rod. Thus, an uniform film of PDMS of ~2 mm thickness was obtained. To make

PDMS substrates more stable with time, they were cured by using a thermal treatment (100 °C for 2 h). Samples were stored at RT until used.

4.1.3. 3D rGO foams

3D rGO scaffolds (in the shape of foams) were fabricated by a freeze-casting methodology. Briefly, GO slurry was gently dispersed in distilled water (5 mg·mL^{-1}) and pipetted into tap covers of 0.5 mL Eppendorf tubes (50 μl). Samples were then frozen at −80 °C overnight and subsequently freeze-dried for 24 h. The resulting cylindrical and porous monoliths were thermally treated at 200 °C for 30 min. Prior to implantation, scaffolds were sterilized under UV radiation (for 30 min) and finally infiltrated with sterile cell culture grade water at 4 °C until complete immersion (at least 48 h).

4.1.4. 3D rGO microfibers (rGO MFs) and microfibers-based scaffolds (rGO-MFs)

A GO suspension (6.8 mg·mL^{-1} in distilled water) was used to fill in capillary tubes (standard Hirschmann capillary tubes of 120 mm in length and 1.35 mm in diameter), which were later sealed up at their edges and thermally treated at 220 °C for 2h. rGO MFs were removed from the tubes by soft blown and allowed to dry overnight on top of filter paper.

In order to facilitate their implantation, rGO MFs were embedded in a 3D hydrogel scaffold (2 x 2 x 2 mm^3). Briefly, MFs were immersed in an aqueous gelatine solution (7.5 wt% in distilled water, from porcine skin, Sigma-Aldrich) in customized methacrylate tubular molds (2 mm in diameter, 5 mm in height, 20 rGO MFs/hydrogel). Hydrogels were then exposed to low temperature conditions (4 °C) overnight for gelation. Thereafter, rGO-MFs scaffolds were extracted from the moulds and cut in cylinders of 2 mm in height. For further crosslinking, samples were exposed to paraformaldehyde (PFA) vapours at 4 °C for 24 h. Prior to implantation, 3D rGO-MFs scaffolds were sterilized by UV

radiation for 30 min in a biological safety cabinet. Dimensions of the resulting implants were ~8 mm^3, in accordance with the lesion site.

4.2. Biomaterials characterization

4.2.1. Morphology characterization by Scanning Electron Microscopy (SEM)

In this thesis, SEM was used to study both NWs and rGO foams morphology. Moreover, neural networks formed on NWs were examined at different time points. In this last case, field emission scanning electron microscopy (FESEM) images were also acquired to obtain more detailed information about the interaction of neural cells with the NWs.

Samples which included neural cultures were rinsed in phosphate-buffered saline (PBS) twice and fixed with glutaraldehyde (2.5 % in PBS) for 45 min as a conventional fixation method for examination by electron microscopy. After washing in distilled water, dehydration was performed by using series of ethanol solutions for 15 min (2 washes) and a final dehydration in absolute ethanol for 30 min. These samples were then dried at RT for at least 24 h. After mounting in stubs and Au coating (10 nm) under vacuum, the morphology of the samples was characterized. If morphology characterization comprised just the biomaterial (without cells), samples were directly mounted in stubs and visualized. After their growth, the morphology of NWs (conductive samples) was evaluated by using a ZEISS EVO HD15 SEM microscope. On the other hand, samples covered with neural cultures were evaluated by using a Hitachi S-3000N SEM microscope working at 15 - 20.0 kV in the secondary electron mode and a field-emission Philips XL30 S-FEG microscope.

4.2.2. Mechanical properties, surface topography and electrical properties by Atomic Force Microscopy (AFM)

In our case, AFM was used with two particular objectives: (1) To evaluate the mechanical properties of 3D rGO foams, neural cells, and spinal cord tissues with and without scaffold implantation; and (2) To obtain information about rGO MFs surface roughness and electrical properties.

4.2.2.1. Mechanical properties of rGO foams, neural cells and spinal slices

AFM measurements were performed by using a commercial instrument (JPK Nanowizard 3, JPK Instruments AG, Germany) mounted on an Axio Observer A1 inverted microscope (Carl Zeiss, Germany). Depending on the biological sample (cells or tissues), different types of cantilevers were used. For cells, we used cantilevers characterized by a spring constant of 0.08 N m^{-1}, a resonant frequency of 17 kHz and a spherical tip with 6.62 μm in diameter (CP-PNPL-SiO-C cantilevers sQube, Germany). The cantilever spring constant *k* was determined by using the thermal noise method as implemented in the AFM software (JPK Nanowizard 3). For spinal cord slices obtained from explants of implanted rats once animals were sacrificed at 120 DPI, we used a modified tipless silicon cantilever (Arrow-TL1, NanoWorld, Switzerland) with a nominal spring constant of 0.07 N m^{-1} and a resonant frequency of 6 kHz. We glued a polystyrene bead with 50 μm in diameter (microParticles GmbH, Germany) to the free end of the cantilever (Norland Optical Adhesive 63, Norland Products Inc., USA).

Force-distance curves were acquired to determine the Young's modulus of neural cells and spinal cord tissues (**Figure M1**). The tip-sample distance was modulated by applying a triangular waveform. For neural cells, the tip velocity was 5 μm s^{-1} (modulation frequency of 1Hz) and the maximum force applied was 3 nN. In this case, 20 different cells were analyzed. On each cell, 126 force-distance curves were taken in a rectangular region of the somata. After taking

each individual force-distance curve, the tip was displaced laterally about 10 μm. The Young's modulus was obtained by fitting a repulsive section of the force-distance curve with a bottom effect correction model for a spherical tip [**Garcia *et al.* 2017 and 2018**]. For tissues, the modulation velocity was 5 μm s^{-1} (modulation frequency of 0.33 Hz) and the maximum force applied was 20 nN. Data represents the average value obtained in three different spinal cord slices. In each sample, 100 individual force-distance curves were taken. The individual force-distance curves were acquired on different locations separated by approximately 100 μm.

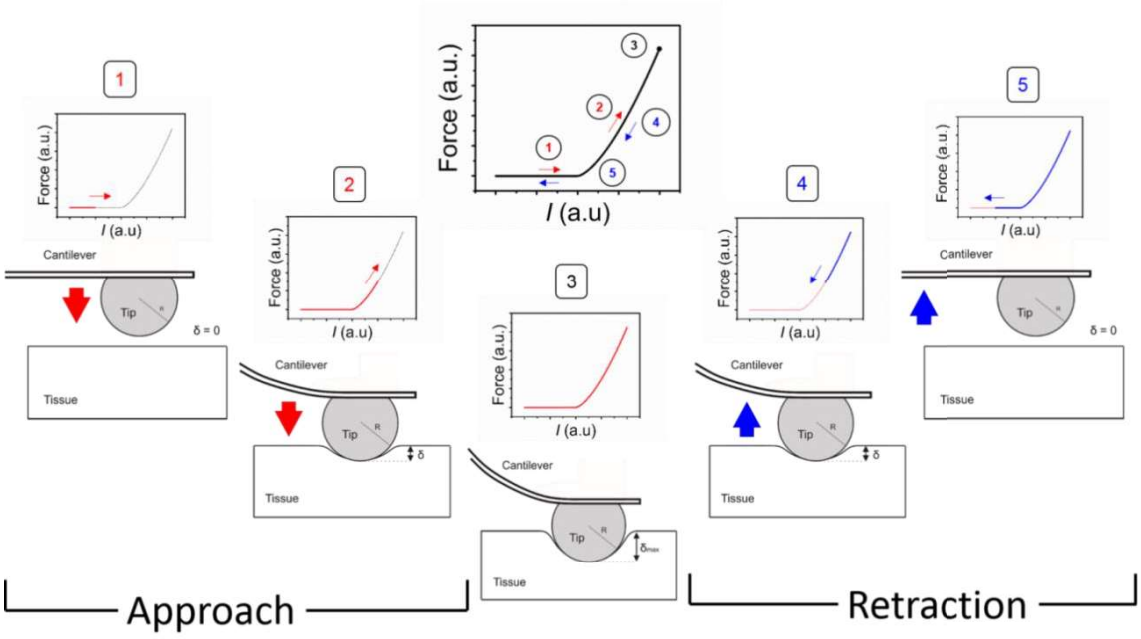

Figure M1. Scheme of a typical force-distance curve experiment. The force-distance curve has two sections, approach, and retraction. In the approach, the cantilever moves toward the sample and indents it until a given force is reached (steps 1-3). In the retraction section, the tip moves away from the sample (steps 4-5). Red and blue colours refer to the approach and the retraction sections of the force-distance curve, respectively.

4.2.2.2. Surface topography and electrical properties of rGO MFs

Single rGO MFs were fixed using double-sided copper conducting tape on the sample holder. Care was taken not to damage the central part of the

fiber, where morphological and electrical characterization was performed. Ag paste was used to properly contact the fiber at the ends. AFM tip positioning on top of the fiber was accomplished with the aid of the optical microscope integrated in the AFM system (**Figure M2**). Measurements were performed with a commercial AFM head (Nanotec, Germany) operated at RT. Dynamic mode was employed for morphological characterization, using PPP-FMR probes (Nanosensors, Switzerland). Conductive-AFM was performed using 25Pt300B Pt-probes (Rocky Mountain Nanotechnology, USA). In the present set-up, the sample was grounded and voltage was applied to the AFM tip. Finally, image analysis was performed by WSxM software [**Horcas *et al.* 2007**].

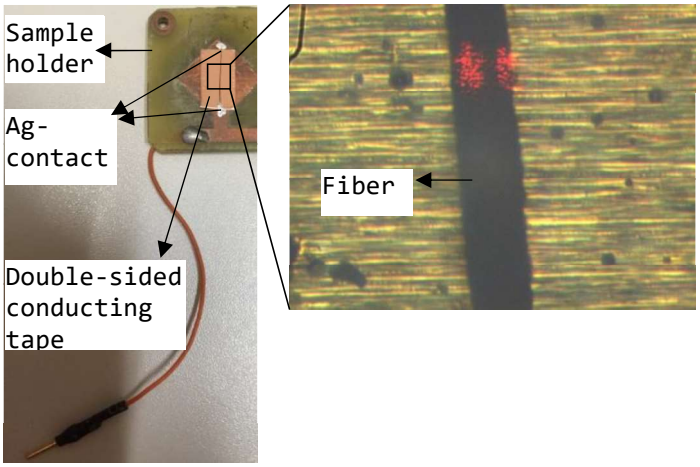

Figure M2. Details on AFM sample preparation and placing on the sample holder.

4.2.3. Chemical composition

4.2.3.1. Fourier-Transform Infrared Spectroscopy (FTIR)

In this work, FTIR was used to demonstrate the presence of chemical groups of interest (such as carboxyl, -COOH, hydroxyl, -OH and epoxy, >O) in the surface of the rGO MFs. Specifically, FTIR spectra were measured on a Spotlight 200 Micro FTIR spectrometer (Perkin-Elmer, USA). Samples were measured both by a Micro-ATR method (100 scans; frequency range: 4000 – 550 cm^{-1}; resolution: 16 cm^{-1}; aperture 0.1x0.1 mm) and by a Macro-Transmission

method (20 scans; frequency range: 4000 – 450 cm^{-1}; resolution: 4 cm^{-1}; aperture 8.94 mm) by using KBr pellet. The pellet was prepared by mixing 0.101 mg of rGO MFs powder and 99.617 mg of KBr.

4.2.3.2. Raman Spectroscopy

In our case, Raman spectroscopy was used for chemical characterization of rGO MFs as a complement to FTIR results. Raman analysis was performed on a confocal Raman microscope Alpha 300R (WiTec), using a 532 nm laser. No special sample preparation was required.

4.2.3.3. X-ray Photoelectron Spectroscopy (XPS)

In this work, comparative XPS studies of GO slurry and 3D foams composed of either GO or rGO (*i.e.,* thermally treated) were performed to characterize the chemical composition of the scaffold and to confirm the reduction degree of the samples caused by the thermal treatment applied. XPS spectra were acquired at normal emission in an UHV chamber with a base pressure of 10^{-10} mbar equipped with a hemispherical electron energy analyzer (SPECS Phoibos 150 spectrometer) and a 2D delay-line detector, using a Mg Al-Kα (1253.6 eV) X-ray source. Spectra were analyzed with the CasaXPS program using a Shirley method for background subtraction, for X-ray source satellite removal, and data processing for quantitative XPS analysis. The absolute binding energies of the photoelectron spectra were determined by referencing to the sp^2 transition of C1s at 284.6 eV determined from a freshly cleaved HOPG (highly oriented pyrolytic graphite) sample. The overall sample composition was determined from survey spectra taken at a pass energy of 20eV. It showed intense C1s and O1s peaks as well as a minor contribution from Na1s, Mn2p and K2p (only in the GO-slurry sample), and S2p. C/O atomic concentrations were determined by measuring C1s and O1s spectra with a pass energy and energy step of 20 and 0.10 eV, respectively, which provided the elemental content of C and O. For more detailed analysis, C1s high-resolution core level

spectra were recorded using an energy step of 0.025 eV and a pass-energy of 10 eV to obtain the narrowest lineshape analysis and proper core level fitting. XPS spectra fitting was done by using the deconvolution of an asymmetric component characteristic of C sp^2 bonding and several mixed percentage of Gaussian-Lorentzian symmetric functions for the rest of components, keeping the full width at half maximum (FWHM) of the peaks and the Gaussian/Lorentzian ratio constant. The energy of the peaks and their relative heights were determined by a least-squares method to account for the emission ascribed to the different chemical environment of carbon atoms according to the values reported **[Della Pelle, *et al.* 2017].**

4.2.4. Thermogravimetric analysis (TGA)

In this work, TGA was performed to obtain information of rGO MFs chemical composition, thermal stability and degradation, as well as to support the results obtained by other techniques (such as FTIR). TGA measurements were done using a TGA Q500 thermogravimetric analyzer (TA Instruments, USA) in nitrogen atmosphere. Measurements were performed from 23.7 ˚C to 980.6 ˚C with a scanning rate of 10 ˚C min^{-1}. The initial sample weight was 0.47 mg.

4.3. *In vitro* Primary neural cell cultures

4.3.1. Rat neural cortical cells (rNCCs)

Neural progenitor cells were obtained from cerebral cortices of E16-E18 Wistar rat embryos as previously described [**Carballo-Vila *et al.* 2009; Serrano *et al.* 2014**]. All the experimental protocols for cell collection adhered to the regulations of the European Commission (directives 2010/63/EU and 86/609/EEC) and the Spanish government (RD53/2013 and ECC/566/2015) for the protection of animals used for scientific purposes. Adult female Wistar rats were provided by a commercial supplier (Harlan Ibérica, Spain) and sacrificed

when gestation reached 16-18 days. For nanoelectrodes studies, atotal of 5 independent cell cultures from 5 different animals with a minimum of 3 replicates per condition in each culture were carried out (≥ 15 arrays per condition). The viability of the so-isolated cells was 90 ± 4 % in average. For high-density assays, cells were seeded at $7.5 \cdot 10^4$ cells cm^{-2} and allowed to attach for 10 min. Immediately after, samples were completely covered with 500 µl of complete Neurobasal™ media containing: B-27 supplement (2 %), streptomycin (100 UI ml^{-1}), penicillin (100 UI ml^{-1}), and L-glutamine (1 mM). For low-density assays, cells were seeded at a density of $2.5 \cdot 10^4$ cells cm^{-2}. In both cases, After 2 h of adhesion in a sterile incubator at 37 °C in a CO_2 atmosphere (5 %), culture media were replaced and cultures maintained for up to 4 weeks. Culture media were half replaced every 3-4 days. Cell culture development was monitored in the periphery of the substrates and control samples by using an Axiovert CFL-40 optical microscope with a coupled Axiocam ICC-1 digital camera (Zeiss, Germany).

4.3.2. Foetal neural progenitor cells (fNPCs) culture for calcium live experiments on PDMS substrates

For the *in vitro* experiments, PDMS samples were treated one-hour prior plating with an air plasma-cleaner (PDC-32G Plasma Cleaner, Harrick Plasma) under low-pressure air plasma (soft conditions) for 5 min. Following, substrates were ultraviolet (UV)-sterilized for 30 min before use. Control samples consisted of glass coverslips coated with PLL (45 µg mL^{-1} in distilled water) under sterile conditions.

fNPCs were isolated and cultured as previously described [**Aurand et al 2014, Sorbo 2019, and Sorbo *et al.* 2020**]. Briefly, fNPCs were derived from Wistar Rat embryos at E15. Pregnant Wistar rats were sacrificed by CO_2 inhalation. Embryos were then extracted and placed in a petri dish containing ice cold Hank's Balanced Salt Solution (HBSS) and, upon decapitation their

brain was isolated. Meninges were also removed. Olfactory bulb and cerebellum were discarded, and the rest of the brains were cut in 2 halves and transferred to another container with clean HBSS. Tissue was digested and cells were dissociated, and subsequently plated at a density of ~1 million cells mL^{-1} in standard serum-free proliferation medium (composed of 3:1 Dulbecco's Modified Eagle's Medium, DMEM : F-12, B-27TM supplement, 2 mM L-glutamine, 100 U mL-1 penicillin/streptomycin). Two growth factors were added to proliferating medium, basic fibroblast growth factor (bFGF) and epidermal growth factor (EGF) (at 20 ng mL^{-1}) for the selection of those neural cells able of proliferate and form neurospheres. Cells were maintained in proliferation medium (with the addition of both bFGF and EGF every 12-24 h) for 3-4 days *in vitro*. When neurospheres were formed, cells were frozen in 1 mL aliquots (with 10% Dimethyl sulfoxide, DMSO) at – 80 °C and then transferred and stored in the liquid nitrogen cell tank until used.

3 days before plating the cells on both PDMS and glass coverslips, cell aliquots were thawed, neurospheres were dissociated and plated in proliferation medium in the presence of bFGF and EGF (added every 12-24 h) to select cells that were able to proliferate and form neurospheres after the congelation process. Right before plating, neurospheres were again dissociated by using ACCUMAX for 5 min at 37 °C, centrifuged (100 g for 5 min) and suspended in neuronal culture medium (composed of NeurobasalTM-A medium, 2% B-27TM supplement, 1% GlutaMAXTM supplement, and 0.05 % gentamicin (50 mg mL^{-1})). Cells viability was checked to be higher than 90% right before plating by using Trypan Blue staining. Cells were finally plated onto both PDMS and glass control substrates at a density of 75000 cells / 150 μL. Cells were let to attached to the surface of both substrates for 10-20 min at 37 °C, 5 % CO_2, and finally, samples were maintained (37 °C, 5 % CO_2) with a final

volume of 2 mL of neuronal culture medium for 15 DIV. Medium was replaced once per week.

4.4. *In vivo* Animal studies

4.4.1. Experimental model of SCI

In this thesis, the experimental model of SCI selected consisted of a right lateral hemisection at C6 level, rostral to the bulk of TB muscle motoneurons, with removal of the hemisected spinal tissue. The animal model of choice was the Wistar rat (~3 months in age). Implants (both rGO foams and rGO-MFs) were placed at the injury site immediately after causing the injury (acute phase), and biocompatibility studies were done, in both cases, 4 months after implantation (chronic state).

4.4.1.1. Clinical relevance

Most SCIs are incomplete injuries at the cervical level. In the clinical classification of spinal cord syndromes, the one related to a hemisection is named Brown-Séquard syndrome. Deficits in these patients include: (1) Loss of motor function, light touch, propioception and vibration sensation ipsilateral to the injury and (2) Loss of pain and temperature sensation contralateral to the injury [**Ahuja *et al.* 2017**].

Among incomplete cervical lesions, injuries at C4-C8 levels with grade C-D in the ASIA scale are the most common. These patients preserve a considerable amount of not damaged spinal tissue, and thus, are able to recover many functions after rehabilitation, including gait, independence for daily life activities (such as getting dressed), and voluntary sphincter control [**McKinley *et al.* 2007**]. Moreover, there are many studies which show that, after this type of lesions, the affectation of the forearm (forelimb) ipsilateral to the lesion is more severe and lasts much longer (becoming chronic) than the impairments of the legs (hindlimbs).

Based on this, we decided to work with a lateral hemisection at C6 as the SCI model of choice because animals will suffer an impairment of the motor function directly related to the loss of circuits caudal to the lesion. So, animals will have affectation of the main extensor of the elbow (TB) ipsilateral to the lesion site (as shown in **Figure M3**), but keeping healthy the shoulder rotator and flexo-extensor musculature (thus, although clearly affected, animals will be able to use this paw for quadruped gait to some extent). As affected hindlimbs recover faster, we can focus on the study of the functional outcome of the main affected limb, the right forelimb, which is involved in the spontaneous behavioural activities of the rats (*e.g.,* grooming and spontaneous exploration). This fact allowed us to adapt behavioural tests already described in the literature to evaluate whether our treatment (scaffold implantation) was beneficial for the recovery of the normal behaviour of the rats or, at least, its presence did not worsen the motor outcome caused by the injury itself. Finally, as most of SCI research has been done in low thoracic and lumbar models, any insights into pro-regenerative features at the cervical level, a more demanding scenario, would be largely useful for clinicians [**López-Dolado, 2012**].

Figure M3. Right TB affectation.

4.4.1.2. Muscular and neurological features of this type of SCI

The TB is a muscle located on the back of the forelimbs, which is primarily responsible for the extension movement of the elbow. TB is also involved in the extension and abduction movements of the shoulder. Its equivalent in the hindlimbs is the *triceps surae* (TS). In quadrupedal animals (like rats), the TB has an anti-gravitational function both during locomotion (*e.g.* gait) and postural control. In humans, the coordinated function of TB and its

antagonist (*biceps brachii*) allows us to make the precise movements of the arm for the manipulation of objects (*e.g.* hold a glass full of water). Moreover, this muscle is also important for other more difficult tasks, such as to manipulate a crutch when we suffer from a leg injury. It is also particularly important for the quadruped gait while we are babies.

The neural circuits involved in TB movement at the spinal cord include different kinds of neurons (*e.g.*, IINs and motoneurons) located in many spinal segments, descending tracts from supraspinal centres (such as those from the cerebral cortex, like the corticospinal tract) and different nucleus of the brainstem (specifically, the reticular formation), and afferent terminals (with sensitive information from muscles, joints and skin). Concretely, motoneurons responsible for TB movements are located in the gray matter between the caudal part of the C6 segment and the ventral part of T1. Each motoneuron innervates a determined number of muscle fibres within the TB, as shown in **Figure M4**.

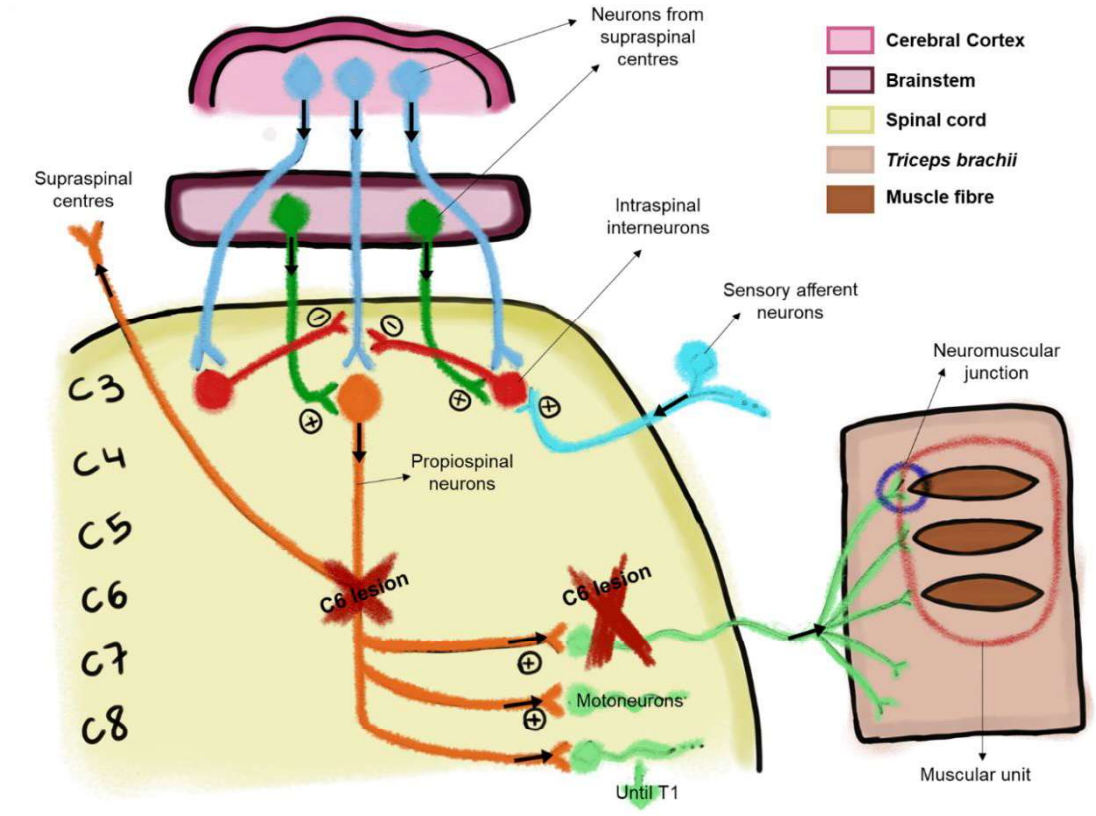

Figure M4. Neuronal circuits involved in TB motor control where C6 lesion can mainly affect both neurons coming from supraspinal centres and motoneurons. Redrawn from Lucas-Osma A, PhD thesis [**Lucas-Osma A, 2011].**

After SCI, neurons within the spinal tissue suffer an axotomy, specially IINs and motoneurons. Indeed, the distal part of the axotomized axon degenerates in a process known as wallerian degeneration. On its turn, the proximal end of the axotomized neuron responds to the injury creating new collateral terminals as an attempt of self-regeneration. This mechanism is being thoroughly studied and considered in the last years for designing strategies for neural repair, especially involving spared terminals of IINs, as explained in the introduction. Moreover, damaged neurons lose synaptic connections from supraspinal centres and/or innervation (mainly) from many IINs. Finally, damaged neurons can also experience atrophy, but this process could be reversed if reinnervation occurs (*i.e.,* recovering initial innervations to the extent possible), although not all neurons respond in the same way to denervation [**Ana Lucas, 2011**].

4.4.2. Biomaterials implantation

All experimental procedures in animals were approved by the Animal Research and Well-Being Committee of the *Hospital Nacional de Parapléjicos* and carried out in accordance with the regulations of the European Commission (directives 2010/63/EU and 86/609/EEC) and the Spanish government (RD53/2013 and ECC/566/2015) for the protection of animals used for scientific purposes.

Adult male rats were used for scaffold implantation at the age of 19.3 ± 1.0 weeks (353.0 ± 10.0 g in weight). Animals were housed at a 12 h light/dark cycle with food and water *ad libitum*. All surgical procedures were performed under intraperitoneal (IP) analgesia with xylacine (10 mg kg^{-1}) and anesthesia with sodium pentobarbital (55 mg kg^{-1}) mixed with atropine (0.05 mg kg^{-1}).

Eyes were covered with Lubrithal™ gel to prevent corneal abrasion and dehydration during surgery. Temperature, colour and respiratory frequency were constantly monitored during the complete surgical procedure. A midline incision was performed on the dorsal skin from the base of the skull up to the T3 backbone level. Superficial and deep muscles were carefully dissected, always along the midline. Vertebrae insertions of deeper muscles were cut at both sides of the spinal processes to get access to the backbone (typically from C4 to T2). After thorough identification, C5 vertebra was removed and the meninges visualized. A square incision was practiced on the dura mater to completely expose the spinal cord at C6 level. By using appropriate micro-scissors, three firm cuts were then carried out at C6 (one rostral, one caudal and one sagittal at the midline) to achieve a right lateral hemisection of approximately 8 mm^3. Immediately after, fragments of neural tissue cut were removed from the lesion site as much as possible. Bleeding was quickly contained by using small sterile pieces of Spongostan®. In animals receiving rGO scaffolds, implants of appropriate dimensions (either 3D rGO foams or 3D rGO-MFs) were implanted at the lesion site to fill in the cavity created (**Figure M5**). Following, a piece of Neuro-Patch® was placed covering the lesion area. Superficial and deep muscles were smoothly approximated with a 4/0 synthetic absorbable sterile surgical suture (Coated VICRYL®), also used to tightly close the skin. A plastic bandage (Nobecutan®) was finally sprayed on top of the sutured area to facilitate healing and avoid infection. Treatment groups included: control without injury (n=6), injury (I, n=9), injury with implantation of the rGO foam scaffold (rGO-SC, n=11), and injury with implantation of the rGO-MFs scaffold (I-MF, n=5). The immediate post-operatory care protocol included subcutaneous administration of antibiotics (enrofloxacine 2.5%, 0.3 mL kg^{-1} every 24 h), analgesia (meloxicam 5 mg mL^{-1}, 0.1 mL kg^{-1}, every 12 h) and saline solution (NaCl 0.9%, 5 mL, once or twice a day depending on the hydration state of the animal) during the first three days. Posteriorly, animals

were frequently observed, at least once per week, to assess animal welfare with major attention placed into signs of pain, distress, dehydration, intestinal obstruction, and respiratory failure. After 4 months of implantation (120 DPI), animals were sacrificed by using a standard perfusion-fixation protocol (PFA 4% in phosphate buffer, PB, 0.1M) and the thoraco-abdominal viscerae and spinal cords were extracted. All organs were examined macroscopically looking for any signs of gross damage before histological processing. In rats dedicated to TEM studies (control, n=1; I, n=3; rGO foams, n=3), a specific perfusion-fixation procedure with a circulating solution containing PFA at 4% and glutaraldehyde at 1% in PB was conducted.

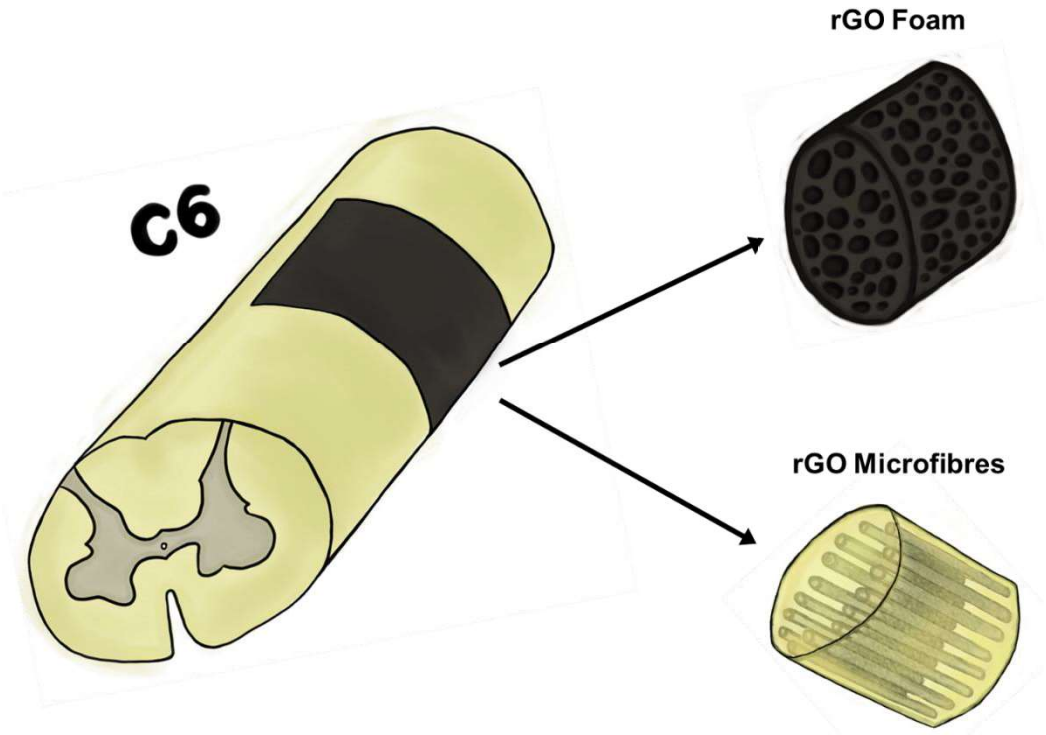

Figure M5. rGO-based biomaterials implanted within the injured spinal cord at C6 level.

4.5. Behavioural tests: Grooming and asymmetry

In order to evaluate the degree of forelimbs motor impairment and to detect eventual worsening of the functional performance four months after 3D rGO foam and rGO-MFs scaffolds implantation, animals were subjected to two

different behavioural tests: grooming and forelimb asymmetry tests (both tests specifically focused on spontaneous motor functions directly related to the lost circuits in the lesion epicenter, that is, the forepaw ipsilateral to the hemisection, as explained before).

First, forelimb use in grooming function was evaluated by using a scoring system adapted from previously described protocols [**Bertelli and Mira, 1993; Gensel *et al.* 2006**]. Briefly, scores were based on the frequency (number of times per minute) that rats were able to reach different positions: (1) Licking of the forepaws and mouth/nose washing, (2) Grooming of the area between the nose and the eyes without reaching eyes, (3) Grooming of the area between the eyes and the ears without reaching ears, (4) Grooming of the ears area, and (5) Grooming of the back area behind the ears, and the back (both at their right and left sides). In our case, we focused our analysis in positions 3, 4, 5, and both back sides. No measurements were done for positions 1 and 2 because of the difficulty of quantification. Stereotypical grooming sequences of at least 50 s of duration were recorded for each animal in their own cage with a video camera. Slow motion video playback (speed = 0.20x) was used to score each forelimb independently. Values were expressed as a function of time.

Second, the differential use of both right and left forepaws to lean on the cage walls in a standing position during the normal exploratory behaviour of the rat was assessed by the asymmetry test [**Schallert *et al.* 2000; Soblosky *et al.* 2001**]. In order to minimize stress, this spontaneous behaviour was recorded for over 5 min in their own cage. When animals were found dramatically inactive, stimuli such as water, paper, food pellets, and tricks (cereal flakes) were used to get them back to an active exploratory behaviour. Videos with more than 60 s of animal inactivity were discarded and recorded periods of inactivity longer than 30 s excluded from analyses. Selected variables of study were: (i) Number of stand-ups on hindlimbs (*StaUp*) and the number of times

that the animal leant on the cage walls by using their (ii) right forepaw (*LeanRFP*), (iii) left forepaw (*LeanLFP*) or (iv) both (*LeanBoth*). Additional attention was placed on the morphology of the paw contact (either open –palm– or close –fist–). Finally, the capacity of the animal to change leaning points with the forepaws while standing up was also observed.

Both the performance and analysis of behavioural tests were done blind in order to avoid experimental bias.

4.6. Cells/tissue-material interaction and tissue responses to rGO biomaterials

4.6.1. Magnetic Resonance Imaging (MRI)

MRI was used to obtain more information about the chronic integration of rGO foams within the spinal tissue, and to evaluate possible signs of tissue damage after their implantation. Immediately after the perfusion-fixation procedure and the subsequent spinal cord extraction, the fragment between C4 and T1, which contains the main spinal cord structures involved in the rat anterior limb function, was cut under a magnifying glass and left overnight in PFA (4 % in PBS). Afterwards, the tissue was washed several times with 0.1 M PB and placed inside a glass vial already filled in with Fluorinert™ medium, which was carefully sealed avoiding bubbles with parafilm. MRI images were acquired in a 7T Bruker Biospin MRI machine (Ettlingen, Germany) BioSpec 70/30. The different measurements were made using images of a turbo spin echo sequence enhanced in T2 (RARE turbo) and axial acquisition. A Weasis 2.6.0 viewer was used for the visualization and evaluation of the images. The lesion/scaffold dimensions, their volume and the presence of malacia/mass effect in the SCI epicenter were analyzed, as well as the number, location, size and intensity of the non-primarily damaged areas rostral and caudal to the SCI epicenter. Once the images were obtained, the spinal cord tissue was extracted

from the glass vial, washed repeatedly with PB to eliminate the preserving medium and used for histological and immunofluorescence studies.

4.6.2. Histological studies

All perfused tissue samples (both organs and spinal cord fragments) were placed in PFA (4% in PBS) at 4 °C overnight, followed by 3 days in sucrose (30% in PBS) at 4 °C for cryoprotection. Tissue pieces were mounted on plastic containers, quick-frozen in Optimal Cutting Temperature compound (Tissue Tek, Hatfield, PA) and cut in horizontal sections of 10 μm by using a Leica CM1900 or a Microm HM550 cryostat with an angle of 10°. In the case of spinal cords, the entire C5-C7 fragment was cut in sagittal sections from right to left. Organs were stained with conventional hematoxylin-eosin stain. Spinal cords were examined after Masson's trichrome for visualizing collagen. In all cases, panoramic images at low magnification were collected by using an Olympus BX61 microscope for anatomical mapping. Specific details of the histological staining techniques used are provided below.

4.6.2.1. Hematoxylin and eosin staining (H&E)

In our study, H&E was used for the study of histopathological effects of rGO biomaterials in key organs (kidneys, liver, lungs and spleen). In this case, samples were left to dry overnight at RT. Slices were then fixed with PFA 4% (in PB 0.1M). Samples were then washed with PBS 1X and permeabilized in a solution containing Triton 1.5% (in PBS 1X) for 30 min at RT. Slices underwent then a quick washing with distilled water. Following, samples were stained by the Carazzi's hematoxilin solution for 30 min at RT. Afterwards, slices were rinsed in an acid alcohol solution (1% HCl in 70% ethanol) for few seconds and washed again. Then, samples were rinsed in an ammonia solution (0.2% NH_4OH in distilled water). Slices were counterstained with the eosin solution for few seconds, and dehydration was performed by using series of ethanol

solutions until a final dehydration in absolute ethanol. Finally, samples were cleared with xylene and mounted. Carazzi's hematoxylin and aqueous eosin (0.1%) were prepared according to the protocol of García del Moral Garrido [**1993**].

4.6.2.2. Masson's trichrome staining

In our case, Masson's trichrome was used to detect the presence of collagen at the epicentre of the lesion and its surroundings in all injured animals (with and without rGO implants; **Figure M6**). A kit was used in this case. Samples were stained according to manufacturer instructions [**PanReac - CEIVD18ES]**.

4.6.3. Ultrastructural characterization by transmission electron microscopy (TEM)

In this thesis, regarding metallic NWs, TEM studies were performed to obtain higher resolution details about the interaction between neural cells and NWs, as a complement to SEM studies. With respect to rGO foams, TEM studies were performed: (1) To obtain information of the location of rGO nanosheets in the spinal cord; (2) To study the formation of cavities at the lesion site due to the presence of the implanted material; (3) To study the interaction of rGO with cellular and subcellular structures; (4) To evaluate changes in rGO sheets density as indicators of eventual biodegradation; (5) To obtain ultrastructural details of the neuronal components present within our scaffold after implantation; and (6) To look for toxicity signs in vital organs.

Following a conventional procedure, both *in vitro* culture samples and spinal cord slices were first fixed (in the case of NWs, or refixed in the case of spinal slices) with a mixture of PFA 4 % and glutaraldehyde 1 % in PB for 15 min. All samples were then post-fixed in osmic tetroxide (1 % in distilled water) for an additional hour. Dehydration was then carried out by immersion in

successive solutions of ethanol at increasing concentrations (30, 50, 70, 95, and 100 %), with a final step in pure acetone. Samples were included in the resin Durcupán by consecutive immersion steps at increasing concentrations (1:3, 1:1, 3:1 in acetone). Final samples in pure resin were then polymerized at 60 °C for 48 h. Ultrathin sections (*ca.* 60 nm) were obtained and subsequently stained with uracil acetate and lead citrate. The visualization of all samples was carried out by using a Jeol JEM 1010 microscope (Tokyo, Japan) at 80 kV with a coupled camera (Gatan SC200, Pleasanton, CA, USA) for image acquisition.

In the case of samples from rGO foams implanted animals, images were processed by using the Fiji software for quantitative estimations. Features of rGO dissociation were estimated by analyzing the distribution of pixels in the grey scale from images captured at 300,000X at 100 kV in similar conditions of brightness ($N \geq 25$ from 3 different animals per treatment group). Cavities at the lesion site and tissue infiltration degree were estimated by studying the distribution of pixels in the grey scale from images captured at 2,000X at 80 kV in similar conditions ($N \geq 20$ from 3 different animals per treatment group).

4.6.4. Immunofluorescence studies by confocal laser scanning microscopy (CLSM) and epifluorescent microscope

4.6.4.1. Metallic NWs arrays and PDMS substrates

In this thesis, regarding NWs substrates, CLSM experiments were done in order to study neural cells viability and differentiation on these substrates, as well as live calcium dynamics (on both NWs arrays and PDMS substrates).

4.6.4.1.1. Neural cells viability

To test cell viability, cells cultured on the different substrates were analyzed by using a Live/Dead® Viability kit (Life Technologies) according to manufacturer's instructions. This procedure is based on the use of calcein and ethidium homodimer-1 (EthD-1). Calcein-AM is a non-fluorescent cell-

permeable dye that gets converted into a strongly green-light emitting compound (calcein) after contact with intracellular esterases and so retained inside live cells. The permeability of the probe is provided by an acetoxymethyl group (AM), which allows the molecule to be transported through the cellular membrane. Once inside, if the cell is alive, esterases remove the AM group from the probe, which gets trapped within the cell and suffers a change on its chemical structure that allows it to emit fluorescence. On the contrary, EthD-1 is a DNA-intercalating agent that penetrates cell membranes in dead cells and emits orange/red fluorescence when inserted into the DNA double helix due to a change on its structure. After staining, samples were visualized by using a Leica TCS SP5 confocal microscope. Fluorescence of both probes was excited by an Argon laser tuned to 488 nm. After excitation, emitted fluorescence was separated by using a triple dichroic filter 488/561/633 and measured at 505-570 nm for green fluorescence (calcein) and 630-750 nm for red fluorescence (EthD-1). Physical reflection from the metallic electrodes (non-transparent) after excitation at 488 nm was also recorded and used to visualize the material structure and the relative cellular location. To quantify cell viability, at least 5 images were randomly acquired for each substrate from at least 3 independent experiments and the area of alive (green) and dead (red) cells measured and expressed as a percentage of the total image area.

4.6.4.1.2. Neural cells differentiation

rNCCs cultures on the different substrates were fixed with PFA (4% in PBS) at RT for 12 min and then incubated with the following primary antibodies: (1) MAP2 for somas and dendrites in neurons and (2) Vimentin for non-neuron cells including glial cells. Appropriate secondary antibodies were used. For further technical details regarding the antibodies used, please refer to **Table M1**. Both primary and secondary antibodies were dissolved in PBS containing saponin (0.25 %) and fetal goat serum (2 %) to guarantee cell

permeability and to block any non-specific bindings, respectively. Each antibody was incubated for 1h at RT in darkness. Cell nuclei were labelled with 4',6-diamidino-2-phenylindole (DAPI, 3μM, 5 min). After immunostaining, samples were visualized by using a Leica TCS SP5 confocal microscope. The fluorescence of the different fluorochromes was excited and measured as follows: Alexa Fluor® 488 excitation at 488 nm with an argon laser and detection in the range 507–576 nm, Alexa Fluor® 594 excitation at 594 nm with a helium-neon laser and detection in the range 625–689 nm and DAPI excitation at 405 nm with a diode UV laser and detection in the range 423–476 nm. Capture conditions in each case were stablished by using appropriate positive and negative controls and maintained during the acquisition of all the images. The procedure used for the quantification of the immunofluorescence images was based on an automatized protocol created by using the Fiji software in which the observer must only define a threshold of positive staining for each marker stablished from the negative controls. In order to minimize bias effects, quantifications were carried out blind by two independent observers. The area positively stained for each particular marker was expressed as a percentage of the total image area. Reflection mode images were taken to observe the metallic electrodes surface in all cases.

4.6.4.1.3. Live calcium imaging

Oregon-Green 488 BAPTA-1-AM (Molecular probes) was used to test whether neural cells that were active (in terms of the capacity of generation of intracellular calcium transients) after 15 DIV on both substrates. Cells were incubated with the selected dye at a final concentration of 4 μM for 30 min within the cell incubator (37 °C, 5 % CO_2). For calcium recordings, coverslips were placed in a recording chamber mounted on an inverted epifluorescent microscope (Nikon Eclipse Ti-U). Cells were continuously perfused with extracellular saline solution (composed of 150 mM NaCl, 4 mM KCl, 2 mM

CaCl2, 1 mM MgCL2, 10 mM HEPES and 10 mM glucose) with a pH adjusted to 7.4 at RT (by using NaOH) at a perfusion rate of 5 mL min-1. Oregon Green was excited at 488 nm with a mercury lamp. Excitation light was separated from the sample using a 505 nm dichroic mirror and a ND filter. Samples were observed with a 20x objective, and images were continuously acquired using the ORCA-Flash4.0 V2 sCMOS camera (Hamamatsu) camera. Images acquisition conditions were selected by using an imaging software (HCImage live) and consisted of exposure time of 150 ms, binning 4 and capture resolution of 2048 x 2048 pixels. Once all parameters were fixed, samples were wahsed out in order to remove the non-internalised dye, and cells spontaneous activity was recorded for 10 min. Images were analysed with ImageJ software. Transients in calcium intracellular concentration (selected by drawing a region of interest, ROI, around their cell body; at least 60 neurons belonging to two different experiments were selected from each condition) were exported by Clampfit software (pClamp suite, 10.6 version; Axon Instruments) for off-line analysis (the peaks correlated to increases due to elevations in calcium concentration; Oregon Green is a non-ratiometric calcium dye, thus the precise intracellular calcium concentration at different time points could not be calculated). These traces were further examined by using Clampfit software (pClamp, 10.6 version; Axon Instruments). Parameters such as number of events, duration of these events (s) and the inter-event-interval (IEI; which refers to the difference between consecutive peaks onset times) were analysed.

4.6.4.2. rGO materials

Regarding *in vivo* biocompatibility of rGO biomaterials, immunofluorescence studies were performed for the detection of different markers of interest within the spinal cord slices related to neural, inflammatory, fibrotic and vascular components, among others.

Spinal cord tissue samples were allowed to dry at RT for 2-4 h. Afterwards, they underwent a post-fixation with PFA 4X (in PB 0.1M) for 15 min. After 3 washes in PBS, slices were permeabilized in a solution containing 0.2% Triton and 4% normal goat serum (NGS) in PBS (1h at RT). Following, samples were incubated with corresponding primary antibodies diluted in a solution containing 0.2% Triton and 2% NGS in PBS (48h, 4 °C). Then, after 3 washes with PBS, samples were incubated with appropriate secondary antibodies diluted in PBS (2h at RT). Finally, samples were incubated with Hoechst for 15 min at RT and mounted with Immu-Mount™ (Thermo Scientific).

Primary antibodies against MAP2 (for neuronal cell bodies and dendrites), Tau (for neuronal axons), vimentin (for non-neuronal cells including glial and connective tissue cells), glial fibrillary acidic protein (GFAP, for astrocytes), CD68 protein (ED1 for macrophages), rat endothelial cell antigen 1 (RECA-1, for endothelial cells in blood vessels), laminin (for basement membranes in blood vessels), β-III tubulin (for cytoskeleton microtubules in neurites), and SMI311 (for neuronal neurofilaments) were used. Cell nuclei were visualized by labelling with Hoechst (1 mg mL^{-1}). Secondary antibodies were selected accordingly. More details on the antibodies used have been included in **Table M1**.

Fluorescence images were collected by using Confocal Leica TCS SP5 microscopes. Capture conditions were fixed by using spinal cord slices incubated just with secondary antibodies. Then, all images were captured under these conditions. All fluorescence images were automatically quantified by using a customized macro in Fiji software as the number of pixels (correspondent μm^2) positively stained for each particular fluorescence marker after the definition of a common threshold value of positive labelling applied to all experimental groups. Control spinal cords and contralateral left hemicords

in injured animals served as reference values to define correspondent threshold values for each marker. At least three non-overlapping images per animal were acquired in each position of interest (N ≥ 3 images of each fluorescence marker per study region of each independent animal, from at least 3 different animals per group). Areas under study include (**Figure M6**): Left hemicord (LH), perilesional areas at 1-2 mm from the lesion site (PL12), caudal interface of the lesion (CIF), rostral interface of the lesion (RIF), lesion site without rGO-MFs (L), and lesion site with the rGO foam (SC) or with rGO-MFs (MF). In animals receiving rGO foam implants, the lesion epicentre was not subdivided in L and SC regions because the scaffold occupied the entire injury gap. On the contrary, lesion epicentre in rGO-MFs implanted animals was comprised by L and MF areas. Additional bright field images were taken to properly define the location of the rGO implants in all cases.

For rGO foams (rGO-SC), values of the positive stained area for the different markers of interest (expressed as a percentage of the total image area in μm^2) were obtained from all fluorescence images and these values directly used for calculations. However, in the case of rGO-MFs, first, values of the positive stained area for the different markers of interest (expressed as a percentage of the total image area in μm^2) were obtained from all fluorescence images. Second, the mean value was then calculated for the control group for each particular marker and normalized to 100. Finally, data of the positive stained area obtained from the analysis of all images from injured animals were referred to this value (100) as a percentage.

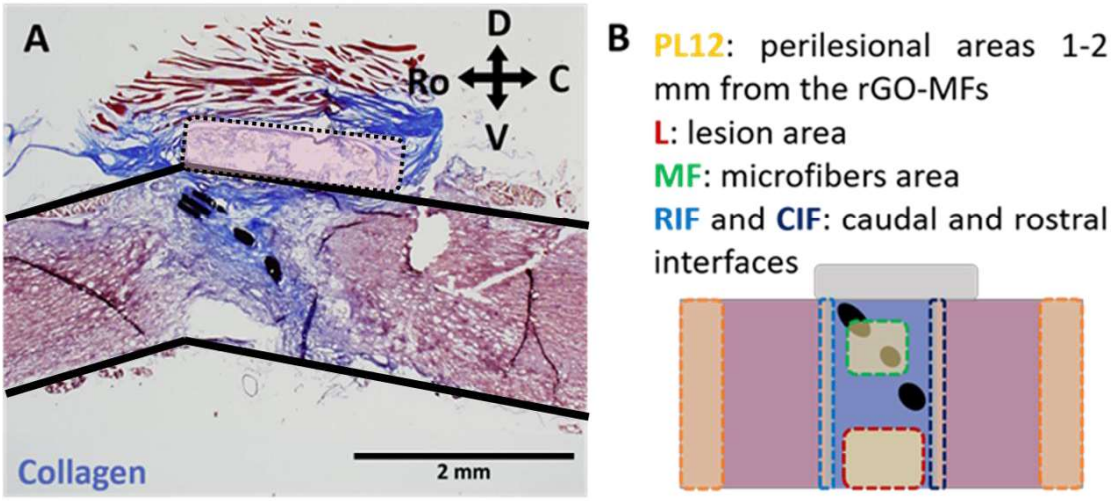

Figure M6. Areas under study in rGO-MFs implanted animals. A) Representative Masson's trichrome staining image of a spinal cord slice containing the rGO-MFs implant. The Neuropatch® area is contained in the dotted rounded line. Collagen appears stained in blue. B) Regions of interest at the injured spinal cord for immunofluorescence studies. D: dorsal; V: ventral, Ro: rostral, C: caudal.

Table M1. Specific details of antibodies/staining used in immunofluorescence studies in this thesis.

Antibodies/staining used *in vitro*								
Antibodies	**Provider**	**Reference**	**Host**	**Clone**	**Isotype**	**Stock concentration**	**Dilution**	**Working concentration**
MAP2	Sigma Aldrich	M1406	mouse	Monoclonal clone AP-20	IgG1	2.0 - 5.0 mg/mL	1:500	4.0 - 10.0 µg/mL
Vimentin	Sigma Aldrich	SAB4300676	rabbit	Polyclonal	IgG	1.0 mg/mL	1:500	2.0 µg/mL
Alexa Fluor 488 goat α-mouse IgG	Life Technol.	A-11029	goat	Polyclonal	IgG	2.0 mg/mL	1:700	2.8 µg/mL
Alexa Fluor 594 goat α-rabbit IgG	Life Technol.	A-11037	goat	Polyclonal	IgG	2.0 mg/mL	1:700	2.8 µg/mL
DAPI	Sigma Aldrich	D8417	-	-	-	5.0 mg/mL (14 mM)	1:4700	3 µM
Antibodies/staining used *in vivo*								
MAP2	Sigma Aldrich	M1406	mouse	Monoclonal clone AP-20	IgG1	2.0 - 5.0 mg/mL	1:500	4.0 - 10 µg/mL
Tau	Sigma Aldrich	T6402	rabbit	Polyclonal	-	40 - 100 mg/mL	1:200	200 - 500 µg/mL
Vimentin	Sigma Aldrich	SAB4300676	rabbit	Polyclonal	IgG	1.0 mg/mL	1:500	2.0 µg/mL
GFAP	Sigma Aldrich	G3893	mouse	Monoclonal clone G-A-5	IgG1	4.0 - 8.0 mg/mL	1:400	10 - 20 µg/mL
ED1	Chemicom	MAB1435	mouse	Monoclonal clone ED-1	IgG1	1.0 mg/mL	1:100	10 µg/mL
CD86	BD Biosciences	RUO 555016	mouse	Monoclonal Clone 24F	IgG1, κ	0.5 mg/mL	1:100	5.0 µg/mL
Arginase I	Santa Cruz	SC-20150	rabbit	Polyclonal	IgG	0.2 mg/mL	1:100	2.0 µg/mL

RECA-1	BioRad	MCA970R	mouse	Monoclonal clone HIS52	IgG1	0.5 mg/mL	1:250	2.0 μg/mL
Laminin	LSBio	LS-C96142	chicken	Polyclonal	-	1 mg/mL	1:500	2 μg/ml
Alexa Fluor 488 goat α-mouse IgG	Life Technologies	A-11029	goat	Polyclonal	IgG	2.0 mg/mL	1:700	2.8 μg/mL
Alexa Fluor 594 goat α-rabbit IgG	Life Technologies	A-11037	goat	Polyclonal	IgG	2.0 mg/mL	1:700	2.8 μg/mL
Hoechst	Sigma Aldrich	H6024	-	-	-	1.0 mg/mL	1:700	1.42 μg/mL

4.7. Statistics

Quantified parameters were expressed as the mean ± standard deviation (in all cases, $n \geq 3$). When necessary, statistical analyses were performed by using the Statistical Package for the Social Sciences software (SPSS, version 17.0), except for AFM measurements in which Origin platform (OriginLab) was used. For parametric analysis to compare more than 2 groups, analyses of variance (ANOVA) followed by either Scheffé or Games-Howell post-hoc tests (homogeneous and heterogeneous variances, respectively, as dictated by Levene's test) was used. For comparisons between two independent groups, a T-test was used. For non-parametric analysis as those for MRI data, the Mann-Whitney U test was used for comparisons among groups. In all cases, the statistical significance levels were defined as: $p < 0.05$*, $p<0.01$** and $p<0.005$***.

In the box plots, the line and square inside correspond to the median and the mean of the distribution, respectively. The top and bottom of the box represent, respectively, the 75th and 25th percentiles. The whiskers out of the box denote the range of outer-most data that fall within 1.5 x interquartile range. Additionally, single data points were overlapped with their correspondent box plots.

5. RESULTS

5.1. Au and Ni electrode arrays and PDMS substrates

5.1.1. Nanoelectrodes fabrication and characterization

The fabrication and morphological characterization of the NWs electrodes by SEM (**Figure R1**) were carried out by the group headed by Dr. M. Teresa González at IMDEA-Nanociencia (Beatriz Rodilla and Ana Arché, PhD students). In this thesis, electrodes corresponded to arrays of Au (Au-NWs; **Figure R1a-b**) and Ni (Ni-NWs; **Figure R1e-f**) nanowires grown on top of flexible Au plane substrates. Au and Ni flat electrodes were fabricated as reference samples as well (**Figure R1c**). As can be noticed in F**igure R1**, both Au and Ni NWs present a very similar morphology, where NWs maintain a vertical arrangement, but they are not distributed following a strict pattern over the base. Thus, the density of NWs is not exactly the same in every part of the arrays. Importantly, the resulting nanoelectrode arrays were flexible, thus facilitating their implantation and interaction with neural tissues (**Figure R1d**).

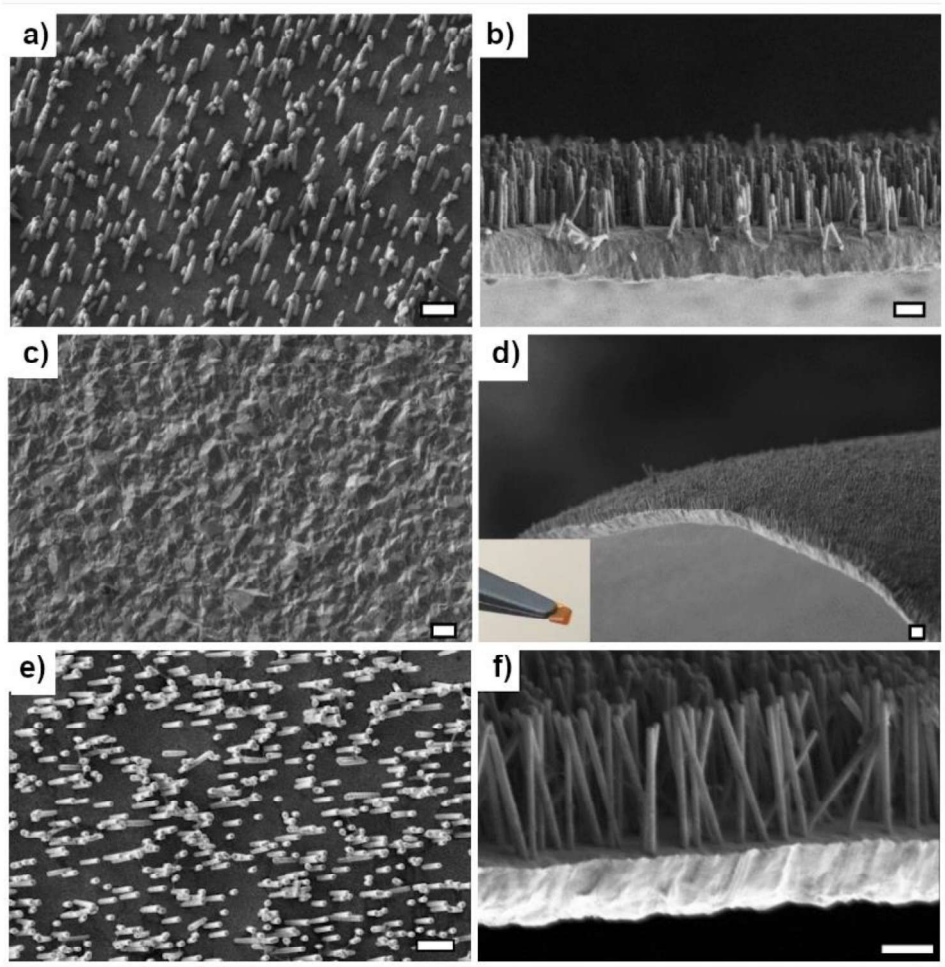

Figure R1. Au- and Ni-NWs morphological characterization. a) Representative SEM image in top view and b) cross-section of an Au-NWs electrode in which both, the base and the nanostructured active part can be seen. c) Representative SEM image of a planar Au-Flat electrode. d) SEM image showing the flexibility of the electrodes. e) Representative SEM image in top view and f) cross-section of a Ni-NWs electrode. Scale bars represent 1 μm in all images.

5.1.2. PLL coating of the nanoelectrodes for improving cell attachment

In order to test the *in vitro* biocompatibility of NWs substrates, as well as of their flat control counterparts, different tests were performed. Initial experiments demonstrated that primary neural cells presented little adherence when plated on these platforms if bare (**Figure R2**). Specifically, cells grouped to form clumps that retained weak adhesion to the substrates. Attached cells on the substrates were rare and displayed affected morphologies.

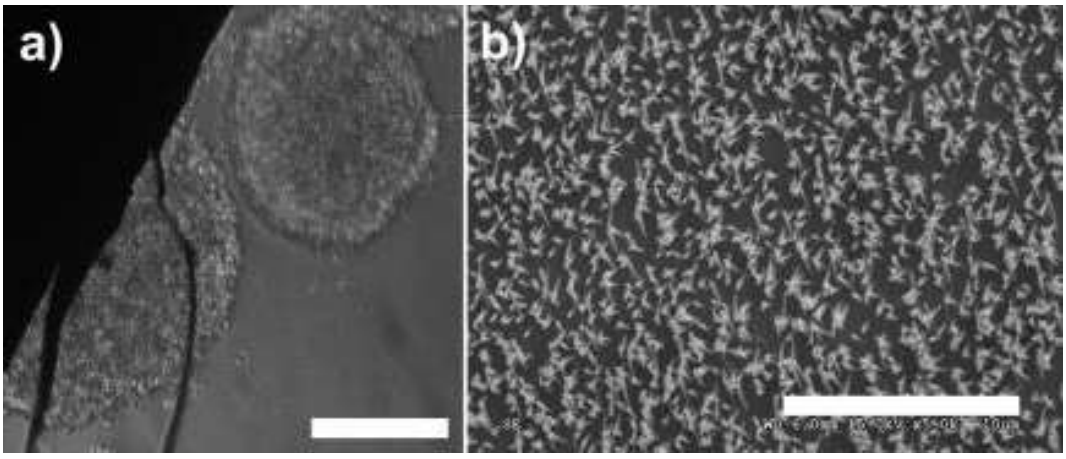

Figure R2. Representative images of rNCC cultures on bare metallic electrode substrates. a) Optical microscopy image at 2 days showing cell clumps at the electrode border. b) SEM micrograph at 14 days. Scale bars represent 100 (a) and 10 μm (b).

To address this issue, all samples were biofunctionalized with PLL. To confirm that PLL was able to properly cover their surface, experiments using fluorescence-labelled PLL (*i.e.*, PLL-FITC) were performed (**Figure R3**). Results confirmed that the surface of the samples was homogeneously covered with this polymer faithfully reproducing their characteristic nanotopographical features as later proved by SEM, FESEM and TEM.

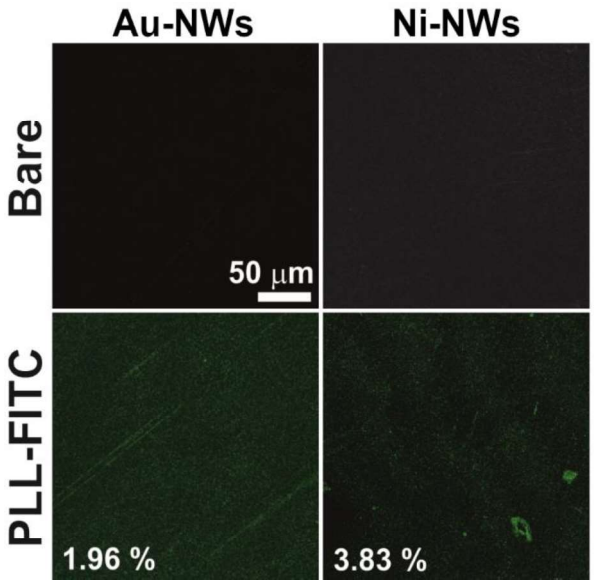

Figure R3. Immunofluorescence studies to illustrate PLL coating on electrode substrates carried out by PLL-FITC labelling and CLSM.

5.1.3. Primary neural cells development on Au-NWs and Ni-NWs

rNCC cultures were performed at both high (75,000 cells cm^{-2}) and low (25,000 cells cm^{-2}) cell seeding densities. Analyses were first focused on the NWs platforms after 14 days *in vitro* (DIV). These two different densities were used to confirm that cells were able to attach to the substrate not only when forced at high concentration, but also at regular cell seeding densities indicating a correct interaction with the NWs. As observed by SEM (**Figures R4-R6**), neural cells were able to properly adhere to the surface and develop, maintaining their typical morphology and forming interconnected cultures, on both Au-NWs (**Figure R4a**) and Ni-NWs (**Figure R5a**). Standard glass coverslips were used as reference material for comparison (**Figure R6**).

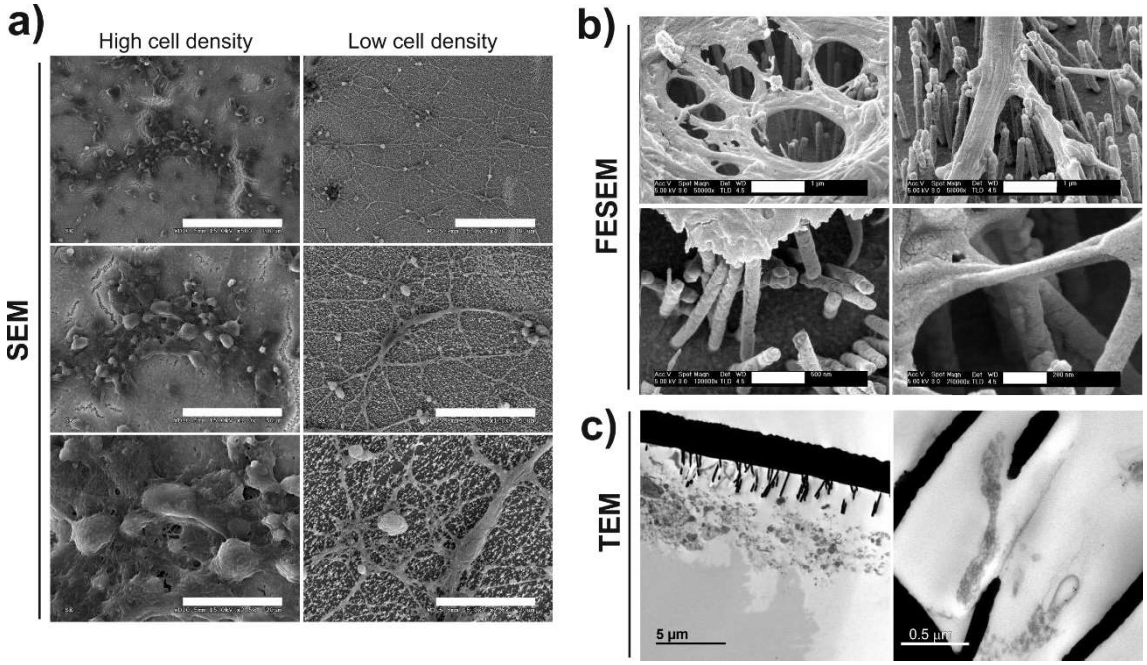

Figure R4. Morphological evaluation of rNCC cultures at high- and low-density seeding conditions on Au-NWs electrodes. Representative a) SEM, b) FESEM and c) TEM micrographs of cultures at 14 DIV are shown. Scale bars represent: (a) 100 µm (top), 50 µm (middle) and 20 µm (bottom); (b) 1 µm (top), 500 nm (bottom left) and 200 nm (bottom right) and (c) 5 µm (left) and 0.5 µm (right).

Additional FESEM studies were done to obtain more detailed information about the interaction between neural cells and nanoelectrodes (**Figures R4b and R5b**). Images revealed the formation of close interfaces between different parts of the neurons and the NWs surface, on both Au-NWs and Ni-NWs. Concretely, cell body and neurites used these structures as a support for their growth, making close contacts either with the NWs side walls or the base of the nanoelectrodes. Importantly, neither the cell body nor its prolongations seemed to be pierced by the NWs, as also confirmed by TEM images (**Figures R4c and R5c**).

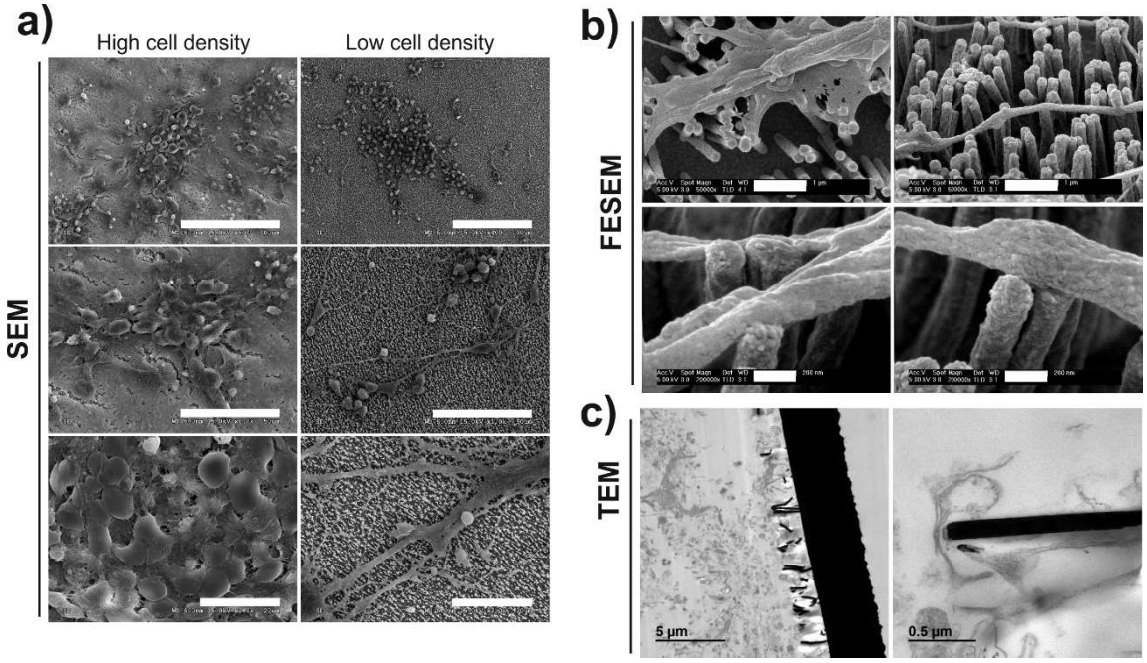

Figure R5. Morphological evaluation of rNCC cultures at high- and low-density seeding conditions on Ni-NWs electrodes. Representative a) SEM, b) FESEM and c) TEM micrographs of cultures at 14 DIV are shown. Scale bars represent: (a) 100 µm (top), 50 µm (middle) and 20 µm (bottom); (b) 1 µm (top) and 200 nm (bottom) and (c) 5 µm (left) and 0.5 µm (right).

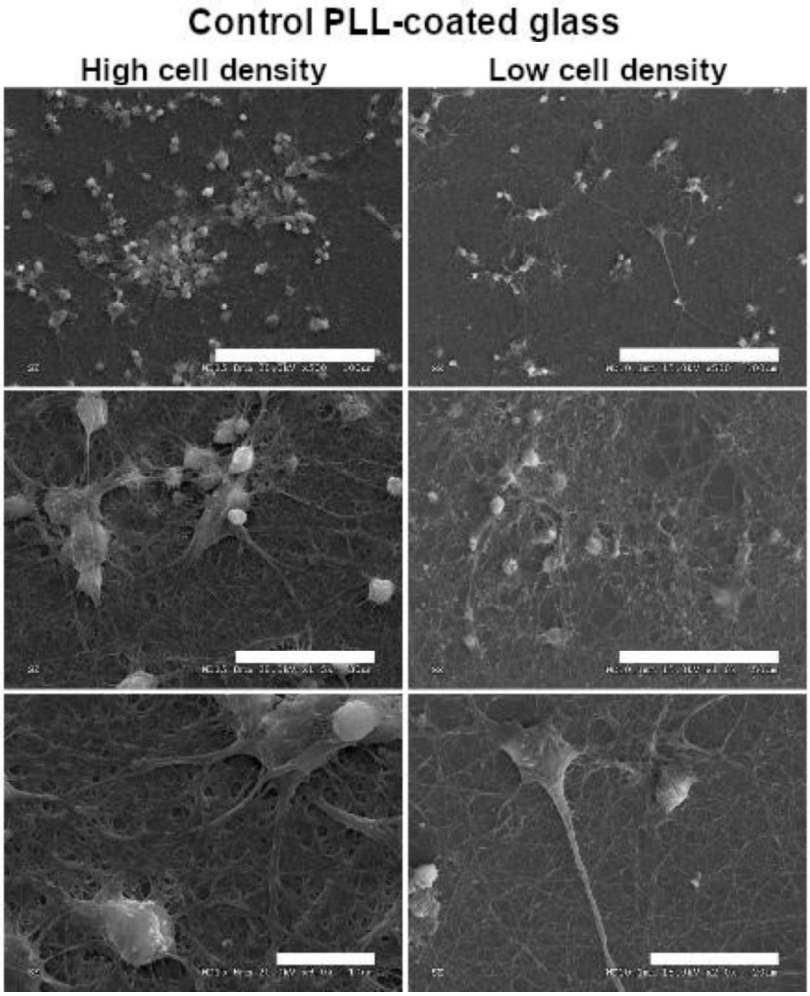

Figure R6. Morphological evaluation of rNCC cultures at high- and low-density seeding conditions on glass coverslips (control). Representative SEM micrographs of cultures at 14 DIV are shown. Scale bars represent 100 μm (top), 50 μm (middle right), 30 μm (middle left), 20 μm (bottom right) and 10 μm (bottom left).

When challenged at longer culture times, both types of nanostructures supported the growth of highly confluent cultures after 21 DIV (**Figure R7**). However, when cultures were maintained for up to 28 DIV (**Figure R8**), cells preserved their morphological features only on Au substrates, whereas those cultures on Ni-NWs started to clump likely due to a significant deterioration of their adhesive capabilities.

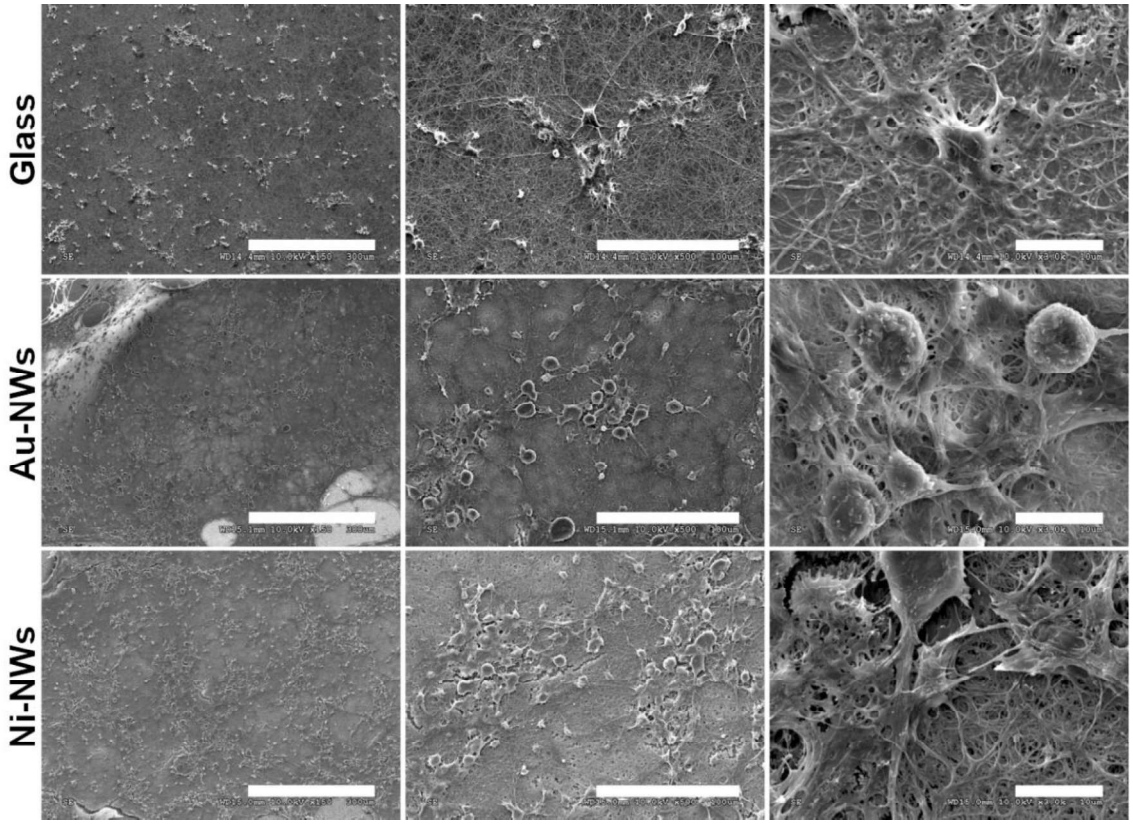

Figure R7. Morphological evaluation of rNCC cultures at 21 DIV on Au-NWs and Ni-NWs substrates. Cultures on glass coverslips are included for comparison. Representative SEM micrographs are shown. Scale bars represent 300 μm (left), 100 μm (middle) and 10 μm (right).

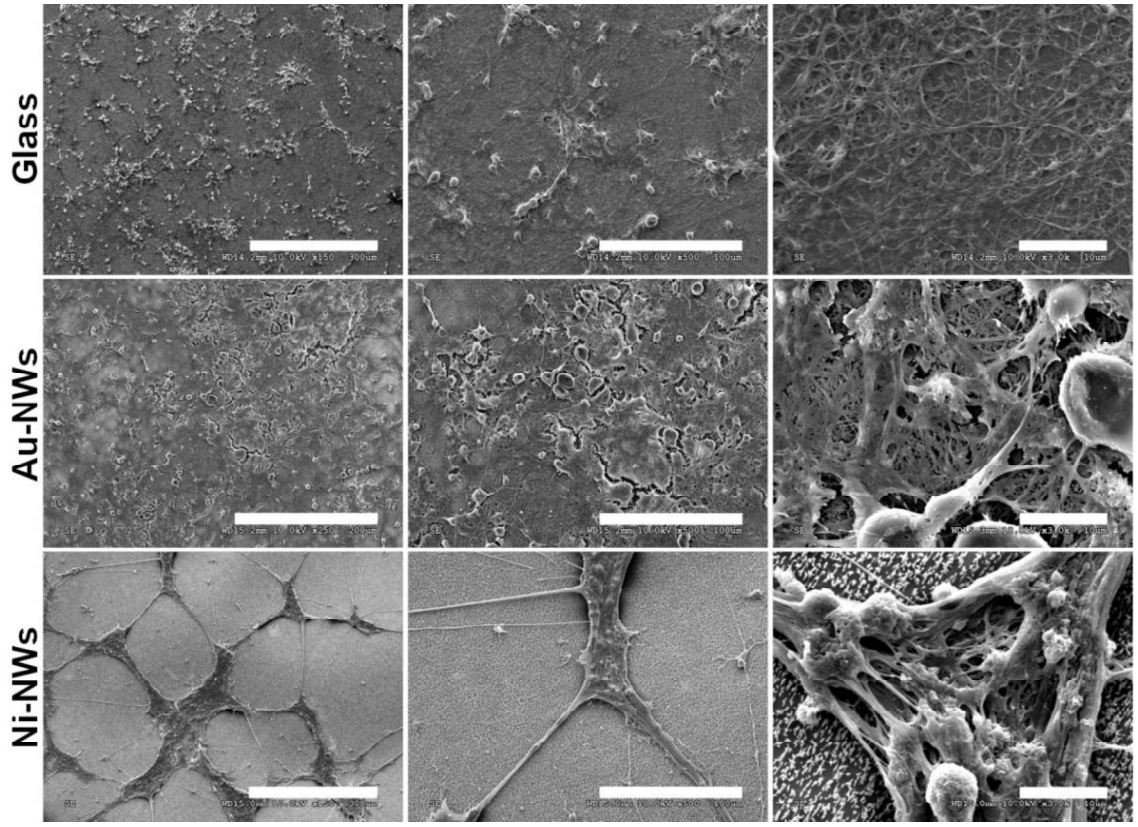

Figure R8. Morphological evaluation of rNCC cultures at 28 DIV on Au-NWs and Ni-NWs substrates. Cultures on glass coverslips are included for comparison. Representative SEM micrographs are shown. Scale bars represent 300 μm (top and bottom left), 200 μm (middle left), 100μm (middle) and 10 μm (right).

In order to elucidate the role played by topographical features and chemical composition in neural network development *in vitro*, neural cell behaviour was also studied on equivalent flat Au and Ni electrodes (Au-Flat and Ni-Flat, respectively) (**Figure R9**). In Au-Flat, neural cells were able to form comparable networks to Au-NWs at the different time points investigated. However, when cultured onto Ni-Flat surfaces, cells soon started to clump and fasciculate their neurites.

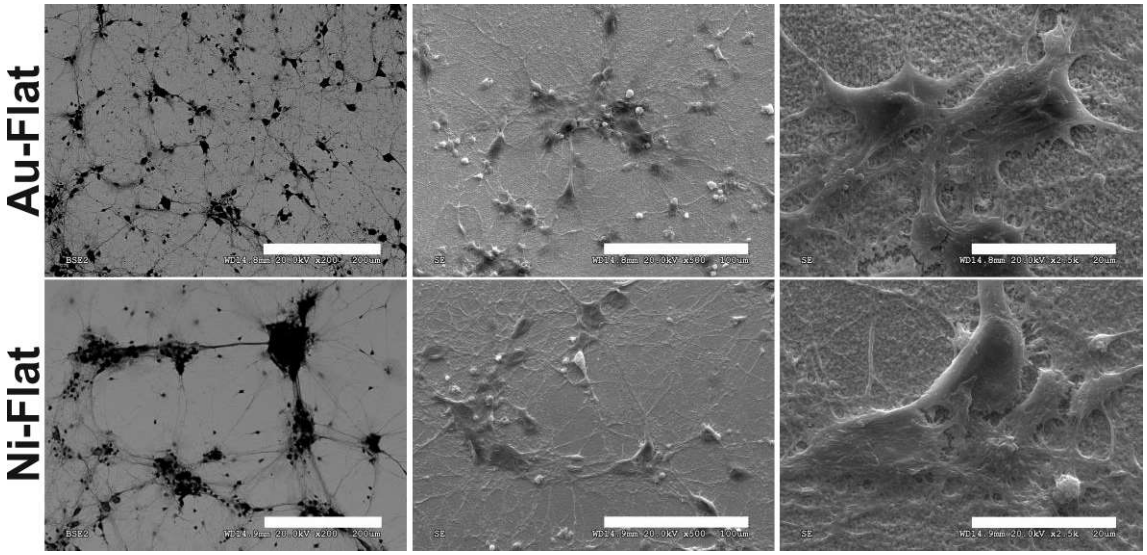

Figure R9. Morphological evaluation of rNCC cultures on Au-Flat and Ni-Flat electrodes. Representative SEM micrographs of cultures at 14 DIV are shown. Scale bars represent 200 μm (left), 100 μm (middle) and 20 μm (right).

5.1.4. Primary neural cells viability on Au-NWs and Ni-NWs

Viability after 14 DIV was then evaluated by using a live-dead kit based on calcein and EthD-1. So, alive cells are labelled in green and dead cells in red (**Figure R10**). Cells cultured on both Au-NWs and Ni-NWs showed a high viability in terms of surface area covered by viable cells, similar to those on glass substrates (Au-NWs *vs.* control, $p > 0.999$; Ni-NWs *vs.* control, $p = 0.739$). When focused on flat nanoelectrodes, cells on Au-Flat reached control viability values. On the contrary, Ni-Flat were poorly colonized, with a significantly inferior surface area covered by viable cells ($p = 0.021$ *vs.* control).

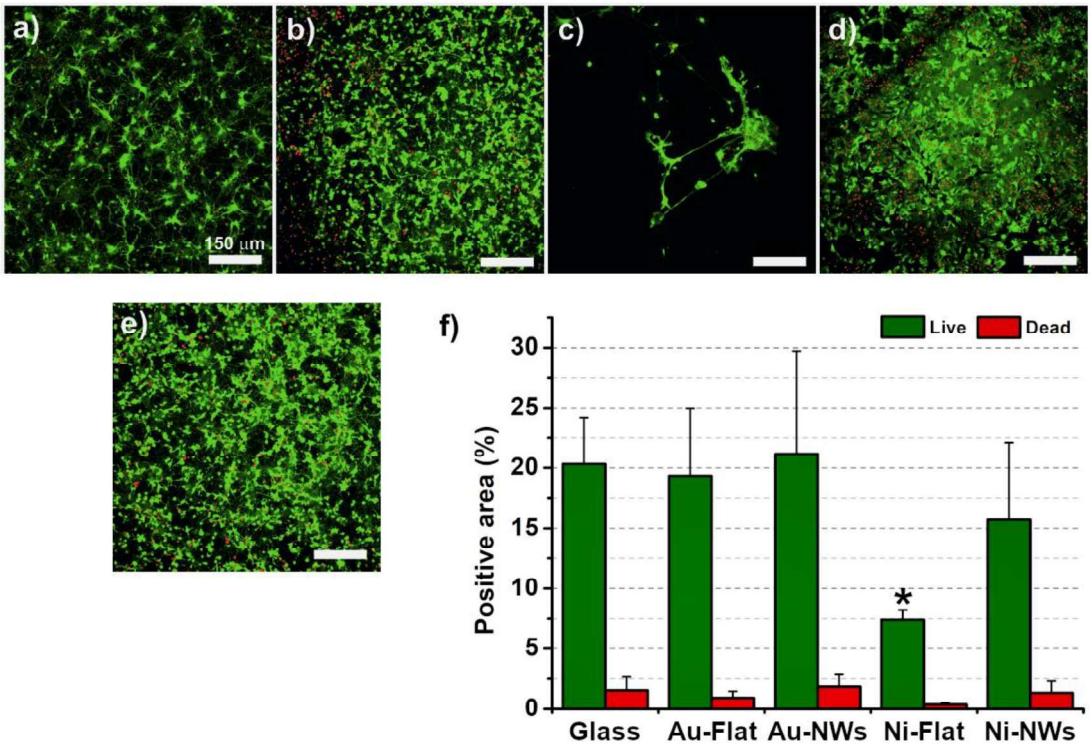

Figure R10. Viability studies of rNCC cultures on the different electrode substrates at 14 DIV by CLSM. Alive cells are labelled in green (calcein) and dead cells in red (EthD-1). a) Au-Flat, b) Au-NWs, c) Ni-Flat, d) Ni-NWs electrodes, and e) glass coverslip (control). f) Normalized positive area for alive and dead cells. Statistics: * $p < 0.05$ (with respect to control).

5.1.5. Primary neural cells differentiation on Au-NWs and Ni-NWs

The influence of Au-NWs and Ni-NWs on cellular differentiation was next analysed on neural cells *in vitro* (**Figure R11**). Neural phenotype was detected by using immunolabelling against MAP2 protein, whereas non-neuronal phenotypes were identified by vimentin presence. Then, positive area for each marker was analysed in all the samples. Under these experimental conditions, most cells reached a neuronal phenotype in all Au samples tested (NWs and flat substrates), like results obtained on glass control samples (MAP2: Au-NWs, $p = 0.794$; Au-Flat, $p = 0.248$; vimentin: Au-NWs, $p = 0.380$; Au-Flat, $p = 0.886$; all results are referred to glass coverslips). Contrarily, Ni had a different influence on this feature. Ni-NWs topography facilitated neuronal

differentiation over non-neuronal cells development in a comparable manner to Au-NWs and control substrates, but reduced the amount of non-neuronal cells ($p = 0.035$ with respect to control and $p = 0.32$ with respect to Au-NWs). On its turn, Ni-Flat substrates reduced the amount of neuronal cells ($p = 0.037$ with respect to control).

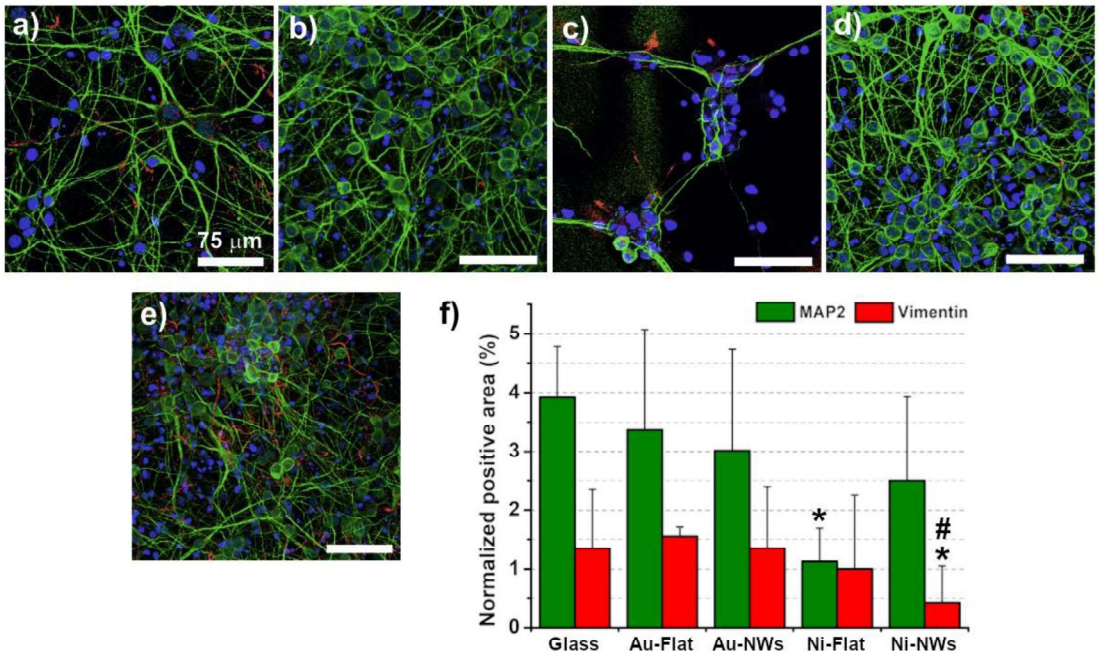

Figure R11. Differentiation studies of rNCC cultures on the different electrode substrates at 14 DIV by CLSM. Neurons are labelled for MAP2 (green) and non-neuronal cells including glial cells for vimentin (red). In all cases, cell nuclei were stained with DAPI (blue). a) Au-Flat, b) Au-NWs, c) Ni-Flat, d) Ni-NWs electrodes, and e) glass coverslip (control). f) Normalized positive area for neurons ($MAP2^+$) and non-neuronal cells ($vimentin^+$). Glass coverslips were used as a control substrate. Statistics: * $p < 0.05$ (with respect to control) and # $p < 0.05$ (with respect to Au-NWs).

5.1.6. Neural network activity by live calcium imaging on PDMS substrates

In vitro results regarding calcium imaging experiments showed that cells cultured on both substrates were active after 14 DIV. fNPCs activity seemed to

be slightly affected when these cells were interfaced to PDMS in terms of mean number of events (PDMS: 2 ± 2 nº of events; Control: 4 ± 5 nº of events), duration of the calcium events (PDMS: 12.8 ± 8.3 s; Control: 18.3 ± 14.1 s), and IEI duration (PDMS: 131.8 ± 117.7 s; Control: 109.0 ± 96.0 s). However, fNPCs belonging to just two independent experiments have been studied. Thus, further experiments including an augmented number of neurons should be analysed in future experiments to obtain robust conclusions.

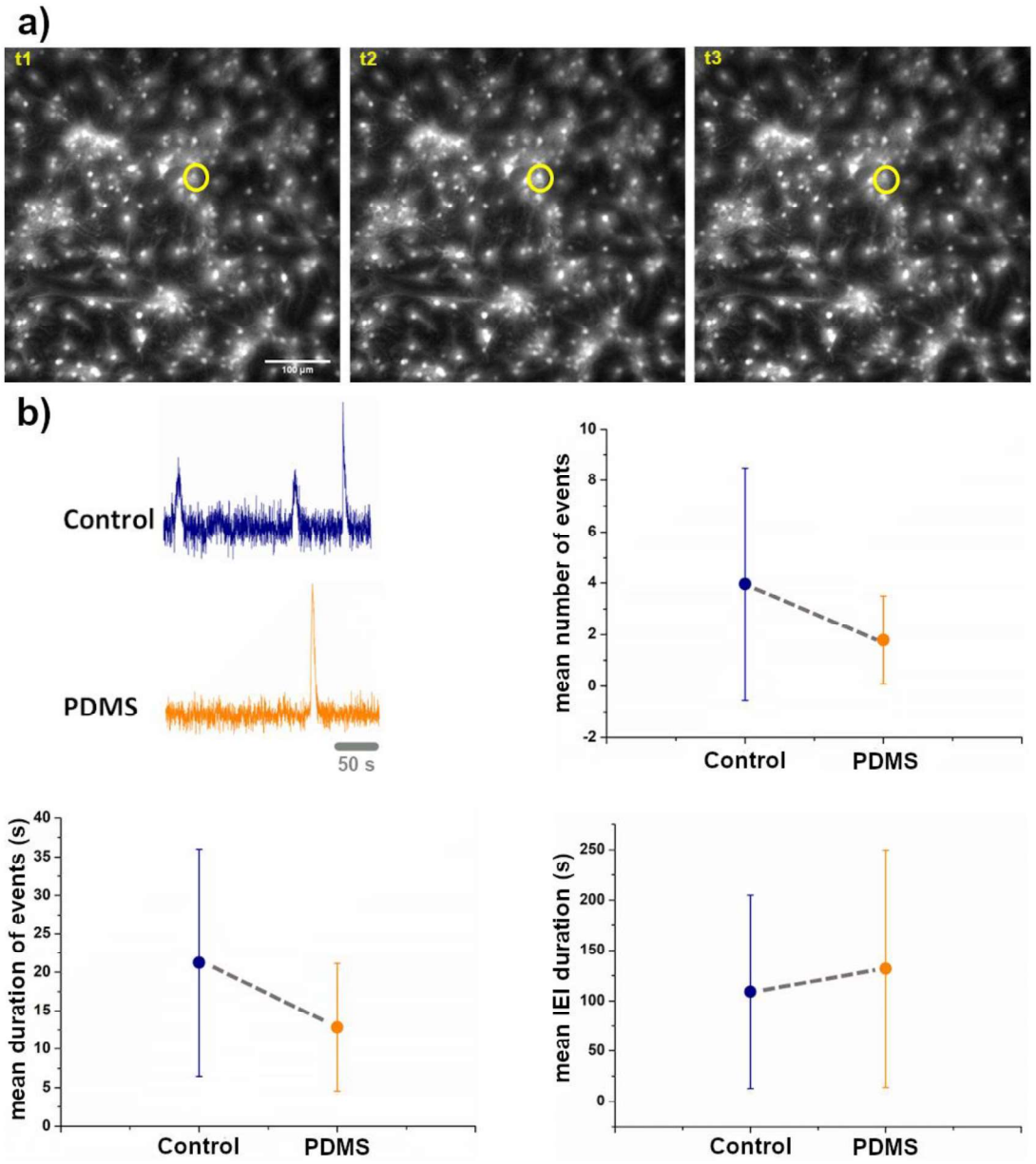

Figure R12. Preliminary results of the analysis of calcium events produced by fNPCs after 14DIV. A) Example of a transient calcium elevation in one neural cell (yellow circle) with time (from t1 to t3). B) Example of traces belonging to calcium transients from neural cells cultured on both control and PDMS substrates, and mean number, mean duration (s), and mean IEI of calcium events generated by Control and PDMS growth conditions when spontaneous activity was recorded for 10 minutes.

5.2. GDMs (I): rGO foams

5.2.1. Fabrication and physico-chemical characterization of rGO foams

As previously described, rGO foams were fabricated from GO slurry. Slurry refers to a viscous semi-liquid dispersion of GO nano and microsheets suspended in a very small portion of solvent. Thus, to obtain information about the morphology of GO sheets in this dispersion, TEM analysis was used (**Figure R13A**). GO was forming piled-up layers of micro-sized sheets able to interact among them. Following, these sheets were dispersed in distilled water at the desired GO concentration for scaffold fabrication. Once prepared, a freeze-casting methodology was used to obtain a very soft randomly porous 3D scaffold (foam-like), followed by a thermal treatment for GO reduction. Once the rGO implant was obtained, it was characterized by SEM (**Figure R13B**). This technique allowed confirming the high-degree porosity of the foam (43.87 ± 3.46 %), with a mean pore size of 31.88 ± 19.43 μm, in concordance with the dimensions of cellular components such as neurites and microvessels. Interestingly, these foams had partition walls relatively flat and smooth, with transversal sections on the size of hundreds of nm. Afterwards, comparative XPS studies of GO slurry, GO and rGO scaffolds were performed for the chemical characterization of the relative amount of oxygen-containing functional groups (with focus on C-OH, O-C-O and O-C=O groups) at the surface of the three samples (**Figure R13C; Table R1**). Results confirmed a significant reduction of GO in the final scaffolds produced by thermal treatment, accompanied by a marked decrease of their corresponding O/C ratio from 0.84% (GO slurry) to 0.28% (rGO foam). There were also two symmetric contributions related to carbon atoms bound to oxygen at the energy shifted values reported in the literature for hydroxyl (C-OH; orange peak), carbonyl (C-O; magenta peak) and carboxyl (C=O; blue peak) groups [**Della Pellea *et al.***

2017]. Finally, the feature at a binding energy of 290.8 eV (broader than any of the previous ones) was clearly associated to the characteristic π-π* shake-up transition (red peak) consistent with a majority existence of sp^2 configurations in the sample [**Della Pellea *et al.* 2017**].

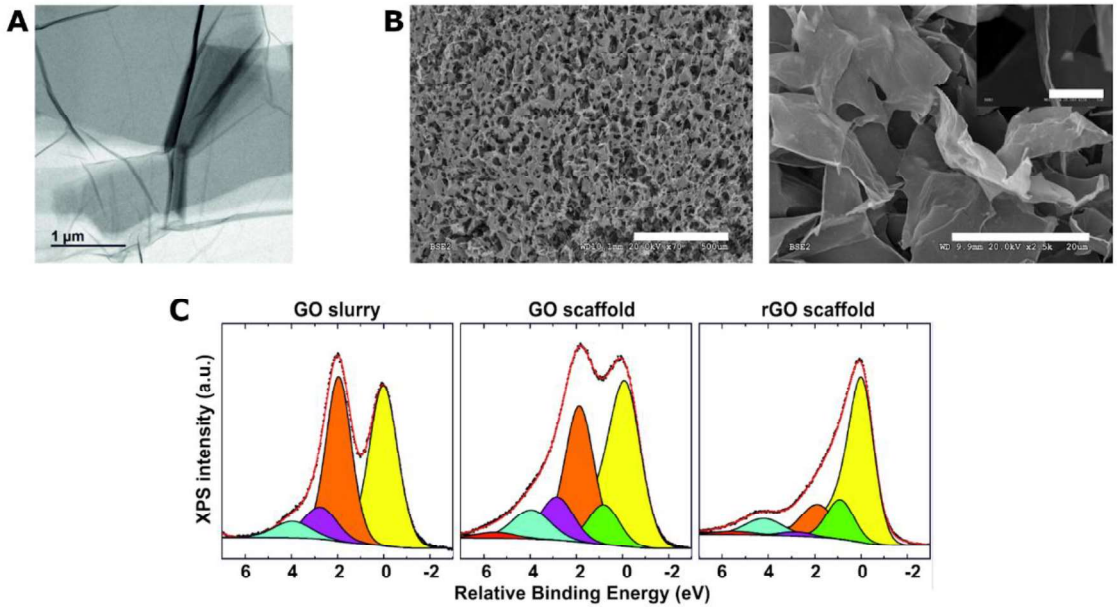

Figure R13. Physico-chemical characterization of rGO foams. A) Representative TEM image of GO sheets from the slurry. B) Morphological characterization of 3D rGO foams by SEM. Scale bars: 500 µm (left), 20 µm (right) and 5 µm (inset). C) C1s XPS spectra corresponding to GO slurry, GO scaffold and rGO scaffold together with the fit composed of chemically shifted components associated to different C chemical bonding, respectively. XPS spectra were normalized to the maximum intensity peak in each case. Data points are represented as black symbols and Shirley background and component peaks using solid lines. The fitting curve (red line) resulted from the addition of contributions belonging to: C=C graphitic structures (yellow), C-H or C-C defective graphitic, sp^3 configurations (green), C-OH carbonyl groups (orange), O-C-O carbonyl groups (magenta), O-C=O carboxylic groups (cyan), and π-π* transitions coming from graphitic structures (red).

Table R1. Relative percentage of peak areas for each type of atomic bonding obtained by XPS C1s analysis of the studied samples and their correspondent O/C atomic ratio.

Sample	C sp^2	C-C/H	C-OH	O-C-O	O-C=O	π-π*	O/C (at)
GO slurry	-	44.0	40.1	10.1	5.8	-	0.84
GO scaffold	39.9	9.3	30.1	10.7	8.3	1.7	0.38
rGO scaffold	57.5	14.9	15.1	1.8	8.7	2.0	0.28

Due to the relevance of the mechanical compliance that must exist between biomaterials and tissues at the site of implantation, we next mechanically characterized rGO foams by AFM. First, the elastic response of the rGO scaffolds prepared was quantified by their Young's modulus, *E*, and compared with that from neural cells and spinal cord tissues. Values were obtained from AFM-based indentation experiments, as previously described for other biological samples [**Garcia *et al.* 2017** and **2018**]. In order to get familiar with neural tissues, force-distance curves obtained on spinal cord slices were first acquired (**Figure R14A**). For this purpose, the tip was approached towards the sample until a force of 20 nN was detected. The figure shows that the maximum indentation is sample dependent, which reflects the different Young's moduli of the different types of tissues, all taken with the same cantilever-tip system. For the fixed spinal cord tissue (**Figure R14B-C**), the grey matter (GM) was indented around 3 μm and the white matter (WM), 4.5 μm. The living spinal cord tissue was softer, with the maximum indentations reaching values of 5 μm (GM) and ~7.5 μm (WM). Results from rGO scaffolds confirmed their macroscopic softness, characterized by a Young's moduli value of 1326 ± 1004 Pa (**Figure R14C**). Comparatively, single cortical neurons cultured *in vitro* were characterized by a *ca.* 3-fold lower Young's modulus value (417 ± 106 Pa; $p < 0.001$), which was itself significantly higher than the values obtained on GM and WM regions from fresh spinal cord slices (275 ± 99

Pa and 97 ± 69, respectively; $p < 0.001$). When compared to the elastic response of PFA-fixed spinal cord tissue, the Young's modulus values of both GM and WM significantly increased with respect to their fresh counterparts (1324 ± 1202 Pa and 296 ± 211, respectively; $p < 0.001$), but similar to those obtained for the rGO scaffold in the case of GM areas ($p > 0.999$).

AFM-indentation measurements were then carried out on the spinal cord tissue containing the rGO foams implanted for 4 months (**Figure R14D**). The interface tissue showed a significantly lower Young's modulus (54 ± 29 Pa; $p < 0.001$). However, the lesion site carrying the rGO scaffolds displayed the significantly highest Young's modulus (3624 ± 2664 Pa; $p < 0.001$), even when compared to the rGO scaffolds before implantation (1326 ± 1004 Pa), likely due to collagen deposition and massive cell infiltration of the foam. Importantly, this decrease in the elasticity of the right hemicord holding the scaffold was not transmitted to the left counterpart spinal tissue, as its elastic response was found in range with the one found in the fresh control spinal cord tissue (237 ± 66 and 225 ± 109 Pa, respectively; $p = 0.366$; control spinal cord tissue calculated as the average of values for GM and WM).

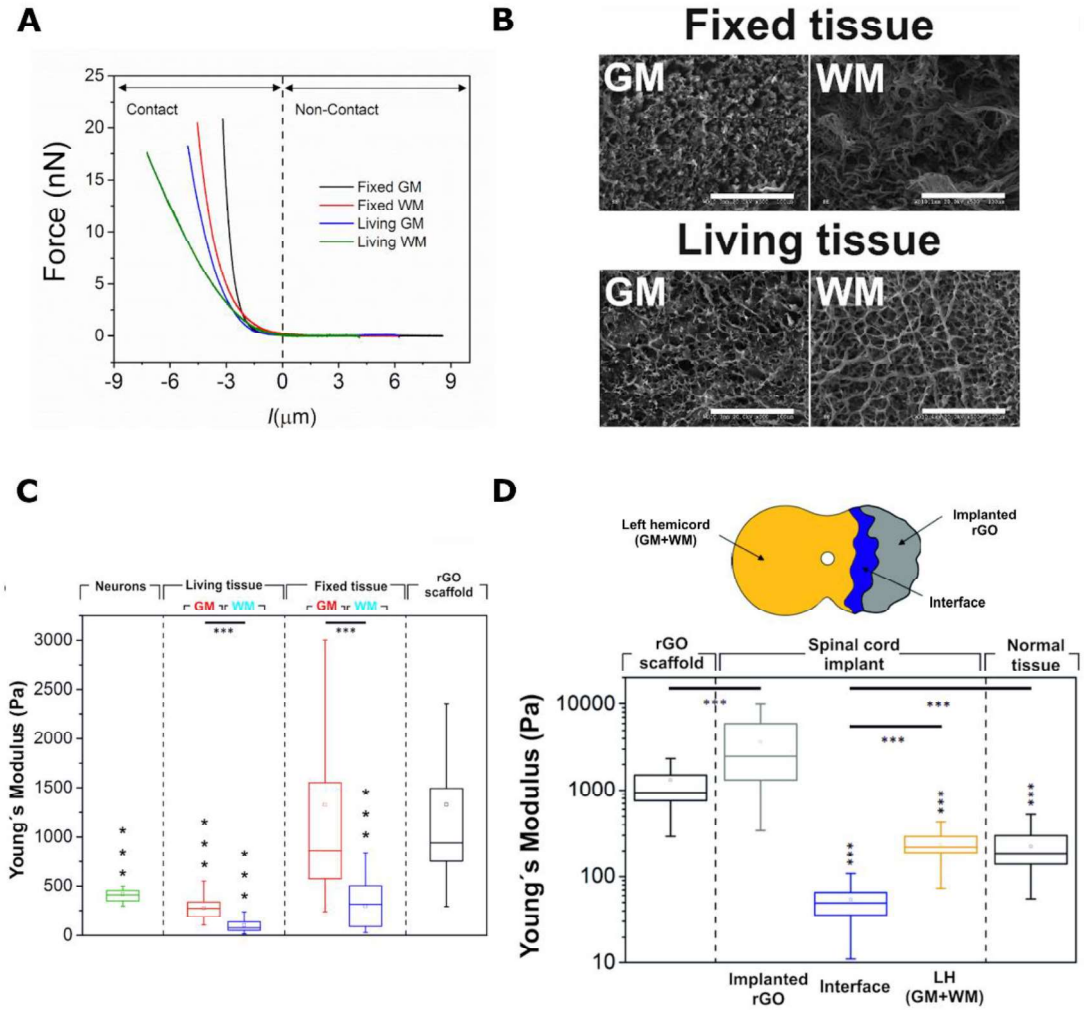

Figure R14. Detailed mechanical characterization of rGO-spinal tissue interactions. A) Force-distance curves obtained on both living (fresh) and fixed spinal cord slices**.** B) Representative SEM images of living and fixed spinal cords at both grey matter (GM) and white matter (WM) areas (scale bars: 100 μm). C) Nanomechanical characterization of spinal cord tissue (living and fixed), neural cells and rGO scaffolds as obtained from AFM-based measurements (expressed as Young's moduli). D) Scheme of the main regions under study on the rGO-implanted spinal cord tissue and nanomechanical characterization of 4-month rGO implants in comparison to rGO scaffold and spinal cord tissue. In the plots, statistical significance: $p < 0.001$***. Horizontal asterisks refer to comparisons indicated by bars and vertical asterisks refer to comparisons with rGO scaffold. GM: Grey matter; LH: Left hemicord; WM: White matter.

5.2.2. Evaluation of animal spontaneous behaviour at 120 DPI

After implantation of the rGO foams at the laterally hemisected C6 spinal cord, animals were expected to suffer a chronic impairment of their right forelimb, along with a less severe affectation of their hindlimbs (this last typically evolving to spontaneous functional recovery). Consequently, the lesion model of choice allowed us to focus on the evaluation of the progressive recovery of the main affected limb by using two behavioural tests which involved the use of both forelimbs during spontaneous animal behaviour. Selected tests were forelimb asymmetry and grooming behavioural tests (**Figure R15**). Evaluation was performed at 10 DPI (subacute stage), 30 DPI (early chronic stage) and 120 DPI (late chronic stage). First, we evaluated the differences in the total time that animals spent either exploring their cage or grooming as a possible sign of animal welfare impairment. No significant differences were found in either case (**Figure R15A-B**; exploration of the cage during asymmetry test $p = 0.903$; grooming $p = 0.768$).

Asymmetry results were consistent with the fact that the right forepaw remained chronically affected (from 10 DPI to 120 DPI; **Figure R15C-D**). Specifically, all injured animals, including those carrying the rGO foams, significantly overused their left forelimb when they leant on their cage walls, contrary to control (*i.e.*, non-injured) rats that preferred to use both forelimbs ($p < 0.001$). Interestingly, no statistically significant differences were found neither on the use of their right forelimb ($p = 0.164$) nor on the frequency of stand-ups ($p = 0.272$) among all 3 experimental groups.

Following, the rate of the different positions reached during grooming tests were quantified, with focus on positions 3 to 5, and both sides of the back (**Figure R15E-F**). All animals were able to reach position 3 with their affected paw. Additionally, injured animals at 120 DPI, including those carrying the rGO scaffold, were able to touched further, position 4, but typically failed to

reach position 5 or their right back side (although they still managed to get to it in some occasion). This was relevant because implanted animals were unable to reach positions 4, 5, and their back right side at earlier time points (10 and 30 DPI). However, all injured animals (including rats carrying the implant for four months) groomed significantly less intensively with their affected right forelimb at the most challenging positions (5 and right back side) when compared to healthy control rats ($p = 0.002$ and $p = 0.024$, respectively to control). Regarding left forelimbs, all animals were able to reach the most challenging positions (5 and left backside), without significant differences on their use in any of the positions among all animal groups. Overall, no major impairments due to the chronic presence of the foam were found in injured animals after four months of implantation.

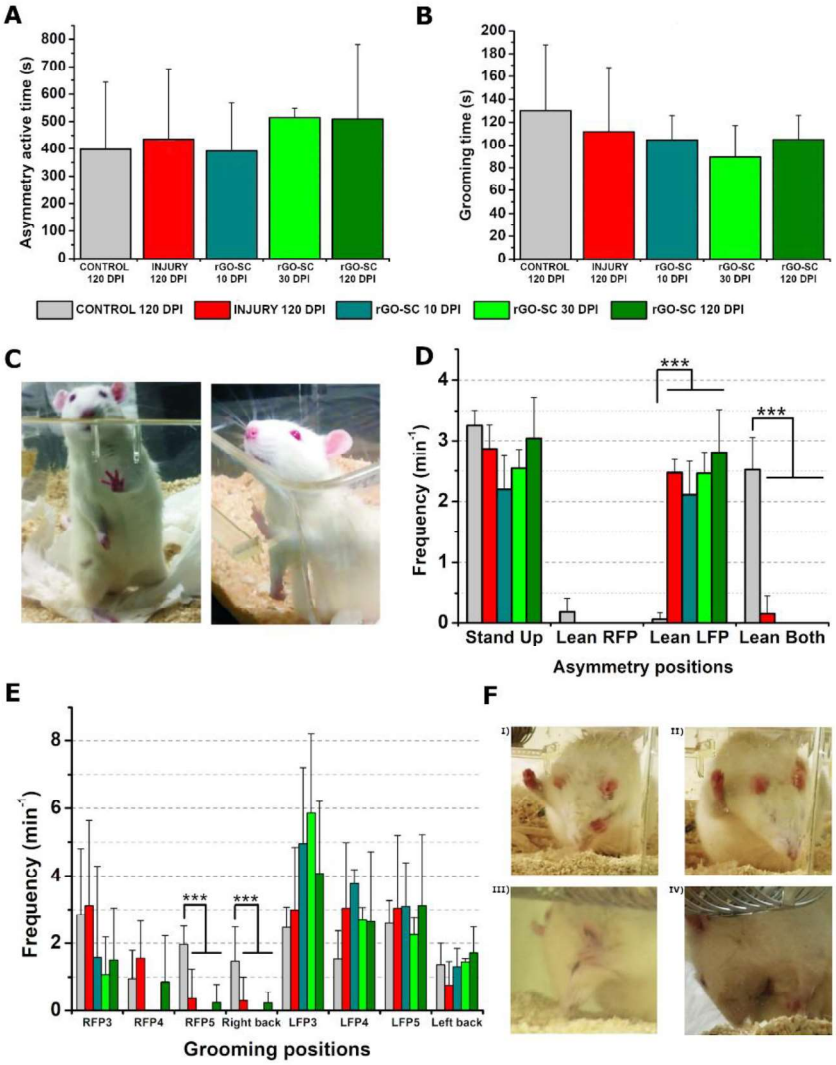

Figure R15. Behavioural tests for evaluating forelimb function in rats carrying rGO foams. A-B) Total time that rats were active during (A) asymmetry tests and (B) grooming tests. C) Representative images of implanted rats leaning on the left forepaw during asymmetry tests. D) Frequency (min^{-1}) of the different parameters measured in asymmetry tests: standing position (*Stand Up*), leant on either RFP, LFP, or both. E) Frequency (min^{-1}) of the different positions reached during grooming tests. F) Representative images of the use of the RFP by rGO-implanted animals failing positions 4 (I) and 5 (II), and attaining position 5 (III) and right back side (IV). Statistics: $p<0.05$* and $p<0.005$***. rGO-SC: Injured animals carrying the rGO foam implant. RFP: Right forepaw; LFP: Left forepaw.

5.2.3. MRI examination of rGO foam integration at the lesion site

A clinical inspired MRI protocol (**Figure R16**) was used to:

1. Describe the morphology of the lesion epicentre (C6) in all the three body-axis (i.e., coronal, transversal, and sagittal) with and without the rGO foam implant (**Figure R16A**).

2. Search for radiological signs of damage directly and indirectly caused by the hemisection along the entire cervical enlargement (which include the metameres between the caudal part of C4 and the caudal part of T1).

T2 MRI images demonstrated that lesion epicentre comprised the entire C6 hemicord tissue fragment (**Figure R16B**). Its dimensions were significantly larger in rats receiving the rGO foams, when we referred to the mean maximum transversal diameter (2.40 ± 0.06 mm in rGO rats versus 1.06 ± 0.14 mm in I rats; $p = 0.008$; **Figure R16C**). Moreover, slight left displacements relative to the midline were found in the coronal sections corresponding to the implant (0.26 ± 0.11 mm). Importantly, although according to this result it is possible to think that the scaffold caused a "mass effect", no signs of compressive damage were detected in either the contralateral hemicord or the rostral/caudal regions (**Figure R16D**). No radiological signs of either syringomyelia (*i.e.,* cavities filled with cerebrospinal fluid) or hematomyelia (*i.e.,* hemorrage) were found in any of the injured animals. Furthermore, the interface volume was indirectly quantified in the rGO group by subtracting the volume of the scaffold itself from the total volume of the lesion area. First, the mean lesion volume was calculated, showing that it was higher in rats carrying the rGO implant. (26.41 ± 3.24 mm^3 in rGO rats versus 6.29 ± 1.28 mm^3 in I rats; $p = 0.008$; **Figure R16E**). Interestingly, the mean volume of the interface was not higher than the volume of the lesion itself in the I group (5.30 ± 3.25 mm^3 *vs.* 6.29 ± 1.28 mm^3, respectively; $p = 0.784$; **Figure R16E**). Therefore, most of the total lesion volume

increment in rGO rats was primarily due to the scaffold itself but not to an increment of the surrounding interface.

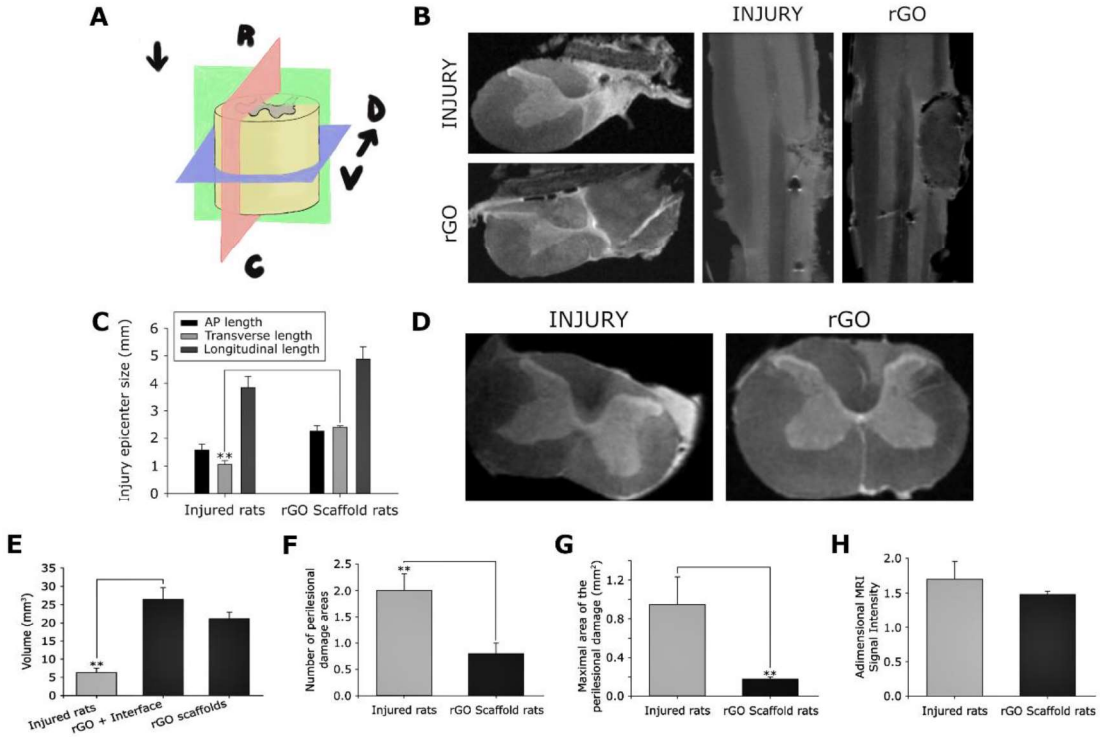

Figure R16. MRI features of spinal cord tissue receiving rGO foam implants. A) Scheme of the different planes under study with respect to the spinal cord: coronal (green), transversal or axial (blue) and sagittal (red). Dorsal and ventral GM horns are indicated for spatial orientation. B) Representative spinal cord MRI images corresponding to axial (left) and coronal (right) scans of I and rGO rats. C) Quantification of the lesion epicenter size. D) Axial scans of representative perilesional damaged areas in both I and rGO rats and respective quantifications including (E) total lesion volume, (F) number of perilesional damage areas, (G) maximal area of the perilesional damage, and (H) signal intensity of perilesional damage areas. Statistics: $p < 0.01$**.

Areas of perilesional damage were always identified in the ipsilateral side of the spinal cord in both groups, both above or below the lesion (following the antero-posterior axis), at a similar distance from the lesion epicentre (2.64 ± 0.85 mm in I rats and 1.92 ± 0.53 mm in rGO rats; $p = 0.566$). Importantly, rGO

scaffolds presence significantly decreased the number or perilesional damage areas with respect to injured rats without implants ($p < 0.01$; **Figure R16F**). Additionally, these areas presented a similar extension along the coronal sections (2.76 ± 0.38 mm^2 in I rats and 1.89 ± 0.72 mm^2 in rGO rats; $p = 0.286$). Nevertheless, the mean damage surface was significantly larger in rats without rGO scaffolds (0.95 ± 0.29 mm^2 in I rats and 0.18 ± 0.03 mm^2 in rGO rats; $p = 0.005$; **Figure R16G**), corresponding to hyper-intense areas, which were suggestive of gliosis. Finally, a similar mean MRI signal intensity was measured in both groups (1.70 ± 0.26 in I rats and 1.48 ± 0.49 in rGO rats; $p = 0.102$; **Figure R16H**), thus suggesting the same type of phenomenon taking place in both groups of injured animals but being more dramatic in those rats without the implants.

5.2.3. Spinal tissue-scaffold interactions and cells infiltration in rGO foams

An important limitation of SCI models is the difficulty to clearly differentiate the lesion epicentre boundaries, characterized by the augmented infiltration of different kinds of cells. In this work, different techniques, including MRI (as stated above), conventional histology, electron microscopy and immunofluorescence, were used for the study of the injury site and its borders. First, by using a conventional Masson's trichrome staining, we visually identified the infiltration of both cells and collagen fibers in the lesion area of all injured animals (**Figure R17A**). Interestingly, they were more abundant within the rGO foam than at the interfaces. Despite this cell significant infiltration, some small cavities were still identified due to the gap generated after the injury. Importantly, the evolution of the injured tissue with time revealed that the chronic implantation of the rGO foams significantly reduced the area occupied by cavities at the lesion site, being 5.6 ± 2.8%, in comparison to 29.4 ± 10.3% in I rats ($p = 0.023$).

TEM was then used to study at a higher magnification and with augmented resolution the central part of the injury. Tissue contained within the implants was identified thanks to the presence of rGO microsheets clearly distinguishable (**Figure R17B**). Lesion areas filled with rGO foams were more compact than those in injured animals without the implant. On the contrary, the lesion area in I rats was mainly characterized by presenting a lot of empty space and few disorganized tissue elements. From TEM images (visualized and acquired under similar conditions), the intensity of grey colour could be easily associated with different degrees of tissue densities, being the whitish colour related to the empty space just filled with the resin. By means of this, the distribution of grey-scale pixels was studied in low magnification TEM images (2000X) of the lesion site in both I and rGO rats to further measure tissue compactness at the injury site (**Figure R17C**). Significant differences were detected between both groups, with a predominant peak in the whitish region corresponding to pure resin without biological content in rats without rGO foams (maximum peaks location: pixel 78 and 163 for rGO, and 158 and 224 for I rats, where 1 corresponds to black and 241 to white colours; statistically significant differences between groups were found at pixel ranges 3-34, 90-195 and 205-254, at least $p < 0.05$).

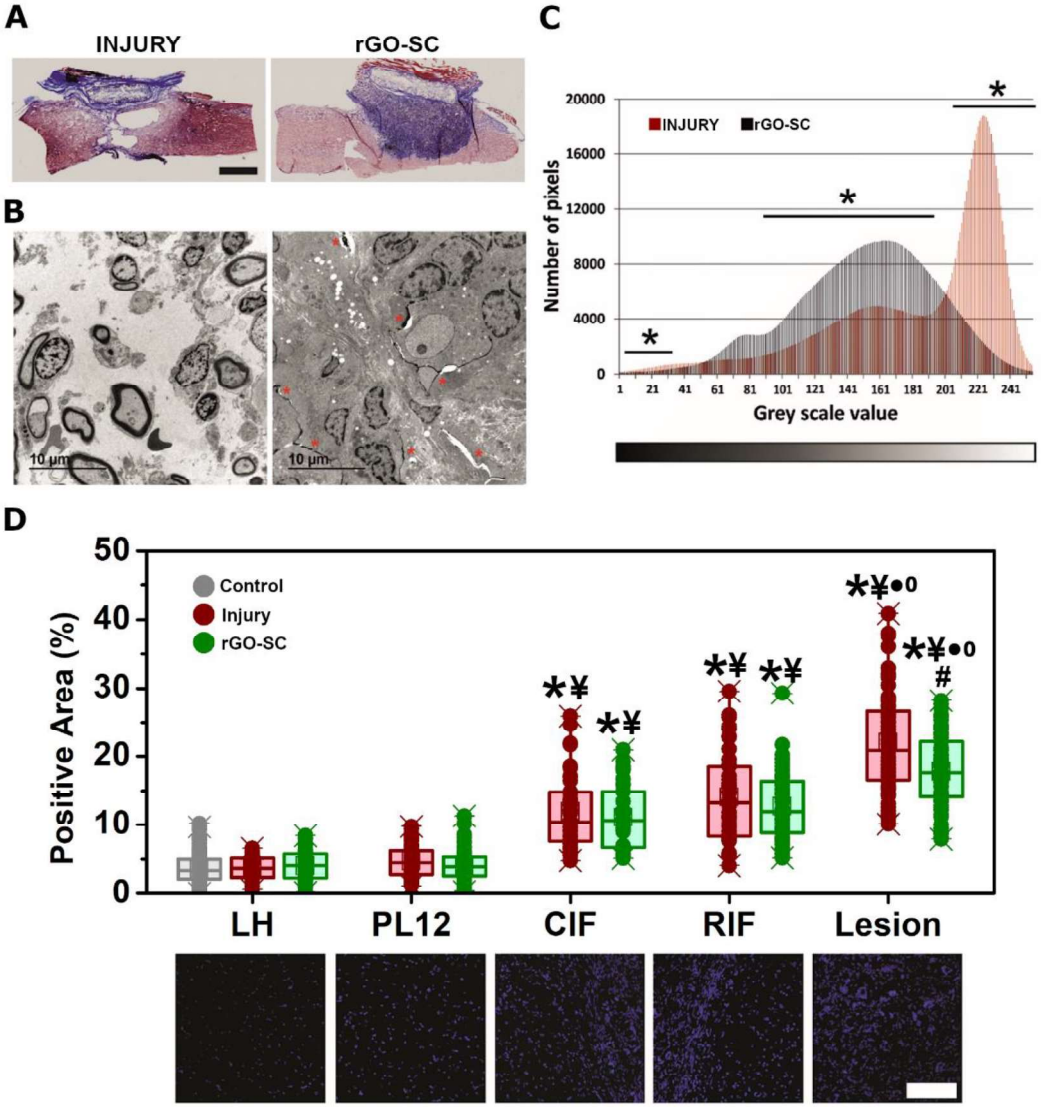

Figure R17. rGO foam colonization by cells and collagen at the spinal tissue. A) Representative spinal cord sections stained for collagen from I (left) and rGO (right) rats. Scale bar: 1 mm. B) Representative TEM images illustrating the lesion site in I (left) and rGO (right) rats. rGO scaffold walls are indicated with red asterisks. Scale bars: 10 µm. C) Pseudo-quantitative estimations of the organization degree at the lesion site in I and rGO rats by analyses of variations in the grey-scale values of the images. Statistical comparisons: $p < 0.05$*. D) Cell density on the different areas under study in rGO rats as measured by Hoechst staining and CLSM. Control and injured rats without scaffolds are shown for comparisons. LH: Left hemicord; PL12: Perilesional areas at 1-2 mm from the lesion border; CIF: Caudal interface; RIF: Rostral interface. Scale bar: 150 µm.

Statistics: Significant differences with respect to (*) LH, (¥) PL12, (^{0}) CIF, (•) RIF, and (#) I group ($p < 0.05$).

The degree of cell colonization was specifically quantified by Hoechst staining (**Figure R17D**). The first observable consequence at the cellular level was a significant increase in cell density both at the lesion epicentre and, to a lower extent, in its caudal and rostral interfaces in all injured animals. Most of these lesion-infiltrating cells might have been recruited by the release of chemotactic messengers from blood vessels in the surroundings but also resulted from the proliferation of local cells at the injured spinal cord at early lesion times. Indeed, we already observed significant cell colonization of comparable rGO scaffolds at 10 DPI and 30 DPI [**López-Dolado *et al.* 2015** and **2016**]. When compared with injured rats without scaffolds, two major significant features were identified. First, the presence of the rGO scaffold significantly decreased cell density at the lesion site ($p < 0.001$). Second, the absence of scaffold (I rats) slightly increased cell density in PL12 with respect to their corresponding LH ($p = 0.023$).

5.2.4. New functional vessels formation within the lesion epicentre supported by rGO foams

Blood vessels restoration within the rGO implant was investigated by the presence of two proteins: RECA-1 (marker of mature vascular endothelial cells) and laminin (major component of the basal lamina in vasculature). Importantly, a significant amount of RECA-1 was detected within the rGO foams (**Figure R18A**), thus demonstrating the existence of new small-sized blood vessels (*i.e.*, microvessels) likely formed from pre-existing ones at the interface (*i.e.*, angiogenesis). Specifically, an average of 109.47 ± 19.43 sectioned vascular structures per mm^2 of scaffold, with an area of $1.02 \pm 0.55 \cdot 10^4$ μm^2 mm^{-2} and a diameter of 10.16 ± 6.21 μm were colonizing the interior areas of the scaffold. Although the number of vascular structures that were able to grow through the

scaffold was significantly inferior to the number of vessels in GM of control rats (284.20 ± 41.21 μm^2 mm^{-2}; $p < 0.001$), their diameter was similar (9.07 ± 6.34 μm; $p = 0.202$). When focused on laminin, no significant differences were found in the amount of positive staining of this marker between the scaffold and LH in rGO rats ($p > 0.05$). Contrarily, laminin expression was markedly higher in the lesion area of I animals than within the scaffold area ($p \leq 0.001$).

Additionally, TEM analysis of the vascular elements present inside the rGO foam was carried out. Images showed blood vessels of different sizes within this material (**Figure R18B**). Endothelial cells and supporting pericytes were also clearly identifiable. Importantly, blood components (such as erythrocytes) were detected inside the vascular structures which invaded the scaffold (**Figure R18C**). Thus, it was demonstrated that, at least, some of these structures were actively functioning for blood supply and waste removal at the lesion site.

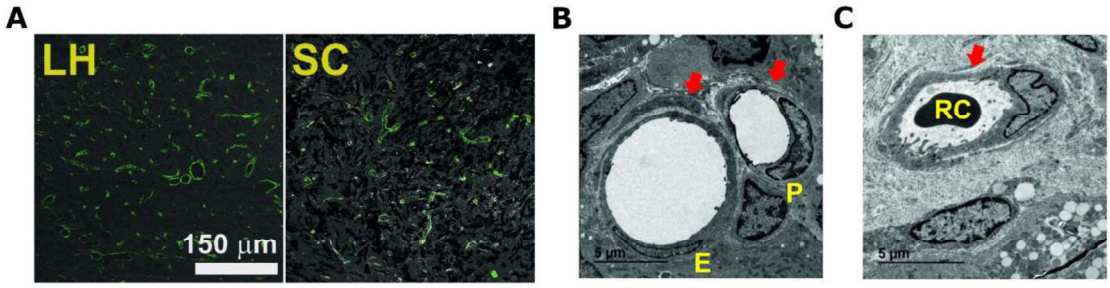

Figure R18. Analysis of microvessels formation at the lesion epicentre in rGO rats. A) Representative immunofluorescence images for RECA-1 (green) and laminin (white) at both left hemicord (LH) and inside the rGO scaffold (SC) areas. B-C) Representative TEM images illustrating the wall structure of the microvessels formed (red arrows) containing mature endothelial cells (E) and pericytes (P) and their functional nature demonstrated by the presence of red blood cells in their lumen (RC).

5.2.5. Ingrowth of myelinated VGluT2^{+} neural tissue components within rGO foams

Neural components were primarily visualized by labelling for MAP2 and Tau, two major cytoskeleton proteins expressed by neurons (**Figure R19A**). As expected, all injured animals experienced a dramatic reduction of both neuronal markers when compared to LH ($p < 0.001$). Nonetheless, the presence of limited but detectable positive labelling at the lesion site for these two proteins was further corroborated with two additional neuronal markers, β-III tubulin and SMI311 (**Figure R19B-D**). Both markers to cytoskeletal proteins specifically present in the microtubules (β-III tubulin) and neurofilaments (SMI311). Interestingly, positive staining for both markers was found in all five animals carrying rGO scaffolds dedicated to these studies, as shown in both immunofluorescence images and the 3D-plot of **Figure R19C**. Curiously, when images for both markers were merged, apart from double-stained neurites (positive for both proteins), elements uniquely stained for either β-III tubulin or SMI311 were also found (**Figure R19D**). Concretely, β-III tubulin neurites

accounted for 5.45 ± 1.75 mm per μm^2 of the total image area, whereas SMI311 presented a total positive area of 3.71 ± 2.57 mm per μm^2.

We next investigated the chemical nature of these new neurites by looking at specific neurotransmitters (**Figure R19E-F**). The presence of vesicular glutamate transporter 2 (VGluT2) was used for identifying excitatory glutamatergic fibers, tyrosine hydroxylase (TH) for excitatory dopaminergic fibers and serotonin (5-HT) for inhibitory serotoninergic ones. In all cases, GM of control rats was used for comparison. Neurites growing within the rGO foam were predominantly positive for VGluT2. TH, if present, was negligible. Regarding 5-HT, although positive labelling was observed within the scaffold, neither the morphology of the staining nor the association with β-III tubulin neurites was detected, so we attributed this finding to either non-specific binding sites for the antibody or early immature serotoninergic fibers. When the presence of all three neurotransmitter systems was studied in PL12 and LH in rGO rats (**Figure R19F**), no statistically significant changes were detected in comparison to control rats in any case (VGluT2: 107.8 ± 17% and 120.1 ± 31.9%, $p = 0.467$; TH: 82.5 ± 65.9% and 72.6 ± 57.5%, $p = 0.746$; 5-HT: 128.8 ± 72.0% and 115.4 ± 45.6%, $p = 0.713$, respectively for PL12 and LH). Finally, detailed morphological TEM analysis of the ingrowth of neurites within the rGO foams revealed the existence of organized multi-layer myelin coatings in some of these neural elements (**Figure R19G**).

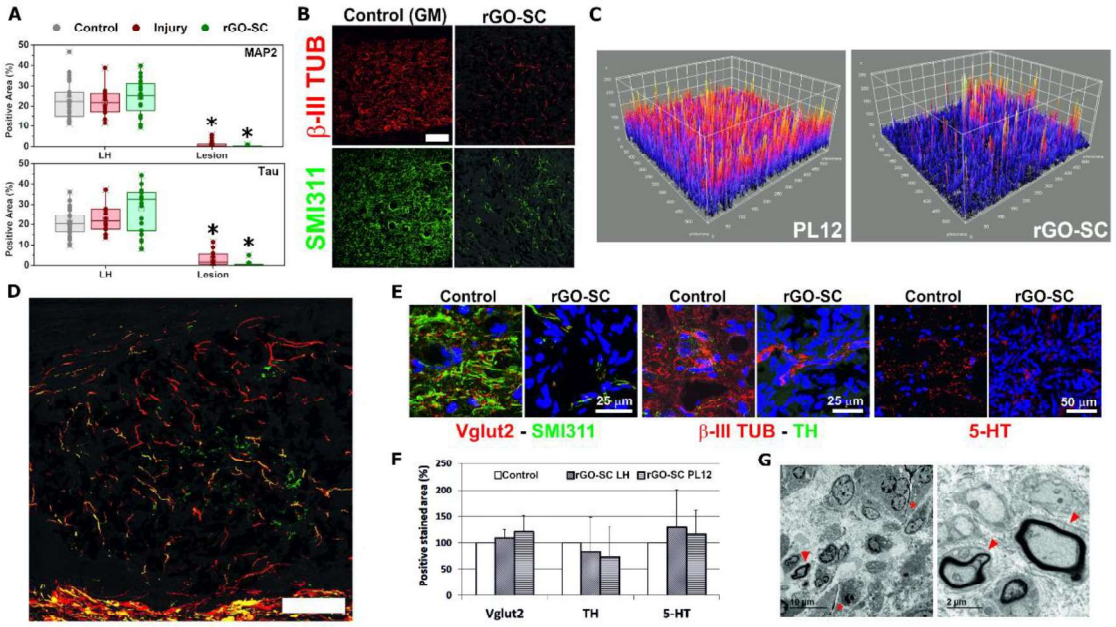

Figure R19. Analysis of neuronal components at the lesion epicentre of rGO rats. A) MAP2 and Tau quantifications from immunofluorescence images. B) Representative CLSM images for β-III tubulin and SMI311. GM in control rats is shown for comparison. Scale bar: 150 μm. Statistics: Significant differences with respect to (*) LH ($p < 0.05$). C) 3D reconstruction plots for β-III tubulin in PL12 and rGO (image area 555.61 × 555.61 μm^2). D) Illustrative CLSM image merging β-III tubulin and SMI311 labeling. Scale bar: 150 μm. E) Representative CLSM images for VGluT2, TH and 5-HT in control (healthy GM) and lesion site in rGO rats. Counterstaining with SMI311 and β-III tubulin for neurites location. Cell nuclei stained with Hoechst. F) Quantitative data for VGluT2, TH and 5-HT at LH and PL12 from rGO-SC rats in comparison to GM in control rats (healthy spinal cord tissue). G) Representative TEM images evidencing the presence of myelinated axons (red arrow heads) within rGO foams (red asterisks). LH: Left hemicord; PL12: Perilesional areas at 1–2mm from the lesion border; TH: Tyrosine hydroxylase; VGluT2: Vesicular glutamate transporter 2; 5-HT: Serotonin.

5.2.6. Reduction in macrophages, vimentin⁺ cells and astrocytes infiltrating rGO foams

When immune cells were studied at the lesion site, the presence of the rGO implants dramatically reduced the amount of macrophages positively labelled for ED1 (which is the most used antibody for macrophages, directed against the CD68 protein present in the pro-inflammatory –M1-like– subtype) invading the lesion with respect to I rats (**Figure R20A;** $p < 0.001$), being just slightly above values found at the LH ($p = 0.042$). This result seems to indicate that rGO presence promoted the attenuation of the immune response. Similarly, vimentin (that is an intermediate filament expressed in many cell types of the CNS, including astrocytes) was significantly less abundant within the rGO biomaterial (**Figure R20B;** $p < 0.001$). Finally, activated astrocytes labelled as GFAP⁺ cells did not significantly penetrate into the rGO foam ($p < 0.001$ with respect to LH). On the contrary, a significant amount of GFAP⁺ cells were found at the lesion site in I rats ($p = 0.002$; **Figure R20C**).

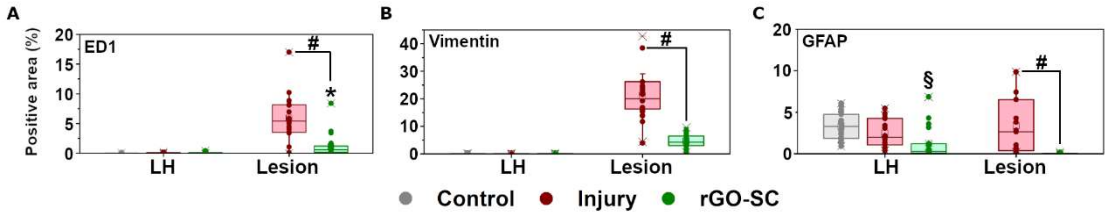

Figure R20. Quantitative data from immunofluorescence images of ED1 (A), vimentin (B) and GFAP (C) at the lesion epicentre of rGO rats. Results from control GM and I rats are shown for comparison. LH: Left hemicord. Statistics: Significant differences with respect to (*) LH, (#) I rats, and (§) control ($p < 0.05$).

5.2.7. Effects of rGO foam implantation at the lesion borders

We next characterized the areas surrounding the lesion epicentre: rostral and caudal interfaces (RIF and CIF), and the perilesional area (PL12), in comparison to the contralateral GM hemicord tissue (LH). Representative immunofluorescence images of the markers under investigation in rGO-SC rats

are summarized in **Figure R21,** including also those from I rats and control rats for comparison.

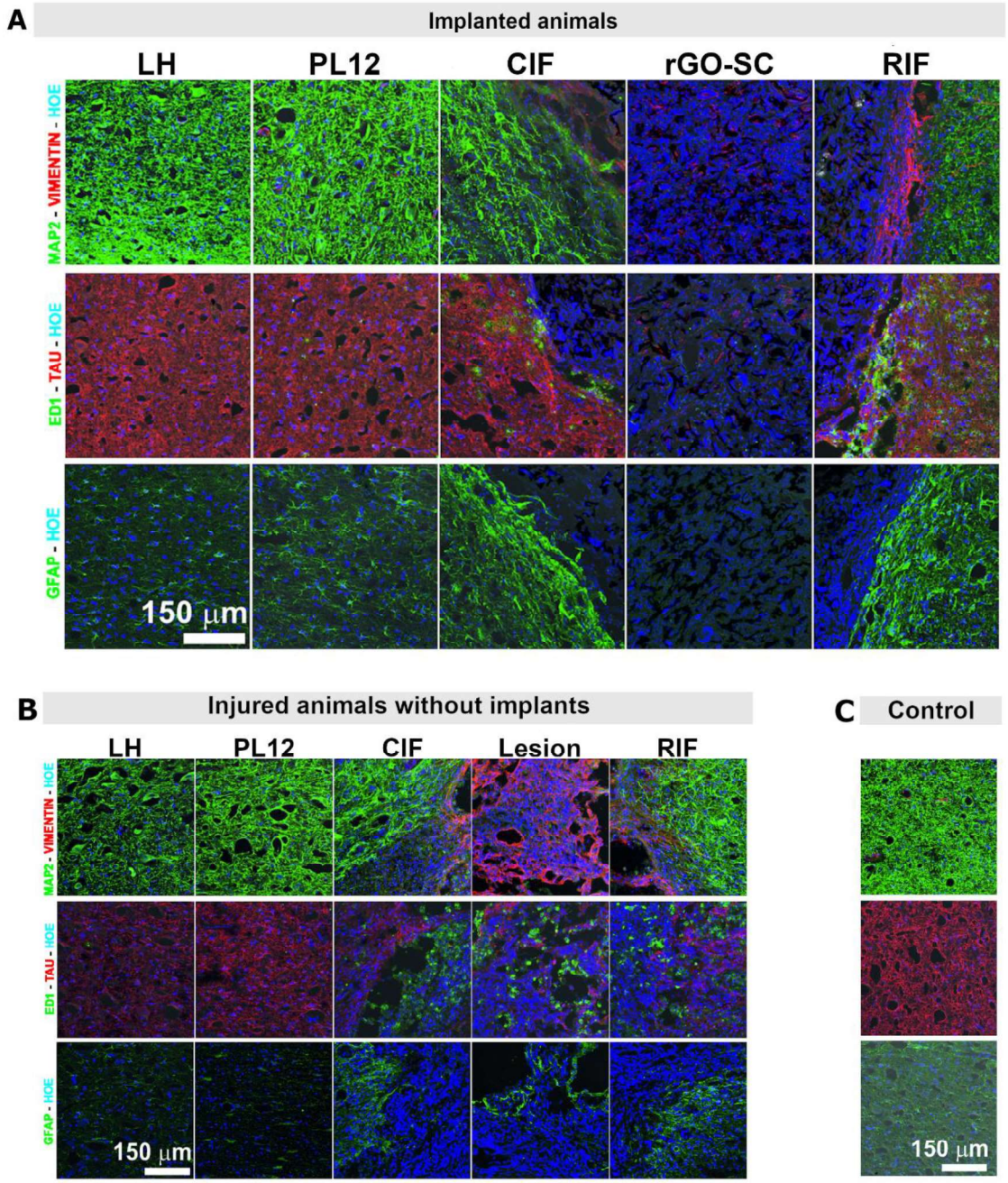

Figure R21. Immunofluorescence characterization of areas located at the lesion surroundings in injured rats carrying rGO foams (A), injured animals without scaffolds (B) and control rats (C). LH: Left hemicord; PL12: Perilesional area; CIF: Caudal interface; RIF: Rostral interface. Scale bars: 150 µm.

Regarding vascular components (**Figure R22**), RECA-1^{+} stained area did not significantly vary with respect to the control GM at any of these locations including LH, PL12, CIF and RIF ($p > 0.05$). However, laminin at the interface tissue around the scaffold dramatically augmented ($p \leq 0.002$ for both CIF and RIF with respect to rGO-SC LH). Interestingly, RIF experienced a more remarkable increase in laminin than CIF ($p = 0.001$). Laminin expression in I rats was markedly higher than in rGO-SC rats around the lesion site ($p \leq 0.001$).

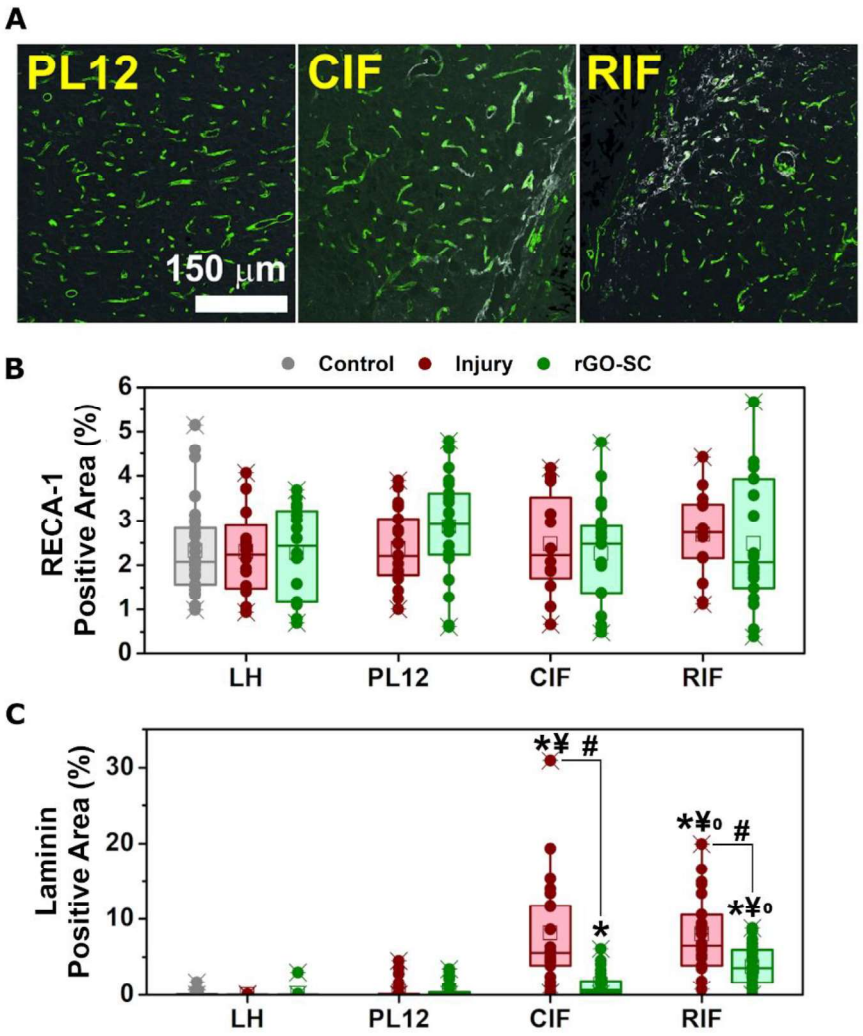

Figure R22. Vascular components at the lesion surroundings. A) Representative fluorescence images regarding the presence of vascular structures positive for RECA-1 and laminin from implanted rGO rats. Quantitative data obtained from CLSM images for (B) RECA-1 and (C) laminin at the different locations under study. LH: Left hemicord; PL12: Perilesional area; CIF: Caudal interface; RIF: Rostral interface;. Statistics: Significant differences with respect to (*) LH, (¥) PL12, (^{0}) CIF, and (#) I group ($p < 0.05$).

When focused on neuronal components positively stained for MAP2 and Tau, no statistically significant differences were found in either LH or PL12 (**Figure R23A-B**; $p = 0.589$ for MAP2 and $p = 0.051$ for Tau at LH; $p = 0.347$ for MAP2 and $p = 0.741$ for Tau at PL12; rGO *vs*. control). However, the interface tissue, both rostral and caudally (RIF and CIF, respectively), experienced a significant decrease in the presence of MAP2 and Tau in rGO-SC rats ($p < 0.02$ for CIF and RIF with respect to MAP2 LH; $p < 0.009$ for CIF and RIF with

respect to Tau LH; rGO *vs*. control). In any case, the presence of both proteins was comparable in both regions for both injured groups (MAP2: p = 0.613 for CIF and p = 0.512 for RIF; Tau p = 0.124 for CIF and p = 0.510 for RIF; rGO *vs*. I animals for all the regions).

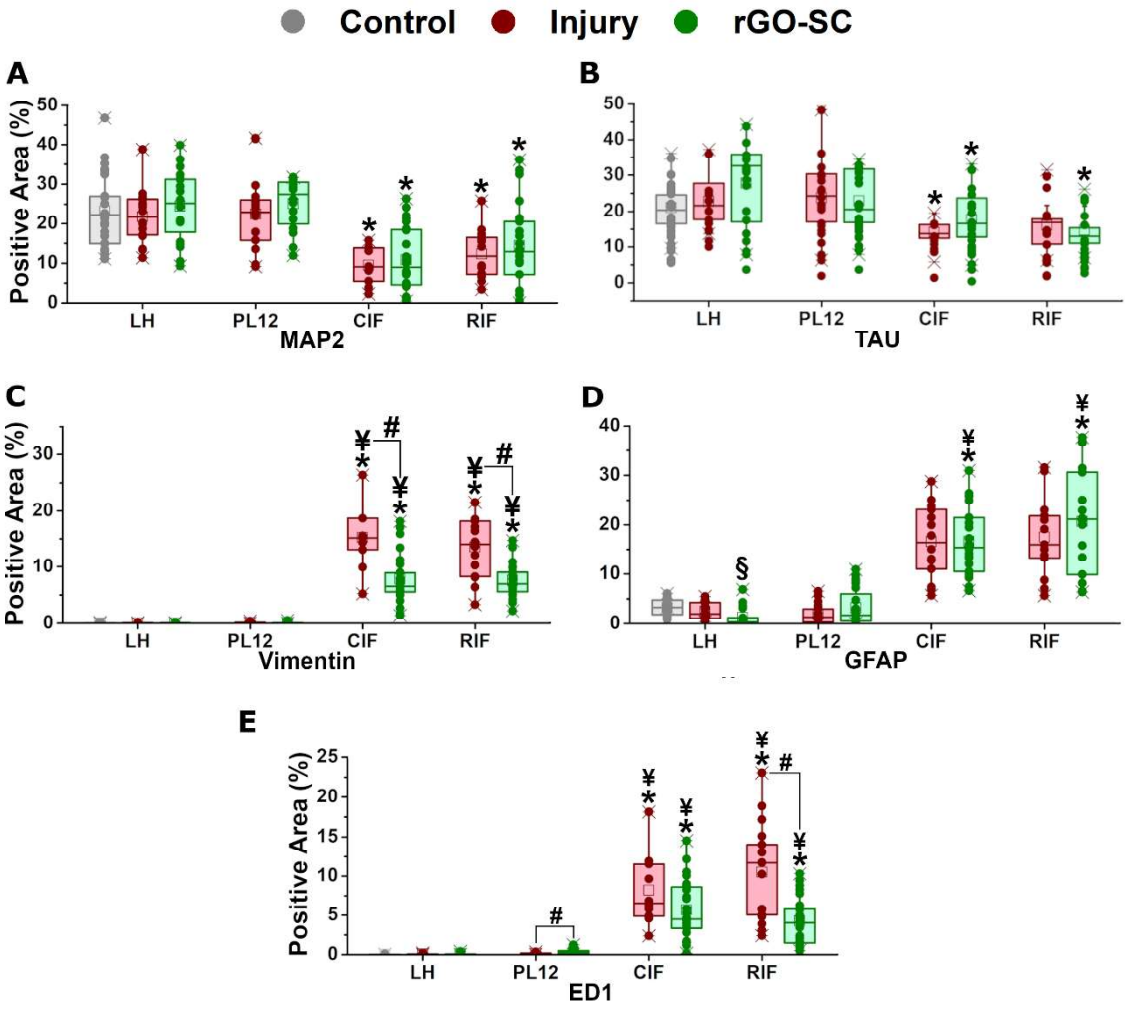

Figure R23. Quantitative data obtained from CLSM images for the different markers under study at the surroundings of the lesion. LH: Left hemicord; PL12: Perilesional area at 1-2 mm of lesion borders; CIF: Caudal interface; RIF: Rostral interface. Statistics: Significant differences with respect to (*) LH, (¥) PL12, (§) to control group, and (#) I rats ($p < 0.05$).

The presence of ED1$^+$ cells was significantly abundant at both CIF and RIF in the two groups of injured animals, I and rGO-SC rats (**Figure R23E**; $p < 0.003$ with respect to LH and PL12). Moreover, the amount of macrophages did

not differ at CIF between I and rGO-SC rats ($p = 0.095$), but did at PL12 ($p = 0.003$) and RIF ($p = 0.001$). Furthermore, the interface tissue in both I and rGO-SC rats was also characterized by the significant presence of cells positive for vimentin (**Figure R23C**; $p \leq 0.001$ for both CIF and RIF with respect to PL12 and LH). There were significant differences attributed to the presence of the rGO foam for vimentin at both interfaces ($p < 0.002$). Regarding astrocytes, their presence was significantly restricted to the interface area (**Figure R23D**; $p < 0.001$ with respect to LH, PL12 and lesion areas for both CIF and RIF) in rGO-SC rats. In any of the markers under investigation, LH in animals carrying rGO foams showed no statistically significant differences when compared with undamaged GM in control rats except for a slight decrease in GFAP ($p = 0.001$).

5.2.8. Preliminary insights of rGO foam degradation in the injured spinal cord

We used TEM to identify possible signs of rGO foam degradation and microsheets dissociation from the main scaffold structure (**Figure R24A**). High-magnification TEM images (300,000X) were obtained to study semi-quantitative changes in the degree of compaction of rGO sheets contained in the scaffold walls. Comparisons among rGO foams before and after progressive times of implantation (10, 30 and 120 DPI) revealed a significant increase of the thickness of the foam walls (**Figure R24B**; rGO: 84.1 ± 35.6 nm; rGO-10 DPI: 90.2 ± 46.3 nm, $p = 0.789$ with respect to rGO; rGO-30 DPI: 108.4 ± 51.5 nm, $p = 0.005$ with respect to rGO and $p = 0.097$ with respect to rGO-10 DPI; rGO-120 DPI: 138.0 ± 54.6 nm, $p < 0.001$ with respect to rGO, $p < 0.001$ with respect to rGO-10 DPI and $p = 0.004$ with respect to rGO-30 DPI), accompanied by a clear fading of their colour intensity. In addition, individualized small fragments of rGO sheets were even visible in the surroundings of the walls (red asterisks). When estimated as the variation in colour (**Figure R24C**), significant changes in the distribution of greyscale pixels were observed with the time of implantation

(maximum peaks location: 229 for rGO, 221 for rGO-10DPI, 206 for rGO-30DPI, and 202 for rGO-120DPI, where 1 corresponds to black and 241 to white; statistically significant differences among pixel ranges 85–200 and 215–250, at least $p < 0.05$). In this case, we associated black pixels at early stages shifting to lighter values in later ones with rGO sheets disassembly from the foam walls. On the contrary, the shift of white ones to darker values could correlate with an increase in the degree of tissue compactness (as shown before when analysing tissue cavities, **Figure R17C**) and so, an increase in the degree of tissue ingrowth within the scaffold. Both shifts were accompanied by an expected increase of pixels with intermediate grey values. Importantly, rGO fragments were frequently found intracellularly, either directly in contact with cytoplasmic components or internalized within them. For instance, hints of attempts of internalization by phagocytosis-like mechanisms were noticed (**Figure R24D**). Internalized rGO was sometimes included in intracellular compartments (**Figure R24E-F**), or directly in contact with cytoplasmic components (**Figure R24G-H**). Disassembly of rGO sheets was also noticed within cells (**Figure R 24H**).

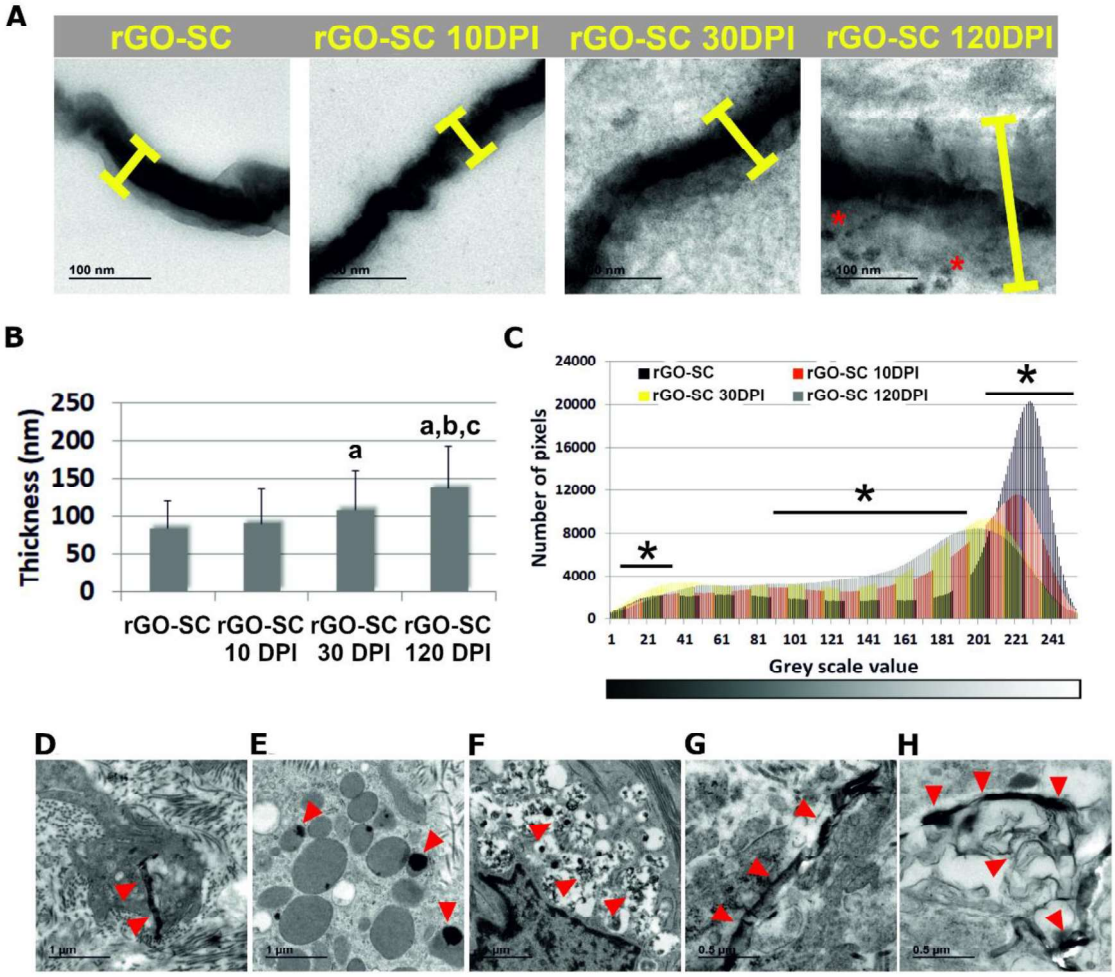

Figure R24. Preliminary scaffold disassembly and biodegradation features in rGO rats by TEM. A) Representative high-magnification images illustrating details of rGO foams over implantation time. Yellow lines indicate rGO scaffold wall thickness and red asterisks point out dissociation clues in their immediate periphery. B) Wall thickness variation over time. Statistics: Significant differences with respect to (a) rGO, (b) rGO 10DPI, and (c) rGO 30DPI ($p < 0.05$). C) Pseudo-quantitative estimations of rGO scaffold disassembly by analyses of the variations in grey-scale pixels from TEM images. Statistics: $p < 0.05$*. (D-H) Specific morphological features of internalized rGO fragments indicative of eventual biodegradation processes ongoing (red arrow heads).

5.2.9. Absence of systemic toxicity signs after 120 DPI

Major organs, including kidney, liver, lungs and spleen, were examined for signs of systemic toxicity due to eventual rGO foam degradation and

biodistribution by using H&E staining and TEM (**Figure R25**). Importantly, neither signs of either macroscopic or microscopic organ damage, nor rGO microsheets or bigger fragments were found in any of the tissues analysed after 4 months of implantation.

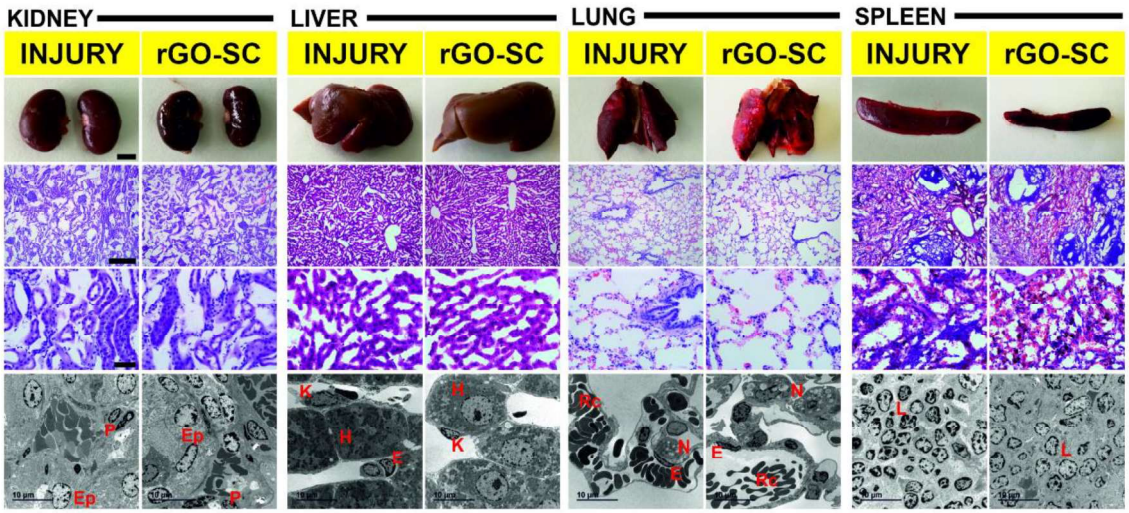

Figure R25. Histopathological and tissue structural analyses in key organs (*i.e.*, kidneys, liver, lungs and spleen) after 4-month rGO foam implantation at the injured spinal cord. Representative images from macroscopic views (top), H&E staining (middle) and TEM analyses (bottom). Scale bars: 2 mm, 250 μm, 50 μm, and 10 μm, from top to bottom. Images from organs in hemisected rats without rGO scaffolds (I rats) are shown for comparison. E: Endothelial cell; Ep: Epithelial cell; H: Hepatocyte; K: Kuffer cell; L: Lymphocytes; N: Neumocyte; P: Podocyte; Rc: Red blood cell.

5.3. GDMs (II): rGO-MFs

5.3.1. Physico-chemical characterization of rGO MFs

First, AFM was used for the study of the rGO MFs surface topography. A tiered surface was observed with the average step heights of hundred nm (**Figure R26A-B**). The overall surface roughness of this area, characterized by the root-mean-square (rms) value, amounted to 0.9 μm. Additionally, local current maps were acquired to assess the conducting properties of the rGO MFs. Current versus voltage curves were obtained at different locations of the fiber and plotted as shown in **Figure R26C**. From the low voltage region (± 0.2 V), the resistance of the tip-MF junction could be estimated as the inverse of the slope, with an average value of 50 kΩ. **Figure R26D** presents the simultaneous topography and current images acquired with a tip voltage of 0.2 V. Current map showed a subtle correlation with topography, with higher values measured at the terrace plateau and lower currents, at the step edges. At these rougher areas, the tip-sample contact was probably not so well defined, which might affect the measured current.

Chemical characterization of rGO MFs was performed by using FTIR (**Figure R26E**). For analysis, results were compared to those found on GO FTIR spectrum reported in other works [**Guo *et al.* 2017**]. Peaks obtained corresponded to the presence of different oxygen-functional groups, as well as to the interaction between carbon and hydrogen atoms: –OH (3448 cm^{-1}, mostly due to adsorbed water), –C–H (2928 cm^{-1}), –C=O (1764 cm^{-1}), –C=C (1540 – 1640 cm^{-1}), –C–O and –C–OH (1000-1400 cm^{-1}). Moreover, results from Raman spectrum analysis (**Figure R26F**) allowed to identify the characteristic peaks of GO at ~1350 cm^{-1} (D peak) and ~1590 cm^{-1} (G peak), respectively. The characteristic 2D peak also appeared at ~2700 cm^{-1}.

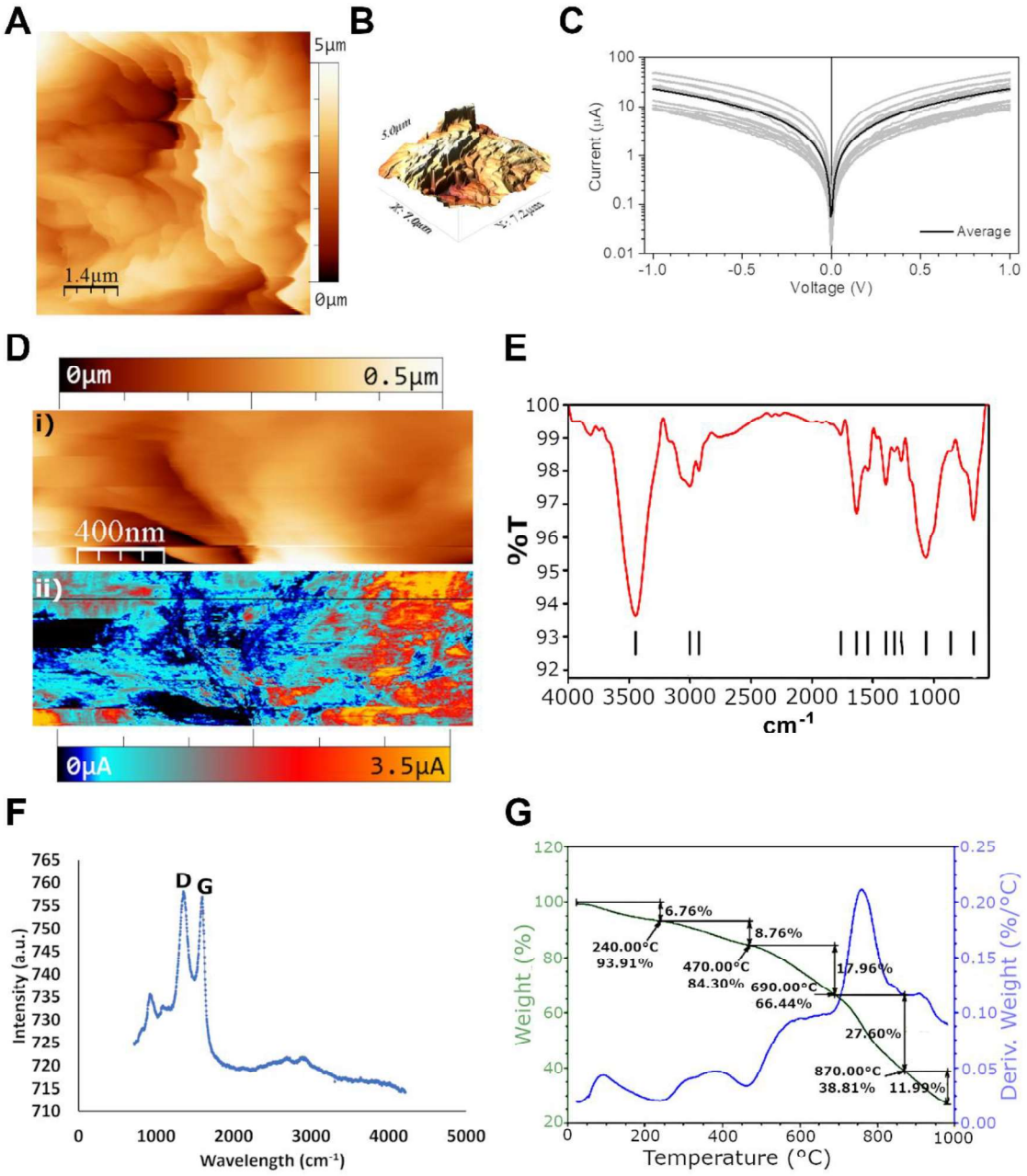

Figure R26. Detailed physico-chemical characterization of rGO MFs. A-D) AFM studies of the surface topography and conductivity of rGO MFs. Representative (A) top view and (B) surface plot of rGO MF topography. (C) Current *vs.* voltage curves obtained at different locations of the MF surface. (D) Topography (Ai) and current (Aii) images simultaneously acquired by using a tip voltage of 0.2 V. E) FTIR, B) Raman and C) TGA spectra of the rGO MFs.

To support these chemical results as well as to obtain information about sample thermal stability and decomposition, TGA analysis was performed

(**Figure R26G**). Four main regions of weight loss were detected in a temperature range of *ca.* 600 °C. The first one mainly corresponding to the release of adsorbed water occurred at 240 °C (loss of 6.76% of the total weight). This was followed by the loss of an additional 8.76% of the material weight at 470 °C, due to the decomposition of oxygen containing groups (such as hydroxyl, carbonyl, and epoxy previously detected by FTIR). Finally, the remaining carbon sample degradation comprised two additional steps, one at 690 °C (17.96%) and the last one at 870 °C (27.60%).

5.3.2. Affected right forelimb evaluation in rGO-MFs implanted animals

After chronic implantation of the rGO-MFs scaffold, asymmetry and grooming tests were performed in order to detect any additional impairments on the affected right forepaw caused by the biomaterial implantation. First, no significant differences were found when the total time that animals spent on the performance of both behavioural tests was compared among the three experimental groups (**Figure R27A-B**; active time during asymmetry test, $p = 0.974$, and grooming, $p = 0.572$). When the paw use for body support was analysed by the asymmetry test (**Figure R27C-D**), control animals characterized for the preferential and simultaneous use of both paws, in contrast to injured animals without the implant ($p < 0.000$). Interestingly, implanted animals (I-MF) did not show significant differences in any of the parameters studied with respect to control rats (Stand Up: $p = 0.803$; Lean RFP: $p = 0.749$; Lean LFP: $p = 0.174$; Lean both: $p = 0.333$). For instance, I-MF animals showed a tendency toward a higher use of both forepaws ($p = 0.333$ with respect to control rats), instead of overusing their LFP as shown in I rats ($p = 0.174$ with respect to control rats). However, no statistical differences were found between I-MF and I groups in the frequency of leaning on both forepaws ($p = 0.329$). No statistically

significant differences were found in the use of the RFP among the three groups ($p = 0.291$) or in the frequency of stand-ups ($p = 0.623$) either.

When focused on spontaneous grooming activity (**Figure R27E-G**), I-MF rats were able to reach the three positions related to the use of the affected RFP (*i.e.*, RFP3, RFP4 and RFP5). A tendency toward an augmented use of this paw to reach positions 3 and 4 was detected in animals carrying rGO-MFs, but it was not statistically significant in comparison to the other groups (position 3, $p = 0.571$; position 4, $p = 0.189$). Importantly, rats carrying the rGO-MFs scaffold were able to reach the most challenging position (RFP5) in a similar way than control animals ($p = 0.178$), contrarily to I rats ($p = 0.045$). Regarding the use of the LFP, implanted animals groomed more intensively to reach position 3 than the other two groups ($p = 0.027$ with respect to control; $p = 0.039$ with respect to I rats). However, no differences were detected for positions 4 and 5 among all animals. Finally, the frequency of exploration of the back region was not affected either for the right or for the left side.

After behavioural tests, animals were sacrificed and the total body weight (**Table R2**), along with the organ weight referred to total body weight of selected organs (*i.e.*, kidneys, liver, lungs and spleen) (**Table R3**), were calculated as course indicators of systemic toxicity. No statistically significant differences were found in any case. Careful histological evaluation of organs referred no signs of systemic toxicity either (**Figure R28**).

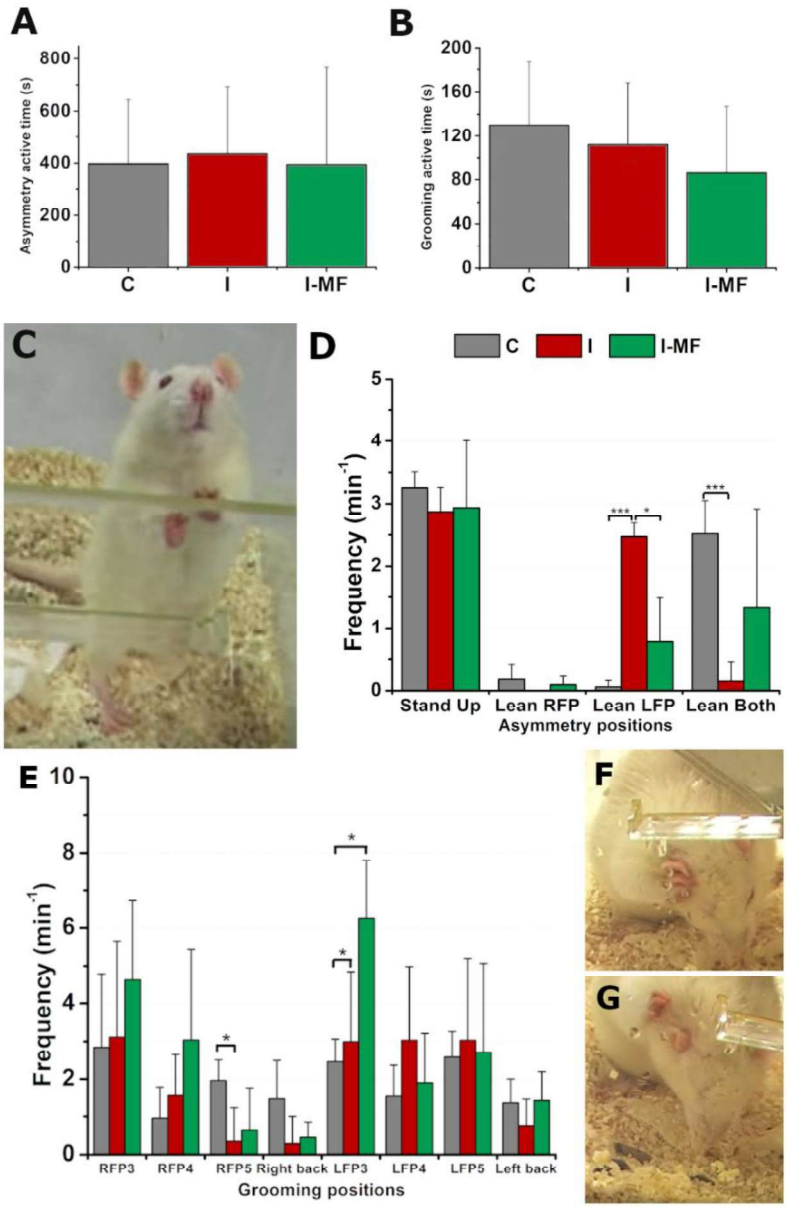

Figure R27. Behavioural tests for evaluating forelimb function in I-MF animals. Total time (s) that rats were active exploring their cage during (A) asymmetry tests and (B) grooming tests. C) Representative image of I-MF rats leaning on both forepaws during asymmetry tests. D) Frequency (min^{-1}) of the different parameters measured in asymmetry tests: standing position (*Stand Up*), leant on either RFP, LFP, or both forepaws. E) Frequency (min^{-1}) of the different positions reached during grooming tests. Representative images illustrating animals attaining positions 4 (F) and 5 (G) with the impaired RFP during grooming tests with the impaired RFP. Statistics: $p < 0.05$* and $p < 0.005$***. C:

Control, I: Injured animals, I-MF: Injured animals carrying the rGO-MFs implant. LFP: Left forepaw; RFP: Right forepaw.

Table R2. Animal total weight (g) expressed as mean value ± standard deviation after 4 months of implantation (120 DPI). C: Control; I: Injured animals; I-MF: Injured animals carrying the rGO-MFs implant.

Experimental groups	Total body weight (g)
C	540.50 ± 135.05
I	418.67 ± 19.82
I-MF	410.60 ± 46.88

Table R3. Ratios of organ weight/total body weight corresponding to kidneys, liver, lungs and spleen after 120 DPI. C: Control; I: Injured animals; I-MF: Injured animals carrying the rGO-MFs implant. Results are expressed as mean ± standard deviation.

Organ weight (g)/Total weight (g)	C	I	I-MF
Kidneys	0.54 ± 0.11	0.53 ± 0.04	0.56 ± 0.07
Liver	2.97 ± 0.27	2.86 ± 0.15	2.80 ± 0.19
Lungs	0.68 ± 0.28	0.56 ± 0.14	0.60 ± 0.08
Spleen	0.16 ± 0.01	0.18 ± 0.01	0.28 ± 0.20

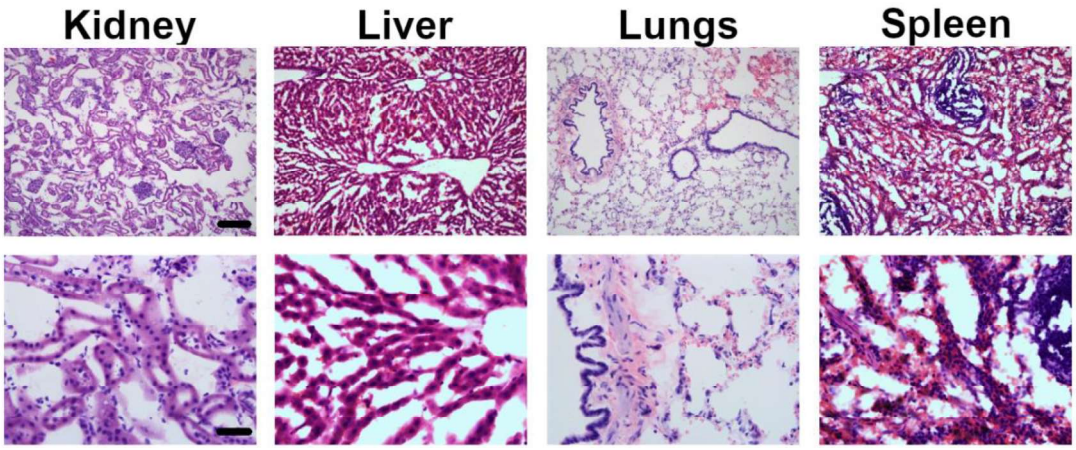

Figure R28. Histopathological studies of key organs (*i.e.*, kidneys, liver, lungs and spleen) after 4-month rGO-MFs implantation at the injured spinal cord.

Representative images from H&E staining at different magnifications. Scale bars: 250 μm (top) and 50 μm (bottom).

5.3.3. Characterization of the lesion epicentre after rGO-MFs implantation

Afterwards, spinal cords were collected, and scaffold integration after four months was assessed. From a macroscopic view, scaffolds appeared well integrated within the spinal cord tissue (**Figure R29A-C**). Cells and collagen infiltration were then observed within the implant by Masson's trichrome staining (**Figure R29D-E**), thus helping to the stabilization of the rGO-MFs scaffold within the lesion site. Cell and collagen density also increased at both rostral and caudal interfaces.

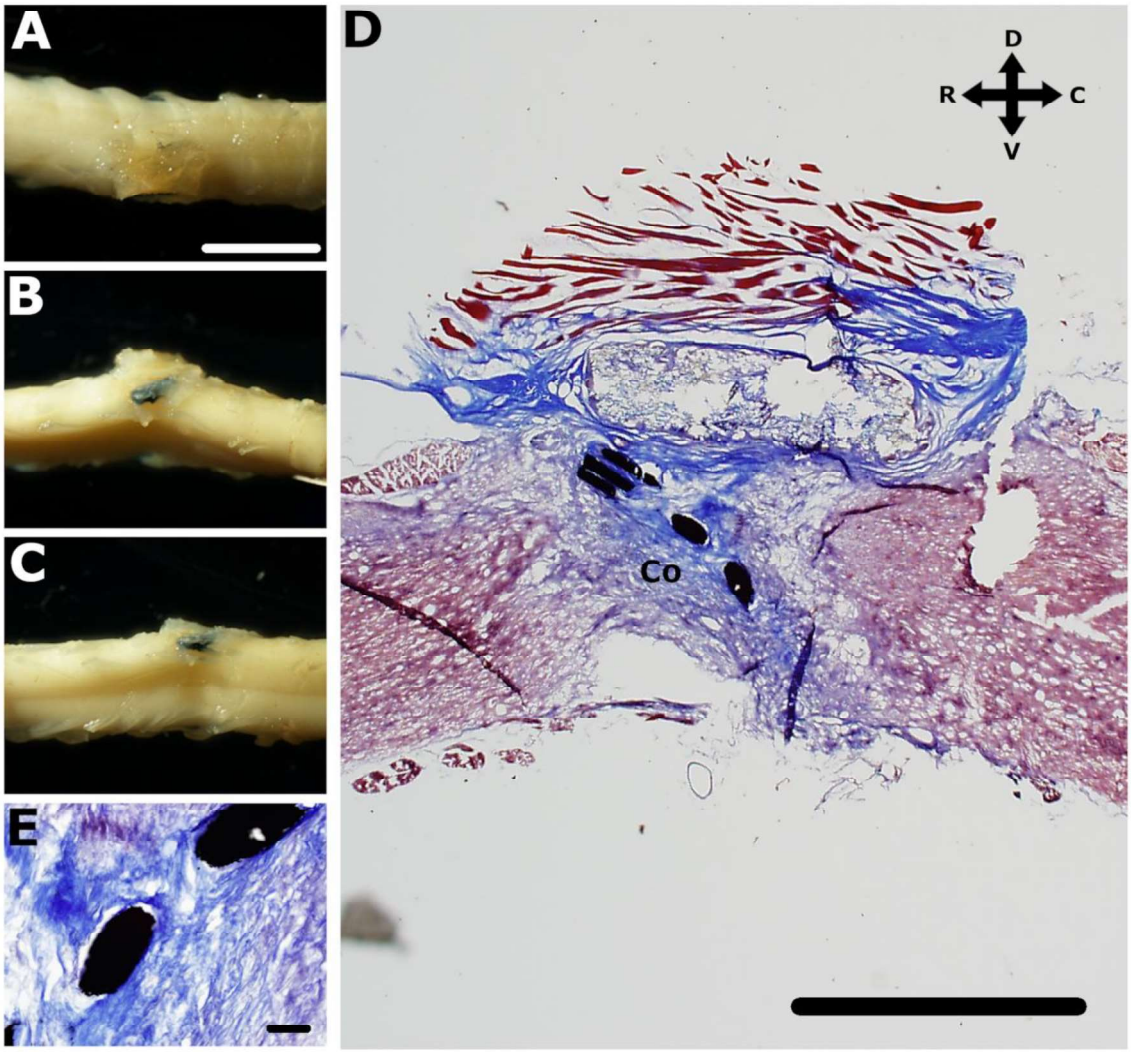

Figure R29. Representative images of *ex vivo* explants of spinal cords carrying the rGO-MFs implant: (A) top, (B) side and (C) bottom views. D, E) Masson's Trichrome staining images at different magnifications, with collagen stained in blue. Scale bars: 0.5 cm (A-C), 2 mm (D) and 100 μm (E). D: Dorsal, V: Ventral, R: Rostral, C: Caudal, Co: Collagen.

We then evaluated the ability of rGO-MFs to guide vascular remodelling within the epicentre of the lesion area. For this purpose, positive labelling against RECA-1 and laminin markers was examined (**Figure R30**). Interestingly, no significant differences were found regarding the amount of RECA-1$^+$ vascular structures between the lesion area of I-MF animals and control GM of uninjured rats ($p = 0.414$), but it existed if focused on laminin$^+$ components ($p <$

0.000). Moreover, a significantly marked increase of vascular components seemed to colonize the lesion area (L) of injured animals without rGO-MFs in comparison to both control tissue (RECA-1: $p = 0.011$; laminin: $p < 0.000$) and areas contained in the lesion epicentre of I-MF animals (L(I) *vs.* L(I-MF): RECA-1 $p = 0.003$ and laminin $p = 0.001$; L(I) *vs.* MF(I-MF) in both cases: $p < 0.000$).

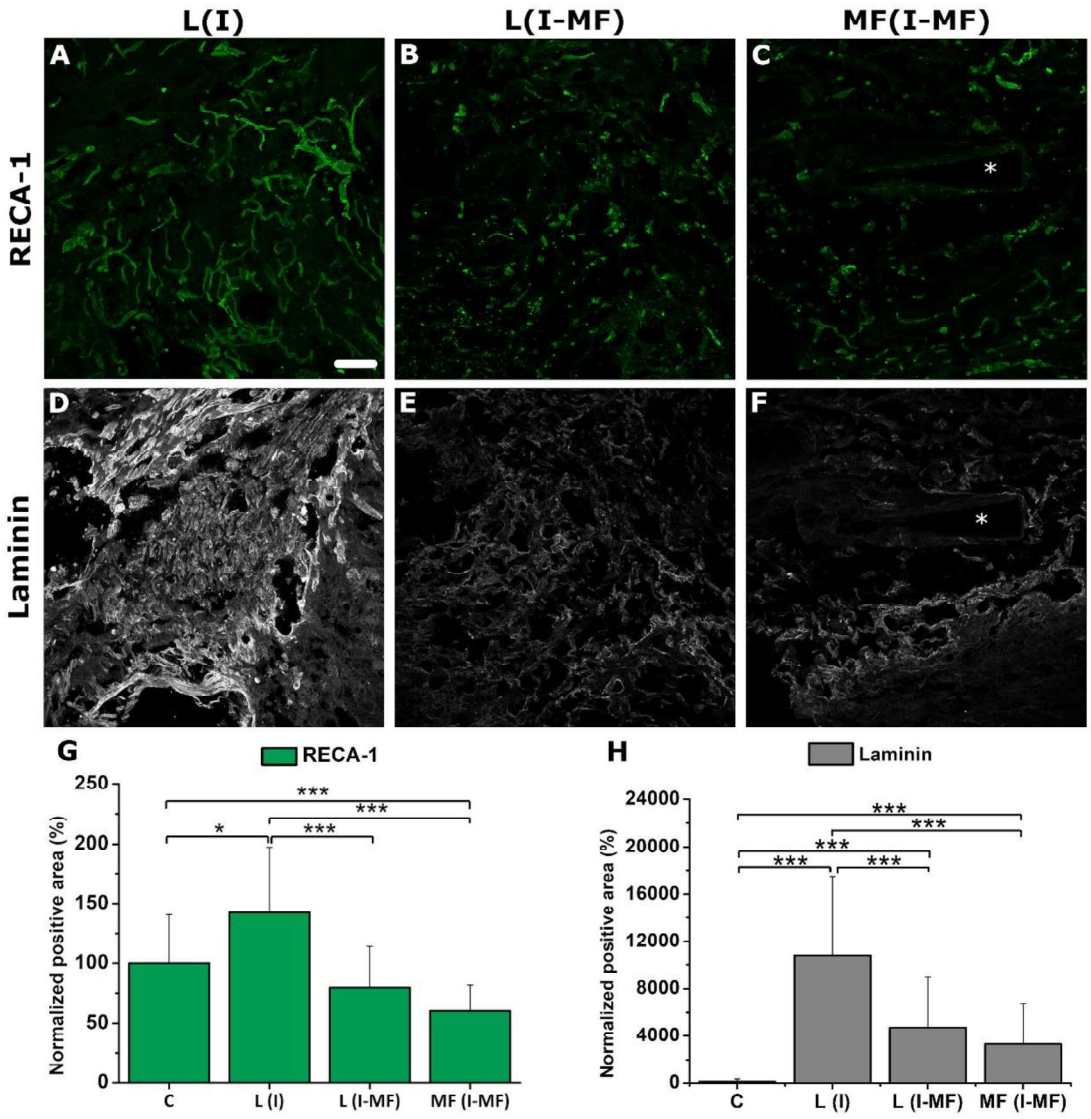

Figure R30. Vascular remodelling at the lesion epicentre in injured animals. A-F) Representative fluorescence images by CLSM regarding the presence of vascular structures positive for RECA-1 and laminin in I (A,D) and I-MF (B-C,E-F) animals. Quantitative results of the presence of (G) RECA-1 and (H) laminin. C: Control; L(I): Lesion area in injured animals; L(I-MF): Lesion area in rats carrying the implant; MF(I-MF): Tissue area immediately adjacent to rGO MFs. Statistics: $p < 0.05$* and $p < 0.005$***. Asterisks in fluorescence images indicate the location of the MFs. Scale bar: 100 μm.

Neurites regrowth within the injured area was first studied at the lesion epicentre by analysing the presence of MAP2 and Tau proteins (**Figure R31**). As expected, their existance was dramatically affected with respect to control GM

due to the injury generated (MAP2: $p < 0.000$ in both L and MF areas; Tau: L area $p = 0.011$, MF area $p < 0.000$). However, they were clearly detected in close contact with the rGO MFs in all animals carrying the implants, being significantly more abundant in the immediate surrounding area of the MFs (MF) than in the lesion (L) region of I rats (MAP2: $p = 0.005$; Tau: $p = 0.049$). Curiously, this result was also found when this comparison of the presence of $MAP2^+$ structures was made with the L region of I-MF animals ($p = 0.043$), but it was not the case for Tau^+ structures ($p = 0.217$). As the main purpose of biomaterials implantation is restoring neural tissue integrity, the presence of two additional neuronal markers, β-III tubulin and SMI311, was studied at this point (**Figure R31**). In agreement with MAP2 and Tau results, their presence was also significantly affected within the lesion epicentre (β-III tubulin: in both L and MF area $p < 0.000$; SMI311: in both L and MF areas $p < 0.000$), but still distinguishable at the injury site of all implanted rats. No statistical differences were found for SMI311 when L and MF regions of I and I-MF animals were compared. Contrarily to MAP2 and Tau, β-III tubulin decreased both in the close proximity of the rGO MFs (MF area of I-MF *vs.* L area of I animals: $p = 0.001$) and in L area (I-MF *vs.* I $p = 0.001$) in I-MF animals in comparison to I rats.

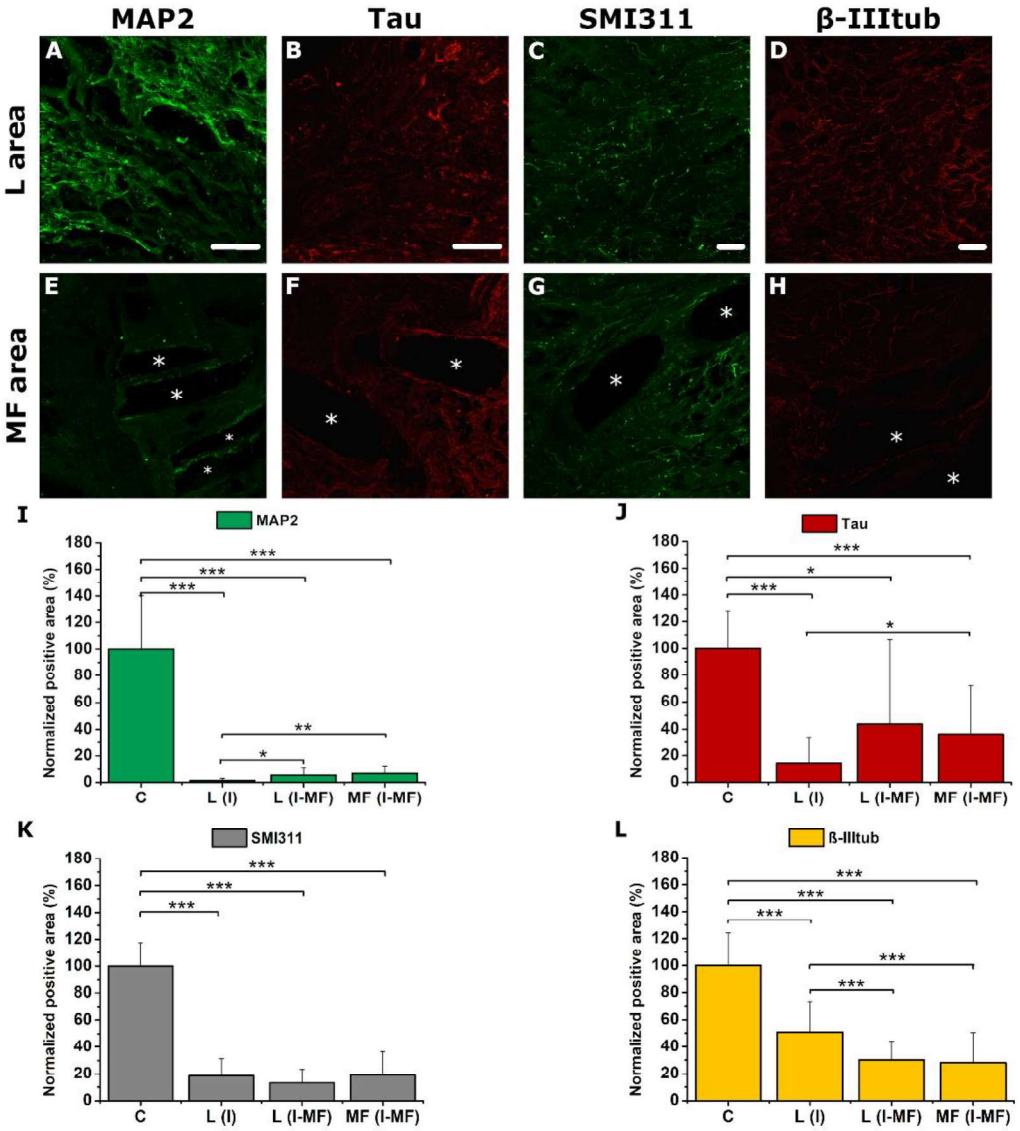

Figure R31. Immunofluorescence characterization of neuronal markers at the lesion epicentre. A-H) Representative CLSM images for the different markers under study in lesion (L) and MFs (MF) areas of I-MF animals after 120 DPI. I-L) Quantitative results of the diverse neuronal markers analysed. C: Control; L(I): Lesion area in injured animals; L(I-MF): Lesion area in rats carrying the implant; MF(I-MF): Tissue area immediately adjacent to rGO MFs. I-MF: Injured animals carrying implants. Statistics: $p<0.05$* and $p<0.005$***. Asterisks in images indicate the location of the MFs. Scale bars: 100 μm.

5.3.4. Examination of inflammatory responses at the lesion epicentre

Changes in the immune response caused by rGO-MFs implantation were studied by the presence of $ED1^+$ cells accounting for macrophages (**Figure R32A-D**). As it could be expected, the lesion epicentre (L and MF areas) of both groups of injured animals presented an increase in the amount of these cells with respect to control tissue (L area: C *vs.* I and C *vs.* I-MF $p < 0.000$; MF area: C *vs.* I-MFs $p = 0.004$). Importantly, biomaterial implantation did not augment the amount of macrophages with respect to I rats at the lesion epicentre (L area: $p = 0.996$; MF area: $p = 0.991$).

To deepen on the characterization of the different phenotypes of macrophages present at the lesion site, preliminary qualitative studies to demonstrate the presence of both M1-like ($CD86^+$) and M2-like (Arginase I^+, $ArgI^+$) macrophages, as well as eventual double-stained cells, in the lesion site were carried out (**Figure R33**). Cells positive for both markers were found but further studies are needed to quantify both macrophage populations and the specific role played by the rGO-MFs in their immunomodulation.

In addition, cells positive for vimentin were investigated (**Figure R32E-H**). The amount of this sort of cells was significantly higher in both groups of injured animals at the lesion epicentre than in controls ($p < 0.001$ for both L and MF regions). However, there was a statistically significant decrease in the amount of $vimentin^+$ cells in direct contact with the rGO MFs (MF) in comparison to L area of I rats ($p < 0.001$). This difference was not found in L area between injured groups ($p = 0.507$).

Finally, the capacity of rGO-MFs for attracting astrocytes ($GFAP^+$) at the lesion site was studied (**Figure R32I-L**). Specifically, the amount of $GFAP^+$ cells did not significantly vary among both groups of injured animals and control rats (L area: $p = 0.498$; MF area: $p = 0.133$).

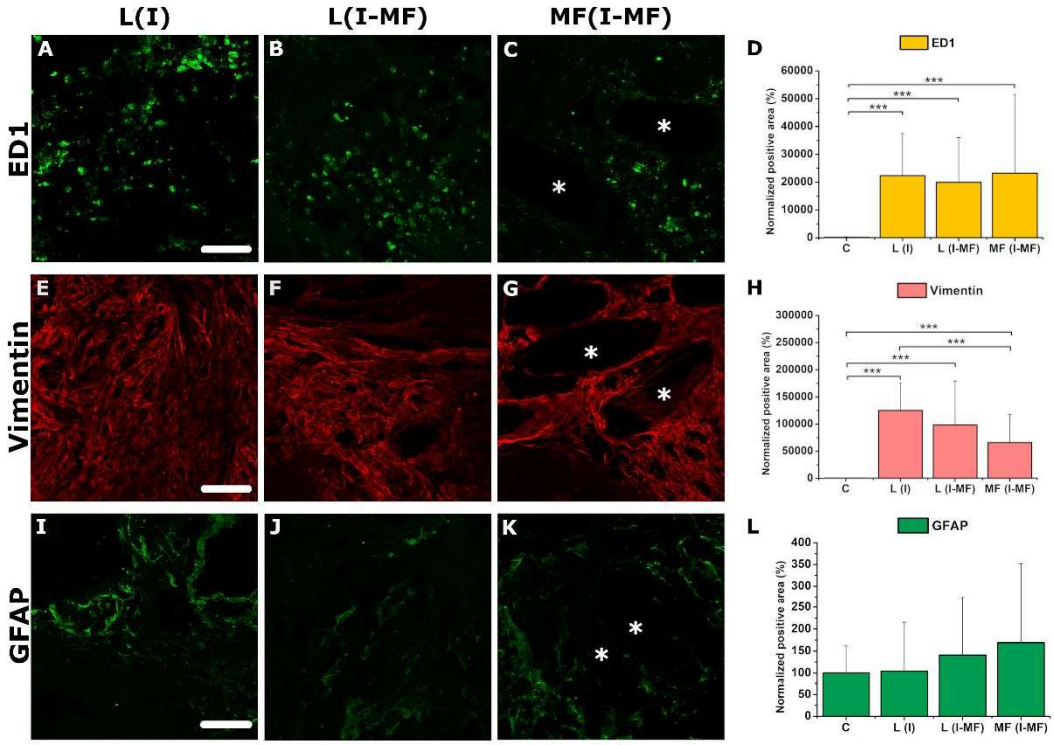

Figure R32. Representative CLSM immunofluorescence images for ED1 (A-C), vimentin (E-G) and GFAP (I-K) at the lesion epicentre and respective quantitative data for each marker (D, H, L). C: Control; L(I): Lesion area in injured animals; L(I-MF): Lesion area in rats carrying the implant; MF(I-MF): Tissue area immediately adjacent to rGO MFs. Statistics: $p < 0.005$***. Scale bars: 100 μm. Asterisks included in fluorescence images are indicative of the position of the MFs.

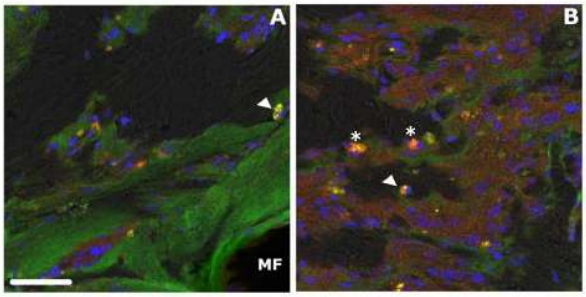

Figure R33. Representative CLSM immunofluorescence images for CD86 (green, M1-like macrophages) and ArgI (red, M2-like macrophages) at the injured spinal cord (A: MF area; B: L area) from I-MF animals. Arrow heads indicate the presence of double positive macrophages ($CD86^+/ArgI^+$). Asterisks indicate the presence of $ArgI^+$ macrophages. Cell nuclei were stained with Hoechst(blue). Scale bar: 50 μm.

5.3.5. Effects at the lesion borders after rGO-MFs implantation

All markers for detecting vascular and neuronal components, as well as macrophages, astrocytes and connective cells, described above were also analysed in the areas surrounding the lesion epicentre (RIF, CIF, PL12 and LH). Representative immunofluorescence images are displayed in **Figure R34**, from which quantifications were carried out (**Figure R35**).

When focused on vascular elements, no significant differences were detected for RECA-1 in any of the surrounding areas in comparison with control tissue (**Figure R35A**). Interestingly, laminin was significantly less abundant at LH in I and I-MF animals (**Figure R35B**; control *vs.* I $p = 0.030$, control *vs.* I-MF $p = 0.022$), and at PL12 in I-MF animals (control *vs.* I-MF $p = 0.019$). Contrarily, laminin levels were significantly higher at both interfaces in all injured animals (in all cases for control *vs.* I and control *vs.* I-MF: $p < 0.000$ for both RIF and CIF). However, laminin abundance was significantly decreased at RIF and PL12 (but not at CIF and LH) due to rGO-MFs when compared to those regions on I rats (RIF: I *vs.* I-MF $p = 0.001$; PL12 I *vs.* I-MF $p = 0.038$).

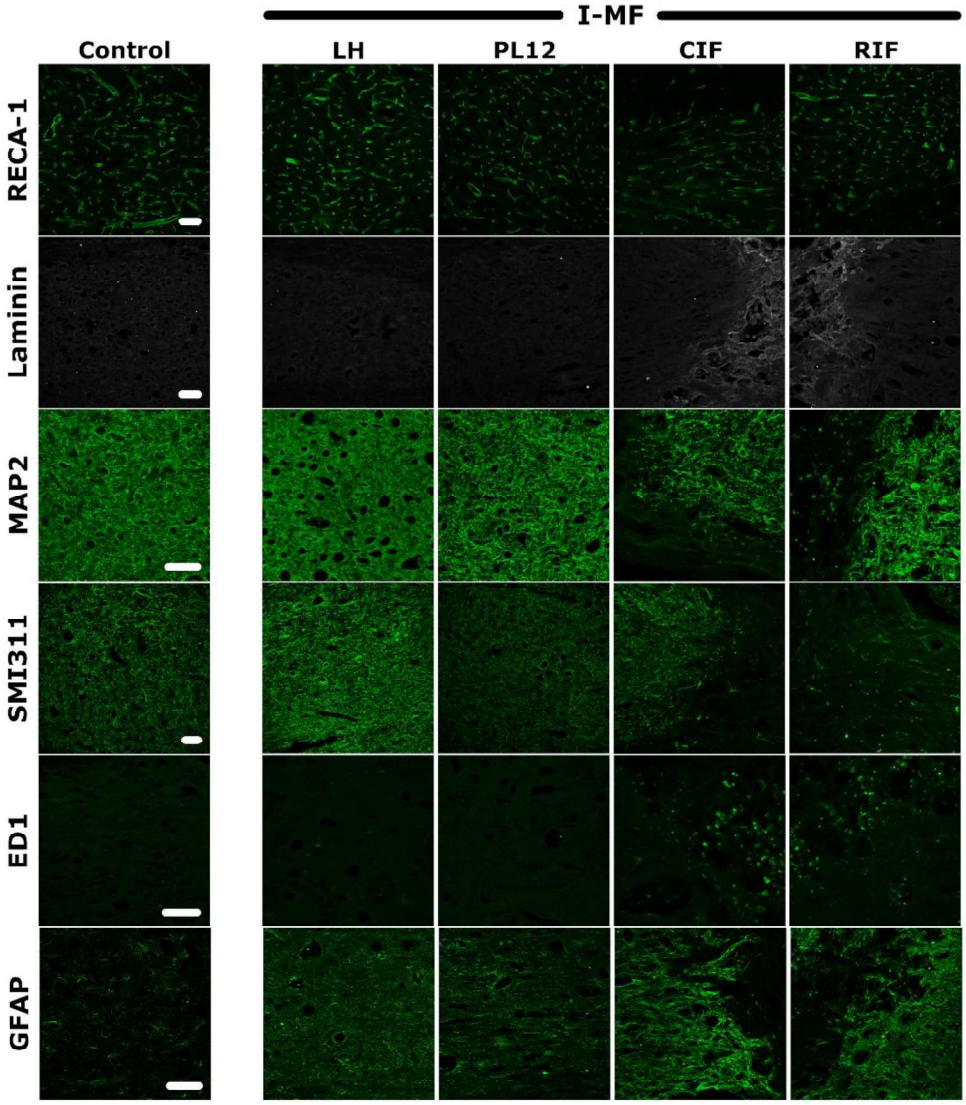

Figure R34. Immunofluorescence characterization of areas located at the lesion surroundings in injured rats carrying the rGO-MFs implant. Representative CLSM images at the lesion borders (CIF: Caudal interface; RIF: Rostral interface); Perilesional area (PL12); Left hemicord (LH). Control images are supplied for comparison. Scale bars: 100 μm.

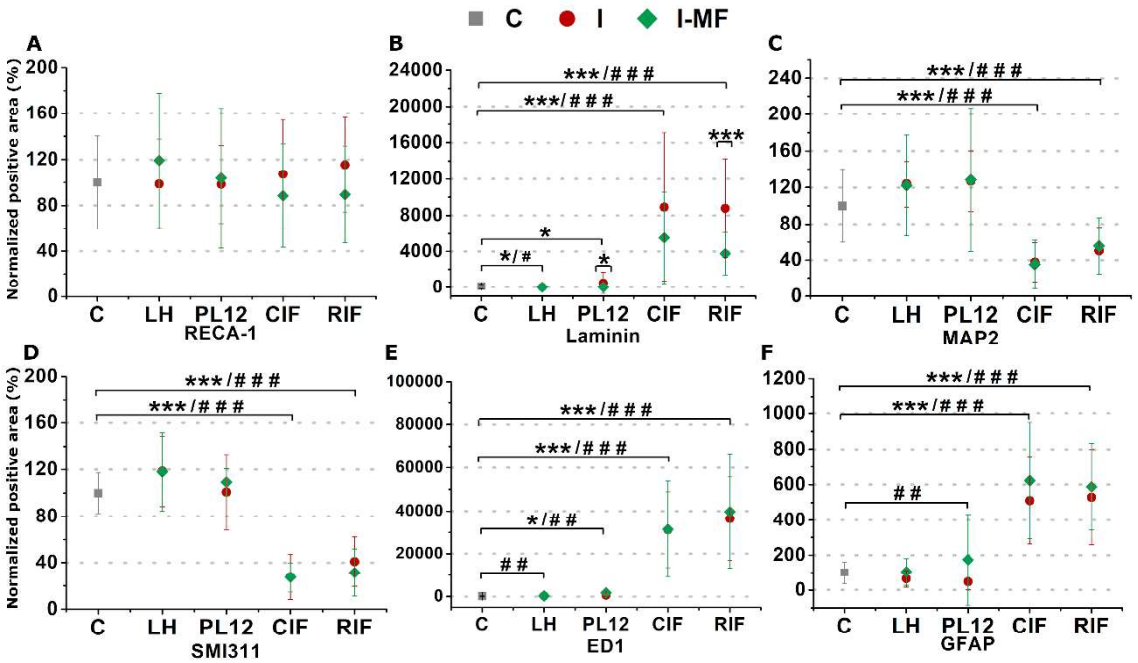

Figure R35: Quantitative data (normalized positive area, %) obtained from CLSM images for the different markers under study. LH: Left hemicord; PL12: Perilesional area; CIF: Caudal interface; RIF: Rostral interface. Statistics: (*) comparisons with I-MF and (#) comparisons between control (C) and I groups: $p < 0.05$*/#, $p < 0.01$**/## and $p < 0.005$***/###.

In this case, MAP2 and SMI311 markers were selected for the study of neuronal components outside the lesion epicentre (**Figure R35C-D**). Although their presence significantly decreased both at RIF and CIF in all injured animals ($p \leq 0.005$ for all comparisons), it did not aggravate as a consequence of rGO-MFs implantation within the lesion site (MAP2 RIF: $p = 0.936$, CIF $p = 0.989$; SMI311 RIF: $p = 0.563$; CIF $p = 0.998$). Importantly, these markers did not differ between I-MF and control groups in LH and PL12 areas.

ED1$^+$ cells increased at both interfaces and PL12 area in all injured animals (Figure **R35E**; CIF and RIF in all cases: $p < 0.005$; PL12: control *vs.* I $p = 0.005$) in comparison to control rats. Importantly, no significant differences were found at these locations between I and I-MF rats. In addition, the amount of macrophages was not statistically different at LH between rGO-MFs implanted and control rats ($p = 0.065$).

Finally, activated astrocytes were predominant at both interfaces in both I and I-MF rats (**Figure R35F**; $p < 0.000$ for all comparisons). Nonetheless, no statistical differences were found between I and I-MF rats at these locations (RIF $p = 0.845$, CIF $p = 0.598$). Besides, there were no significant differences in LH and PL12 areas with respect to control tissue, but they existed in the case of the PL12 area of injured animals without scaffolds (control *vs.* I $p = 0.005$).

6. DISCUSSION

6.1. Au and Ni nanoelectrode arrays

In this thesis, the *in vitro* biocompatibility of diverse nanostructured electrode arrays was first investigated. These nanoelectrodes are thought to be part of a more complex device for electrical stimulation at the injured spinal cord. In particular, the role that two important physico-chemical properties such as chemical composition and topography play in the behaviour of neural cells interfaced with the arrays was studied aiming to the selection of the best material for further use. On the one hand, two different metals with different physico-chemical properties, Ni and Au, were compared. On the other hand, vertical NWs and equivalent flat electrodes of either Ni or Au were explored.

Au has been widely used in nanotechnology and nanomedicine research for the fabrication of nanoparticles and electrode arrays due to its favourable properties regarding processability, biocompatibility, electrical conductivity and stability (*i.e.,* poor degradation *in vivo*) [**Ashraf *et al.* 2016**]. On the contrary, important concerns about Ni biocompatibility have been documented, depending on the concentration, type of exposure (*e.g.,* inhalation, food uptake, skin contact or as part of orthopaedic implants) [**Das *et al.* 2018**], and whether it is presented as part of water soluble compounds or not (being more toxic those that are soluble). Indeed, some non-desired results have been obtained when confronted to cerebral neurons [**Das *et al.* 2018; Song *et al.* 2017**]. In this thesis, Ni was used in its oxidized form, which is more stable over time. Moreover, as immobilized on an Au-base, the probability to be released and induce toxicity by cell uptake was also diminished. The rationale behind its selection was its robustness and superior mechanical properties over Au, accepting the potential need of further functionalization if selected for bio-applications (*e.g.,* coating with biocompatible polymers such as PDMS).

Homogeneous and reproducible flexible platforms were obtained with both elements. Regarding NWs substrates, the first step was to create an Au non-cracked flexible base of approximately 1 μm-thick. Then, 2 μm-long NWs composed of either Au or Ni were grown by electrodeposition over it. Following, to ensure both chemical and mechanical equivalence between the nanostructured samples and their flat counterparts, the flexible Au bases were used as Au-Flat substrates, whereas a very thin layer of Ni was electrodeposited over this Au base to obtain Ni-Flat substrates.

Results of *in vitro* biocompatibility tests with embryonic neural cells showed no significant differences regarding cell viability either between both kinds of Au electrodes (NWs *vs.* flat substrates), or when nanostructured Au platforms and Au-Flat substrates were compared to control (glass) samples. This was consistent with the well-known biocompatibility of this material. Interestingly, no significant differences were either found with Ni-NWs samples under the experimental conditions used. However, Ni-Flat substrates significantly reduced cell viability, agreeing with biocompatibility issues previously found in the literature. This result could be a consequence of poorer neural cell adhesion in comparison to Ni-NWs, which was identified by a clear tendency of cortical cells to clump, along with neurites fasciculation, since the first time point evaluated. Cell clumping and fasciculation were also present, albeit to a lesser extent, in Ni-NWs, but started at longer time points (28 DIV). We hypothesized that, as NWs topography offered more sites for cell components adhesion, this feature could counter, at least in part, the low biocompatibility of Ni.

When focused on neural differentiation, the amount of neuronal cells (referred as area positively stained for MAP2) found on these substrates after 14 DIV was not significantly different among Au-NWs, Au-Flat and Ni-NWs when compared to control samples. Nevertheless, the normalized positive area

representative of neuron-like cells markedly decreased on Ni-Flat samples. This means that, besides having a reduced amount of cells able to develop on Ni-Flat, the proportion of neurons decreased in comparison with the rest of experimental groups. Interestingly, when we focused on vimentin, it was shown that Ni-NWs significantly reduced the area occupied by vimentin$^+$ cells with respect to Au-NWs and glass controls. Vimentin is an intermediate filament protein of the cytoskeleton of a wide variety of cell types, including fibroblasts [**Robinson-Bennet and Han, 2005**], and many cells of the CNS, especially glial cells (such as astrocytes) and immature neural progenitor cells [**Chen *et al.* 2018**]. In the *in vitro* cultures of these experiments, vimentin was used as a marker to label non-neural cells, including glial cells present in the network. Glial cells are the main components of the fibro-glial scar formed after *in vivo* biomaterial implantation within the CNS [**Seidlits *et al.* 2008**]. Regarding nanoelectrode arrays implantation, the decrease in the area occupied by glial cells directly interfacing Ni-NWs could be beneficial to avoid the formation of the above-mentioned fibro-glial scar, which would drive to nanoelectrodes encapsulation. This scaring would drive the appearance of a physical barrier between the electrodes and the neurons, thus, hampering neuronal stimulation [**Adewole *et al.* 2019; Salatino *et al.* 2017**]. So, this feature might anticipate some beneficial effects of Ni-NWs implantation in the neural tissue, but further *in vitro* and *in vivo* experiments should be done to confirm this hypothesis.

Based on these results, nanotopography features of Ni-based substrates seemed to promote a higher predominance of neurons in comparison to their flat counterparts. This was consistent with results published by Vallejo-Giraldo *et al*. [**2018**], where nanoscale surface patterning led to a selective reduction of astroglial cell adhesion. However, this was not the case for Au substrates, which

remain statistically similar to glass controls, pointing towards an additional role of chemical composition on these responses.

Based on these findings, we could state that Au substrates performed superiorly than Ni ones in terms of cell viability and neuronal development, which are two key parameters for the future use of these nanostructured arrays as neural interfaces at the injured spinal cord. However, it is interesting to point out how the incorporation of nanotopography features in Ni substrates (Ni-NWs) significantly reversed some of the adverse effects found, being both neural cell viability and the amount of neuron-like cells more similar to control glass substrates and Au electrodes.

In line with our findings, primary nerve cells obtained from dorsal root ganglia showed an improvement in cell survival when cultured on top of epitaxial GaP NWs (2.5 μm long and 50 nm wide) with respect to planar substrates [**Hällström *et al.* 2007**]. Effects on neural cell growth and development exerted by topography have been also described for other structures rather than NWs, including grooves, pores, nanopillars and MFs [**Marcus *et al.* 2017; Seidlits *et al.* 2008; Tan *et al.* 2018**]. For example, studies with NSCs described the influence of hierarchically patterned substrates containing both microgroove (1.5 μm) and nanopore (10 nm in diameter) patterns to direct neuronal development of these cells by inducing changes at the molecular level in different signalling pathways [**Yang *et al.* 2014**]. Topography-dependent differentiation patterns have been also found on human hESCs [**Ankam *et al.* 2013**]. Concretely, the presence of different types of structured patterns on the substrate favoured the differentiation of ESCs towards either neuronal (gratings) or glial (pillars and wells) phenotypes. Relevant differences in composition, size and inter-distance of the different nanostructures in these studies with respect to the NWs used in this thesis make difficult straightforward comparisons of the results obtained. For

example, pillars of this last study were composed of PDMS, with 1 μm in length and 1 μm in diameter [**Ankam *et al.* 2013**], whereas our NWs were made of metals, with 2 μm in length and 100 nm in diameter. Even more than separately, Stevens and colleagues proved that chemical composition and topography can act synergistically to influence ESCs differentiation on metallic thin films [**LaPointe *et al.* 2013**]. Based on these works, besides nanotopography and chemical composition, the specific cell source and inherent characteristics of each neural cell type under study might also play a relevant role in the overall biological responses to neural interfaces found.

Focused again on Ni-NWs, although not significant, inferior biological responses were obtained in general. Other groups have also published detrimental effects on cellular normal functioning when Ni-composed nanostructures were confronted to different kinds of cells. For instance, individual Ni NWs can be internalized by immortalized fibroblasts [**Song *et al.* 2010**], human colorectal carcinoma HCT116 cells [**Margineanu *et al.* 2016**], osteosarcoma UMR-106 cells [**Prina-Mello *et al.* 2006**], rat marrow stroma cells, osteoblast MC3T3-E1 cells [**Prina-Mello *et al.* 2006**] and monocytic THP-1 cells [**Byrne *et al.* 2009**]. If able to directly interact with cells in dispersion, and once internalized, it has been proposed that Ni-induced toxicity effects could be related to mitochondrial dysfunction, which results in an increase of reactive oxygen species (ROS) and thus, in an impairment of cell metabolism [**Song *et al.* 2017**]. In line with this fact, Felix *et al*. [**2016**] demonstrated the reduction of metabolic activity of human WI-38 fibroblasts when cultured on individual NWs (1 μm in length and 31 nm in diameter). Moreover, in HeLa cells, individual Ni NWs (1 μm in length and 50 nm in diameter) induced cell cycle arrest and apoptosis mediated by the generation of ROS, with significant dose- and length-dependent effects [**Ma *et al.* 2014**]. Similar results were obtained with human pancreatic adenocarcinoma Panc-1 cells (NWs of 6.5 μm in length

and 215 nm in diameter). We hypothesize that, in our case, the fact of being arranged in a nanostructured array, in which individual wires cannot be internalized by cells, significantly improved cell responses. Additionally, our NWs typically present more biocompatible dimensions, including shorter lengths and wider diameters than those reported in some toxicity studies with Ni NWs.

As more appropriate results were obtained with Au samples considering the particular purpose of this thesis, these specific nanoelectrodes are being considered for the fabrication of the neural bypass proposed. In addition, besides their intrinsic interest as advanced platforms for neural stimulation and recording, this type of NWs could be advantageous to be incorporated into other kind of devices for different applications in biomedicine. For instance, similar Au NWs arrays (also grown by template assisted-electrodeposition but using an anodic aluminium oxide template) have been described as highly efficient platforms for the capture and electrochemical release of circulating tumour cells after being biofunctionalized [**Zhai *et al.* 2017**]. Also related to potential applications in oncology, silicon NWs (150 nm in diameter and 2.6 μm in length) decorated with Au are being explored as highly efficient near-infrared (NIR) hyperthermia and photothermal agents for cancer treatment [**Convertino *et al.* 2018**]. Finally, NWs of other materials apart from metallic elements have been investigated for the modulation of neuronal activity. Concretely, free-standing single coaxial silicon NWs grown in the presence of atomic Au diffused on the NW surface (where Au nanoclusters were used as a catalyst in a chemical vapour deposition) enhanced the photoelectrochemical process involved in the stimulation of action potentials in primary rat dorsal root ganglion neurons [**Parameswaran *et al.* 2018**]. The versatility of our fabrication system allowed us for the configuration of biocompatible NWs in the shape of flexible millimetre size arrays as well as individual electrodes if

needed, so they can be customized and envisioned for a plethora of biomedical applications.

Finally, we detected spontaneous and repetitive calcium events when fNPCs were cultured onto PDMS substrates. Calcium is an intracellular messenger present in many kinds of cells, including neural cells. It is located in the cytoplasm (both bound to intracellular proteins and as free ions, being the free ones those which are active and can interact with calcium indicators) and within intracellular compartments, such as the endoplasmic reticulum and the mitochondria. Its intracellular concentration is maintained in the cells thanks to different mechanisms, including influx and efflux of this ion through different kind of receptors (such as ionotropic glutamate receptors), channels (voltage-gated calcium channels) and ion exchangers, among others. It has been also demonstrated that transient rises in intracellular calcium concentration are associated with electrical events due to neural networks activity (e.g., an action potential generation can cause an increase in cytoplasmic calcium concentration, by facilitating calcium influx through voltage-gated dependent calcium channels activation) [**Grienberger and Konnerth, 2012**]. Taking everything into consideration, we demonstrated that these cells were active after 14 DIV on PDMS samples. However, further experiments involving the use of pharmacology should be performed to corroborate our results as well as to robustly confirm that all the ROIs that we have selected for the analysis corresponded to neurons (such as tetrodotoxin application, which is a very well known blocker of voltage-gated fast sodium channels, responsible for the generation of action potentials) and not to astrocytes, that are also present in this kind of primary cultures, but to a lesser extent.

6.2. GDMs: rGO Foams and Microfibers

As an alternative to nanostructured metallic interfaces, previous studies of our laboratory pioneered the implantation of rGO 3D scaffolds (foams and MFs) after an incomplete cervical SCI for neural repair. Results at subacute and early chronic phases after implantation demonstrated the capacity of these structures to facilitate spinal tissue restoration without causing toxic responses neither local nor systemically in any case [**López-Dolado *et al.* 2015 and 2016; González-Mayorga *et al.* 2017**]. Indeed, first signs of neural tissue restoration at the lesion epicentre were evidenced by the detection of few but distinguishable neural components in the inner part of the rGO foams [**López-Dolado *et al.* 2015 and 2016**] and in the close proximity of the MFs [**González-Mayorga *et al.* 2017**]. Importantly, these neural components were supported by vascular structures at the lesion site in all the cases. Encouraged by these positive findings, we herein specifically examined the regenerative potential of these platforms when chronically interfaced with the cervical hemisected spinal cord after four months of implantation [**Domínguez-Bajo *et al.* 2019 and 2020**].

Initial characterization of both materials showed adequate features for the long chronic implantation at the injured spinal tissue. On the one hand, the highly porous nature of rGO foams allowed the infiltration of different kinds of cells and ECM components. Comparatively, a diverse variety of 3D scaffolds have demonstrated this capacity when explored for spinal cord treatment in different animal models, such as block copolymers of PLGA and PLL implanted in non-human Old-World primates [**Slotkin *et al.* 2017**], among many others. Rather than random porosity, the alignment of the porous structure in the shape of inner channels to provide certain guidance for tissue ingrowth was also pursued in some other approaches, such as in PCL microchannel scaffolds made by Shahriari *et al.* **[2017],** PLGA scaffolds fabricated by Pawar *et al.* **[2015]**, rGO scaffolds explored by López-Dolado *et al.* **[2015]**, and HA hydrogels

produced by Wen *et al.* **[2016]**. In this thesis, as the use of hierarchically ordered channels did not provide evident advantages [**López-Dolado *et al.* 2015**], rGO foams were alternatively fabricated as 3D scaffolds with random porosity to allow the necessary transversal regrowth of neurites required for intraspinal circuits restoration (which include the participation of IINs). Directionality in neural tissue regeneration can be also imposed by using more permissive architectures such as MFs or nanofibers [rGO microfibers - **González-Mayorga *et al.* 2017**; aligned poly (ε -caprolactone-co-ethyl ethylene phosphate) nanofibers - **Nguyen *et al.* 2017**]. In this thesis, rGO MFs were also investigated to guide the regrowth of neural tracts within the spinal cord tissue in desired directions (*e.g.,* rostral-to-caudal). Characterization studies revealed that the surface topography of the MFs had a certain degree of roughness, which was hypothesized to facilitate, along with the adsorptive properties of rGO, the adhesion of molecules and cells. The rGO MFs fabricated in this thesis presented a rougher surface than the ones previously reported by the group [**Serrano *et al.* 2018; González-Mayorga *et al.* 2017**], likely due to the use of a different source of GO flakes (a home-made synthesis by the Hummers' modified method *vs.* a commercial source). FTIR measurements confirmed the presence of oxygenated graphene, in agreement with the characterization carried out by other groups for this type of rGO-based materials [**Guo *et al.* 2016**]. On its turn, Raman spectroscopy allowed to confirm a uniform distribution of rGO along the MFs analysed.

After thorough characterization, we next proceeded with the implantation of both rGO scaffolds to specifically examine their regenerative potential when chronically interfaced with a cervical incomplete SCI in rats. Precisely, our SCI model of selection consisted of a right hemisection at C6 level. In this model, animals present affectation of both hindlimbs and the right forelimb (ipsilateral to the lesion) because of the loss of neural circuits at the

lesion epicentre. Nonetheless, while the RFP remained chronically damaged, both hindlimbs quickly recovered to an almost undamaged state [**López-Dolado *et al.* 2013**]. Regarding the choice of SCI model, the majority of studies found in the literature use SCI models based on low thoracic (T8-T10) injuries [in the area comprised by/or next to T8: **Kubinová *et al.* 2015; Fan *et al.* 2017**; T9-T10: **Chen *et al.* 2015; Yang *et al.* 2017; Hong *et al.* 2020**; T10-T11: **Shin *et al.* 2018**], followed by cervical [C4-C5: **Pawar *et al.* 2015**; C2: **Bonnet *et al.* 2020**], and lumbar [L1: **Kim *et al.* 2018**] ones. Indeed, most works comprise complete transections [**Chen *et al.* 2015; Yang *et al.* 2017**], although hemisections [**Kubinová *et al.* 2015; Pawar *et al.* 2015; Shin *et al.* 2018**] contusion compression models [**Hong *et al.* 2020; Wang *et al.* 2020]** and compression models **[Pakulska *et al.* 2017**] are also being explored. For more details about the different SCI models used in research, as well as information on the diverse animal models explored in the study of this pathology, including small mammals (such as mice) as well as large animal models (such as pigs and non-human primates), please refer to elsewhere [**Permuy *et al.* 2020; Talac *et al.* 2004**]. At this point, it is important to note that direct correlations between experimental SCI studies are not straightforward as many differences arise from the level of injury, the injury size and subsequent amount of remaining neural tissue and the animal model of selection (*e.g.,* different muscle and organ affectation followed by different patterns of recovery).

Moreover, the tests selected for the evaluation of locomotor recovery cannot be used indistinctly but largely depend on the level of injury. For example, for thoracic models, where the main affectation occurs in hindlimbs, the Basso, Beattie and Bresnahan (BBB) locomotor test [**Basso *et al.* 1995**] is the one of choice. In cervical models like ours, this test would not be useful though, being behavioural tests more suitable as they focus on the assessment of forepaws use and overall performance. To this regard, in this thesis, two

different tests involving the specific use of forelimbs during rat spontaneous behaviour were selected as screening tests to identify impairments caused by the implants: forelimb asymmetry and grooming tests. Both tests are quite comparable to the clinical tools used to evaluate functional independence for daily activities in SCI patients [**Itzkovich *et al.* 2018**]. Indeed, the subacute and chronic functional impairments caused by the unilateral hemisection practised agreed with previous findings in cervical SCI models [**López-Dolado *et al.* 2013; Filli *et al.* 2011**]. Interestingly, all animals (regardless the presence of the implant) spent the same amount of time being active during both tests, which could be a sign of the absence of major distress or pain caused by the rGO substrates. Regarding rGO foams, the material did not worsen behavioural outcomes with respect to injured animals without implants. Interestingly, it seemed that rGO-MFs tended to decrease differences between control and implanted rats to a higher extent than rGO foams. Firstly, this was detected based on the use of the LFP and simultaneous leaning of both forepaws in asymmetry tests. Secondly, grooming tests indicated a tendency towards improved recovery of the motor ability of the RFP, although it was not statistically significant. In any case, we did not discard additional minor motor behavioural improvements also occurring, as studies regarding upper limbs in humans evidence that clinical tests may fail discriminating more discrete functional changes [**De los Reyes-Guzmán *et al.* 2010**]. More specific tests to evaluate motor forelimbs activity at further time points are necessary to demonstrate that the presence of these scaffolds can significantly improve right forelimb mobility. Among them, the limb grip strength test could be used to evaluate the affected forelimb strength with time [**Anderson *et al.* 2009**] (similar to handheld dynamometry testing used in human patients [**Sisto and Dyson-Hudson, 2007**; **clinical trial gov identifier: NCT04265560**]). Furthermore, the horizontal ladder test, to evaluate all limbs coordination and how animals grab the rungs [**Ahmed *et al.* 2019**], and the CatWalk system for gait analysis

[**Hamers *et al.* 2006; Kappos *et al.* 2017**], to obtain more detailed quantitative information about possible impairments in the affected paws and deficits and improvements in animal locomotion over time, would be useful as well. For more information on behavioural tests used for the functional evaluation after SCI in animal models, please refer to elsewhere [**Ahmed *et al.* 2019**].

Motor function outcomes are commonly assessed when biomaterials are implanted at the injured spinal cord. In this thesis, rGO materials did not worsen (when compared to injured animals without scaffolds) and tended to decrease behavioural differences (with respect to uninjured control animals) without any kind of functionalization after four months of implantation. A significant number of works have demonstrated improvements in locomotor activity at different time points and in diverse experimental models. But, in contrast to our case, the great majority of these implants were included as combinatorial therapies. For example, biomaterials combined with a wide diversity of cells, such as NSCs [**Wang *et al.* 2020**] and MSCs [**Li *et al.* 2017**], are two of the most largely explored. Indeed, more than one cell type can be used simultaneously, such as in work by Yang *et al*. [**2017**], where Schwann cells were seeded in combination with bone marrow-derived MSCs. In these approaches, biomaterials are commonly used to facilitate cell delivery and improve the viability and integration of cells by protecting them and supporting their growth. As their implantation has shown promising results for neural repair, this strategy is receiving considerable attention in clinical trials. Some examples of already approved clinical trials between phases I/II, which are recruiting patients or enrolling them by invitation, include the use of collagen scaffolds loaded with MSCs [**NCT02510365**], with NSCs [**NCT02688049**] and bone marrow mononuclear cells [**NCT02688062**], as well as autologous implants from peripheral nerves in combination with olfactory glial cells from the patient's OB [**NCT03933072**]. However, little is known about the

mechanisms through which transplanted cells promote repair and mediate functional improvements [**Assinck *et al.* 2017**]. Moreover, cell transplantation retains some important drawbacks like tumorigenic potential and absence of preclinical results at long chronic stages. Nonetheless, efforts are being done by the research community to address these issues [**Assinck *et al.* 2017**].

Other strategies for combinatorial therapies with biomaterials include the incorporation of different factors, such as growth and neurotrophic factors [EGF and bFGF - **Grulova *et al.* 2015;** bFGF - **Chen *et al.* 2015;** BDNF and NT3 - **Li *et al.* 2016;** functionalized with an epidermal growth factor receptor antibody - **Xu *et al.* 2017**; NT3 - **Rao *et al.* 2018**], drugs such as methylprednisolone [**Zhang *et al.* 2018**], inhibitory components of the glial scar [**Pakulska *et al.* 2017**], Au nanoparticles [**Papastefanaki *et al.* 2015**], and brain decellularized ECM elements [**Hong *et al.* 2020**]. In fact, many of these studies combine several of these strategies in the same implant. Despite important progress, there is still controversy in the identification of the best way of administration and anchorage of these molecules in order to guarantee persistence of their effects over time.

It is also important to mention that, in this thesis, experimental groups included healthy rats (uninjured), hemisected rats not carrying any implants and hemisected rats with implants (either rGO foams or rGO-MFs). In this last case, a gelatin hydrogel group was not included because previous studies demonstrated stability of gelatin hydrogels in PBS at 37 °C for only two months [**González-Mayorga *et al.* 2017**]. We then hypothesized even shorter hydrogel degradation *in vivo*, and then just a temporal presence of this material at the lesion site in the whole period of investigation. Nonetheless, recent work with collagen scaffolds has demonstrated the variable influence that this material might exert in relevant parameters for neural repair [**Fan *et al.* 2017**], from negligible to significant contributions. Taking these aspects into consideration,

this experimental group will be included in future studies to discriminate the exact contribution of the gelatin supportive matrix on the obtained results. In any case, it is important to highlight the fact that, contrarily to other tissues such as peripheral nerves and skin, there are not reference biomaterials for SCI studies. Indeed, the number of different materials that have been and continues to be explored for neural regeneration in the spinal cord is large and increasing, with promising results in many cases. This matter complicates comparisons and conclusions on the selection of the best biomaterials when biological responses to their implantation are compared.

Another important parameter to discuss is the time from injury at which biomaterials are implanted. In our case, as in most of the works referenced in this thesis, implants are placed at the lesion cavity right after injury. Nevertheless, biomaterials can be also applied sometime after injury, as performed in work by Chen *et al.* [**2015**; 5 days after SCI, subacute phase] and Wang *et al*. [**2020** – 1 week after SCI, subacute phase]. This second approach will be considered for future studies in our laboratory, as it might be closer to the clinical application of biomaterials in a larger number of scenarios. Specifically, while acute application of biomaterials is contemplated in our model (although not necessarily simple at the clinical stage), their feasibility in chronic SCI patients (a major population target) implies a second injury for the removal of scarred neural tissue at the lesion site before biomaterial implantation [**Bradbury and McMahon, 2006**]. In this case, biomaterial proper integration within the injured tissue, which has been already reorganized after the initial injury, might be affected. From the clinical point of view, the selection of either one or the other approach would depend on the lesion severity and always ensuring patient constants stabilization and survival first. Indeed, most of the clinical trials which combine scaffolds and cells implantation previously mentioned, select patients who suffer from a chronic SCI with ASIA A without

significant further improvements for years of lesion [**NCT02688049; NCT02688062; NCT03933072**]. However, they do not specify the exact amount of time required since the injury. There is only one trial that recruited patients who presented no more than 21 days after the injury ["Classification ASIA A, occurring within past 21 days"; once patients have passed the spinal shock; **NCT02510365**].

After biomaterial implantation, one of the very first things to be considered for seamless integration is the absence of mechanical mismatch between the spinal cord tissue and the biomaterial. Contrary to lesions at the brain and likely related to its softer nature, injuries at the spinal cord typically result in irregular and diffuse boundaries with a varying degree of tissue damage among animals [**Moeendarbary *et al.* 2017**]. This softening is also significant outside of the lesion epicentre. These features, along with the uncertainty in delimiting lesion extension, add variability to the results obtained. In our case, this was more evident in injured rats without rGO scaffolds. Conversely, the presence of the rGO foam clearly assisted the structural stabilization of the spinal tissue by completely filling the lesion site, which diminished these phenomena. However, in the case of rGO-MFs implants, this requirement was not completely fulfilled as rGO MFs did not occupy the totality of the lesion epicentre once the gelatin hydrogel got dissolved. It should be noted that this fact is also a limitation to adequately compare results among studies. Specifically, most works distinguish between the inner part of the lesion and its borders, without specification of sub-regions within these two areas or distinction between rostral and caudal lesion stumps.

In order to obtain a more detailed mechanical characterization of the implant-spinal tissue interactions, AFM studies were performed in the case of rGO foams. As expected from damage in CNS tissues [**Moeendarbary *et al.* 2017**], the interface tissue showed a significantly lower Young's modulus than

the native spinal tissue. However, the lesion site carrying the foams displayed a significantly higher Young's modulus, even higher than the rGO foam before implantation. This was attributed to collagen deposition and massive cell infiltration within the foam. Importantly, this decrease in elasticity of the right hemicord holding the scaffold was not transmitted to the left counterpart spinal tissue, as its elastic response was found in range with the one found in the fresh spinal cord tissue. In the particular case of rGO-MFs, while the mechanical properties of the gelatin hydrogel where they were integrated were expected to be in range with those of the neural tissue, rGO-MFs were stiffer than both. The small dimensions of the rGO-MFs and their flexibility, measured as their bending ability (up to 105°) [**González-Mayorga *et al.* 2017**] were hypothesized to be responsible for not inducing significant fibrotic responses derived from eventual mechanical friction with the spinal cord tissue in comparison to injured rats. This mechanical compliance found by AFM was further corroborated by MRI studies for rGO foams. MRI images showed absence of both perilesional and compressive damage in surrounding spinal cord regions. Similar results are also expected for the rGO-MFs implant but further experiments should be done to confirm this hypothesis.

It is known that penetrating injuries at the spinal cord are typically characterized by a massive infiltration of cells at the lesion area, including the entrance of meningeal fibroblasts and other vascular components that partly come from the disruption of the meninges. It is also widely accepted that the existence of collagen, which in our case was present at the lesion epicentre and both interfaces in rGO foams and rGO-MFs, as well as other fibrotic and connective tissue elements, can be detrimental for neural tissue regeneration by scarring [**Dias *et al.* 2018**]. Unfortunately, the specific cellular origin of the cells and molecules that participate more actively in the formation of the fibrotic scar is still under controversy [**Dias *et al.* 2018; Soderblom *et al.* 2013; Loy *et al.***

2002; Zhu *et al.* 2015]. Nonetheless, it has been demonstrated that the progeny of a subset of pericytes (A pericytes) has a major role in the formation of the fibrotic component of the fibro-glial scar at the spinal cord and the participation in neural repair mechanisms [**Göritz *et al.* 2011**]. In an attempt to prevent this massive connective tissue infiltration and proliferation at the lesion, Alves-Sampaio *et al*. [**2016**] performed a duraplasty right after their MFs-based scaffold implantation. Contrarily to prior expectations, their results demonstrated that this surgical procedure negatively affected axonal growth at the lesion site. In our approach, we covered the lesion area with a piece of Neuro-Patch®, which is a fibred microstructured synthetic tissue based on polyesterurethane, as a suturable duramater substitution (as clinically done for human patients) [**Bamps *et al.* 2017; Holmström *et al.* 2018**]. It is hard to quantify how much the patch reduced the amount of infiltrating cells and ECM proteins from external tissues, but, at least, it diminished the adherence with muscle tissues located above (in eventual contact with the spinal tissue because of vertebra removal), which are an additional source of connective cells. Further research could be devoted to optimize rGO biomaterials features for a controlled decrease in the fibrotic component of this scar. In this sense, it was demonstrated that a moderate inhibition of A pericytes proliferation resulted in the formation of a smaller scar, which was able of promoting the appearance of a regenerative scenario for axonal regrowth [**Dias *et al.* 2018**]. Besides implants were rightly situated within the spinal cord, little cavities were found at the lesion epicentre and the interfaces. Moreover, reorganized tissue at the lesion site in the presence of rGO foams was more compact, as shown by histological and TEM images, in comparison to injured animals without implants. All these features further assisted the supportive function and structural stabilization of the lesion site described for these scaffolds. A tendency towards the reduction in the amount and size of lesion cavities have been also detected after the implantation of other biomaterials at different time points [**Fan *et al.* 2017;**

Oudega *et al.* 2019; Chen *et al.* 2015; Slotkin *et al.* 2017; Hong *et al.* 2020]. Again, most of biomaterials that caused this effect followed a combinatorial strategy for their fabrication, contrary to our rGO scaffolds that were not either functionalized or being used as carriers of any external therapeutic molecules.

Vascular remodelling for proper blood supply is essential for the regeneration of every damaged tissue [**Loy *et al.* 2002**]. This fact is even more important for supporting neural cells growth and development, because its absence is known as one of the major limitations after SCI [**Haggerty *et al.* 2018**]. For this reason, we specifically investigated the abundance of blood vessels at the lesion site by using RECA-1, commonly described in the literature for the identification of vascular structures after biomaterial implantation, and laminin. Results demonstrated that blood vessels were able to grow at the lesion site, comprising the inner part of the rGO foams and both I and MF areas related to rGO-MFs implants. Similar vascular remodelling findings appeared (after different time points of implantation) when methacrylate based hydrogels [**Chen *et al.* 2015**], biofunctionalized alginate scaffolds [**Grulova *et al.* 2015**], poly(2-hydroxyethyl methacrylate) scaffolds [**Kubinová *et al.* 2015**] and poly(glycolic acid) (PGA) scaffolds seeded with mouse NPCs [**Shin *et al.* 2018**] were implanted at the injured spinal cord. In this line, and sharing more similarities with our rGO-MFs implants in terms of shape and topographical guidance for tissue regeneration, satisfactory results for vascular remodelling were also found for PEDOT functionalized graphite MFs [**Alves-Sampaio *et al.* 2016**], aligned PLA MFs [**Hurtado *et al.* 2011**], and photocrosslinked gelatin methacryloyl MFs hydrogels [**Chen *et al.* 2019**].

Neural tissue regeneration was next studied by immunolabelling of neuronal cytoskeleton proteins. As expected, their presence at the lesion epicentre was dramatically affected by the injury practised, but still positive labelling for all markers employed was detected within rGO foams as well as in

the proximities of rGO-MFs. The pattern of positive labelling for the different markers did not coincide completely because antibodies used do not bind exactly to the same cytoskeleton neuronal components. For example, the predominant expression of β-III tubulin against other neurite markers (such as SMI311) was not surprising as, during mammalian and avian development, this protein is considered the earliest neuron-associated cytoskeletal marker [**Moody *et al.* 1989; Lee *et al.* 1990**]. Importantly, its expression is maintained in mature neurons and confers microtubules a more dynamic nature, likely related to neurites in the process of development and growth [**Panda *et al.* 1994**]. Another important detail is that some of the neural structures found within the rGO foams were myelinated (as demonstrated by TEM studies). This suggested the presence of certain amount of mature axons at this point. Neural spinal components regrowth and reorganization are the most evaluated parameters in studies comprising the use of biomaterials for SCI treatment. Other biomaterials implanted at the injured spinal cord with positive findings to this respect include poly(2-hydroxyethyl methacrylate) hydrogels [**Kubinová *et al.* 2015**], graphene-based nanoribbons [**Kim *et al.* 2018**], functionalized HA hydrogels [**Wen *et al.* 2016**], acellular spinal cord scaffolds encapsulated in a biofunctionalized thermosensitive hydrogel [**Xu *et al.* 2016**], polymeric PLGA scaffolds loaded with Schwann cells and MSCs [**Yang *et al.* 2017**], biofunctionalized collagen scaffolds [**Fan *et al.* 2017**], PCL scaffolds [**Shahriari *et al.* 2017**], PGA functionalized scaffolds loaded with hNPCs [**Shin *et al.* 2018**], electrically conductive polymers based on a plant-derived polyphenol, tannic acid and polypyrrole [**Zhou *et al.* 2018**], functionalized chitosan scaffolds [**Rao *et al.* 2018; Oudega *et al.* 2019**], microscale printed scaffolds loaded with NPCs [**Koffler *et al.* 2019**], PLGA scaffolds [**Pawar *et al.* 2015**] and poly(N-isopropylacrylamide)-PEG copolymers [**Bonnet *et al.* 2020**], among others. Moreover, additional studies with biofunctionalized HA scaffolds containing PLGA microspheres [**Wen *et al.* 2016**], porous scaffolds of PLGA and PLL

[**Slotkin *et al.* 2017**], PLGA scaffolds loaded with Schwann cells and MSCs [**Yang *et al.* 2017**], and functionalized collagen scaffolds [**Li *et al.* 2016; Fan *et al.* 2017**] also demonstrated the presence of myelinated components at the injured spinal area after different periods of material implantation [*ca.* 30 and 60 DPI - **Wen *et al.* 2016** and **Yang *et al.* 2017;** *ca.* 90 DPI - **Slotkin *et al.* 2017** and **Fan *et al.* 2017**].

Neuronal remodelling in the presence of implanted rGO biomaterials could have two hypothetical major origins: descending tracts and intraspinal circuits. The contribution of descending tracts to forelimb motor function is relatively well defined. It mainly includes the corticospinal tract (with origin in the brain cortex) and rubrospinal tracts (originated in the brainstem) [**Freund *et al.* 2012; Laliberte *et al.* 2019**]. One of our hypotheses is that the newly formed axons found within the rGO foams might have origin in brainstem nuclei, more largely devoted to forelimb rather than hindlimb motor neurons [**Esposito *et al.* 2014**]. The abundance of $VGluT2^{+}$ labelling in these neurites could agree with this brainstem nuclei origin, as glutamate (in particular the VGluT2 system) is the predominant transmitter pathway in the brainstem neurons responsible for excitatory motor commands [**Hägglund *et al.* 2010**]. These results support the hypothesis of rGO foams reinforcing intrinsic plastic adaptations in pre-existing reticulo-propiospinal connections after cervical injuries. However, there are important drawbacks regarding research on neural tracts regeneration by using animal models that need to be considered. First, it is not clear how the regeneration of neuronal components (and the sprouting of spared axons) contributes to functional recovery, mainly due to the fact that the proportion of fibres that regenerate is frequently small. Some groups have reported that regeneration percentages between 2 and 7% of corticospinal and rubrospinal tracts allowed improvements in animal motor outcomes [**Bradbury and McMahon, 2006**]. Thus, it is important to question whether this modest amount

of tract restoration is sufficient to support the functional ameliorations observed. Another issue relates to the limited distance that central axons can extend collaterals and regenerate. For example, in this thesis, the animal model was the Wistar rat, which has spinal segments of approximately 2 mm in length. In these animals, the distance that nervous terminals should travel to regenerate comprises few millimetres or even less. This leaves important concerns about the translation of results to real human patients where spinal segments are larger [**Bradbury and McMahon, 2006**]. For this reason, focus on the reorganization of intraspinal neural circuits which involve IINs (avoiding the regeneration of axonal tracts for long distances) has been extensively proposed as alternative pathways for neuronal recovery. As the injury practised in this thesis is performed at C6 spinal level, both supraspinal and intraspinal axons that innervate C7-C8 segments are interrupted. Based on behavioural results, we can speculate that implanted biomaterials could either allow or facilitate the sprouting of cervical propiospinal premotor neurons located in the C3-C4 segments above the lesion, that project to C7-C8 segments, as their potential to convey an internal copy of premotor signals to perform the forelimb skilled movements has been reported in rats, cats, monkeys and humans [**McCambridge *et al.* 2014, Azim *et al.* 2014**]. Indeed, there are two particular subpopulations of IINs at the spinal cord that provide glutamatergic inputs to the intraspinal circuits which can be related to neural tissue regeneration [**Laliberte *et al.* 2019**], what would also agree with the positive VGluT2 labelling found at this point. These subpopulations are V2a and V3 interneurons, related to left-right and general locomotor coordination. This explanation is consistent with the ability of interneurons included in intraspinal circuits to reroute in order to bypass the lesion. However, both hypotheses are speculative and should be addressed in future work by, for instance, anterograde and retrograde tracing, immunofluorescence against more specific tract markers, and diffusion tensor imaging techniques.

As it has been widely reported, any biomaterial implantation typically evokes an inflammatory reaction, which involves the recruitment of macrophages (among other inflammatory cells) to the lesion site [**Pires and Pêgo, 2015**]. In our case, slightly different results were obtained depending on the selected rGO scaffold. On the one hand, the amount of $ED1^+$ cells (likely accounting for M1-like –proinflammatory- macrophages) was significantly decreased at the lesion inside rGO foams after 4 months of implantation. In agreement with these results, conductive polymer hydrogels of a plant-derived polyphenol combined with tannic acid and polypyrrole also lowered these cells [**Zhou *et al.* 2018**]. On the other hand, rGO-MFs did not cause significant differences in the amount of $ED1^+$ cells at the lesion epicentre with respect to injured rats without implants. This means that the presence of rGO scaffolds did not exacerbate the inflammatory reaction caused by the injury itself in any case. Actually, macrophages were mainly found at the borders of the scaffolds. Similar results were described by Joo *et al*. with collagen implants [**2012**]. Additionally, other groups also reported the "not worsening" or mitigation of the inflammatory response after the implantation of copolymers of PLGA and PLL [**Slotkin *et al.* 2017**], even modulating the total population of macrophages to obtain a superior amount of those which favour the attenuation of the inflammation, such as demonstrated by Hong and colleagues [**2020**] with the use of a collagen-based implant combined with porcine brain decellularized ECM, among others. In this line, future efforts in our laboratory will focus on the specific activation of pro-regenerative immune responses using rGO-based biomaterials. In relation to glial cells, no astrocytes ($GFAP^+$ cells) were found colonizing either the internal parts of rGO foams or the close proximities of the rGO MFs. Finally, cells positively labelled for vimentin were abundant at both the lesion site and surroundings in both biomaterials. We hypothesize that this kind of cells might have a positive role at the lesion site, as vimentin is considered a marker of immature glial cells and NSCs [**Yabe *et al.* 2003**].

However, as vimentin is expressed in a wide variety of cells, more specific studies should be carried out to elucidate their real role in this case.

When focused on the surroundings of the lesion site, rGO implants were able to produce beneficial effects in the spinal tissue areas that extended beyond the lesion epicentre. Regarding RECA-1^{+} components, our rGO biomaterials did not alter the mature vascularization of the neural tissue in none of the areas analysed out of the lesion core. These preserved structures could necessarily facilitate vascular remodelling at the lesion site. Interestingly, when the analyses were focused on laminin, a noticeable increase of this marker was evident at both rostral and caudal interfaces in all injured animals, as a possible indicator of augmented angiogenesis at this point. Nonetheless, this increment was less pronounced in all implanted animals in comparison to injured animals without implants. Based on these results, we can speculate that rGO implants could have a role in the facilitation of the maturation of new vascular structures at the lesion site and interfaces of the injured spinal tissue. However, apart from being a major component of the blood vessels basal lamina [**Burnside and Bradbury, 2014**], laminin is produced by a wide variety of cells within the CNS, such as astrocytes and pericytes, among others. By interacting with its receptors, laminin is involved in many processes such as angiogenesis, CNS cells adhesion, migration, differentiation, neurite outgrowth, and even inflammatory cells infiltration [**Nirwane and Yao, 2018; Simon-Assman *et al.* 2011**]. For instance, it has been reported that laminin secreted by astrocytes forming the glial scar might support axonal growth and guidance [**Frisén *et al.* 1995**]. For this reason, we can also hypothesize that the presence of this protein at the lesion interfaces could assist neural components regeneration. As expected, neural components were also severely affected at both interfaces in all injured animals, but their loss was not aggravated due to the presence of the implants. In addition, neuronal structures were largely preserved regardless the

implant at certain distance from the lesion epicentre (PL12). When focused on macrophages, their presence was significantly decreased at the rostral interface and perilesional areas in animals receiving rGO foams, whereas no changes were observed in those implanted with rGO-MFs when compared to injured rats without scaffolds.

The presence of astrocytes was restricted to the interface areas after the implantation of both scaffolds. In fact, there were no evidences of significant penetration into the rGO foam or the lesion site in rGO-MFs. These results agree with previous findings by Slotkin *et al*. [**2017**], Raspa *et al*. [**2016**], Alves-Sampaio *et al*. [**2016**] and Hong *et al*. [**2020**], where astrocytes were retained at the borders of the scaffolds and rarely migrated to the lesion epicentre. In agreement with the tendency observed in our rGO-MFs implants, some other biomaterials based on MFs [**Chen *et al.* 2019; Joo *et al.* 2012; Reis *et al.* 2018; Sugai *et al.* 2015**] and other material strategies [**Kim *et al.* 2015; Fan *et al.* 2017**] also led to a decrease in the presence of astrocytes at the injury site. On the contrary, Hurtado *et al*. [**2011**], and Koffler *et al*. [**2019**] found astrocytes in close contact with the inner parts of the implanted biomaterials and regenerating neuronal structures. In the vast majority of works, the presence of astrocytes at the lesion area was related to the formation of the fibro-glial scar. The main function of this scar is to limit and restrain the inflammatory response derived from the trauma and materials implantation [**Barnabé-Heider *et al.* 2010**]. Specifically, it has been described that astrocytes which take part in the scar formation have two different cellular origins. They can be either pre-existing astrocytes that migrate and reorganize at this point or ependymal cells-derived astrocytes [**Barnabé-Heider *et al.* 2010**]. However, this second group is GFAP negative [**Meletis *et al.* 2008**], so, in this thesis, astrocytes identified as $GFAP^+$ cells should belong to the first type. Nonetheless, the understanding of this scar as an impediment for neural tissue regeneration has been recently discarded,

because neither preventing astrocyte scar formation nor removing chronic astrocyte-based scars lead to spontaneous regeneration of nervous terminals [**Anderson *et al.* 2016; Göritz *et al.* 2011**]. Moreover, astrocytes are the most abundant non-neuronal highly differentiated cells in the CNS [**Nathan and Li, 2017**]. Indeed, it has been demonstrated that astrocytes are more abundant in the developing spinal cord than in the brain [**Yoon *et al.* 2017**], so using them as a target to facilitate neural repair might provide valuable benefits in neural tissue engineering. Importantly, astrocytes actively participate in synapse functioning, formation and modulation [**Allen and Eroglu, 2017; Clarke and Barres, 2013; Lee and Chung, 2019; Chung *et al.* 2015**]. For example, although further work is required to determine how this astrocyte-based modulation occurs, it has been demonstrated that, in the absence of astrocytes, motor neurons had more inhibitory synapses but fewer excitatory ones. This indicates that astrocytes are needed to support the appropriate formation and maintenance of both types of synapses within the spinal cord [**Tsai *et al.* 2012; Clarke and Barres, 2013**]. Furthermore, it has been proved that transplantation of astrocytes derived from embryonic glial-restricted precursor cells and induced by the bone morphogenetic protein promoted extensive axonal growth and motor function recovery in a rodent SCI model by the secretion of a protein called periostin [**Shih *et al.* 2014**]. Finally, it has been also reported, although only in *in vitro* studies yet, that astrocytes in the brain parenchyma have an intrinsic ability to generate neurons under favourable conditions [**Magnusson and Frisén, 2016**]. The mechanisms behind this process are still unknown, as well as their eventual contribution to functional recovery. Taking together, it seems reasonable to devote further research to have a better control over the migration and permanence of astrocytes both at the lesion border (but preventing the chronic presence of the glial scar) and in close contact with the neuronal structures located within the lesion epicentre at certain time frames of SCI recovery still to be determined.

Biodegradation of implantable devices is an attractive feature frequently pursued [**Campana *et al.* 2014**]. Regarding GDMs, recent *in vitro* work with human myeloperoxidase and degranulating neutrophils pointed out towards graphene not to be biopersistent [**Kurapati *et al.* 2018**]. Indeed, *in vitro* experiments demonstrated that human-neurophils-derived myeloperoxidase was able to biodegrade GO sheets dispersed in water but failed to metabolize more aggregated GO sheets [**Kurapati *et al.* 2015**]. Additional *in vitro* experiments demonstrated that products from GO degradation by myeloperoxidase dependent mechanisms were non-genotoxic when evaluated on a human bronchial epithelial cell line [**Mukherjee *et al.* 2018**]. Furthermore, Bianco and colleagues [**Kurapati and Bianco 2018**] showed that another enzyme known as DNAzyme, which also presents peroxidase activity, was able to perform the *in vitro* degradation of highly-water dispersible GO sheets, and this mechanism was also hypothesized to work for the biodegradation of other GDMs, such as rGO. Based on these results, we hypothesize that the biodegradation of our rGO materials can be occurring *in vivo* and is largely dependent on the initial disassembly of the rGO sheets from the main scaffolding structure with time. However, further experiments need to be performed to confirm this hypothesis.

Graphene degradation processes mediated by peroxidase activity have been also studied in other organisms such as white rot funghi [**Peng *et al.* 2020**]. However, the vast majority of studies regarding GDMs degradation have been done *in vitro.* Thus, *in vivo* scenarios to validate these results should be explored [**Martin *et al.* 2019**]. In fact, there are no reports to date demonstrating any cues of graphene degradation when implanted at the CNS. In this thesis work, preliminary insights into the biodegradation of the rGO foams at the injured spinal cord were presented. Specifically, TEM was used to identify both dissociation and biodegradation features in the rGO foams implanted.

Qualitative changes in the degree of compaction of rGO sheets on the foam walls were first evidenced. Augmentation in the wall thickness, as well as fading of the area occupied by these structures, was noticed over time. The observed shift of black pixels to lighter values was attributed to the progressive disassembly of rGO sheets in the foams, while the shift of white ones to darker pixels correlated with an increase in the degree of tissue ingrowth within the foam. In any case, further quantitative studies by techniques such as nuclear magnetic resonance (NMR) and Raman spectroscopy might be helpful to identify chemical changes in rGO compatible with biodegradation processes. Preliminary studies in our laboratory by XPS, IR spectroscopy and microscopy failed to detect any chemical changes undoubtedly attributed to biodegradation at the injured spinal cord (data not shown). In this process, action by enzymes and phagocytic immune cells seems pivotal for rGO sheets biodegradation [**Kurapati *et al.* 2018**]. It is worth noting that Li *et al.,* [**2014**] demonstrated that GO degradation could be prevented by its functionalization with PEG and bovine serum albumin, demonstrating that biofunctionalization can influence GDMs degradation, what should be considered for future experiments.

Besides biodegradation of GDMs, mechanisms of cellular uptake for graphene nanomaterials remain also unclear. Previous *in vitro* findings evidenced the entrance of 350 nm graphene flakes by active filopodia of macrophages, while larger ones (2 μm) were able to directly trespass cell membranes perpendicularly [**Yue *et al.* 2012**]. In a different work, 500 nm-sized GO flakes were confirmed to enter by clathrin-mediated endocytosis and larger ones (1 μm) underwent phagocytosis in C2C12 mouse MSCs *in vitro* [**Mu *et al.* 2012**]. Notwithstanding, a more detailed examination of these processes should be performed in further research.

Considering that impairments in the proper functioning of the rat organism could occur as a result of the possible disassembly of rGO sheets

fragments from the rGO scaffolds and their posterior entrance into the bloodstream, the presence of signs of systemic damage was also evaluated. Previous work with GDMs demonstrated accumulation and eventual organ toxicity signs after GO injection in the bloodstream [**Wang *et al.* 2011; Zhang *et al.* 2011; Liu *et al.* 2012**]. For instance, GO nanosheets dispersions at different doses (*i.e.*, 0, 0.1, 0.25 and 0.4 mg) were administered via a single tail injection in mice [**Wang *et al.* 2011**]. Animals were sacrificed after 1, 7 and 30 days. Results showed that doses below 0.25 mg did not cause obvious toxicity signs, whereas 0.4 mg dose injection resulted in the death of animals since the first time point evaluated. GO sheets mainly accumulated in the lungs, but they were also evident in liver, kidneys and spleen. In another work [**Zhang *et al.* 2011**], GO nanoparticles were also injected intravenously at a concentration of 1 and 10 mg kg^{-1} in Sprague-Dawley rats. Signs of toxicity were clearly identified after 14 days for the highest dose injected, such as pulmonary oedema and granuloma formation because the majority of GO particles were intercepted and accumulated in the lungs, especially those with larger sizes. Some particles were also detected in liver and spleen. No impairments were seen in animals receiving 1 mg kg^{-1} injection. Liu *et al*. [**2012**] showed that GO particles of different sizes (from 100 nm to 5 μm) and intravenously injected at 1 mg kg^{-1} were internalized in lungs and liver. Interestingly, the biodistribution of these GO particles differed according to their size. Specifically, small nanoparticles preferentially accumulated in the liver, while larger nanoparticles were trapped in the lungs. Moreover, when the dose of small GO nanoparticles was incremented (from 1 mg kg^{-1} up to 10 mg kg^{-1}), an increase of pulmonary uptake within the lungs was observed, accompanied by a decrease in liver accumulation. In our case, rGO nanosheets were assembled forming either the walls of rGO foams or, even more compactly, rGO-MFs, instead of being dispersed in solution as in the works mentioned above. Moreover, the implants used in this thesis were directly placed within the spinal cord instead of being

injected intravenously into the blood flow. These two pivotal facts make more difficult the massive liberation of rGO nanosheets into the blood circulation system. However, this event could eventually happen to a minor extent, for instance, by direct disassembly of rGO biomaterials during implantation surgery or chronic degradation phenomena. Importantly, in our case, no major signs of distress were either detected during pain monitoring, behavioural tests or major organ weight ratios measurements. Thorough histological and TEM studies for rGO foams did not show alterations in major organs either. Nonetheless, further studies at longer time points of implantation are required to discard systemic toxicity of these materials and their degradation by-products at the long-term. For more detailed information about graphene biodegradation and toxicity, please refer to recent and complete reviews in the topic [**Fadeel *et al.* 2018; Peng *et al.* 2020**].

As a final remark, it is worth noting that one of the most outstanding properties of the rGO biomaterials evaluated in this thesis is their capacity to favourably act on several features of SCI without any further functionalization other than the one provided by the own chemistry of the rGO nanosheets used. In this sense, few works have demonstrated satisfactory results by using non-biofunctionalized scaffolds. For instance, Bonnet and colleagues [**2020**] injected a poly(N-isopropylacrylamide)-PEG copolymer in the hemisected left C2 cervical spinal cord. In this case, lesion comprised just one cut, without removing the fragment of spinal tissue as in the injury model chosen in this thesis, and then facilitating regeneration processes. An early attenuation of the immune response measured as cytokine levels (at 15 DPI), as well as improvements in behavioural outcomes (up to 90 DPI), were demonstrated. Furthermore, regenerating axons were visualized within the implant, with little glial cells colonization. In another work, PLGA scaffolds were implanted after cervical hemisection with neural fragment removal at C4-C5 level in transgenic

mice [**Pawar *et al.* 2015**]. Neural components at both rostral and caudal interfaces, as well as within the implant, were detected at 75 DPI. A decrease in the amount of macrophages was observed as well. These effects were hypothesized to translate into the motor improvements detected at the end of this period. Finally, Slotkin *et al*. [**2017**] implanted highly porous scaffolds composed of PLGA and PLL in the T9-T10 hemisected spinal cord of African Green monkeys, in combination with motor training based on treadmill sessions. A thorough functional analysis was then fulfilled with simultaneous electromyography recordings until 90 DPI. Animals demonstrated improvements in locomotor activity. Moreover, an increase in remodelled tissue, along with a decrease in vacuolation, was found at the injury site. Importantly, material implantation favoured the presence of neuronal components within the lesion epicentre, along with a decrease in $GFAP^+$ cells. All together, these works showed promising results after the implantation of chemical and structurally different biomaterials to those described in this thesis, at different time points and by using different animal models of SCI. Nonetheless, in none of those studies, favourable responses found were as complete as the ones induced by rGO foams described in this thesis work. Besides behavioural, vascular, immune and neural improvements already described, individually or in combination, by these and other works, fulfilment of mechanical compliance requirements with the spinal tissue and beneficial effects of implants in perilesional damage as observed by MRI were never described before by any biomaterial implanted at the injured spinal cord. Further studies including the combination of these rGO platforms with biofunctionalization strategies and motor training protocols can be envisioned as a promising avenue to continue this work and make a significant impact in the SCI therapeutics field.

7. CONCLUSIONS

Regarding *in vitro* biocompatibility studies of flexible, metallic and nanostructured arrays, we can conclude that:

1. Both nanostructure and chemical composition, alone and/or in combination, play a major role in the interaction of embryonic cortical neural cells with nanostructured electrode arrays. Particularly, nanostructured Ni electrodes increased neural cell survival, boosted neuronal differentiation and reduced glial cells with respect to their flat counterparts. On the contrary, for Au-based substrates, which were more advantageous in terms of neuronal development and cell viability, nanotopography seemed to have negligible effects on these parameters.

2. Based on the biocompatibility results obtained, Au electrode substrates have been preferentially selected for further experimental research within the ByAxon project in order to design a flexible device able to act as a bypass when interfaced with the injured spinal cord.

3. fNPCs were active (in terms of being able to produce intracellular calcium elevations) after 14 DIV when cultured on PDMS, showing good *in vitro* biocompatibility results in case PDMS is needed to cover Au-NWs in the fabrication of the final device for further *in vivo* experiments.

Regarding *in vivo* biocompatibility and neural regeneration capability of rGO foams and rGO-MFs in an experimental model of SCI in rats, we can conclude that:

1. Both rGO-based biomaterials mediated neural and vascular components regeneration at the lesion epicentre in the absence of any additional biological functionalization or therapeutic drug loading. rGO scaffolds allowed nervous terminals growth either within the foams or in the close proximities of the MFs, which in turn were assisted by RECA-1 positive blood vessels indicative of vascular remodelling.
2. None of these rGO scaffolds worsened the inflammatory response caused by the injury itself. Specifically, a decrease in the amount of macrophages was evidenced due to the presence of rGO foams, whereas rGO-MFs did not exacerbate inflammatory reactions after their chronic implantation.
3. Neither signs of systemic toxicity in major organs, nor impairments in animal spontaneous forelimbs use were found due to the implantation of these rGO-based scaffolds.
4. Ultrastructural changes in rGO foams, possibly due to the initiation of biodegradative processes of the rGO sheets conforming the scaffolds, were evidenced by TEM analysis for the first time at the rat injured spinal cord *in vivo*.
5. AFM and MRI findings demonstrated that rGO foams implantation supported the stabilization of the injured spinal cord without causing any mechanical damage to the contralateral hemicord and decreasing perilesional areas of gliosis both above and below the lesion epicentre.

8. FUTURE WORK

8.1. Complementary ongoing work and future directions regarding nanostructured electrode arrays

In vitro biocompatibility results regarding nanoelectrode arrays, especially Au platforms, encourage further investigation for their use in the fabrication of an implant able of working as a local bypass at the spinal cord. Ongoing research in our laboratory includes additional calcium imaging experiments of neural cells cultured on Au substrates fabricated with both polycarbonate and alumina templates. These tests will allow us to detect calcium transient elevations in order to confirm whether neural networks formed on the nanostructured electrodes at different time points are active, and the functional implications of such substrates on neural activity. Regarding *in vitro* biocompatibility, studies to assess whether the selected electrodes could provoke non-desired changes in the ionic properties of the extracellular medium will be also performed. Core/shell Ni/Au nanoelectrodes are also under investigation *in vitro*. Additionally, preliminary *in vivo* biocompatibility tests have started including the implantation of the nanostructure electrode arrays with the most satisfactory *in vitro* performance at the injured spinal cord of adult Wistar rats.

As future directions, nanostructured electrodes grown by using alumina templates will be examined in more detail. This second type of templates allows a better control of topographical parameters, such as NW size (diameter and length) and interdistance. Thus, these experiments will be useful to know whether NWs organization on the arrays can influence neural cells development and behaviour at different time points (from 2 weeks to even months). Furthermore, *in vitro* studies of electrical stimulation of neural cells through the most biocompatible nanostructured electrodes fabricated will be

initiated to examine their performance as interfaces for neural cells/tissues stimulation in terms of calcium-transients visualization.

8.2. Complementary ongoing work and future directions regarding rGO scaffolds for traumatic SCI

In view of the encouraging findings described in this thesis, these rGO-based biomaterials deserve further investigation as useful implantable platforms to mediate neural repair at the injured spinal cord. Ongoing work in the laboratory includes the incorporation of rehabilitation programmes based on locomotor training applied to SCI rats receiving rGO implants. Preliminary results have already demonstrated improvements in behavioural outcomes of rats exposed to treadmill routines. In this sense, it has been hypothesized that the neural recovery associated to the application of motor training protocols is facilitated by the reorganization of intraspinal circuits thanks to the sensory feedback from areas below the injury.

As it has been exposed, ideal SCI treatment should follow a combinatorial approach for the simultaneous targeting of the different spinal tissue processes affected. In this line, one could take advantage of the oxygenated groups already present in rGO for its functionalization with different drugs and factors (such as growth factors including neurotrophins). The main aims of this functionalization would be: to increase the number of neuronal components within the lesion epicentre, to minimize the chronic presence of the fibro-glial scar surrounding the implant, to modulate the immune response at chronic stages, and to facilitate the presence of astrocytes within the lesion site for the recovery of the native spinal tissue. Other than functionalization, future directions of this work also include the study of the origin of the new neural components found at the lesion site. Specifically, neuronal tracing (*e.g.* retrograde tracing to know the precise neuronal pathway to what the nervous terminals found within the implant belong) and diffusor tensor imaging (to check whether newly formed axons are able to cross the injury gap from one stump to the other to bridge the lesion) will be explored.

Moreover, further TEM and immunofluorescence studies would be helpful to examine axonal myelination and the formation of new synapses over time (*e.g.* synaptophysin). To this respect, the use of transgenic mice and rats with concrete axonal tracts (*e.g.* rubrospinal tract) marked could be considered. Indeed, in order to assess if neuronal components found at the lesion site belong to new functional neural networks, electrophysiology experiments could be performed. For example, electrical or magnetic stimuli could be applied to the cerebral motor cortex of the animals and the evoked responses in the affected muscles (*e.g.* TB) measured. Following with functional outcomes, more behavioural tests involving the use of the affected forepaw could be performed, such as the grip strength tests, to study the impact of biomaterial implantation in TB functionality over time. Other useful tests could be the horizontal ladder and Cat-Walk to identify potential improvements in motor coordination due to the presence of the rGO scaffolds. At muscle tissues, histological and proteomics analysis could be done to investigate signs of muscular atrophy of the affected forepaw and its eventual reversion. Vascular reorganization could be also characterized in more detail to distinguish between mature and newly formed vessels, as well as to verify whether they are functional or not (as preliminarily shown by TEM). Possible variations in the presence of microglia over time and their activation state could be also investigated, as well as populations of macrophages in their pro-regenerative or pro-inflammatory phenotypes. Further studies will also include the gelatin control group in the case of rGO-MFs. In addition, as the biodegradability of GDMs *in vivo* is still an open debate, inspection of signs of rGO implants disassembly and biodegradation at chronic time points will be further evaluated. Finally, rGO scaffolds should be challenged to implantation in chronified SCI lesions (although it implies causing a second acute injury), and, if beneficial effects are obtained, larger animal models, which share more similar features to humans such as pigs, should be used for biomaterial testing.

References

Abbott J, Ye T, Krenek K, *et al*. A nanoelectrode array for obtaining intracellular recordings from thousands of connected neurons. *Nat Biomed Eng*. 2020;4(2):232-241. doi:10.1038/s41551-019-0455-7

Acarón Ledesma H, Li X, Carvalho-de-Souza JL, *et al.* An atlas of nano-enabled neural interfaces. *Nat Nanotechnol*. 2019;14(7):645-657. doi:10.1038/s41565-019-0487-x

Adewole DO, Serruya MD, Wolf JA, *et al.* Bioactive neuroelectronic interfaces. *Front Neurosci.* 2019;13:269. doi:10.3389/fnins.2019.00269

Ahmed RU, Alam M, Zheng YP. Experimental spinal cord injury and behavioral tests in laboratory rats. *Heliyon*. 2019;5(3):e01324. doi: 10.1016/j.heliyon.2019.e01324

Ahuja CS, Wilson JR, Nori S, *et al.* Traumatic spinal cord injury. *Nat Rev Dis Primers*. 2017;3:17018. doi:10.1038/nrdp.2017.18

Ajetunmobi A, Prina-Mello A, Volkov Y, *et al*. Nanotechnologies for the study of the central nervous system. *Prog Neurobiol*. 2014;123:18-36. doi:10.1016/j.pneurobio.2014.09.004

Akhavan O, Ghaderi E, Shirazian SA, *et al.* Rolled graphene oxide foams as three-dimensional scaffolds for growth of neural fibers using electrical stimulation of stem cells. *Carbon*. 2016;97:71-77. doi: 10.1016/j.carbon.2015.06.079.

Allen NJ and Eroglu C. Cell biology of astrocyte-synapse interactions. *Neuron*. 2017;96(3):697-708. doi:10.1016/j.neuron.2017.09.056

Alstermark B, Lundberg A, Norrsell U, *et al*. Integration in descending motor pathways controlling the forelimb in the cat. 9. Differential behavioural defects after spinal cord lesions interrupting defined pathways from higher centres to motoneurones. *Exp Brain Res*. 1981;42(3-4):299-318. doi:10.1007/BF00237496

Alstermark B, Lundberg A, Pettersson LG, *et al.* Motor recovery after serial spinal cord lesions of defined descending pathways in cats. *Neurosci Res*. 1987;5(1):68-73. doi:10.1016/0168-0102(87)90024-1

Alstermark B and Sasaki S. Integration in descending motor pathways controlling the forelimb in the cat. 15. Comparison of the projection from excitatory C3-C4 propriospinal neurones to different species of forelimb motoneurons. *Exp Brain Res*. 1986;63(3):543-556. doi:10.1007/BF00237477

Alto LT, Havton LA, Conner JM, *et al.* Chemotropic guidance facilitates axonal regeneration and synapse formation after spinal cord injury. *Nat Neurosci*. 2009;12(9):1106-1113. doi:10.1038/nn.2365

Alves-Sampaio A, García-Rama C, Collazos-Castro JE. Biofunctionalized PEDOT-coated microfibers for the treatment of spinal cord injury. *Biomaterials*. 2016;89:98-113. doi:10.1016/j.biomaterials.2016.02.037

Anderson MA, Burda JE, Ren Y, *et al*. Astrocyte scar formation aids central nervous system axon regeneration. *Nature.* 2016;532(7598):195-200. doi:10.1038/nature17623

Anderson MA, O'Shea TM, Burda JE, *et al*. Required growth facilitators propel axon regeneration across complete spinal cord injury. *Nature*. 2018;561(7723):396-400. doi:10.1038/s41586-018-0467-6

Anderson KD, Sharp KG, Steward O. Bilateral cervical contusion spinal cord injury in rats. *Exp Neurol*. 2009;220(1):9-22. doi:10.1016/j.expneurol.2009.06.012

Ankam S, Suryana M, Chan LY, *et al*. Substrate topography and size determine the fate of human embryonic stem cells to neuronal or glial lineage. *Acta Biomater.* 2013;9(1):4535-4545. doi:10.1016/j.actbio.2012.08.018

Ashraf S, Pelaz B, del Pino P, *et al*. Gold-based nanomaterials for applications in nanomedicine. *Top Curr Chem*. 2016;370:169-202. doi:10.1007/978-3-319-22942-3_6

Assinck P, Duncan GJ, Hilton BJ, *et al.* Cell transplantation therapy for spinal cord injury. *Nat Neurosci.* 2017;20(5):637-647. doi:10.1038/nn.4541

Atala A. Engineering organs. *Curr Opin Biotechnol.* 2009;20(5):575-592. doi:10.1016/j.copbio.2009.10.003

Aurand ER, Usmani S, Medelin M, *et al*. Nanostructures to engineer 3D neural-interfaces: Directing axonal navigation toward successful bridging of spinal segments. *Adv Funct Mater*. 2018;28:1700550. doi:10.1002/adfm.201700550

Aurand ER, Wagner JL, Shandas R, *et al*. Hydrogel formulation determines cell fate of fetal and adult neural progenitor cells. *Stem Cell Res*. 2014;12(1):11-23. doi:10.1016/j.scr.2013.09.013

Azim E, Jiang J, Alstermark B, *et al*. Skilled reaching relies on a V2a propriospinal internal copy circuit. *Nature*. 2014;508(7496):357-363. doi:10.1038/nature13021

Bai H, Sheng K, Zhang P, *et al.* Graphene oxide/conducting polymer composite hydrogels. *J Mater Chem*. 2011;21:18653–18658. doi:10.1039/C1JM13918E

Bakeine GJ, Ban J, Grenci G, *et al.* Design, fabrication and evaluation of nanoscale surface topography as a tool in directing differentiation and organisation of embryonic stem-cell-derived neural precursors. *Microelectronic Engineering*. 2009;86(4-6):1435-1438. doi:10.1016/j.mee.2009.01.032

Baklaushev VP, Bogush VG, Kalsin VA, *et al*. Tissue engineered neural constructs composed of neural precursor cells, recombinant spidroin and PRP for neural tissue regeneration. *Sci Rep*. 2019;9(1):3161. doi:10.1038/s41598-019-39341-9

Baldissera F, Cavallari P, Fournier E, *et al*. Evidence for mutual inhibition of opposite Ia interneurones in the human upper limb. *Exp Brain Res*. 1987;66(1):106-114. doi:10.1007/BF00236207

Bamps S, Put E, Soors P, *et al.* Spinal cord herniation after brachial plexus injury [published correction appears in *Surg Neurol Int*. 2018;9:22. Soors, Peter [added]]. *Surg Neurol Int*. 2017;8:305. doi:10.4103/sni.sni_329_17

Baptista PM and Atala A. Chapter 1 - Regenerative Medicine: The Hurdles and Hopes, Editor(s): Jeffrey Laurence, Translating Regenerative Medicine to the Clinic, Academic Press, 2016, pages 3-7, ISBN 9780128005484, doi:10.1016/B978-0-12-800548-4.00001-2.

Bareyre FM, Kerschensteiner M, Raineteau O, *et al.* The injured spinal cord spontaneously forms a new intraspinal circuit in adult rats. *Nat Neurosci*. 2004;7(3):269-277. doi:10.1038/nn1195

Barnabé-Heider F, Göritz C, Sabelström H, *et al*. Origin of new glial cells in intact and injured adult spinal cord. *Cell Stem Cell*. 2010;7(4):470-482. doi:10.1016/j.stem.2010.07.014

Basso DM, Beattie MS, Bresnahan JC. A sensitive and reliable locomotor rating scale for open field testing in rats. *J Neurotrauma*. 1995;12(1):1-21. doi:10.1089/neu.1995.12.1

Bergmann CP, Stumpf A. Chapter 2: Biomaterials. Dental ceramics, topics in mining, metallurgy and materials engineering, 2013; pages 9-11, Springer-Verlag Berlin Heidelberg, ISBN 978-3-642-38224-6. doi: 10.1007/978-3-642-38224-6_2

Bertelli JA, Mira JC. Behavioral evaluating methods in the objective clinical assessment of motor function after experimental brachial plexus reconstruction in the rat. *J Neurosci Methods*. 1993;46(3):203-208. doi:10.1016/0165-0270(93)90068-3

Boido M, Ghibaudi M, Gentile P, *et al.* Chitosan-based hydrogel to support the paracrine activity of mesenchymal stem cells in spinal cord injury treatment. *Sci Rep*. 2019;9(1):6402. doi:10.1038/s41598-019-42848-w

Bonnet M, Trimaille T, Brezun JM, *et al*. Motor and sensitive recovery after injection of a physically cross-linked PNIPAAm-g-PEG hydrogel in rat hemisectioned spinal cord. *Mater Sci Eng C Mater Biol Appl*. 2020;107:110354. doi:10.1016/j.msec.2019.110354

Bouyer LJ, Rossignol S. Contribution of cutaneous inputs from the hindpaw to the control of locomotion. II. Spinal cats. *J Neurophysiol*. 2003;90(6):3640-3653. doi:10.1152/jn.00497.2003

Bradbury EJ and McMahon SB. Spinal cord repair strategies: why do they work? *Nat Rev Neurosci*. 2006;7(8):644-653. doi:10.1038/nrn1964

Brown TG. The intrinsic factors in the act of progression in the mammal. *Proc Roy Soc B*. 1911;84:308 – 319. doi: 10.1098/rspb.1911.0077

Brüggemann D, Wolfrum B, Maybeck V, *et al.* Nanostructured gold microelectrodes for extracellular recording from electrogenic cells. Nanotechnology. 2011;22(26):265104. doi:10.1088/0957-4484/22/26/265104

Bunge MB, Wood PM. Realizing the maximum potential of Schwann cells to promote recovery from spinal cord injury. *Handb Clin Neurol*. 2012;109:523-540. doi:10.1016/B978-0-444-52137-8.00032-2

Burnside ER, Bradbury EJ. Manipulating the extracellular matrix and its role in brain and spinal cord plasticity and repair. *Neuropathol Appl Neurobiol*. 2014;40(1):26-59. doi:10.1111/nan.12114

Byrne F, Prina-Mello A, Whelan A, *et al*. High content analysis of the biocompatibility of nickel nanowires. *J Magn Magn Mater*. 2009;321:1341-1345. doi: 10.1016/j.jmmm.2009.02.035

Campana A, Cramer T, Simon DT, *et al.* Electrocardiographic recording with conformable organic electrochemical transistor fabricated on resorbable bioscaffold. *Adv Mater*. 2014;26(23):3874-3878. doi:10.1002/adma.201400263

Carballo-Vila M, Moreno-Burriel B, Chinarro E, *et al.* Titanium oxide as substrate for neural cell growth. *J Biomed Mater Res A*. 2009;90(1):94-105. doi:10.1002/jbm.a.32058

Champney TH. Neuroanatomía clínica esencial. Parte 1, capítulo 4: Médula espinal, page 54. 2017, Panamericana, ISBN 978-607-97368-8-0 (electronic version).

Chang L, Hu J, Chen F, *et al*. Nanoscale bio-platforms for living cell interrogation: current status and future perspectives. *Nanoscale*. 2016;8(6):3181-3206. doi:10.1039/c5nr06694h

Chen C, Bai X, Ding Y, *et al.* Electrical stimulation as a novel tool for regulating cell behavior in tissue engineering. *Biomater Res*. 2019b;23:25. doi:10.1186/s40824-019-0176-8

Chen B, He J, Yang H, *et al*. Repair of spinal cord injury by implantation of bFGF-incorporated HEMA-MOETACL hydrogel in rats. *Sci Rep*. 2015;5:9017. doi:10.1038/srep09017

Chen M, Puschmann TB, Marasek P, *et al*. Increased neuronal differentiation of neural progenitor cells derived from phosphovimentin-deficient mice. *Mol Neurobiol*. 2018;55(7):5478-5489. doi:10.1007/s12035-017-0759-0

Chen C, Tang J, Gu Y, *et al.* Bioinspired hydrogel electrospun fibers for spinal cord regeneration. *Adv Funct Mater*. 2019;29:1806899. doi:10.1002/adfm.201806899

Cheng C, Li S, Thomas A, *et al.* Functional graphene nanomaterials based architectures: Biointeractions, fabrications, and emerging biological applications. *Chem Rev*. 2017;117(3):1826-1914. doi:10.1021/acs.chemrev.6b00520

Chiacchiaretta M, Bramini M, Rocchi A, *et al*. Graphene oxide upregulates the homeostatic functions of primary astrocytes and modulates astrocyte-to-neuron communication. *Nano Lett*. 2018;18(9):5827-5838. doi:10.1021/acs.nanolett.8b02487

Chiappini C. Nanoneedle-based sensing in biological systems. *ACS Sens*. 2017;2(8):1086-1102. doi:10.1021/acssensors.7b00350

Choi S, Han SI, Jung D, *et al*. Highly conductive, stretchable and biocompatible Ag-Au core-sheath nanowire composite for wearable and implantable bioelectronics. *Nat Nanotechnol*. 2018;13(11):1048-1056. doi:10.1038/s41565-018-0226-8

Chung WS, Allen NJ, Eroglu C. Astrocytes control synapse formation, function, and elimination. *Cold Spring Harb Perspect Biol*. 2015;7(9):a020370. doi:10.1101/cshperspect.a020370

Chung K, Coggeshall RE. Propriospinal fibers in the rat. *J Comp Neurol*. 1983;217(1):47-53. doi:10.1002/cne.902170105

Chung K, Langford LA, Coggeshall RE. Primary afferent and propriospinal fibers in the rat dorsal and dorsolateral funiculi. *J Comp Neurol*. 1987;263(1):68-75. doi:10.1002/cne.902630106

Clarke LE, Barres BA. Emerging roles of astrocytes in neural circuit development [published correction appears in *Nat Rev Neurosci*. 2013 Jun;14(6):451]. *Nat Rev Neurosci*. 2013;14(5):311-321. doi:10.1038/nrn3484

Convertino A, Mussi V, Maiolo L, *et al*. Array of disordered silicon nanowires coated by a gold film for combined NIR photothermal treatment of cancer cells and Raman monitoring of the process evolution. *Nanotechnology*. 2018;29(41):415102. doi:10.1088/1361-6528/aad6cd

Courtine G and Sofroniew MV. Spinal cord repair: Advances in biology and technology. *Nat Med*. 2019;25(6):898-908. doi:10.1038/s41591-019-0475-6

Courtine G, Song B, Roy RR, *et al.* Recovery of supraspinal control of stepping via indirect propriospinal relay connections after spinal cord injury. *Nat Med*. 2008;14(1):69-74. doi:10.1038/nm1682

Das S, Carnicer-Lombarte A, Fawcett JW, *et al.* Bio-inspired nano tools for neuroscience. *Prog Neurobiol*. 2016;142:1-22. doi:10.1016/j.pneurobio.2016.04.008

Das KK, Reddy RC, Bagoji IB, *et al*. Primary concept of nickel toxicity - an overview. *J Basic Clin Physiol Pharmacol*. 2018;30(2):141-152. doi:10.1515/jbcpp-2017-0171

De los Reyes-Guzmán A, Gil-Agudo A, Peñasco-Martín B, *et al*. Kinematic analysis of the daily activity of drinking from a glass in a population with cervical spinal cord injury. *J Neuroeng Rehabil*. 2010;7:41. doi:10.1186/1743-0003-7-41

Defterali Ç, Verdejo R, Peponi L, *et al*. Thermally reduced graphene is a permissive material for neurons and astrocytes and de novo neurogenesis in the adult olfactory bulb *in vivo*. *Biomaterials*. 2016;82:84-93. doi:10.1016/j.biomaterials.2015.12.010

Della Pelle F, Di Battista R, Vázquez L, *et al*. Press-transferred carbon black nanoparticles for class-selective antioxidant electrochemical detection. *Appl Mater Today*. 2017; 9:29. doi: 10.1016/j.apmt.2017.04.012

DePaul MA, Lin CY, Silver J, *et al*. Combinatory repair strategy to promote axon regeneration and functional recovery after chronic spinal cord injury. *Sci Rep.* 2017;7(1):9018. doi:10.1038/s41598-017-09432-6

Dias DO, Kim H, Holl D, *et al*. Reducing pericyte-derived scarring promotes recovery after spinal cord injury. *Cell.* 2018;173(1):153-165.e22. doi:10.1016/j.cell.2018.02.004

Dipalo M, Amin H, Lovato L, *et al*. Intracellular and extracellular recording of spontaneous action potentials in mammalian neurons and cardiac cells with 3D plasmonic nanoelectrodes. *Nano Lett*. 2017;17(6):3932-3939. doi:10.1021/acs.nanolett.7b01523

Domínguez-Bajo A, González-Mayorga A, Guerrero CR, *et al*. Myelinated axons and functional blood vessels populate mechanically compliant rGO foams in chronic cervical hemisected rats. *Biomaterials.* 2019;192:461-474. doi:10.1016/j.biomaterials.2018.11.024

Domínguez-Bajo A, González-Mayorga A, López-Dolado E, *et al.* Graphene oxide microfibers promote regenerative responses after chronic implantation in the cervical injured spinal cord. *ACS Biomat. Sci. & Eng*. 2020;6(4):2401-2414. doi: 10.1021/acsbiomaterials.0c00345

Dreyer DR, Park S, Bielawski CW, *et al*. The chemistry of graphene oxide. *Chem Soc Rev.* 2010;39(1):228-240. doi:10.1039/b917103g

D'souza AA, Shegokar R. Polyethylene glycol (PEG): a versatile polymer for pharmaceutical applications. *Expert Opin Drug Deliv*. 2016;13(9):1257-75. doi: 10.1080/17425247.2016.1182485.

Du BL, Zeng CG, Zhang W, *et al*. A comparative study of gelatin sponge scaffolds and PLGA scaffolds transplanted to completely transected spinal cord of rat. *J Biomed Mater Res A*. 2014;102(6):1715-1725. doi:10.1002/jbm.a.34835

Dulin JN, Adler AF, Kumamaru H, *et al*. Injured adult motor and sensory axons regenerate into appropriate organotypic domains of neural progenitor grafts. *Nat Commun*. 2018;9(1):84. doi:10.1038/s41467-017-02613-x

Eidelberg E, Walden JG, Nguyen LH. Locomotor control in macaque monkeys. *Brain*. 1981;104(Pt 4):647-663. doi:10.1093/brain/104.4.647-a

Esposito MS, Capelli P, Arber S. Brainstem nucleus MdV mediates skilled forelimb motor tasks. *Nature*. 2014;508(7496):351-356. doi:10.1038/nature13023

Fadeel B, Bussy C, Merino S, *et al.* Safety assessment of graphene-based materials: Focus on human health and the environment. *ACS Nano.* 2018;12(11):10582-10620. doi:10.1021/acsnano.8b04758

Fan C, Li X, Xiao Z, *et al*. A modified collagen scaffold facilitates endogenous neurogenesis for acute spinal cord injury repair. *Acta Biomater*. 2017;51:304-316. doi:10.1016/j.actbio.2017.01.009

Fang Q, Zhang Y, Chen X, *et al*. Three-dimensional graphene enhances neural stem cell proliferation through metabolic regulation. *Front Bioeng Biotechnol*. 2020;7:436. doi:10.3389/fbioe.2019.00436

Feiner R, Dvir T. Tissue–electronics interfaces: from implantable devices to engineered tissues. *Nat Rev Mater.* 2018;3:17076. doi: 10.1038/natrevmats.2017.76

Felix LP, Perez JE, Contreras MF, *et al.* Cytotoxic effects of nickel nanowires in human fibroblasts. *Toxicol Rep.* 2016;3:373-380. doi:10.1016/j.toxrep.2016.03.004

Feng ZQ, Wang T, Zhao B, *et al.* Soft graphene nanofibers designed for the acceleration of nerve growth and development. *Adv Mater.* 2015;27(41):6462-6468. doi:10.1002/adma.201503319

Ferrero B, Di Liberto A. Chapter 2 - Spinal cord injury: Role of neurophysiology. Spinal Cord Injury (SCI) Repair Strategies, 2020, Editor(s): Giuseppe Perale, Filippo Rossi, ISBN 9780081028070, Elsevier Ltd. doi:10.1016/B978-0-08-102807-0.00002-8

Filli L, Engmann AK, Zörner B, *et al.* Bridging the gap: a reticulo-propriospinal detour bypassing an incomplete spinal cord injury. *J Neurosci*. 2014;34(40):13399-13410. doi:10.1523/JNEUROSCI.0701-14.2014

Filli L, Zörner B, Weinmann O, *et al*. Motor deficits and recovery in rats with unilateral spinal cord hemisection mimic the Brown-Sequard syndrome. *Brain*. 2011;134(Pt 8):2261-2273. doi:10.1093/brain/awr167

Freund P, Schneider T, Nagy Z, *et al.* Degeneration of the injured cervical cord is associated with remote changes in corticospinal tract integrity and upper limb impairment. *PLoS One*. 2012;7(12):e51729. doi:10.1371/journal.pone.0051729

Frisén J, Haegerstrand A, Risling M, *et al*. Spinal axons in central nervous system scar tissue are closely related to laminin-immunoreactive astrocytes. *Neuroscience.* 1995;65(1):293-304. doi:10.1016/0306-4522(94)00467-j

Führmann T, Anandakumaran PN, Payne SL, *et al.* Combined delivery of chondroitinase ABC and human induced pluripotent stem cell-derived neuroepithelial cells promote tissue repair in an animal model of spinal cord injury. *Biomed Mater*. 2018;13(2):024103. doi:10.1088/1748-605X/aa96dc

Führmann T, Anandakumaran PN, Shoichet MS. Combinatorial therapies after spinal cord injury: How can biomaterials help? *Adv Healthc Mater*. 2017;6(10):10.1002/adhm.201601130. doi:10.1002/adhm.201601130

Führmann T and Shoichet MS. The role of biomaterials in overcoming barriers to regeneration in the central nervous system. *Biomed Mater*. 2018;13(5):050201. doi:10.1088/1748-605X/aac2f6

Gao SJ, Liu Y, Wang HJ, *et al*. New approach to treating spinal cord injury using PEG-TAT-modified, cyclosporine-A-loaded PLGA/polymeric liposomes. *J Drug Target*. 2017;25(1):75-82. doi:10.1080/1061186X.2016.1191082

García del Moral Garrido R. Laboratorio de anatomía patológica. Hematoxylin eosin protocol (page 156) and aqueous eosin (page 140). 1993, ISBN: 8448102290, Interamericana-McGraw-Hill.

Garcia PD, Garcia R. Determination of the elastic moduli of a single cell cultured on a rigid support by force microscopy. *Biophys J*. 2018;114(12):2923-2932. doi:10.1016/j.bpj.2018.05.012

Garcia PD, Guerrero CR, Garcia R. Time-resolved nanomechanics of a single cell under the depolymerization of the cytoskeleton. *Nanoscale*. 2017;9(33):12051-12059. doi:10.1039/c7nr03419a

Garcia-Ovejero D, Arevalo-Martin A, Paniagua-Torija B, *et al.* The ependymal region of the adult human spinal cord differs from other species and shows ependymoma-like features. *Brain*. 2015;138(Pt 6):1583-1597. doi:10.1093/brain/awv089

Garcia-Porrero *et al.* 2015a: García-Porrero JA, Hurlé JM. Neuroanatomía Humana. Parte II, capítulo 3: Componentes del sistema nervioso central. Anatomía macroscópica de la médula espinal, pages 26-29. 2015, Panamericana, ISBN 978-84-9835-857-5 (electronic version).

Garcia-*Porrero et al.* 2015b: García-Porrero JA and Hurlé JM. Neuroanatomía Humana. García-Porrero. Parte III. Capítulo 10. Médula espinal: estructura y sistematización, page 103. 2015, Panamericana, ISBN 978-84-9835-857-5 (electronic version).

Garcia-Porrero *et al.* 2015c: García-Porrero JA and Hurlé JM. Neuroanatomía Humana. Parte IV. Sección 1. Capítulo 21: Sistema de información somatosensorial, page 232. 2015, Panamericana, ISBN 978-84-9835-857-5 (electronic version).

Garcia-*Porrero et al.* 2015d: J.A. García-Porrero, J.M. Hurlé. Neuroanatomía Humana. García-Porrero. Parte III. Capítulo 10. Médula espinal: estructura y sistematización, page 103. 2015, Panamericana, ISBN 978-84-9835-857-5 (electronic version).

Garcia-Porrero *et al.* 2015e: J.A. García-Porrero, J.M. Hurlé. Neuroanatomía Humana. Parte II. Capítulo 3: Componentes del sistema nervioso central. Anatomía macroscópica de la médula espinal, page 29. 2015, Panamericana, ISBN 978-84-9835-857-5 (electronic version).

Garcia-Porrero *et al.* 2015f: J.A. García-Porrero, J.M. Hurlé. Neuroanatomía Humana. Parte IV. Sección 1. Capítulo 21: Sistema de información somatosensorial, page 232. 2015, Panamericana, ISBN 978-84-9835-857-5 (electronic version).

Gensel JC, Tovar CA, Hamers FP, *et al*. Behavioral and histological characterization of unilateral cervical spinal cord contusion injury in rats. *J Neurotrauma.* 2006;23(1):36-54. doi:10.1089/neu.2006.23.36

González-Mayorga A, López-Dolado E, Gutiérrez MC, *et al*. Favorable biological responses of neural cells and tissue interacting with graphene oxide microfibers. *ACS Omega*. 2017;2(11):8253-8263. doi:10.1021/acsomega.7b01354

Göritz C, Dias DO, Tomilin N, *et al*. A pericyte origin of spinal cord scar tissue. *Science*. 2011;333(6039):238-242. doi:10.1126/science.1203165

Grassner L, Marschallinger J, Dünser MW, *et al.* Nontraumatic spinal cord injury at the neurological intensive care unit: spectrum, causes of admission and predictors of mortality. *Ther Adv Neurol Disord*. 2016;9(2):85-94. doi:10.1177/1756285615621687

Grienberger C, Konnerth A. Imaging calcium in neurons. Neuron. 2012;73(5):862-885. doi:10.1016/j.neuron.2012.02.011

Grijalvo S, Nieto-Díaz M, Maza RM, *et al*. Alginate hydrogels as scaffolds and delivery systems to repair the damaged spinal cord. *Biotechnol J.* 2019;14(12):e1900275. doi:10.1002/biot.201900275

Grill WM. Signal Considerations for Chronically Implanted Electrodes for Brain Interfacing. In: Reichert WM, ed. Indwelling Neural Implants: Strategies for Contending with the In Vivo Environment. Boca Raton (FL): CRC Press/Taylor & Francis; 2008.

Grillner S, Zangger P. The effect of dorsal root transection on the efferent motor pattern in the cat's hindlimb during locomotion. *Acta Physiol Scand*. 1984;120(3):393-405. doi:10.1111/j.1748-1716.1984.tb07400.x

Grulova I, Slovinska L, Blaško J, *et al*. Delivery of alginate scaffold releasing two trophic factors for spinal cord injury repair. *Sci Rep*. 2015;5:13702. doi:10.1038/srep13702

Guha A and Tator CH. Acute cardiovascular effects of experimental spinal cord injury. *J Trauma*. 1988;28(4):481-490. doi:10.1097/00005373-198804000-00011

Guha A, Tator CH, Rochon J. Spinal cord blood flow and systemic blood pressure after experimental spinal cord injury in rats. *Stroke*. 1989;20(3):372-377. doi:10.1161/01.str.20.3.372

Guild WR, Harrison JH, Merril JP, *et al*. Successful homotransplantation of the kidney in an identical twin. *Trans Am Clin Climatol Assoc.* 1955;67:167-173.

Guo W, Qiu J, Liu J, *et al.* Graphene microfiber as a scaffold for regulation of neural stem cells differentiation. *Sci Rep*. 2017;7(1):5678. doi:10.1038/s41598-017-06051-z

Guo W, Zhang X, Yu X, *et al*. Self-powered electrical stimulation for enhancing neural differentiation of mesenchymal stem cells on graphene-poly(3,4-ethylenedioxythiophene) hybrid microfibers. *ACS Nano*. 2016;10(5):5086-5095. doi:10.1021/acsnano.6b00200

Haggerty AE, Maldonado-Lasunción I, Oudega M. Biomaterials for revascularization and immunomodulation after spinal cord injury. *Biomed Mater*. 2018;13(4):044105. doi:10.1088/1748-605X/aaa9d8

Hägglund M, Borgius L, Dougherty KJ, *et al*. Activation of groups of excitatory neurons in the mammalian spinal cord or hindbrain evokes locomotion. *Nat Neurosci*. 2010;13(2):246-252. doi:10.1038/nn.2482

Hai A, Shappir J, Spira ME. Long-term, multisite, parallel, in-cell recording and stimulation by an array of extracellular microelectrodes [published correction appears in *J Neurophysiol*. 2011 Feb;105(2):985]. *J Neurophysiol*. 2010;104(1):559-568. doi:10.1152/jn.00265.2010

Hällström W, Mårtensson T, Prinz C, *et al*. Gallium phosphide nanowires as a substrate for cultured neurons. *Nano Lett*. 2007;7(10):2960-2965. doi:10.1021/nl070728e

Hamers FP, Koopmans GC, Joosten EA. CatWalk-assisted gait analysis in the assessment of spinal cord injury. *J Neurotrauma*. 2006;23(3-4):537-548. doi:10.1089/neu.2006.23.537

Han S, Lee JY, Heo EY, *et al*. Implantation of a Matrigel-loaded agarose scaffold promotes functional regeneration of axons after spinal cord injury in rat. *Biochem Biophys Res Commun*. 2018;496(3):785-791. doi:10.1016/j.bbrc.2018.01.157

Harrison RG. The outgrowth of the nerve fiber as a mode of protoplasmic extension. *J Exp Zool*. 1910;9:787–846.

He Z, Zhang S, Song Q, *et al*. The structural development of primary cultured hippocampal neurons on a graphene substrate. *Colloids Surf B Biointerfaces*. 2016;146:442-451. doi:10.1016/j.colsurfb.2016.06.045

Hench LL. Biomaterials. *Science*. 1980;208(4446):826-31. doi: 10.1126/science.6246576

Hench LL, Thompson I. Twenty-first century challenges for biomaterials. *J R Soc Interface*. 2010;7 Suppl 4(Suppl 4):S379-S391. doi:10.1098/rsif.2010.0151.focus

Hodgetts SI, Harvey AR. Neurotrophic factors used to treat spinal cord injury. *Vitam Horm.* 2017;104:405-457. doi:10.1016/bs.vh.2016.11.007

Holmström U, Tsitsopoulos PP, Flygt H, *et al.* Neurosurgical untethering with or without syrinx drainage results in high patient satisfaction and favorable clinical outcome in post-traumatic myelopathy patients. *Spinal Cord*. 2018;56(9):873-882. doi:10.1038/s41393-018-0094-y

Hong JY, Seo Y, Davaa G, *et al*. Decellularized brain matrix enhances macrophage polarization and functional improvements in rat spinal cord injury. *Acta Biomater*. 2020;101:357-371. doi:10.1016/j.actbio.2019.11.012

Horcas I, Fernández R, Gómez-Rodríguez JM, *et al*. WSXM: A software for scanning probe microscopy and a tool for nanotechnology. *Rev Sci Instrum*. 2007;78(1):013705. doi:10.1063/1.2432410

Hurtado A, Cregg JM, Wang HB, *et al*. Robust CNS regeneration after complete spinal cord transection using aligned poly-L-lactic acid microfibers. *Biomaterials*. 2011;32(26):6068-6079. doi:10.1016/j.biomaterials.2011.05.006

Ikeda T, Ikeda K, Yamamoto K, *et al*. Fabrication and characteristics of chitosan sponge as a tissue engineering scaffold. *Biomed Res Int*. 2014;2014:786892. doi:10.1155/2014/786892

Isik S, Berdondini L, Oni J, *et al*. Cell-compatible array of three-dimensional tip electrodes for the detection of nitric oxide release. *Biosensors and Bioelectronics.* 2005;20(8):1566-1572. doi:10.1016/j.bios.2004.08.022

Itzkovich M, Shefler H, Front L, *et al*. SCIM III (Spinal Cord Independence Measure version III): Reliability of assessment by interview and comparison with assessment by observation. *Spinal Cord*. 2018;56(1):46-51. doi:10.1038/sc.2017.97

Joo NY, Knowles JC, Lee GS, *et al*. Effects of phosphate glass fiber-collagen scaffolds on functional recovery of completely transected rat spinal cords. *Acta Biomater*. 2012;8(5):1802-1812. doi:10.1016/j.actbio.2012.01.026

Kaneko S, Iwanami A, Nakamura M, *et al*. A selective Sema3A inhibitor enhances regenerative responses and functional recovery of the injured spinal cord. *Nat Med*. 2006;12(12):1380-1389. doi:10.1038/nm1505

Kappos EA, Sieber PK, Engels PE, *et al*. Validity and reliability of the CatWalk system as a static and dynamic gait analysis tool for the assessment of functional nerve recovery in small animal models. *Brain Behav*. 2017;7(7):e00723. doi:10.1002/brb3.723

Keirstead HS, Levine JM, Blakemore WF. Response of the oligodendrocyte progenitor cell population (defined by NG2 labelling) to demyelination of the adult spinal cord. *Glia*. 1998;22(2):161-170. doi:10.1002/(SICI)1098-1136(199802)22:2<161::AID-GLIA7>3.0.CO;2-A

Kim MS, Kim JH, Min BH, *et al*. Polymeric scaffolds for regenerative medicine. *Polymer Reviews*. 2011;51(1):23-52. doi: 10.1080/15583724.2010.537800

Kim CY, Sikkema WKA, Kim J, *et al*. Effect of graphene nanoribbons (TexasPEG) on locomotor function recovery in a rat model of lumbar spinal cord transection. *Neural Regen Res*. 2018;13(8):1440-1446. doi:10.4103/1673-5374.235301

Kirshblum *et al.* 2011a: Kirshblum SC, Waring W, Biering-Sorensen F, *et al*. Reference for the 2011 revision of the International Standards for Neurological Classification of Spinal Cord Injury. *J Spinal Cord Med.* 2011;34(6):547-554. doi:10.1179/107902611X13186000420242

Kirshblum *et al.* 2011b: Kirshblum SC, Burns SP, Biering-Sorensen F, *et al*. International standards for neurological classification of spinal cord injury (revised 2011b). *J Spinal Cord Med*. 2011;34(6):535-546. doi:10.1179/204577211X13207446293695

Kitko KE, Hong T, Lazarenko RM, *et al*. Membrane cholesterol mediates the cellular effects of monolayer graphene substrates. *Nat Commun*. 2018;9(1):796. doi:10.1038/s41467-018-03185-0

Koch D, Rosoff WJ, Jiang J, *et al*. Strength in the periphery: growth cone biomechanics and substrate rigidity response in peripheral and central nervous system neurons. *Biophys J*. 2012;102(3):452-460. doi:10.1016/j.bpj.2011.12.025

Koffler J, Zhu W, Qu X, *et al*. Biomimetic 3D-printed scaffolds for spinal cord injury repair. *Nat Med*. 2019;25(2):263-269. doi:10.1038/s41591-018-0296-z

Kubinová Š. Biomaterials and magnetic stem cell delivery in the treatment of spinal cord injury. *Neurochem Res*. 2020;45(1):171-179. doi:10.1007/s11064-019-02808-2

Kubinová Š, Horák D, Hejčl A, *et al*. SIKVAV-modified highly superporous PHEMA scaffolds with oriented pores for spinal cord injury repair. *J Tissue Eng Regen Med.* 2015;9(11):1298-1309. doi:10.1002/term.1694

Kumar S and Parekh SH. Linking graphene-based material physicochemical properties with molecular adsorption, structure and cell fate. *Commun Chem.* 2020;3:8. doi: 10.1038/s42004-019-0254-9

Kurapati R and Bianco A. Peroxidase mimicking DNAzymes degrade graphene oxide. *Nanoscale*. 2018;10(41):19316-19321. doi:10.1039/c8nr06535g

Kurapati R, Mukherjee SP, Martín C, *et al*. Degradation of single-layer and few-layer graphene by neutrophil myeloperoxidase. *Angew Chem Int Ed Engl*. 2018;57(36):11722-11727. doi:10.1002/anie.201806906

Kurapati R, Russier J, Squillaci MA, *et al*. Dispersibility-dependent biodegradation of graphene oxide by myeloperoxidase. *Small.* 2015;11(32):3985-3994. doi:10.1002/smll.201500038

Kushchayev SV, Giers MB, Hom Eng D, *et al.* Hyaluronic acid scaffold has a neuroprotective effect in hemisection spinal cord injury. *J Neurosurg Spine*. 2016;25(1):114-124. doi:10.3171/2015.9.SPINE15628

Lacour S, Courtine G, Guck J. Materials and technologies for soft implantable neuroprostheses. *Nat Rev Mater*. 2016;1:16063. doi:10.1038/natrevmats.2016.63

Laliberte AM, Goltash S, Lalonde NR, *et al*. Propriospinal neurons: Essential elements of locomotor control in the intact and possibly the injured spinal cord. *Front Cell Neurosci.* 2019;13:512. doi:10.3389/fncel.2019.00512

Lan L, Tian FR, ZhuGe DL, *et al.* Implantable porous gelatin microspheres sustained release of bFGF and improved its neuroprotective effect on rats after spinal cord injury. *PLoS One*. 2017;12(3):e0173814. doi:10.1371/journal.pone.0173814

Langer R and Vacanti JP. Tissue engineering. *Science*. 1993;260(5110):920-926. doi:10.1126/science.8493529

Lapointe VL, Fernandes AT, Bell NC, *et al*. Nanoscale topography and chemistry affect embryonic stem cell self-renewal and early differentiation. *Adv Healthc Mater.* 2013;2(12):1644-1650. doi:10.1002/adhm.201200382

Lavrov I, Courtine G, Dy CJ, *et al.* Facilitation of stepping with epidural stimulation in spinal rats: role of sensory input. *J Neurosci*. 2008;28(31):7774-7780. doi:10.1523/JNEUROSCI.1069-08.2008

Lazurko C, Harden S, Suuronen E, *et al*. Biomaterials for organ and tissue repair. *Front. Young Minds*. 2019;7:8. doi: 10.3389/frym.2019.00008

Lee E, Chung WS. Glial Control of synapse number in healthy and diseased brain. *Front Cell Neurosci*. 2019;13:42. doi:10.3389/fncel.2019.00042

Lee JK, Geoffroy CG, Chan AF, *et al.* Assessing spinal axon regeneration and sprouting in Nogo-, MAG-, and OMgp-deficient mice. *Neuron*. 2010;66(5):663-670. doi:10.1016/j.neuron.2010.05.002

Lee MK, Tuttle JB, Rebhun LI, *et al*. The expression and posttranslational modification of a neuron-specific beta-tubulin isotype during chick embryogenesis. *Cell Motil Cytoskeleton*. 1990;17(2):118-132. doi:10.1002/cm.970170207

Li X, Fan C, Xiao Z, *et al*. A collagen microchannel scaffold carrying paclitaxel-liposomes induces neuronal differentiation of neural stem cells through Wnt/β-catenin signaling for spinal cord injury repair. *Biomaterials*. 2018;183:114-127. doi:10.1016/j.biomaterials.2018.08.037

Li Y, Feng L, Shi X, *et al*. Surface coating-dependent cytotoxicity and degradation of graphene derivatives: towards the design of non-toxic, degradable nano-graphene. *Small*. 2014;10(8):1544-1554. doi:10.1002/smll.201303234

Li X, Han J, Zhao Y, *et al*. Functionalized collagen scaffold implantation and cAMP administration collectively facilitate spinal cord regeneration. *Acta Biomater.* 2016;30:233-245. doi:10.1016/j.actbio.2015.11.023

Li X, Tan J, Xiao Z, *et al*. Transplantation of hUC-MSCs seeded collagen scaffolds reduces scar formation and promotes functional recovery in canines with chronic spinal cord injury. *Sci Rep*. 2017;7:43559. doi:10.1038/srep43559

Li N, Zhang Q, Gao S, *et al*. Three-dimensional graphene foam as a biocompatible and conductive scaffold for neural stem cells. *Sci Rep*. 2013;3:1604. doi:10.1038/srep01604

Li N, Zhang X, Song Q, *et al*. The promotion of neurite sprouting and outgrowth of mouse hippocampal cells in culture by graphene substrates. *Biomaterials*. 2011;32(35):9374-9382. doi:10.1016/j.biomaterials.2011.08.065

Lichtenstein MP, Carretero NM, Pérez E, *et al*. Biosafety assessment of conducting nanostructured materials by using co-cultures of neurons and astrocytes. *Neurotoxicology*. 2018;68:115-125. doi:10.1016/j.neuro.2018.07.010

Lin ZC, Xie C, Osakada Y, *et al*. Iridium oxide nanotube electrodes for sensitive and prolonged intracellular measurement of action potentials. *Nat Commun*. 2014;5:3206. doi:10.1038/ncomms4206

Lin L, Zhuang X, Huang R, *et al*. Size-dependent effects of suspended graphene oxide nanoparticles on the cellular fate of mouse neural stem cells. *Int J Nanomedicine.* 2020;15:1421-1435. doi:10.2147/IJN.S225722

Liu S, Xie YY, Wang B. Role and prospects of regenerative biomaterials in the repair of spinal cord injury. *Neural Regen Res*. 2019;14(8):1352-1363. doi:10.4103/1673-5374.253512

Liu JH, Yang ST, Wang H, *et al*. Effect of size and dose on the biodistribution of graphene oxide in mice. *Nanomedicine (Lond)*. 2012;7(12):1801-1812. doi:10.2217/nnm.12.60

Liu Y, Ye H, Satkunendrarajah K, *et al*. A self-assembling peptide reduces glial scarring, attenuates post-traumatic inflammation and promotes neurological recovery following spinal cord injury. *Acta Biomater*. 2013;9(9):8075-8088. doi:10.1016/j.actbio.2013.06.001

López-Dolado E. Thesis project: Biomecánica de la locomoción en un modelo experimental de hemisección medular cervical. Universidad Autónoma de Madrid (Madrid). 2012.

López-Dolado E, González-Mayorga A, Gutiérrez MC, *et al*. Immunomodulatory and angiogenic responses induced by graphene oxide scaffolds in chronic spinal hemisected rats. *Biomaterials*. 2016;99:72-81. doi:10.1016/j.biomaterials.2016.05.012

López-Dolado E, González-Mayorga A, Portolés MT, *et al*. Subacute tissue response to 3D graphene oxide scaffolds implanted in the injured rat spinal cord. *Adv Healthc Mater*. 2015;4(12):1861-1868. doi:10.1002/adhm.201500333

López-Dolado E, Lucas-Osma AM, Collazos-Castro JE. Dynamic motor compensations with permanent, focal loss of forelimb force after cervical spinal cord injury. *J Neurotrauma.* 2013;30(3):191-210. doi:10.1089/neu.2012.2530

Loy DN, Crawford CH, Darnall JB, *et al*. Temporal progression of angiogenesis and basal lamina deposition after contusive spinal cord injury in the adult rat. *J Comp Neurol*. 2002;445(4):308-324. doi:10.1002/cne.10168

Lucas-Osma A. Thesis Project: Anatomía de los circuitos neuronales que controlan el Triceps Braquial y su modificación tras una lesión medular. Universidad Autónoma de Madrid (Madrid). 2011.

Lundberg A. Descending control of forelimb movements in the cat. *Brain Res Bull*. 1999;50(5-6):323-324. doi:10.1016/s0361-9230(99)00151-3

Lysaght MJ, Reyes J. The growth of tissue engineering. *Tissue Eng*. 2001;7(5):485-493. doi:10.1089/107632701753213110

Ma C, Song M, Zhang Y, *et al*. Nickel nanowires induce cell cycle arrest and apoptosis by generation of reactive oxygen species in HeLa cells. *Toxicol Rep*. 2014;1:114-121. doi:10.1016/j.toxrep.2014.04.008

Magnusson JP, Frisén J. Stars from the darkest night: unlocking the neurogenic potential of astrocytes in different brain regions. *Development*. 2016;143(7):1075-1086. doi:10.1242/dev.133975

Mahumane GD, Kumar P, du Toit LC, *et al.* 3D scaffolds for brain tissue regeneration: architectural challenges. *Biomater Sci*. 2018;6(11):2812-2837. doi:10.1039/c8bm00422f

Marchini A, Raspa A, Pugliese R, *et al*. Multifunctionalized hydrogels foster hNSC maturation in 3D cultures and neural regeneration in spinal cord injuries. *Proc Natl Acad Sci U S A*. 2019;116(15):7483-7492. doi:10.1073/pnas.1818392116

Marcus M, Baranes K, Park M, *et al.* Interactions of neurons with physical environments. *Adv Healthc Mater*. 2017;6(15): doi:10.1002/adhm.201700267

Margineanu MB, Julfakyan K, Sommer C, *et al*. Semi-automated quantification of living cells with internalized nanostructures. *J Nanobiotechnology*. 2016;14:4. doi:10.1186/s12951-015-0153-x

Martín C, Kostarelos K, Prato M, *et al*. Biocompatibility and biodegradability of 2D materials: Graphene and beyond. *Chem Commun (Camb).* 2019;55(39):5540-5546. doi:10.1039/c9cc01205b

May Z, Fenrich KK, Dahlby J, *et al.* Following spinal cord injury transected reticulospinal tract axons develop new collateral inputs to spinal interneurons in parallel with locomotor recovery. *Neural Plast.* 2017;2017:1932875. doi:10.1155/2017/1932875

McCambridge AB, Stinear JW, Byblow WD. A dissociation between propriospinal facilitation and inhibition after bilateral transcranial direct current stimulation. *J Neurophysiol.* 2014;111(11):2187-2195. doi:10.1152/jn.00879.2013

McGuire AF, Santoro F, Cui B. Interfacing cells with vertical nanoscale devices: Applications and characterization. *Annu Rev Anal Chem (Palo Alto Calif).* 2018;11(1):101-126. doi:10.1146/annurev-anchem-061417-125705

McKenna JE, Whishaw IQ. Complete compensation in skilled reaching success with associated impairments in limb synergies, after dorsal column lesion in the rat. *J Neurosci.* 1999;19(5):1885-1894. doi:10.1523/JNEUROSCI.19-05-01885.1999

McKinley WO, Seel RT, Hardman JT. Nontraumatic spinal cord injury: incidence, epidemiology, and functional outcome. *Arch Phys Med Rehabil*. 1999;80(6):619-623. doi:10.1016/s0003-9993(99)90162-4

McKinley W, Santos K, Meade M, *et al*. Incidence and outcomes of spinal cord injury clinical syndromes. *J Spinal Cord Med*. 2007;30(3):215-224. doi:10.1080/10790268.2007.11753929

Meletis K, Barnabé-Heider F, Carlén M, *et al.* Spinal cord injury reveals multilineage differentiation of ependymal cells. *PLoS Biol*. 2008;6(7):e182. doi:10.1371/journal.pbio.0060182

Mendonça MC, Soares ES, de Jesus MB, *et al*. PEGylation of reduced graphene oxide induces toxicity in cells of the blood-brain barrier: An *in vitro* and *in vivo* study. *Mol Pharm.* 2016;13(11):3913-3924. doi:10.1021/acs.molpharmaceut.6b00696

Moeendarbary E, Weber IP, Sheridan GK, *et al.* The soft mechanical signature of glial scars in the central nervous system. *Nat Commun*. 2017;8:14787. doi:10.1038/ncomms14787

Moody SA, Quigg MS, Frankfurter A. Development of the peripheral trigeminal system in the chick revealed by an isotype-specific anti-beta-tubulin monoclonal antibody. *J Comp Neurol*. 1989;279(4):567-580. doi:10.1002/cne.902790406

Moral-Vico J, Sánchez-Redondo S, Lichtenstein MP, *et al*. Nanocomposites of iridium oxide and conducting polymers as electroactive phases in biological media. *Acta Biomater*. 2014;10(5):2177-2186. doi:10.1016/j.actbio.2013.12.051

Moshayedi P, Costa Lda F, Christ A, *et al*. Mechanosensitivity of astrocytes on optimized polyacrylamide gels analyzed by quantitative morphometry. *J Phys Condens Matter*. 2010;22(19):194114. doi:10.1088/0953-8984/22/19/194114

Mu Q, Su G, Li L, *et al*. Size-dependent cell uptake of protein-coated graphene oxide nanosheets. *ACS Appl Mater Interfaces*. 2012;4(4):2259-2266. doi:10.1021/am300253c

Mukherjee SP, Gliga AR, Lazzaretto B, *et al*. Graphene oxide is degraded by neutrophils and the degradation products are non-genotoxic. *Nanoscale*. 2018;10(3):1180-1188. doi:10.1039/c7nr03552g

Nathan FM and Li S. Environmental cues determine the fate of astrocytes after spinal cord injury. *Neural Regen Res*. 2017;12(12):1964-1970. doi:10.4103/1673-5374.221144

National Spinal Cord Injury Statistical Center, Facts and figures at a glance. Birmingham, AL: University of Alabama at Birmingham, 2020. https://www.nscisc.uab.edu/Public/Facts%20and%20Figures%202020.pdf. Last retrieval: 17/07/2020.

Nguyen LH, Gao M, Lin J, *et al*. Three-dimensional aligned nanofibers-hydrogel scaffold for controlled non-viral drug/gene delivery to direct axon regeneration in spinal cord injury treatment [published correction appears in *Sci Rep.* 2018 Aug 24;8(1):13057]. *Sci Rep*. 2017;7:42212. doi:10.1038/srep42212

Ning C, Zhou L, Tan G. Fourth-generation biomedical materials. *Materials Today*. 2016; 19(1): 2-3. doi: 10.1016/j.mattod.2015.11.005

Nirwane A and Yao Y. Laminins and their receptors in the CNS. *Biol Rev Camb Philos Soc*. 2018;10.1111/brv.12454. doi:10.1111/brv.12454

Novikova LN, Pettersson J, Brohlin M, *et al*. Biodegradable poly-beta-hydroxybutyrate scaffold seeded with Schwann cells to promote spinal cord repair. *Biomaterials*. 2008;29(9):1198-1206. doi:10.1016/j.biomaterials.2007.11.033

Ojeda *et al*. 2004a: Ojeda JL and Icardo JM. Neuroanatomía humana: Aspectos funcionales y clínicos. Primera parte. Capítulo 2. Anatomía macroscópica y estructura general de la médula espinal, pages 18-19. 2004, Masson, ISBN 84-458-1408-7.

Ojeda *et al.* 2004b: Ojeda JL and Icardo JM. Neuroanatomía humana: Aspectos funcionales y clínicos. Segunda parte, capítulo 12: Vías de información somatoestésicas, page 140. 2004, Masson, ISBN 84-458-1408-7.

Orive G, Anitua E, Pedraz JL, *et al*. Biomaterials for promoting brain protection, repair and regeneration. *Nat Rev Neurosci*. 2009;10(9):682-692. doi:10.1038/nrn2685

Oudega M, Hao P, Shang J, *et al*. Validation study of neurotrophin-3-releasing chitosan facilitation of neural tissue generation in the severely injured adult rat spinal cord. *Exp Neurol*. 2019;312:51-62. doi:10.1016/j.expneurol.2018.11.003

Oudega M and Xu XM. Schwann cell transplantation for repair of the adult spinal cord. *J Neurotrauma*. 2006;23(3-4):453-467. doi:10.1089/neu.2006.23.453

Pakulska MM, Tator CH, Shoichet MS. Local delivery of chondroitinase ABC with or without stromal cell-derived factor 1α promotes functional repair in the injured rat spinal cord. *Biomaterials*. 2017;134:13-21. doi:10.1016/j.biomaterials.2017.04.016

Pampaloni NP, Lottner M, Giugliano M, *et al*. Single-layer graphene modulates neuronal communication and augments membrane ion currents. *Nat Nanotechnol.* 2018;13(8):755-764. doi:10.1038/s41565-018-0163-6

Pan S, Qi Z, Li Q, *et al*. Graphene oxide-PLGA hybrid nanofibres for the local delivery of IGF-1 and BDNF in spinal cord repair [published correction appears in *Artif Cells Nanomed Biotechnol*. 2020 Dec;48(1):703-704*]. Artif Cells Nanomed Biotechnol*. 2019;47(1):651-664. doi:10.1080/21691401.2019.1575843

Panda D, Miller HP, Banerjee A, *et al*. Microtubule dynamics in vitro are regulated by the tubulin isotype composition. *Proc Natl Acad Sci U S A*. 1994;91(24):11358-11362. doi:10.1073/pnas.91.24.11358

Paniagua-Torija B, Norenberg M, Arevalo-Martin A, *et al*. Cells in the adult human spinal cord ependymal region do not proliferate after injury. *J Pathol*. 2018;246(4):415-421. doi:10.1002/path.5151

Papa S, Mauri E, Rossi F, *et al.* Chapter 1 - Introduction to spinal cord injury as clinical pathology. Spinal Cord Injury (SCI) Repair Strategies, 2020, pages 1-12, Editor(s): Giuseppe Perale, Filippo Rossi, ISBN 9780081028070, 2020 Elsevier Ltd. doi:10.1016/B978-0-08-102807-0.00001-6

Papastefanaki F, Jakovcevski I, Poulia N, *et al*. Intraspinal delivery of polyethylene glycol-coated gold nanoparticles promotes functional recovery after spinal cord injury. *Mol Ther.* 2015;23(6):993-1002. doi:10.1038/mt.2015.50

Parameswaran R, Carvalho-de-Souza JL, Jiang Y, *et al*. Photoelectrochemical modulation of neuronal activity with free-standing coaxial silicon nanowires. *Nat Nanotechnol*. 2018;13(3):260-266. doi:10.1038/s41565-017-0041-7

Park J, Lim E, Back S, *et al*. Nerve regeneration following spinal cord injury using matrix metalloproteinase-sensitive, hyaluronic acid-based biomimetic hydrogel scaffold containing brain-derived neurotrophic factor. *J Biomed Mater Res A*. 2010;93(3):1091-1099. doi:10.1002/jbm.a.32519

Park SY, Park J, Sim SH, *et al.* Enhanced differentiation of human neural stem cells into neurons on graphene. *Adv Mater*. 2011;23(36):H263-H267. doi:10.1002/adma.201101503

Patel H, Bonde M, Srinivasan G. Biodegradable polymer scaffold for tissue engineering. *Trends Biomater. Artif. Organs*. 2011;25(1):20-29.

Pathak MM, Nourse JL, Tran T, *et al*. Stretch-activated ion channel Piezo1 directs lineage choice in human neural stem cells. *Proc Natl Acad Sci U S A*. 2014;111(45):16148-16153. doi:10.1073/pnas.1409802111

Patolsky F, Timko BP, Yu G, *et al*. Detection, stimulation, and inhibition of neuronal signals with high-density nanowire transistor arrays [published correction appears in *Science*. 2007 Jul 20;317(5836):320]. *Science*. 2006;313(5790):1100-1104. doi:10.1126/science.1128640

Pauvert V, Pierrot-Deseilligny E, Rothwell JC. Role of spinal premotoneurones in mediating corticospinal input to forearm motoneurones in man. *J Physiol*. 1998;508 (Pt 1)(Pt 1):301-312. doi:10.1111/j.1469-7793.1998.301br.x

Pawar K, Cummings BJ, Thomas A, *et al*. Biomaterial bridges enable regeneration and re-entry of corticospinal tract axons into the caudal spinal cord after SCI: Association with recovery of forelimb function. *Biomaterials*. 2015;65:1-12. doi:10.1016/j.biomaterials.2015.05.032

Peng Z, Liu X, Zhang W, *et al*. Advances in the application, toxicity and degradation of carbon nanomaterials in environment: A review. *Environ Int*. 2020;134:105298. doi:10.1016/j.envint.2019.105298

Permuy M, López-Peña M, González-Cantalapiedra A, *et al.* Chapter 13 - Reliability on animal models, Spinal Cord Injury (SCI) Repair Strategies, Woodhead Publishing, 2020, pages 249-277, Editor(s): Giuseppe Perale, Filippo Rossi, ISBN 9780081028070, doi: 10.1016/B978-0-08-102807-0.00013-2

Pettikiriarachchi JTS, Parish CL, Shoichet MS, *et al.* Biomaterials for brain tissue engineering. *Aust J Chem*. 2010; 63:1143-1154. doi: 10.1071/CH10159

Pires LR, Pêgo AP. Bridging the lesion-engineering a permissive substrate for nerve regeneration. *Regen Biomater*. 2015;2(3):203-214. doi:10.1093/rb/rbv012

Prina-Mello A, Diao Z, Coey JM. Internalization of ferromagnetic nanowires by different living cells. *J Nanobiotechnology*. 2006;4:9. doi:10.1186/1477-3155-4-9

Puelles Lopez *et al*. 2008a: Puelles López L, Martínez Pérez S, Martínez de la Torre M. Neuroanatomía. Sección IV, capítulo 14. Regiones transversales (subdivisión anteroposterior), page 94. 2008, Panamericana, ISBN 978-84-9835-896-4 (electronic version).

Puelles Lopez *et al.* 2008b: Puelles López L, Martínez Pérez S, Martínez de la Torre M. Neuroanatomía. Sección V, capítulo 15. Médula espinal, page 97. 2008, Panamericana, ISBN 978-84-9835-896-4 (electronic version).

Rao JS, Zhao C, Zhang A, *et al*. NT3-chitosan enables de novo regeneration and functional recovery in monkeys after spinal cord injury. *Proc Natl Acad Sci U S A.* 2018;115(24):E5595-E5604. doi:10.1073/pnas.1804735115

Raspa A, Marchini A, Pugliese R, *et al*. A biocompatibility study of new nanofibrous scaffolds for nervous system regeneration. *Nanoscale.* 2016;8(1):253-265. doi:10.1039/c5nr03698d

Rauti R, Lozano N, León V, *et al*. Graphene oxide nanosheets reshape synaptic function in cultured brain networks. *ACS Nano*. 2016;10(4):4459-4471. doi:10.1021/acsnano.6b00130

Reina G, González-Domínguez JM, Criado A, *et al*. Promises, facts and challenges for graphene in biomedical applications. *Chem Soc Rev*. 2017;46(15):4400-4416. doi:10.1039/c7cs00363c

Reis KP, Sperling LE, Teixeira C, *et al*. Application of PLGA/FGF-2 coaxial microfibers in spinal cord tissue engineering: An *in vitro* and *in vivo* investigation. *Regen Med*. 2018;13(7):785-801. doi:10.2217/rme-2018-0060

Robinson JT, Jorgolli M, Shalek AK, *et al*. Vertical nanowire electrode arrays as a scalable platform for intracellular interfacing to neuronal circuits. *Nat Nanotechnol.* 2012;7(3):180-184. doi:10.1038/nnano.2011.249

Robinson-Bennett B, Han A. Chapter 30: Role of immunohistochemistry in elucidating lung cancer metastatic to the ovary from primary ovarian carcinoma. Handbook of immunohistochemistry and in situ hybridization of human carcinomas. 2005; 4, Editor: Hayat MA, ISSN: 1874-5784, doi: 10.1016/S1874-5784(05)80116-3

Roman JA, Reucroft I, Martin RA, *et al*. Local release of paclitaxel from aligned, electrospun microfibers promotes axonal extension. *Adv Healthc Mater*. 2016;5(20):2628-2635. doi:10.1002/adhm.201600415

Salatino JW, Ludwig KA, Kozai TDY, *et al.* Glial responses to implanted electrodes in the brain [published correction appears in *Nat Biomed Eng*. 2018 Jan;2(1):52]. *Nat Biomed Eng*. 2017;1(11):862-877. doi:10.1038/s41551-017-0154-1

Salgado AJ, Oliveira JM, Martins A, *et al*. Tissue engineering and regenerative medicine: Past, present, and future. *Int Rev Neurobiol*. 2013;108:1-33. doi:10.1016/B978-0-12-410499-0.00001-0

Schallert T, Fleming SM, Leasure JL, *et al*. CNS plasticity and assessment of forelimb sensorimotor outcome in unilateral rat models of stroke, cortical ablation, parkinsonism and spinal cord injury. *Neuropharmacology*. 2000;39(5):777-787. doi:10.1016/s0028-3908(00)00005-8

Schwab JM, Zhang Y, Kopp MA, *et al.* The paradox of chronic neuroinflammation, systemic immune suppression, autoimmunity after traumatic chronic spinal cord injury. *Exp Neurol*. 2014;258:121-129. doi:10.1016/j.expneurol.2014.04.023

Secomandi N, Franceschi Biagioni A, Kostarelos K, *et al*. Thin graphene oxide nanoflakes modulate glutamatergic synapses in the amygdala cultured circuits: Exploiting synaptic approaches to anxiety disorders. *Nanomedicine*. 2020;26:102174. doi:10.1016/j.nano.2020.102174

Seidlits SK, Lee JY, Schmidt CE. Nanostructured scaffolds for neural applications. *Nanomedicine (Lond).* 2008;3(2):183-199. doi:10.2217/17435889.3.2.183

Seif-Naraghi SB, Christman KL. Chapter 3 - Tissue engineering and the role of biomaterial scaffolds: The evolution of cardiac tissue engineering, Editor(s): Regina Coeli dos Santos Goldenberg, Antonio Carlos Campos de Carvalho, Resident stem cells and regenerative therapy, Academic Press, 2013, pages 43-67, ISBN 9780124160125, doi:10.1016/B978-0-12-416012-5.00003-7.

Sensharma P, Madhumathi G, Jayant RD, *et al*. Biomaterials and cells for neural tissue engineering: Current choices. *Mater Sci Eng C Mater Biol Appl*. 2017;77:1302-1315. doi:10.1016/j.msec.2017.03.264

Serrano MC, Feito MJ, González-Mayorga A, *et al*. Response of macrophages and neural cells in contact with reduced graphene oxide microfibers. *Biomater Sci*. 2018;6(11):2987-2997. doi:10.1039/c8bm00902c

Serrano MC, Patiño J, García-Rama C, *et al*. 3D free-standing porous scaffolds made of graphene oxide as substrates for neural cell growth. *J Mater Chem B*. 2014;2(34):5698-5706. doi:10.1039/c4tb00652f

Shah S, Yin PT, Uehara TM, *et al*. Guiding stem cell differentiation into oligodendrocytes using graphene-nanofiber hybrid scaffolds. *Adv Mater*. 2014;26(22):3673-3680. doi:10.1002/adma.201400523

Shahriari D, Koffler JY, Tuszynski MH, *et al*. Hierarchically ordered porous and high-volume polycaprolactone microchannel scaffolds enhanced axon growth in transected spinal cords. *Tissue Eng Part A*. 2017;23(9-10):415-425. doi:10.1089/ten.TEA.2016.0378

Shin JE, Jung K, Kim M, *et al*. Brain and spinal cord injury repair by implantation of human neural progenitor cells seeded onto polymer scaffolds. *Exp Mol Med*. 2018;50(4):39. doi:10.1038/s12276-018-0054-9

Shih CH, Lacagnina M, Leuer-Bisciotti K, *et al.* Astroglial-derived periostin promotes axonal regeneration after spinal cord injury. *J Neurosci*. 2014;34(7):2438-2443. doi:10.1523/JNEUROSCI.2947-13.2014

Shu B, Sun X, Liu R, *et al*. Restoring electrical connection using a conductive biomaterial provides a new therapeutic strategy for rats with spinal cord injury. *Neurosci Lett*. 2019;692:33-40. doi:10.1016/j.neulet.2018.10.031

Simon-Assmann P, Orend G, Mammadova-Bach E, *et al*. Role of laminins in physiological and pathological angiogenesis. *Int J Dev Biol*. 2011;55(4-5):455-465. doi:10.1387/ijdb.103223ps

Singh DP, Herrera CE, Singh B, *et al*. Graphene oxide: An efficient material and recent approach for biotechnological and biomedical applications. *Mater Sci Eng C Mater Biol Appl*. 2018;86:173-197. doi:10.1016/j.msec.2018.01.004

Sisto SA, Dyson-Hudson T. Dynamometry testing in spinal cord injury. *J Rehabil Res Dev*. 2007;44(1):123-136. doi:10.1682/jrrd.2005.11.0172

Sławińska U, Majczyński H, Dai Y, *et al.* The upright posture improves plantar stepping and alters responses to serotonergic drugs in spinal rats. *J Physiol*. 2012;590(7):1721-1736. doi:10.1113/jphysiol.2011.224931

Slotkin JR, Pritchard CD, Luque B, *et al*. Biodegradable scaffolds promote tissue remodeling and functional improvement in non-human primates with acute spinal cord injury. *Biomaterials*. 2017;123:63-76. doi:10.1016/j.biomaterials.2017.01.024

Soares S, von Boxberg Y, Nothias F. Repair strategies for traumatic spinal cord injury, with special emphasis on novel biomaterial-based approaches. *Rev Neurol (Paris).* 2020;176(4):252-260. doi:10.1016/j.neurol.2019.07.029

Soblosky JS, Song JH, Dinh DH. Graded unilateral cervical spinal cord injury in the rat: evaluation of forelimb recovery and histological effects. *Behav Brain Res*. 2001;119(1):1-13. doi:10.1016/s0166-4328(00)00328-4

Soderblom C, Luo X, Blumenthal E, *et al*. Perivascular fibroblasts form the fibrotic scar after contusive spinal cord injury. *J Neurosci*. 2013;33(34):13882-13887. doi:10.1523/JNEUROSCI.2524-13.2013

Song X, Fiati Kenston SS, Kong L, *et al*. Molecular mechanisms of nickel induced neurotoxicity and chemoprevention. *Toxicology*. 2017;392:47-54. doi:10.1016/j.tox.2017.10.006

Song MM, Song WJ, Bi H, *et al*. Cytotoxicity and cellular uptake of iron nanowires. *Biomaterials*. 2010;31(7):1509-1517. doi:10.1016/j.biomaterials.2009.11.034

Sorbo T. Thesis project: Exploring hybrid networks made by neurons and progenitor cells. International School for Advanced Studies / Scuola Internazionale Superiore di Studi Avanzati (ISAS / SISSA). Trieste (Italy). 2019.

Sorbo T, Musto M, Ballerini L. Neuronal progenitor cell-identity specified by synaptic integration to postnatal hippocampal circuits in culture. 2020. Under revision.

Spira ME and Hai A. Multi-electrode array technologies for neuroscience and cardiology. *Nat Nanotechnol*. 2013;8(2):83-94. doi:10.1038/nnano.2012.265

Subramanian A, Krishnan UM, Sethuraman S. Development of biomaterial scaffold for nerve tissue engineering: Biomaterial mediated neural regeneration. *J Biomed Sci*. 2009;16(1):108. doi:10.1186/1423-0127-16-108

Sugai K, Nishimura S, Kato-Negishi M, *et al*. Neural stem/progenitor cell-laden microfibers promote transplant survival in a mouse transected spinal cord injury model. *J Neurosci Res*. 2015;93(12):1826-1838. doi:10.1002/jnr.23636

Sun G, Shao J, Deng D, *et al*. A chitosan scaffold infused with neurotrophin-3 and human umbilical cord mesenchymal stem cells suppresses inflammation and promotes functional recovery after spinal cord injury in mice. *Int J Clin Exp Med*. 2017;10(8):11672-11679. www.ijcem.com /ISSN:1940-5901/IJCEM0050341

Suyatin DB, Wallman L, Thelin J, *et al*. Nanowire-based electrode for acute in vivo neural recordings in the brain. *PLoS One*. 2013;8(2):e56673. doi:10.1371/journal.pone.0056673

Takeoka A, Vollenweider I, Courtine G, *et al*. Muscle spindle feedback directs locomotor recovery and circuit reorganization after spinal cord injury. *Cell.* 2014;159(7):1626-1639. doi:10.1016/j.cell.2014.11.019

Talac R, Friedman JA, Moore MJ, *et al*. Animal models of spinal cord injury for evaluation of tissue engineering treatment strategies. *Biomaterials*. 2004;25(9):1505-1510. doi:10.1016/s0142-9612(03)00497-6

Tan KKB, Lim WWM, Chai C, *et al*. Sequential application of discrete topographical patterns enhances derivation of functional mesencephalic dopaminergic neurons from human induced pluripotent stem cells. *Sci Rep.* 2018;8(1):9567. doi:10.1038/s41598-018-27653-1

Tang M, Li J, He L, *et al*. Transcriptomic profiling of neural stem cell differentiation on graphene substrates. *Colloids Surf B Biointerfaces*. 2019;182:110324. doi:10.1016/j.colsurfb.2019.06.054

Tang M, Song Q, Li N, *et al*. Enhancement of electrical signaling in neural networks on graphene films. *Biomaterials*. 2013;34(27):6402-6411. doi:10.1016/j.biomaterials.2013.05.024

Tavangarian F and Li Y. Carbon nanostructures as nerve scaffolds for repairing large gaps in severed nerves. *Ceramics Int*. 2012;38:6075–6090. doi:10.1016/j.ceramint.2012.05.038

Terraf P, Kouhsari SM, Ai J, *et al*. Tissue-engineered regeneration of hemisected spinal cord using human endometrial stem cells, poly ε-caprolactone scaffolds, and crocin as a neuroprotective agent. *Mol Neurobiol*. 2016;54(7):5657-5667. doi:10.1007/s12035-016-0089-7

Timko BP, Cohen-Karni T, Qing Q, *et al*. Design and implementation of functional nanoelectronic interfaces with biomolecules, cells, and tissue using nanowire device arrays. *IEEE Trans Nanotechnol*. 2010;9(3):269-280. doi:10.1109/TNANO.2009.2031807

Torres Alaminos, M. Aspectos epidemiológicos de la lesión medular en el Hospital Nacional de Parapléjicos. 2018;12(2):122. http://scielo.isciii.es/scielo.php?script=sci_arttext&pid=S1988-348X2018000200002&lng=es&tlng=es. Last retrieved: 30/5/2020

Tsai HH, Li H, Fuentealba LC, *et al*. Regional astrocyte allocation regulates CNS synaptogenesis and repair. *Science*. 2012;337(6092):358-362. doi:10.1126/science.1222381

Usmani S, Aurand ER, Medelin M, *et al*. 3D meshes of carbon nanotubes guide functional reconnection of segregated spinal explants. *Sci Adv*. 2016;2(7):e1600087. doi:10.1126/sciadv.1600087

Vallejo-Giraldo C, Krukiewicz K, Calaresu I, *et al*. Attenuated glial reactivity on topographically functionalized poly(3,4-ethylenedioxythiophene):P-toluene sulfonate (PEDOT:PTS) neuroelectrodes fabricated by microimprint lithography. *Small*. 2018;14(28):e1800863. doi:10.1002/smll.201800863

Vara H, Collazos-Castro JE. Enhanced spinal cord microstimulation using conducting polymer-coated carbon microfibers. *Acta Biomater*. 2019;90:71-86. doi:10.1016/j.actbio.2019.03.037

Wang J, Chu R, Ni N, *et al*. The effect of Matrigel as scaffold material for neural stem cell transplantation for treating spinal cord injury. *Sci Rep*. 2020;10(1):2576. doi:10.1038/s41598-020-59148-3

Wang Y, Lee WC, Manga KK, *et al*. Fluorinated graphene for promoting neuro-induction of stem cells. *Adv Mater*. 2012;24(31):4285-4290. doi:10.1002/adma.201200846

Wang K, Ruan J, Song H, *et al*. Biocompatibility of graphene oxide. *Nanoscale Res Lett.* 2011;6:8. doi:10.1007/s11671-010-9751-6

Wen Y, Yu S, Wu Y, *et al*. Spinal cord injury repair by implantation of structured hyaluronic acid scaffold with PLGA microspheres in the rat. *Cell Tissue Res*. 2016;364(1):17-28. doi:10.1007/s00441-015-2298-1

Williams DF. On the nature of biomaterials. *Biomaterials*. 2009;30(30):5897-909. doi: 10.1016/j.biomaterials.2009.07.027

Xia L, Zhu W, Wang Y, *et al*. Regulation of neural stem cell proliferation and differentiation by graphene-based biomaterials. *Neural Plast.* 2019;2019:3608386. doi:10.1155/2019/3608386

Xie C, Hanson L, Xie W, *et al.* Noninvasive neuron pinning with nanopillar arrays. *Nano Lett*. 2010;10(10):4020-4024. doi:10.1021/nl101950x

Xie C, Lin Z, Hanson L, *et al*. Intracellular recording of action potentials by nanopillar electroporation. *Nat Nanotechnol*. 2012;7(3):185-190. doi:10.1038/nnano.2012.8

Xu HL, Tian FR, Lu CT, *et al*. Thermo-sensitive hydrogels combined with decellularised matrix deliver bFGF for the functional recovery of rats after a spinal cord injury. *Sci Rep*. 2016;6:38332. doi:10.1038/srep38332

Xu B, Zhao Y, Xiao Z, *et al*. A dual functional scaffold tethered with EGFR antibody promotes neural stem cell retention and neuronal differentiation for spinal cord injury repair. *Adv Healthc Mater*. 2017;6(9). doi:10.1002/adhm.201601279

Yabe JT, Chan WK, Wang FS, *et al*. Regulation of the transition from vimentin to neurofilaments during neuronal differentiation. *Cell Motil Cytoskeleton*. 2003;56(3):193-205. doi:10.1002/cm.10137

Yang Y, Asiri AM, Tang Z, *et al*. Graphene based materials for biomedical applications. *Mater. Today*. 2013;16:365–373. doi: 10.1016/j.mattod.2013.09.004

Yang K, Jung H, Lee HR, *et al*. Multiscale, hierarchically patterned topography for directing human neural stem cells into functional neurons. *ACS Nano*. 2014;8(8):7809-7822. doi:10.1021/nn501182f

Yang EZ, Zhang GW, Xu JG, *et al*. Multichannel polymer scaffold seeded with activated Schwann cells and bone mesenchymal stem cells improves axonal regeneration and functional recovery after rat spinal cord injury. *Acta Pharmacol Sin*. 2017;38(5):623-637. doi:10.1038/aps.2017.11

Yao S, Yu S, Cao Z, *et al*. Hierarchically aligned fibrin nanofiber hydrogel accelerated axonal regrowth and locomotor function recovery in rat spinal cord injury. *Int J Nanomedicine*. 2018;13:2883-2895. doi:10.2147/IJN.S159356

Yoon H, Walters G, Paulsen AR, *et al.* Astrocyte heterogeneity across the brain and spinal cord occurs developmentally, in adulthood and in response to demyelination. *PLoS One*. 2017;12(7):e0180697. doi:10.1371/journal.pone.0180697

Yue H, Wei W, Yue Z, *et al*. The role of the lateral dimension of graphene oxide in the regulation of cellular responses. *Biomaterials.* 2012;33(16):4013-4021. doi:10.1016/j.biomaterials.2012.02.021

Zhai TT, Ye D, Zhang QW, *et al.* Highly efficient capture and electrochemical release of circulating tumor cells by using aptamers modified gold nanowire arrays. *ACS Appl Mater Interfaces*. 2017;9(40):34706-34714. doi:10.1021/acsami.7b11107

Zhang S, Wang XJ, Li WS, *et al*. Polycaprolactone/polysialic acid hybrid, multifunctional nanofiber scaffolds for treatment of spinal cord injury. *Acta Biomater*. 2018;77:15-27. doi:10.1016/j.actbio.2018.06.038

Zhang X, Yin J, Peng C, *et al*. Distribution and biocompatibility studies of graphene oxide in mice after intravenous administration. *Carbon*. 2011;49(3):986-995. doi: 10.1016/j.carbon.2010.11.005.

Zhang K, Zheng H, Liang S, *et al.* Aligned PLLA nanofibrous scaffolds coated with graphene oxide for promoting neural cell growth. *Acta Biomater*. 2016;37:131-142. doi:10.1016/j.actbio.2016.04.008

Zheng B, Atwal J, Ho C, *et al*. Genetic deletion of the Nogo receptor does not reduce neurite inhibition in vitro or promote corticospinal tract regeneration in vivo. *Proc Natl Acad Sci U S A*. 2005;102(4):1205-1210. doi:10.1073/pnas.0409026102

Zhou L, Fan L, Yi X, *et al*. Soft conducting polymer hydrogels cross-linked and doped by tannic acid for spinal cord injury repair. *ACS Nano*. 2018;12(11):10957-10967. doi:10.1021/acsnano.8b04609

Zhu Y, Soderblom C, Trojanowsky M, *et al*. Fibronectin matrix assembly after spinal cord injury. *J Neurotrauma.* 2015;32(15):1158-1167. doi:10.1089/neu.2014.3703

Zustiak SP, Sheth S, Imaninezhad M. Chapter 12 - Pharmacological therapies and factors delivery for spinal cord injury regeneration, Editor(s): Giuseppe Perale, Filippo Rossi, Spinal Cord Injury (SCI) Repair Strategies, Woodhead Publishing, 2020, pages 223-248, ISBN 9780081028070, doi:10.1016/B978-0-08-102807-0.00012-0

Links to clinical trials included in this thesis:

NCT03899584:
https://clinicaltrials.gov/ct2/show/NCT03899584?term=NCT03899584&draw=2&rank=1

NCT03504826:
https://clinicaltrials.gov/ct2/show/NCT03504826?term=NCT03504826&draw=2&rank=1

NCT03925077:
https://clinicaltrials.gov/ct2/show/NCT03925077?term=NCT03925077&draw=2&rank=1

NCT03505034:
https://clinicaltrials.gov/ct2/show/NCT03505034?term=NCT03505034&draw=2&rank=1

NCT04213131:
https://clinicaltrials.gov/ct2/show/NCT04213131?term=NCT04213131&draw=2&rank=1

NCT02574572:
https://clinicaltrials.gov/ct2/show/NCT02574572?term=NCT02574572&draw=2&rank=1

NCT02138110:
https://clinicaltrials.gov/ct2/show/NCT02138110?term=NCT02138110&draw=2&rank=1

NCT03762655:
https://clinicaltrials.gov/ct2/show/NCT03762655?term=NCT03762655&draw=2&rank=1

NCT02510365:
https://clinicaltrials.gov/ct2/show/NCT02510365?term=NCT02510365&draw=2&rank=1

NCT02688049:
https://clinicaltrials.gov/ct2/show/NCT02688049?term=NCT02688049&draw=2&rank=1

NCT02688062:
https://clinicaltrials.gov/ct2/show/NCT02688062?term=NCT02688062&draw=1&rank=1

NCT03933072:
https://clinicaltrials.gov/ct2/show/NCT03933072?term=NCT03933072&draw=2&rank=1

NCT03966794:
https://clinicaltrials.gov/ct2/show/NCT03966794?term=NCT03966794&draw=2&rank=1

NCT04196114:
https://clinicaltrials.gov/ct2/show/NCT04196114?term=NCT04196114&draw=2&rank=1

NCT04265560:
https://clinicaltrials.gov/ct2/show/NCT04265560?term=NCT04265560&draw=2&rank=1

APPENDICES

Co-authors and collaborators of this thesis work

Name	Contribution	Affiliation
María C. Serrano	Supervisor and corresponding author of all the work presented in this thesis	Instituto de Ciencia de Materiales de Madrid (ICMM), Consejo Superior de Investigaciones Científicas (CSIC)
Elisa López-Dolado	Co-supervisor and co-author of all the work presented in this thesis	Hospital Nacional de Parapléjicos (HNP), Servicio de Salud de Castilla-La Mancha (SESCAM)
M. Teresa Portolés Pérez	Academic supervisor	Universidad Complutense de Madrid (UCM)
Ankor González-Mayorga	Co-author of all the work presented in this thesis	HNP-SESCAM
Ricardo García	Co-author and responsible (Group leader) for AFM experiments with rGO foams	ICMM-CSIC
Carlos R. Guerrero	Co-author and responsible for AFM experiments with rGO foams	ICMM-CSIC
F. Javier Palomares	Co-author and responsible (Group leader) for XPS experiments with rGO foams	ICMM-CSIC
Mar García-Hernández	Co-author and responsible (Group leader) for AFM experiments with rGO MFs	ICMM-CSIC
Carmen Munuera	Co-author and responsible for AFM experiments with rGO MFs	ICMM-CSIC
Rodolfo Miranda	Co-author and responsible (ByAxon coordinator) for NWs fabrication and characterization	Instituto Madrileño de Estudios Avanzados (IMDEA Nanociencia)
M. Teresa González	Co-author and responsible (ByAxon co-coordinator) for NWs fabrication and characterization;	IMDEA Nanociencia

	corresponding author of the published paper on NWs	
Julio Camarero	Co-author and responsible (Group leader) for NWs fabrication and characterization	IMDEA Nanociencia
Lucas Pérez	Co-author and responsible (Group leader) for NWs fabrication and characterization	IMDEA Nanociencia & UCM
Beatriz L. Rodilla	Co-author and responsible for NWs fabrication and characterization	IMDEA Nanociencia & UCM
Ana Arché-Núñez	Co-author and responsible for NWs fabrication and characterization	IMDEA Nanociencia
Laura Ballerini	Co-author, corresponding author of the published paper on NWs and supervisor (Group leader) of all the work performed in SISSA	International School for Advanced Studies (SISSA/ISAS)
Denis Scaini	Co-author and supervisor of the fabrication of PDMS substrates	SISSA/ISAS
Ivo Calaresu	Co-author; assistance with the calcium imaging experiments on PDMS, and responsible for the calcium imaging and stimulation experiments included in the published paper on NWs	SISSA/ISAS
Giulia Panattoni	Collaborator; assistance with calcium imaging experiments and analysis regarding PDMS substrates	SISSA/ISAS
Raffaele Casani	Collaborator; assistance with ENPCs cultures regarding calcium experiments on PDMS substrates	SISSA/ISAS
Teresa Sorbo	Collaborator; assistance with ENPCs cultures	SISSA/ISAS

	regarding calcium experiments on PDMS substrates	
Livia Piatti	Collaborator; assistance with Clampfit software	SISSA/ISAS
André Espinha	Collaborator; assistance with figure preparation and formatting for rGO foams paper	-
Daniel García-Ovejero	Collaborator; assistance with fresh spinal cord sectioning by vibratome for rGO foams paper	HNP-SESCAM
Fernando García-García	Collaborator; assistance with MRI studies	HNP-SESCAM
Jose Ángel Rodríguez	Service technician (Group leader); assistance with CLSM studies regarding rGO materials	Service of Microscopy and Image Analysis at the HNP-SESCAM
Javier Mazarío	Service technician (Group leader); assistance with CLSM studies regarding rGO materials	Service of Microscopy and Image Analysis at the HNP-SESCAM
Marina Benito	Service technician; acquisition of MRI images	HNP-SESCAM
Francisco Urbano	Service technician (Group leader); assistance with TEM studies of all materials presented	Interdepartment Investigation Service at Universidad Autónoma de Madrid (SIdI-UAM)
Covadonga Agudo	Service technician; assistance with TEM studies of all materials presented	SIdI-UAM
Luis Larrumbe	Service technician; performance of FTIR studies of rGO MFs	SIdI-UAM
María José de la Mata	Service technician (Group leader); performance of TGA studies of rGO MFs	SIdI-UAM
Ana Zuzuarregui Olasagasti	Service technician; performance of Raman spectroscopy studies of rGO MFs	CIC nanoGUNE
Esperanza Salvador	Service technician (Group leader); acquisition of SEM images regarding	SIdI-UAM

	NWs	
Enrique Rodríguez	Service technician; acquisition of SEM images regarding nanoelectrodes and rGO materials	SIdI-UAM
Isidoro Poveda	Service technician; acquisition of FESEM images regarding NWs	SIdI-UAM
Gabriel Carro	Service technician; acquisition of SEM images regarding NWs	SIdI-UAM
Sylvia Gutiérrez	Service technician (Group leader); assistance with CLSM studies regarding NWs	Advanced Light Microscopy Service at the Centro Nacional de Biotecnología (CNB-CSIC)
Ana Oña	Service technician; assistance with CLSM studies regarding NWs	Advanced Light Microscopy Service at CNB-CSIC
Juan de los Reyes Aguilar	Collaborator (Group leader); assistance with calcium experiments on NWs substrates and ongoing functional studies with rGO scaffolds	HNP-SESCAM
Juliana M. Rosa	Collaborator; assistance with calcium experiments on NWs substrates	HNP-SESCAM
Marta Zaforas	Collaborator; assistance with ongoing functional studies with rGO scaffolds	HNP-SESCAM
Elena Fernández	Collaborator; assistance with ongoing functional studies with rGO scaffolds	HNP-SESCAM
Elena Alonso	Collaborator; assistance with ongoing functional studies with rGO scaffolds	HNP-SESCAM

List of publications associated to this thesis project

Domínguez-Bajo A, González-Mayorga A, López-Dolado E, *et al*. Graphene-derived materials interfacing the spinal cord: Outstanding *in vitro* and *in vivo* findings. *Front Syst Neurosci*. **2017**;11:71.
doi:10.3389/fnsys.2017.00071

Domínguez-Bajo A, González-Mayorga A, Guerrero CR, *et al.* Myelinated axons and functional blood vessels populate mechanically compliant rGO foams in chronic cervical hemisected rats. *Biomaterials*. **2019**;192:461-474. doi:10.1016/j.biomaterials.2018.11.024

Domínguez-Bajo A*, González-Mayorga A, López-Dolado, *et al.* Graphene oxide microfibers promote regenerative responses after chronic implantation in the cervical injured spinal cord. *ACS Biomater Sci Eng*. **2020;**6(4):2401–2414. doi:10.1021/acsbiomaterials.0c00345

Domínguez-Bajo A, Rodilla BL, Calaresu I, *et al*. Interfacing Neurons with Nanostructured Electrodes Modulates Synaptic Circuit Features [published online ahead of print, 2020 Aug 6]. Adv Biosyst. 2020;e2000117. doi:10.1002/adbi.202000117

Rodilla BL, **Domínguez-Bajo A**, Arché-Nuñez A, *et al*. Core/shell NWs structures as biocompatible nanoelectrodes for neural stimulation. **In preparation**.

Domínguez-Bajo A, Rodilla BL, González-Mayorga A, *et al*. Oriented Au nanoelectrode arrays as potential platforms for neural stimulation after spinal cord injury. **In preparation**.

Madroñero-Mariscal R, **Dominguez-Bajo A**, García-García F, *et al*. Feasibility of a human MRI clinical protocol for the assessment of morphological changes in a rat experimental model of spinal cord injury. **In preparation**.

Book chapter: Domínguez-Bajo A, González-Mayorga A, López-Dolado E, *et al.* General aspects of traumatic neural diseases and requirements of CNS implantable biomaterials as diagnostic and/or therapeutic tools, Editor(s): Elisa López-Dolado and M. Concepción Serrano. In Engineering biomaterials for neural applications: Traumatic brain and spinal cord injuries as targets. Springer-Nature. **In preparation**.

Other publications performed during my thesis period:

Book chapter: Viñambres Panizo M, **Domínguez-Bajo A**, Portolés MT, *et al*. Chapter 11 - Nonviral gene therapy: Design and application of inorganic nanoplexes. In micro and nano technologies, nucleic acid nanotheranostics. Editor(s): Marco Filice, Jesús Ruiz-Cabello. Elsevier, **2019**, pages 365-390, ISBN 9780128144701.
doi:10.1016/B978-0-12-814470-1.00011-3

Book chapter: Espinha A, **Domínguez-Bajo A**, González-Mayorga A, *et al*. Graphene-based composites with shape memory effect—Properties, applications, and future perspectives, **2019**. In Handbook of Graphene Set. Editor(s): E. Celasco, A.N. Chaika, T. Stauber, M. Zhang, C. Ozkan, C. Ozkan, U. Ozkan, B. Palys and S.W. Harun.
doi:10.1002/9781119468455.ch60

Fortes Brollo ME, **Domínguez-Bajo A**, Tabero A, *et al*. Combined magnetoliposome formation and drug loading in one step for efficient alternating current-magnetic field remote-controlled drug release. *ACS Appl Mater Interfaces*. **2020**;12(4):4295-4307.
doi:10.1021/acsami.9b20603

Girão AF, Sousa J, **Domínguez-Bajo A**, *et al.* 3D Reduced Graphene Oxide Scaffolds with a Combinatorial Fibrous-Porous Architecture for Neural Tissue Engineering [published online ahead of print, **2020** Aug 21]. ACS Appl Mater Interfaces. 2020;10.1021/acsami.0c10599.
doi:10.1021/acsami.0c10599

Basics of the experimental techniques used in this thesis

Atomic Force Microscopy (AFM)

AFM is a scanning technique employed for obtaining information about material mechanical properties (such as yield stress or hardness of the surface), and surface roughness and topography, among others. In a traditional AFM setup, the sample surface can be scanned by the tip of a cantilever under different conditions (in air, liquid, vacuum or gas conditions) [**Polini *et al.* 2017**]. Different modalities are used to study the above-mentioned features at the nanoscale:

- Contact mode: The cantilever tip is in contact and moves over the sample surface (in this case some damages can occur in fragile samples).
- Tapping mode (intermittent or dynamic) mode: The cantilever touches the surface while oscillating (*i.e.,* periodic contact of the tip with the sample surface).
- Non-contact mode: The cantilever oscillates on the surface but without touching it (this mode does not damage the surface of the samples).

Depending on the modality chosen, different forces can be involved and measured: Mechanical contact, van der Waals forces, chemical bonding, and electrostatic or magnetic interactions, among others. Indeed, in the last years, AFM modes have been improved to allow a better multiparametric analysis of biological systems. For more detailed information about AFM modes that can be used for the visualization and manipulation of biological entities, including cells, proteins and even single molecules, at the sub-nanometre scale, please refer to elsewhere [**Dufrêne *et al.* 2017**].

Confocal Laser Scanning Microscopy (CLSM)

Immunofluorescence is a technique used to detect the presence of specific components in a concrete cell and/or tissue structure (*i.e.*

immunofluorescence experiments can be done both in cell-cultured and/or tissue fixed samples). To perform these experiments, samples are first processed and fixed to preserve cellular integrity, and then subjected to incubation with blocking reagents to prevent non-specific binding of the antibodies. Samples are subsequently incubated with a primary antibody (that interacts in a very specific way with the element of interest), followed by the incubation with the secondary antibody (that will specifically recognize the first one) conjugated to a fluorochrome. This fluorochrome will be able to emit light when excited by a laser from a fluorescence microscope. Alternatively, primary antibodies can be already labelled with fluorochromes, so the use of secondary antibodies is eliminated. In any case, signal will be only visualized where the element of interest is present [**IHC/ICC Protocol Guide, R&D systems**]. In this thesis, immunofluorescence samples were visualized, and images were acquired by using CLSM. Fluorescence probes and dyes, able of emitting fluorescence for instance as a consequence of a structural change driven by binding to particular cellular/tissue components, can be also visualized and studied by using CLSM (as it was done in this thesis for viability studies, calcium imaging and cell nuclei labelling). In this case, the image obtained by using the confocal microscope is achieved by the point by point scanning of the emitted light of the fluorophores after being excited by a laser source. This scanning is done in all the points contained in the different z planes of the sample of interest (in this case, neural cells or spinal tissue). The points of laser incidence are focused on the sample by the objective lens. Once laser light reaches a specific point of the sample, the emitted light comes back through the objective, pass through a mirror and is focused onto the pinhole. Subsequently, this light is measured by a detector, which in this case corresponds to a photomultiplier tube. In this way, only the light from one point of the sample is detected at the same time. The output from the detector is built into an image and displayed by the

computer [**Rai *et al.* 2011**]. For more details about confocal microscopy, please refer to elsewhere [**Semwogerere and Weeks 2005**].

Fourier-Transform transform Infrared Spectroscopy (FTIR)

FTIR is an analytical technique to obtain information of the chemical composition of a compound/material. When materials are irradiated with FTIR light, IR radiation absorption occurs if the IR frequency matches with the vibrational frequency of a chemical bond present in the material structure. The absorbance frequencies are specific of concrete chemical groups (for example, -COOH and -OH) and their chemical environment (their adjacent chemical groups). Moreover, FTIR enables measuring all wavelengths of all chemical groups at the same time. Hence, the IR spectrum is used for the identification of unknown compounds, to speculate about the close intermolecular interaction of specific functional groups contained in the material, and to confirm the presence of chemical groups of the material under study [**Pradhan *et al.* 2017**]. The resulting spectra consist of a plot of absorption, transmission, or reflection intensity versus wavelength or frequency. There is a modality called attenuated total reflection FTIR (ATR-FTIR), frequently employed with biomaterials, where the penetration depth into the sample reaches 1-5 μm [**Omidi *et al.* 2017**]. So, ATR-FTIR monitors a broad region near the surface and still gives much structural information of the sample without destructing it. Moreover, micro-ATR (coupling a microscope, an IR spectrometer and a micro-ATR-crystal) permits ATR-FTIR analysis with high spatial resolution (approx. 1 μm^2 pixel size) [**Ratner, 2012**].

Hematoxylin and eosin staining (H&E)

H&E stain is one of the most commonly used techniques in histology and pathological anatomy laboratories for the study and analysis of the microanatomy of tissue frozen sections, fine needle aspirates (*e.g.* tumour biopsies) and paraffin-fixed embedded tissues. On the one hand, hematoxylin

stains nuclear components, including heterochromatin and nuclei, which will be seen in either dark blue or purple. On the other hand, eosin stains cytoplasmic components, muscle fibers and collagen, which will be marked in pinkish colour, as well as red blood cells in dark red. Hematoxylin is oxidized to haematein and subsequently combined with a mordant (*e.g.* metal ions that boost binding of the dye to the tissue), allowing the staining of chromatin in cell nuclei dark blue to black (haematein is a positively charged molecule that interacts with cell negatively charged components such as DNA). On the other hand, eosin is an acidic (negatively charged) compound which binds to basic compounds (positively charged) like proteins containing amino acid residues such as arginine and lysine, marking them pinkish or dark red. Structures that stain with eosin are called eosinophilic. There are many different H&E formulations in popular use, with various advantages or disadvantages depending on the specific components to be stained [**Sampias and Rolls tutorial; Myers tutorial – both Leica Biosystems; Cardiff *et al.* 2014**].

Live calcium imaging

The calcium ion (Ca^{2+}) is an essential intracellular messenger that regulates a multitude of different physiological pathways in mammalian cells, such as cell cycle (including proliferation), death, and communication. In this last case, for example, calcium triggers exocytosis of neurotransmitter-containing synaptic vesicles in presynaptic terminals of neural cells and is essential for the induction of activity-dependent synaptic plasticity by a transient rise of the calcium levels post-synaptically. When focused on neurons, calcium is contained within the cell in different cellular compartments (*e.g.* dendrites, cell body and presynaptic terminals), as either a free ion, bound to different proteins or retained within internal stores (mainly within the endoplasmic reticulum and mitochondria) [**Grienberger *et al.* 2012**] .

At any given moment, the cytosolic calcium concentration is determined by the balance between calcium influx and efflux, as well as by the exchanges with the internal stores. These ions movements are known as spontaneous calcium events and can be studied with the use of fluorescent indicators. Thus, the detection of these changes as transient elevations in the concentration of cytosolic free calcium ions in different cells of a neural network means that cells are active and connected to each other. There are many types of calcium indicators. One of the classifications divides calcium probes according to their spectral properties in ratiometric and non-ratiometric indicators (dual and single wavelength indicators, respectively). Ratiometric indicators have two excitation or two emission wavelength values, and they show a shift in their excitation or emission spectra after calcium binding. This allows us to obtain fluorescence intensity ratios that can be used to estimate calcium concentration present (in this case) in the cell cytoplasm. On the other hand, non-ratiometric indicators have only one excitation and one emission wavelength values. Thus, an increase in fluorescence intensity can be directly correlated (in this case) to an increase in intracellular calcium concentration. However, fluorescence intensity values obtained with non-ratiometric probes can be influenced by external factors, such as variations in probe loading and photobleaching, among others. This fact is minimized by using ratios when ratiometric indicators are applied. In this thesis, calcium indicators used (Oregon-Green and Fluo-4) are non-ratiometric chemical calcium indicators. Consequently, increases in fluorescence intensity upon binding to free Ca^{2+} ions observed are directly proportional to calcium concentration (more fluorescence intensity corresponds to more calcium bound), but $[Ca^{2+}]$ cannot be measured in a quantitative way because these indicators are non-ratiometric. For more detailed information about the different kinds of calcium indicators and their use, please refer to elsewhere [**Paredes *et al.* 2008; Ratiometric methods - embl**].

Magnetic Resonance imaging (MRI)

MRI is among the most used imaging techniques in clinical neurology for determining the degree of damage to the backbone and spinal cord tissue after SCI. This radiological tool is able of identifying spinal cord transection, hemisection and contusion signs, and help clinicians and researchers to evaluate the presence of oedema, syringomyelia (*i.e.* formation of fluid-filled cysts), hemorrage (*i.e.* hematomyelia) and other anomalies in the tissue (for example, examining areas with different intensity in comparison to control healthy tissue) such as ischemia, cell loss or gliosis, among others [**Ahuja *et al.* 2017**]. In our case, a clinically inspired MRI protocol was used to analyse the cervical spinal cord enlargement (*i.e.* metameres between the caudal part of C4 and the caudal part of T1) in order to:

- Obtain a morphological vision of the lesion site in injured animals (with or without rGO scaffolds).
- Search for radiological signs of damage directly or indirectly caused by the hemisection itself, if present.

From the physical point of view, nuclear magnetic resonance (NMR) is based in the fact that certain atomic nuclei, such as the hydrogen nucleus (^{1}H), possess a property known as "spin", which is dependent on the number of protons. These atomic nuclei can move or rotate in different directions and at different velocities, and these two parameters can be modulated by the application of a strong external magnetic field. Atomic nuclei that possess spin can be also excited by the application of a second radiofrequency (RF) magnetic field. The absorption of energy by each nucleus causes a transition from higher to lower energy and viceversa on relaxation. The energy absorbed (and subsequently emitted) by all the nuclei induces a voltage that can be detected by a coil of wire, amplified, and displayed as the "free-induction decay signal" (FID). In the absence of continued RF pulsation, relaxation processes will return

the system to the equilibrium. In practice, multiple RF pulses are applied to obtain multiple FIDs, which are averaged to obtain a better signal-to-noise ratio. This final averaged signal will be made up of contributions from different nuclei contained in the sample studied (in our case, the spinal cord fragment). The averaged FID can be resolved by a mathematical process known as Fourier transformation into an image, thus, giving what we know as MRI images. For more detailed physical and technical fundamentals, please refer to elsewhere [**Grover *et al.* 2015**].

Masson's trichrome staining

This staining is used for the histological visualization of collagenous connective fibers in tissue sections in a more specific way than conventional H&E. By using this procedure, one could distinguish collagen and bone in blueish-purple or green colour, keratin and muscle fibers in redish, cytoplasm in light red or pink, and cell nuclei in dark blue to black. The varied recipes evolved from Claude L. Pierre Masson's original formulation have different specific applications, but all are suited for distinguishing cells from surrounding connective tissue. The trichrome is applied by immersion of the fixated sample into Weigert's iron hematoxylin, and then three different solutions (A, B, and C) as follows. Weigert's hematoxylin (for cell nuclei) is a sequence of three solutions: ferric chloride in diluted hydrochloric acid, hematoxylin in 95% ethanol, and potassium ferricyanide solution alkalized by sodium borate. Solution A (for cytoplasms) contains acid fuchsin, Xylidine Ponceau, glacial acetic acid, and distilled water. Solution B contains phosphomolybdic acid in distilled water. Finally, solution C (for collagen fibre) contains methyl blue, water blue, Light Green SF yellowish or Fast Green FCF, depending on the preference of more blueish or greenish staining for collagen [**García del Moral Garrido, 1993**].

Raman spectroscopy

As well as FTIR, Raman spectroscopy is a non-destructive technique for investigating molecular vibrations which are specific to different chemical groups, due to the inelastic scattering of IR photons [**Polini *et al.* 2017**]. So, Raman is also based on the interaction of IR radiation with vibrational modes of the examined molecular system, providing complementary information to FTIR spectroscopy. In Raman spectroscopy a light with a determined energy is focused on the surface of the material; most of the light scatters back at the same frequency as the incident beam. However, a small fraction of this light excites vibrations in the sample, and thereby loses or gains energy. These changes of energy in material molecules can be represented by what is known as Raman lines, which in turn can be different depending on variations from an excited to a basal state or vice versa. The frequency shift of the light corresponds to vibrational bands indicative of the molecular structure of the specimen. A Raman spectrum is presented in the shape of intensity *vs.* wavelength shift. Raman spectra can be recorded over a range of 4,000–400 cm^{-1} [**Polini *et al.* 2017; Pradhan *et al.* 2017; Omidi *et al.* 2017; Mitić *et al.* 2017**].

Scanning Electron Microscopy (SEM)

SEM is one of the most common methods for imaging the microstructure, topography and surface morphology of materials, with the ability of obtaining images with magnifications from 10x to more than 300,000x [**Merrett *et al.* 2002**]. In this technique, an electron beam with low energy is radiated to the material and scans the surface of the sample, thus, the material under study must be (or be made) electrically conductive (for example, non-conductive materials can be analysed by SEM if they are coated with a thin layer of metals to make them conductive). Several kinds of interactions occur once the electron beam reaches and enters the material, like the emission of photons and electrons from (or near) the sample surface. These electrons can be detected to

obtain information about the sample. In the case of non-conductive materials, the coating metal layer must be thick enough so that the electrons emitted from the original covered sample cannot penetrate into it [**Ratner, 2012**]. Therefore, in SEM analyses of non-conductors, what is being monitored is the surface of the metal coating, which should reflect the material underneath. Furthermore, different modes of SEM exist for the characterization of materials, such as secondary electrons imaging, backscattered electrons imaging, X-ray mapping and cathodoluminescence. The most common imaging mode is secondary electrons imaging, which collects low-energy (< 50 eV) secondary electrons that are ejected from the atoms at the first few nanometres below the sample surface by inelastic scattering interactions with (primary) beam electrons. Alternatively, backscattered electrons (BSEs) consist of high-energy electrons originating in the electron beam that are reflected, or back-scattered, out of the sample by elastic scattering interactions with sample atoms. Since heavy elements (high atomic number) backscatter electrons more strongly than light elements (low atomic number), and thus appear brighter in the image, BSEs are used to detect contrast between areas with different chemical composition [**Goldstein *et al.* 1981**]. Both modes have been used in this thesis. Additionally, in this thesis, a variant of SEM, known as field emission SEM (FESEM), has been also used. FESEM works in the same way as SEM but it uses a different source of electrons and other kind of detectors, which allows the acquisition of high-quality images of higher magnification than SEM [**Erlandsen *et al.* 2016**].

Thermogravimetric analysis (TGA)

TGA is an experimental technique suitable for monitoring physical and chemical changes in the sample subjected to a controlled heating process [**Mitić *et al.* 2017**]. This technique can be used to study the material weight loss in a set temperature range, giving a temperature (or time) *vs.* mass (or mass percentage) plot [**Polini *et al.* 2017**]. This weight loss could be due to evaporation of volatile

components, loss of water contained in the sample, oxidative decomposition of organic substances and other heterogeneous chemical reactions [**Mitić *et al.* 2017**]. Thus, TGA is often used for determining the compositional analysis of samples, using adequate standards or reference plots. Additionally, TGA represents a useful tool to obtain information regarding thermal and oxidative stability, life expectancy, decomposition profile and moisture and volatiles content [**Polini *et al.* 2017**].

Transmission electron microscopy (TEM)

TEM is often used to acquire information about the morphology and certain aspects of the composition of materials and biological samples, providing high resolution images at the nanometer scale (or even less). In TEM, electrons are emitted from an electron gun and directed to the sample. Due to the interactions with the electrons, depending on the sample (or the specific structure of interest contained within the sample) density, some electrons undergo scattering, others absorption, and some others pass through it. In this case, the image intensity follows the sample density: the denser the sample, the fewer electrons pass through it, and the darker is the image generated (whilst thinner regions with no sample in the beam path appear bright) [**Omidi *et al.* 2017**]. In biocompatibility studies, this technique is also exploited for informing about the specific interaction of materials with cellular structures, such as in our case, the interaction (*e.g.* contact, uptake and/or degradation) of NWs electrodes and rGO structures in close contact with (or inside) different cell types.

X-ray Photoelectron Spectroscopy (XPS)

XPS, also called electron spectroscopy for chemical analysis (ESCA), provides qualitative and quantitative information about the chemical composition, chemical state (*e.g.* oxidation state) and electronic state of the surface of the material under study. After irradiation with X-rays of the sample under high vacuum conditions, the absorption of X-rays by atoms in the sample

causes the ejection of electrons (concretely core and valence electrons, called photoelectrons) which have energies that are unique for each element and sensitive to their chemical states. These electrons are collected by a detector, and a binding energy/signal intensity spectrum (*i.e.* the plot of the detected number of photoelectrons as a function of the binding energy) is given, where the electron binding energy is determined by the difference of the photon energy and the sum of the electron kinetic energy and the work function (which depends on the material and the instrument, and is an adjustable instrumental correction factor). The binding energy of electrons is characteristic of each element, but it is also affected by the formal oxidation state, the local bonding environment (such as the nearest-neighbour atoms), and the bonding hybridization to the nearest-neighbour atoms, among others. The peak intensity of the spectrum is a direct measure of the elemental concentration and provides information on chemical bonding as well. So, a comparison of the position and shape of the peaks with standard spectra from libraries of elements provide researchers information of specific elements at the surface of the sample and their binding state, as the depth of the detection is on the order of 1-10 nm [**Polini *et al.* 2017; Omidi *et al.* 2017; Ratner, 2012; Mitić *et al.* 2017**].

References on fundamentals of the techniques used in this thesis

Ahuja CS, Wilson JR, Nori S, *et al.* Traumatic spinal cord injury. *Nat Rev Dis Primers*. 2017;3:17018. doi:10.1038/nrdp.2017.18

Cardiff RD, Miller CH, Munn RJ. Manual hematoxylin and eosin staining of mouse tissue sections. *Cold Spring Harb Protoc*. 2014;2014(6):655-658. doi:10.1101/pdb.prot073411

Dufrêne YF, Ando T, Garcia R, *et al.* Imaging modes of atomic force microscopy for application in molecular and cell biology. *Nat Nanotechnol.* 2017;12(4):295-307. doi:10.1038/nnano.2017.45

Erlandsen SL, Frethem C, Chen Y. Field emission scanning electron microscopy (FESEM) entering the 21st century: Nanometer resolution and molecular

topography of cell structure. *J Histotechnol*. 2000;23(3):249-259. doi: 10.1179/his.2000.23.3.249

García del Moral Garrido R. Laboratorio de anatomía patológica. Procedures for demonstration of the existence of collagen fibers – Masson's trichrome (pages 176 – 178). 1993, Interamericana-McGraw-Hill.

Goldstein GI, Newbury DE, Echlin P, *et al*. Scanning electron microscopy and X-ray microanalysis. 1981. New York: Plenum Press.

Grienberger C, Konnerth A. Imaging calcium in neurons. Neuron. 2012;73(5):862-885. doi:10.1016/j.neuron.2012.02.011

Grover VP, Tognarelli JM, Crossey MM, *et al*. Magnetic resonance imaging: Principles and techniques: Lessons for clinicians. *J Clin Exp Hepatol.* 2015;5(3):246-255. doi:10.1016/j.jceh.2015.08.001

IHC/ICC Protocol Guide, R&D systems: https://resources.rndsystems.com/images/site/rnd-systems-ihc-protocol-br.pdf. Last retrieval: 24/03/2020.

Merrett K, Cornelius RM, McClung WG, *et al*. Surface analysis methods for characterizing polymeric biomaterials. *J Biomater Sci Polym* Ed. 2002;13(6):593-621. doi:10.1163/156856202320269111

Mitić Ž, Stolić A, Stojanović S, *et al*. Instrumental methods and techniques for structural and physicochemical characterization of biomaterials and bone tissue: A review. *Mater Sci Eng C Mater Biol Appl*. 2017;79:930-949. doi:10.1016/j.msec.2017.05.127

Myers R. tutorial – Leica Biosystems: https://www.leicabiosystems.com/knowledge-pathway/the-basic-chemistry-of-hematoxylin/. Last retrieval: 23/04/2020

Omidi M, Fatehinya A, Farahani M, *et al*. Chapter 7: Characterization of biomaterials, Editor(s): Lobat Tayebi, Keyvan Moharamzadeh, Biomaterials for oral and dental tissue engineering, Woodhead Publishing, 2017, Pages 97-115, ISBN 9780081009611. doi:10.1016/B978-0-08-100961-1.00007-4

Paredes RM, Etzler JC, Watts LT, *et al.* Chemical calcium indicators. *Methods*. 2008;46(3):143-151. doi:10.1016/j.ymeth.2008.09.025

Polini A, Yang F. Chapter 5: Physicochemical characterization of nanofiber composites, Editor(s): Murugan Ramalingam, Seeram Ramakrishna, Nanofiber composites for biomedical applications, Woodhead Publishing, 2017, Pages 97-115, ISBN 9780081001738. doi: 10.1016/B978-0-08-100173-8.00005-3

Pradhan S, Rajamani S, Agrawal G, *et al.* Chapter 7: NMR, FT-IR and raman characterization of biomaterials, Editor(s): Maria Cristina Tanzi, Silvia Farè, Characterization of Polymeric Biomaterials, Woodhead Publishing, 2017, Pages 147-173, ISBN 9780081007372. doi:10.1016/B978-0-08-100737-2.00007-8

Rai V, Dey N. The basics of confocal microscopy, laser scanning, theory and applications, 2011, Chau-Chang Wang, IntechOpen, doi:10.5772/16214. Available from: https://www.intechopen.com/books/laser-scanning-theory-and-applications/the-basics-of-confocal-microscopy

Ratiometric methods – embl: https://www.embl.de/eamnet/html/calcium/ratio.htm. Last retrieval: 19/05/2020.

Ratner BD. Chapter I.1.5 - Surface properties and surface characterization of biomaterials, Editor(s): Buddy D. Ratner, Allan S. Hoffman, Frederick J. Schoen, Jack E. Lemons, Biomaterials Science (Third Edition), Academic Press, 2013, Pages 34-55, ISBN 9780123746269. doi:10.1016/B978-0-08-087780-8.00005-X

Sampias C, and Rolls G tutorial - Leica Biosystems: https://www.leicabiosystems.com/knowledge-pathway/he-staining-overview-a-guide-to-best-practices/. Last retrieval: 23/04/2020.

Semwogerere D, Weeks E. Confocal microscopy. Encyclopedia of biomaterials and biomedical engineering,2005. doi:10.1081/E-EBBE-120024153

Other studies which explore implants based on different biomaterials discussed in this thesis.

Material	Lesion		Animal model	Time of implantation after SCI	Timepoint of study PI (*in vivo* biocompatibility/tissue regeneration results)	Reference
	level	type				
PLL/heparin/bFGF/fibronectin-functionalized PEDOT-MFs + Alginate gel to facilitate microfiber implantation	T10 - T11	Transection	Wistar rats	Right after SCI	2 months: reduced cavity size, vascular remodelling, signs of axonal regeneration, no exacerbation of fibrotic, glial, and immune responses	Alves-Sampaio *et al.* 2016
Chitosan based hydrogels + MSCs	T13	Transection	C57BL/6 J mice	Right after SCI	7 days: good integration of MSCs, no astrogliosis, no increased immune response	Boido *et al.* 2019
Copolymer of poly(N-isopropylacrylamide)-poly(ethylene glycol): (PNIPAAm-g-PEG hydrogel)	C2	Hemisection	Sprague Dawley rats	Right after SCI	Most studies after 12 weeks: better behavioural outcome, lesion cavity filled, signs of neuronal regeneration, no glial cells at the lesion site, no exacerbation of immune response; no signs of material degradation.	Bonnet *et al.* 2020
Hydroxyl ethyl methacrylate [2-(methacryloyloxy)ethyl] trimethylammonium chloride (HEMA-MOETACL) hydrogel + bFGF	T9	Transection	Sprague–Dawley rats	5 days after transection surgery	8 weeks: improvements in motor outcome, reduced lesion cavity, vascular remodelling, signs of neuronal regeneration, no exacerbation of glial response	Chen *et al.* 2015
Photocrosslinked gelatin methacryloyl (GelMA) hydrogel microfibers	T9	Hemisection	Sprague–Dawley rats	Right after SCI	12 weeks: motor improvements, vascular reorganization, signs of neuronal regeneration, no exacerbation of glial response	Chen *et al.* 2019
Peripheral nerve graft bridge (PNG) + aFGF + ChABC	T8	Contusion	Sprague–Dawley rats	8 weeks (removal of injured tissue for material implantation)	32 weeks after material implantation: signs of neuronal regeneration, no exacerbation of glial response, some astrocytes at the lesion site to aid tissue restoration	DePaul *et al.* 2017
Collagen scaffold functionalized + collagen-binding EGFR antibody Fab fragment (CBD-Fab)	T8	Transection	Sprague–Dawley rats	Right after SCI	12 weeks: improved motor recovery, reduced lesion cavity, signs of axonal regeneration	Fan *et al.* 2017
Cyclosporine-A-loaded PLGA/polymeric liposomes	T10	Contusion	Wistar rats	1 day after – Not directly implanted at the spinal cord but tail vein injection	10 days after SCI: motor recovery, signs of neural regeneration	Gao *et al.* 2016
Alginate + EGF + bFGF	T8-T9	Compression	Wistar rats	7 days after SCI (injection in the lesion cavity found)	Most studies 7 weeks after mat implantation: improved motor outcome, reduced lesion cavity, vascular and neural remodelling, no exacerbation of glial response	Grulova *et al.* 2015
Agarose scaffolds containing multiple linear channels	T9-T10	Removal of the dorsal part of the entire segment of the SC	Sprague–Dawley rats	Right after SCI	4 weeks: better motor outcome, signs of neuronal regeneration	Han *et al.* 2018
Porcine brain decellularized extracellular matrix (dECM)	T9	Contusion	Sprague–Dawley rats	30 min after contusion	8 weeks: improved locomotor activity, reduced lesion cavity, vascular and axonal remodelling, attenuation of the immune response	Hong *et al.* 2020
Aligned PLA microfibers	T9-T10	Transection	Sprague–Dawley rats	Right after SCI	4 weeks: vascular and neural regeneration, few astrocytes at lesion epicentre	Hurtado *et al.* 2011
Phosphate-based glass fibers (PGFs) filled with collagen	T9	Transection	Sprague–Dawley rats	Right after SCI	12 weeks: better behavioural outcome, signs of axonal regeneration, no exacerbation of glial and immune responses	Joo *et al.* 2012
PEGylated graphene nanoribons	L1	Transection	Sprague–Dawley rats	Right after SCI	5 weeks: improved locomotor activity, neural regeneration, reduced glial reactivity	Kim *et al.* 2018
μCPP 3D-printed scaffolds (PEG–GelMa scaffolds) + NPCs	T3	Transection	Fischer rats	Right after SCI	4 weeks and 6 months: astrocytes within the scaffold, neural regeneration, good NPCs integration and differentiation towards glial phenotypes	Koffler *et al.* 2019
SIKVAV-modified highly superporous poly(2-hydroxethyl methacrylate) (PHEMA) hydrogels	T8	Transection	Wistar rats	1 week after SCI	2 and 6 months: good integration, signs of vascular and neural regeneration, no astrocytes at the lesion site	Kubinová *et al.* 2016
Porous collagen scaffold + (CBD-EphA4LBD, CBD-PlexinB1LBD and NEP1-40) + collagen-binding neurotrophic factors (CBD-BDNF and CBD-NT3) + cAMP administration	T10	Transection	Sprague–Dawley rats	Right after SCI	12 weeks: better motor outcome, reduced lesion cavity, signs of axonal regeneration, attenuation of the immune response	Li *et al.* 2016
hUC-MSCs seeded collagen scaffolds (NeuroRegen)	T8	Transection	Beagle dogs	2 months after SCI	6 months and 1 year: improvements in motor behaviour, signs of axonal regeneration	Li *et al.* 2017

PTX-encapsulated liposomes into a collagen microchannel scaffold + NSC	T8	Transection	Sprague–Dawley rats	Right after SCI	8 weeks: better behavioural outcome, signs of neuronal regeneration, reduced amount of astrocytes at the lesion site	Li *et al.* 2018
aligned poly (ε -caprolactone-co-ethyl ethylene phosphate) (PCLEEP) electrospun nanofibers within a collagen matrix	C5	Hemisection	Sprague–Dawley rats	Right after SCI	4 weeks: good material integration, signs of neuronal regeneration, no exacerbation of glial response	Nguyen *et al.* 2017
Chitosan scaffold + NT-3	T7-T8	Transection	Wistar rats	Right after SCI	3 months: better motor outcome, signs of axonal regeneration, no astrocytes at the lesion epicentre	Oudega *et al.* 2019
methylcellulose hydrogel (XMC) + ChABC + stromal cell-derived factor 1a (SDF)	T1-T2	Compression	Sprague–Dawley rats	Right after SCI	2 and 8 weeks post injury: Improved locomotor outcome	Pakulska *et al.* 2017
graphene oxide -incorporated PLGA (PLGA/GO) nanofibers + IGF-1 + BDNF	T9-T10	Hemisection	Sprague–Dawley rats	Right after SCI	4 weeks: improved locomotor outcome, reduced cavity size, signs of neuronal regeneration	Pan *et al.* 2019
PEG-functionalized 40-nm-AuNPs	T8-T10	Compression	C57BL/6J mice	Right after SCI	4, 6 and 8 weeks: improved locomotor outcome, signs of axonal regeneration, no exacerbation of glial and immune response	Papastefanaki *et al.* 2015
poly(lactide-co-glycolide) (PLG) bridges with oriented channels/pores	C4-C5	Hemisection	C57Bl6 mice	Right after SCI	10 weeks: improved motor outcome, signs of neural regeneration	Pawar *et al.* 2015
Chitosan scaffolds + NT3	T8	Hemisection	Rhesus monkeys	Right after SCI	From 1 month to 2 years: revascularization, neuronal tissue regeneration, attenuation of glial and immune responses; the scaffold was degraded at the end of the study	Rao *et al.* 2018
PCL–PLGA based scaffolds + self-assembling peptide Ac-FAQ	T9 – T10	2 independent incision sites (right and left sides of the spinal cord)	Sprague–Dawley rats	Right after SCI	1 month: attenuated host response	Raspa *et al.* 2016
PCL microchannel Scaffolds	T3	Transection	Fischer rats	Right after SCI	4 weeks: signs of axonal regeneration	Shahriari *et al.* 2017
PGA-based scaffold + NPCs	T10–T11	Transection	Sprague–Dawley rats	Right after SCI	6 to 16 weeks: improved locomotor outcome, reduced lesion cavity, vascular remodelling, good integration and differentiation of NPCs for neuronal tissue restoration, decreased number of astrocytes at the lesion, attenuation of immune response; scaffold was degraded after 8 weeks	Shin *et al.* 2018
Embedding conductive polypyrrole in an electrospun polylactic acid nanofibrous scaffold (PLA/PPy)	T9	Transection	Sprague–Dawley rats	Right after SCI	1 to 6 weeks: improved locomotor outcome, signs of neuronal regeneration, decrease amount of glial cells	Shu *et al.* 2019
Block copolymer of PLGA and PLL	T9-T10	Hemisection	Non-human Old-World primates	Right after SCI	12 weeks: lesion colonization, neural regeneration, decrease in the amount of astrocytes and no exacerbation of the immune response	Slotkin *et al.* 2017
Collagen-based microfibers + NS/PCs	T9-T10	Transection	C57BL/6J mice	Right after SCI	6 – 11 weeks: good integration and differentiation of the NS/PCs; implant degraded after 11 weeks	Sugai *et al.* 2015
Matrigel scaffold + NSCs	T10	Contusion	Sprague–Dawley rats	1 week after SCI	4 weeks post transplantation: vascular and neural remodelling	Wang *et al.* 2020
Tubular HA hydrogel + anti-Nogo receptor antibody (antiNgR) + PLGA microspheres loaded with BDNF and VEGF	T9-10	Hemisection	Sprague–Dawley rats	Right after SCI	Different timepoints from 2 to 14 weeks after SCI: locomotor recovery, reduced lesion cavity, signs of vascular and neuronal regeneration, attenuation of glial and immune responses	Wen *et al.* 2015
Collagen + collagen-binding epidermal growth factor receptor antibody (collagen + CBD-EGFR-Fab)	T8	Transection	Sprague–Dawley rats	Right after SCI	12 weeks: better locomotor outcome, signs of neural regeneration	Xu *et al.* 2017
Acellular spinal cord scaffold + bFGF encapsulated into a heparin modified poloxamer: bFGF-ASC-HP hydrogel	T9-T10	Hemisection	Sprague–Dawley rats	Right after SCI	28 days: signs of axonal regeneration, attenuation of the glial response	Xu *et al.* 2016
PLGA + Schwann cells + MSCs	T9-T10	Transection	Sprague–Dawley rats	Right after SCI	4 and 8 weeks: improved locomotor behaviour, less cavity size, good integration and differentiation of implanted cells for neural regeneration	Yang *et al.* 2017
PCL/PSA hybrid nanofiber scaffold + methylprednisolone	T10	Transection	Sprague–Dawley rats	Right after SCI	7 weeks: motor improvements, signs of neuronal regeneration, attenuation of glial and immune responses	Zhang *et al.* 2018
biocompatible conducting polymer hydrogel based on a plant-derived polyphenol, tannic acid, cross-linking and doping conducting polypyrrole chains	T9-T10	Hemisection	C57BL/6N mice	Right after SCI	2 and 6 weeks: motor improvements, reduced cyst cavity, signs of neuronal regeneration, attenuation of glial and immune responses	Zhou *et al.* 2018

*PI: post-injury.